Atomistic simulation of bio-relevant ionic and organic species interacting with rutile - Towards the understanding of apatite formation

THÈSE N^{O} 8872 (2018)

PRÉSENTÉE LE 10 DÉCEMBRE 2018
À LA FACULTÉ DES SCIENCES ET TECHNIQUES DE L'INGÉNIEUR
LABORATOIRE DE TECHNOLOGIE DES POUDRES
PROGRAMME DOCTORAL EN SCIENCE ET GÉNIE DES MATÉRIAUX

ÉCOLE POLYTECHNIQUE FÉDÉRALE DE LAUSANNE

POUR L'OBTENTION DU GRADE DE DOCTEUR ÈS SCIENCES

PAR

Azade YAZDAN YAR

acceptée sur proposition du jury:

Prof. C. Hébert, présidente du jury
Prof. P. Bowen, Prof. U. Aschauer, directeurs de thèse
Prof. M. Predota, rapporteur
Dr T. J. Wooster, rapporteur
Prof. E. Amstad, rapporteuse

ÉCOLE POLYTECHNIQUE
FÉDÉRALE DE LAUSANNE

Suisse
2018

To my loved ones.

“It can’t be that you’d be there, and I don’t become your follower
It can’t be that you’d be there as you are,
and I don’t try to be kinder than who I am
or don’t fall deep in love with you.
It can’t be, I know
for spring to be greener than you are …”
Nader Ebrahimi (Mitra Asadollahi)

"نمی‌شود که تو باشیٍ، من عاشق تو نباشم
نمی‌شود که تو باشی درست همین طور که هستی
و من، هزار بار خوب‌تر از این باشم
و باز، هزار بار، عاشق تو نباشم.
نمی‌شود، می‌دانم
نمی‌شود که بهار از تو سبزتر باشد ..."
نادر ابراهیمی

Acknowledgement

First and foremost, I would like to express my sincere gratitude to my supervisor, Prof. Paul Bowen, for giving me the opportunity to join his group and undertake this Ph.D. thesis. Working with him has helped me to thrive scientifically, but also personally.

I would like to sincerely thank my co-director, Prof. Ulrich Aschauer, who always provided me with valuable remarks and insights. I would like to thank him for his continuous guidance over the course of my Ph.D. thesis. Aside from the splendid scientific experience, which I have gained from working under the supervision of my two directors, I look up to both of them and cherish their friendship.

I would like to thank Prof. Heinrich Hofmann, as well as Prof. Karen Scrivener, the heads of LTP and LMC, who both welcomed me in their dynamic and friendly groups. Working in their groups exposed me to other research topics than my own, which I value immensely. I would also like to thank the secretaries of both laboratories for helping me with all the, maybe not always but most of the times administrative, tasks especially Ms. Anne Remillet.

I would like to thank all my past and current colleagues at LTP, PTG and LMC with whom I have certainly spent a lot of time at work, but also share a lot of memories outside work. In specific, I would like to thank Irena, Nadia, Débora, Jirawan, Silvia, Weitian, Abhishek K., Marijana, Milica, Lionel, Sami, Amar, Aurélie, David, Gabie and Masood, who made the passage of time all the much more delightful. I would like to thank my past and current office-mates Aslam, Sandra and Abhishek T. for their friendship but also their helpful scientific discussions, at the beginning of my Ph.D. thesis, and still to date. They always helped me to approach problems with refined ideas.

I would like to thank the group members of my co-director Uli in Bern, Silviya, Maria, Hassan, Chiara and Nathalie, who always welcomed me for my visits to the University of Bern but also uplifted my spirit with their visits in EPFL.

I would like to thank all the students with whom I had the opportunity to work who helped me to understand better other aspects of my Ph.D. thesis, than what I could focus on.

I would like to high five all my friends, who have always made me Laugh Out Loud. They have always reminded me of the cheerful layers of life. In specific, I would like to thank Behzad, Behnoush, Saleh, Ehsan, Farzan, Ali, Nakisa, Vesal, Shahla, Iran, Marjan, Elham and Aida.

My special thanks go to my dear Saeed for his devotion, everlasting encouragement and delightful companionship. Without him, reaching this point would have been all the more challenging.

I am forever indebted to my wonderful family. Their unconditional love and support have always given me the courage to push myself further. My greatest thanks go to my parents, Fakhri and Ali, who most importantly have taught me the value of thinking and caring. I would like to also thank my siblings and in-laws, for always being there for me and the joy they bring to my life, day in day out. I would like to mention my lovely nephew, Ermia, and niece-to-be, Sarah, with whom I impatiently long to reunite, not for their assistance on any matter but rather their joyful presence.

Azade,
June 11, 2018
Écublens

آزاده،
۲۱ خرداد ۱۳۹۷

Abstract

Scientific research has been able to expand the range of biomaterials used in human life successfully. Although materials used for bio-applications are primarily chosen based on their features and characteristics, researchers have not always been able to justify why some materials perform a particular function better than others. Specific functions can either be evaluated by *in vivo* tests where the sample is tested in a living body, or *in vitro* where the sample is tested in a laboratory setting. While *in vivo* tests provide the true performance of a prototype biomaterial, the accuracy of *in vitro* results is limited by the extent to which the *in vivo* conditions are reproduced. Lower cost, the requirement of less expertise and also the important fact that sacrifice of living bodies is avoided *in vitro*, makes *in vitro* testing very attractive. Nevertheless, their limitations in fully reproducing *in vivo* conditions, which in fact has led to discrepancies between *in vivo* and *in vitro* results, still keep the *in vivo* testing very much in the picture.

The focus of this thesis is on apatite formation of titanium-based biomaterials, which are widely used as dental and orthopedic applications. Apatite (a calcium-phosphate mineral) formation on the surface of the biomaterial has been stated to be a measure of the bioactivity. *In vitro*, the ISO standard for evaluation of the apatite formation, or the apatite-forming ability, is via immersing the sample in a solution (SBF – Simulated Body Fluid) similar to human blood plasma in its ionic content. Encouraged by the assets of the *in vitro* method, and to identify parameters which should be treated more carefully *in vitro*, to have a better realization of the *in vivo* condition, this thesis is undertaken in an *in silico* framework.

Atomistic simulation methods, namely molecular dynamics and well-tempered metadynamics, are used in this thesis to investigate apatite formation from different aspects. First, ions which are more abundant in SBFs under physiological conditions were identified and their interaction with the rutile surface was studied. Using free energy calculations, it was possible to identify ions with a favorable interaction with the rutile surface. Among the ionic species which were studied, potassium, sodium, calcium, carbonate and phosphate showed favorable adsorption on the surface. Consequently, these ions may either adsorb on the surface prior to apatite formation, and promote or inhibit it, or may be involved in the apatite formation. Further studies revealed that adsorption of phosphate either in the form of an ionic pair with a calcium ion, or either on a pre-adsorbed calcium on the surface is very favorable, indicating that the current apatite formation mechanism proposed experimentally is reasonable.

Adsorption of several amino acids on the rutile surface was studied and the energetics of the adsorption events were quantified. Initially, the distance between the center of mass of the amino acid from the surface was chosen as the reaction coordinate, which is commonly used. However, the affinity of different amino acids for the surface based on different adsorption conformations could not be explained by this collective variable. The reweighting method was used to project the free energy profile to a two-dimensional phase space, in which energetics of different adsorption conformations, be via the side group, via the backbone, or via both, could be distinguished. It was observed that electrostatic forces between the surface charge point and the backbone group (amine group in specific) lead to the adsorption of amino acids on the surface via their backbone and irrespective of the nature of the side group. However, non-polar side groups did not lead to the adsorption of the amino acids while adsorption via the polar (Ser) and charged side groups (Arg, Lys and Asp) was favored, and the strongest when the charge of the side group was opposite to the charge of the surface.

The effect of pre-adsorbed species on the adsorption of other species on the surface was studied. Results revealed that the Arg and Asp amino acids did not affect the adsorption of ions of interest on the surface, destructively. Calcium and phosphate were both able to compete with the pre-adsorbed amino acids for the charge point on the rutile surface and successfully adsorb in the vicinity of the charge point. Amino acids were also unable to disturb the pre-adsorbed calcium ions on the surface, suggesting that single amino acids do not significantly inhibit apatite formation.

Finally, the adsorption of the TBP hexapeptide on the rutile surface was studied and different adsorption conformations were reported. Comparison with those previously reported in the literature, revealed that the adsorption conformations of TBP are mostly driven by the surface charge density and not the structure of the titanium oxide surface (its crystallinity or the crystallographic surface).

Keywords: Apatite formation, Rutile, Atomistic simulation, Free energy calculations, Interfaces

Résumé

La recherche scientifique a été en mesure d'élargir la gamme de biomatériaux utilisés dans la vie humaine avec succès. Bien que les matériaux utilisés pour les bio-applications sont principalement choisis en fonction de leurs caractéristiques, les chercheurs n'ont pas toujours réussi à justifier pourquoi certains matériaux remplissent une fonction particulière mieux que d’autres. Certaines fonctions peuvent être évaluées par des tests *in vivo* où l'échantillon est testé dans un organisme vivant, ou *in vitro* par lequel l'échantillon est testé en dehors de l’organisme, dans un laboratoire. Tandis que les tests *in vivo* fournissent la vraie performance d'un biomatériau prototype, la précision des résultats *in vitro* est limitée dans la mesure où les conditions *in vivo* sont plus ou moins reproduites. De par leur faible coût, la nécessité d’une expertise moindre et du fait que le sacrifice d’êtres vivants est évité, les tests *in vitro* sont toujours aussi attrayants. Néanmoins, la reproduction complète des conditions *in vivo* étant limitée - voir impossible - *in vitro*, il est difficile d’éviter les incohérences entre les résultats *in vivo* et *in vitro*, les tests *in vivo* demeurent donc au premier plan.

L'objectif de cette thèse est l’étude de la formation d'apatite sur des biomatériaux à la base de titane, qui sont largement utilisés en applications dentaires et orthopédiques. La formation d'apatite (un minéral de phosphate et de calcium) à la surface du biomatériau est considérée comme une mesure de la bioactivité. *In vitro*, la norme ISO pour l'évaluation de la formation d'apatite, ou capacité de formation d'apatite, consiste à immerger l'échantillon dans une solution (SBF - Simulated Body Fluid) similaire au plasma sanguin dans son contenu ionique. Encouragée par les atouts de la méthode *in vitro*, et dans le but d'identifier les paramètres qui devraient être traités plus soigneusement *in vitro*, permettant ainsi une meilleure réalisation des conditions *in vivo*, cette thèse est menée en utilisant une approche *in silico*.

Les méthodes de simulation atomistique, à savoir la dynamique moléculaire et la métadynamique bien tempérée, sont utilisées dans cette thèse pour étudier les différents aspects de la formation de l'apatite. Dans un premier temps, les ions qui sont plus abondants dans les SBFs dans des conditions physiologiques ont été identifiés et leurs interactions avec la surface du rutile a été étudiée. En utilisant des calculs d'énergie libre, il a été possible d'identifier les ions ayant une interaction favorable avec la surface du rutile. Parmi les espèces ioniques étudiées, le potassium, le sodium, le calcium, le carbonate et le phosphate ont montré une adsorption favorable à la surface. Par conséquent, ces ions peuvent soit s'adsorber sur la surface avant la formation d'apatite et favoriser ou inhiber, soit être impliqués dans la formation d'apatite. D'autres études ont montré que l'adsorption du phosphate soit sous la forme d'une paire ionique avec un ion calcium, soit sur un calcium pré-adsorbé sur la surface est très favorable, indiquant que le mécanisme actuel de formation d'apatite proposé expérimentalement est raisonnable.

L'adsorption de plusieurs acides aminés sur la surface du rutile a été étudiée et l'énergie des événements d'adsorption a été quantifiée. Initialement, la distance entre le centre de masse de l'acide aminé et la surface a été choisie comme coordonnée de la réaction, ce qui est couramment utilisée. Cependant, l'affinité des différents acides aminés pour la surface, basée sur différentes conformations d'adsorption, n'a pas pu être expliquée par cette variable collective. La méthode de repondération a été utilisée pour projeter le profil d'énergie libre dans un espace de phase bidimensionnel, dans lequel l'énergétique de différentes conformations d'adsorption, soit via le groupe latéral, via le squelette, soit via les deux, pouvait être distinguée. Il a été observé que les forces électrostatiques entre le point de charge de surface et le groupe squelette (spécifique du groupe amine) conduisent à l'adsorption des acides aminés sur la surface via leur squelette, quelle que soit la nature du groupe latéral. Par ailleurs, les groupes latéraux non polaires n'ont pas conduit à l'adsorption des acides aminés tandis que l'adsorption par les groupes latéraux polaires (Ser) et chargés (Arg, Lys et Asp) a été favorisée, et la plus forte lorsque la charge du groupe latéral était opposée à la charge de la surface.

L'effet des espèces pré-adsorbées sur l'adsorption d'autres espèces à la surface a été étudié. Les résultats ont révélé que les acides aminés Arg et Asp n'ont pas affecté l'adsorption des ions d'intérêt sur la surface de manière destructive. Le calcium et le phosphate étaient tous les deux capables de rivaliser avec les acides aminés pré-adsorbés pour le point de charge sur la surface du rutile et de s'adsorber avec succès en voisinage du point de charge. Les acides aminés étaient également incapables de perturber les ions calcium pré-adsorbés sur la surface, suggérant que les acides aminés à eux seuls n'inhibent pas significativement la formation d'apatite.

Finalement, l'adsorption de l'hexapeptide TBP sur la surface du rutile a été étudiée et différentes conformations d'adsorption ont été rapportées. La comparaison avec celles précédemment publiées dans la littérature, a montré que les conformations d'adsorption de TBP sont principalement dirigées par la densité de charge de surface et non la structure de la surface d'oxyde de titane (sa cristallinité ou la surface cristallographique).

Mots clés : Formation d'apatite, Rutile, Simulation atomistique, Calcul d'énergie libre, Interfaces

Contents

List of Abbreviations

AA	Amino acid
ACP	Amorphous calcium phosphate
AFA	Apatite-forming ability
BMP2	Bone morphogenetic protein-2
BSA	Bovine serum albumin
CV	Collective variable
DFT	Density functional theory
ECM	Extracellular matrix
EED	End-to-end distance
EM	Energy minimization
FN	Fibronectin
HAp	Hydroxyapatite
HSA	Human serum albumin
HSC	High surface charge density
ISO	International standard organization
LF	Lactoferrin
LJ	Lennard-Jones
LSC	Low surface charge density
MD	MD: Molecular dynamics
MM	Molecular mechanics
PBC	Periodic boundary conditions
PP	Polypeptide
QM	Quantum mechanics
RAD	The Arg-Ala-Asp sequence
REST	Replica exchange solute tempering
RGD	The Arg-Gly-Asp sequence
SBF	Simulated body fluid
SCA	Side-chain analogues
SPC/E	Extended simple point charge
SSD	Surface separation distance
TBP	Titanium-binding peptide (RKLPDA: the Arg-Lys-Leu-Pro-Asp-Ala sequence)
THS	A triple helical segment
TIP3P	Three-site transferable intermolecular potential
TIP4P	Four-site transferable intermolecular potential
WT-MTD	Well-tempered metadynamics
MD	MD: Molecular dynamics

Amino acids and their abbreviation

Ala	A	Alanine
Arg	R	Arginine
Asn	N	Asparagine
Asp	D	Aspartic acid
Cys	C	Cysteine
Gln	Q	Glutamine
Glu	E	Glutamic acid
Gly	G	Glycine
His	H	Histidine
Ile	I	Isoleucine
Leu	L	Leucine
Lys	K	Lysine
Met	M	Methionine
Phe	F	Phenylalanine
Pro	P	Proline
Ser	S	Serine
Thr	T	Threonine
Trp	W	Tryptophan
Tyr	Y	Tyrosine
Val	V	Valine

Chapter 1 Introduction

The purpose of this chapter is to introduce the subject under study to the reader and to put the thesis into context. The goals of the thesis are discussed and the structure of the thesis is presented.

1.1 Biomaterials

Biomaterials can be used for different purposes; they can accelerate the healing process or can be used as a replacement for a damaged organ or tissue. Further developments in the field of biomaterials can increase life expectancy. Such developments can address various features or functionalities of biomaterials. For example, a new material/alloy/composite can be tested and prove to perform better than the conventional biomaterials for a specific application. Also, modifications on current biomaterials can lead to a better performance.

Biomaterials should have specific properties. Although their implantation in the body is inevitably accompanied by perturbation, after implantation, they should be biocompatible, which means their benefits should outweigh their harmfulness. They should not be toxic (except in cases where they are required to; *e.g.*, smart bombs in drug delivery for removing cancer cells). They should have wear resistance, as well as corrosion resistance, to avoid unwanted debris being released into the body. Their mechanical properties should be similar to the tissue or organ where they are used. Clearly, they should show the desired response for their application, once implemented in the body. In conclusion, the biomaterial should not cause unexpected or uncontrollable harmful effects in the body and perform the desired functionality (1).

Metals, ceramics and polymers can be used as biomaterials depending on the application. Metals are favorable due to their appropriate biocompatibility, good corrosion resistance and reasonable cost. Ceramics have high strength and a very good wear resistance as well as corrosion resistance. One of the advantages of polymeric biomaterials compared to the other two categories is their light weight (1).

1.2 Bioactivity evaluation of biomaterials

In this thesis, the focus is on Ti-based biomaterials, which possess several of the requirements of a good biomaterial such as inertness to the body environment, biocompatibility and low elastic modulus. In fact, Ti-based biomaterials are widely used for hard tissue replacement such as dental as well as orthopedic applications (1,2). Therefore, the bioactivity of these biomaterials is of great importance.

The definition of bioactivity has evolved. It can be considered as a measure to describe the osseo-conductivity of the implant; or as a series of biophysical and biochemical reactions, which create a chemical interfacial bonding between the implant and the tissue (3,4). Bioactivity can also be considered as the response of the biomaterial to the living tissue via the formation of a bone-like material at the interface of the biomaterial and the body tissue – which is still not a good definition for bioactivity since the biomaterial might be bioactive even if this bone-like material has not formed (5). Due to the difficulties in considering a specific and clear definition for bioactivity, one can consider the apatite-forming ability (AFA) of a material as another measure of its bioactivity. Hydroxylapatite ($Ca_{10}(PO_4)_6(OH)_2$: HAp), is the main component of both human bones and tooth enamel.

In vivo bioactivity testing requires implementing the biomaterial in a living body and examining its performance and interaction with the body tissue after a period of time. While accurate results on the bioactivity of biomaterials can be obtained via *in vivo* testing, there are several drawbacks with this method. *In vivo* testing requires sacrificing living species, which can lead to ethical issues during the handling of animals over the testing period or the sacrifice step, which can be unreasonably painful. Certain scientists discredit research due to the belief that too many samples have been implemented in one living body. In several countries, there are no rules regulating the maximum number of animals which can be sacrificed in a test. Therefore, one might find the number of sacrificed animals unreasonable. Currently, 50-100 million animals are sacrificed each year for experimental purposes (6). It should be noted that the cost of *in vivo* testing (purchasing the animals, implantation and sacrification surgeries, maintenance during the testing period) can be very expensive. Therefore, finding other alternatives for bioactivity evaluation of biomaterials is of great ethical and financial interest.

In vitro testing is simpler compared to *in vivo* testing mainly because it can be performed in a laboratory where the sample is immersed, for a certain period of time, in an aqueous solution under controlled conditions. The challenge for *in vitro* testing is the need to mimic or re-create conditions close to *in vivo* to assure relevant results. *In vitro* testing protocols vary from material to material and based on the feature that is to be tested; *e.g.*, toxicity, biocompatibility, bioactivity, etc. *In vitro* protocols for bioactivity testing, for Ti-based biomaterials, explain the procedure for preparation of the aqueous solution, the sample and experimental testing conditions. Several types of aqueous solutions have been proposed and investigated for Ti-based biomaterials. Simulated body fluid solutions (SBF) are one of the most well-known *in vitro* solutions for the bioactivity evaluation of Ti-based biomaterials. Different versions of SBF exist and scientists are still trying to improve the reliability of testing results carried out *in vitro* via SBFs. SBFs are similar to human blood plasma since they are also ionic solutions (5). The ionic concentration in SBFs is usually similar to human blood plasma. Maybe the most important difference between the two is the fact that the current SBFs for apatite-forming ability of Ti-based biomaterials do not contain any organic components, except tris (tris(hydroxymethyl-aminomethane) – see Table A.2) as the buffering agent, which is in contrast with human blood plasma.

This thesis is part of a Swiss National Science Foundation (SNSF) project aimed at improving the current bioactivity or AFA (apatite-forming ability) tests, which have proven to have some unreliability over recent years (7,8), and to better understand the underlying mechanisms behind HAp formation during such *in vitro* tests. The project has two Ph.D. students; one dedicated to experimental investigations of SBF compositions and HAp growth on Ti-based materials, and the second dedicated to numerical simulations on the fundamental interactions involved at the Ti-based material – SBF interface; both including investigations of SBF solution containing biologically relevant organic components (*e.g.,* proteins and/or amino acids). The main objective of this thesis is to use computational methods to investigate interfaces that influence the behavior of Ti-based samples for biomedical applications, tested *in vivo* or *in vitro*.

In the following, the current model for apatite formation on a treated titanium surface is explained. Also, the events, which take place on a surface *in vivo* are briefly introduced.

1.2.1 Current apatite formation model on a titanium surface

Titanium surfaces are spontaneously passivated in air or water, meaning that an oxide layer forms on the surface. Many beneficial features of Ti-based biomaterials, such as their biocompatibility, is believed to stem from this oxide layer. This layer has a thickness of a few nanometers and consists of various stoichiometric ratios of Ti/O. The O to Ti ratio decreases from approximately 2 to values smaller than 1 from the surface oxide layer towards bulk titanium. No biomaterial can be called inert as all of them induce a host response upon their implantation in the body (3), but untreated titanium surfaces are *bio*inert meaning that they are stable and do not react with the body fluid or body tissue under physiological condition (2). After implantation in the body, bioinert materials, are considered as a foreign body material and are encapsulated by a fibrous non-mineral layer (4).

Even though amorphous phases, which contain atomic species other than Ti and O, are present in the surface oxide layer of Ti-based biomaterials due to earlier surface treatments, for the most part, this layer consists of stable and crystallographic TiO_2 phases (2). Anatase, brookite and rutile are the three main TiO_2 polymorphs. Both anatase and rutile have shown apatite formation on their surface during *in vitro* testing (9). Since rutile is the most common naturally occurring phase of titanium dioxide, and anatase and brookite transform irreversibly to rutile at high temperatures (approximately 700 °C), rutile is studied in this thesis.

Once a titanium surface is alkali and heat treated, upon immersion in SBF, a bone-like material (apatite) will form on the surface (10). The following procedure is known to render the bioinert titanium surface, bioactive. First, an alkali treatment is performed on the surface. Alkali treatments with $NaOH$ and KOH solutions have led to similar results hence here, the alkali treatment using $NaOH$ will be discussed.

After the alkali treatment with the $NaOH$, a sodium titanium hydrogel forms on the surface. The surface is then rinsed and dried. Heat treatment at 600 °C results in the formation of rutile and sodium titanate ($Na_2Ti_5O_{11}$) on the surface. Heat treatment at 800 °C results in a larger transformation to these two phases; a small quantity of anatase was also detected (10). Soaking alkali treated, heat treated, and alkali&heat treated titanium samples in an SBF solution for four weeks led to the formation of an apatite layer on the surface; however, only the alkali&heat treated surface successfully bonded to the bone (11).

The model presented by Kokubo *et al.* (12), which explains the apatite formation on an amorphous sodium titanate surface is described in the following:

i. Formation of $Ti-OH$ groups on the surface due to the ionic exchange of Na^+ by H_3O^+ induces a negative charge on the surface due to dissociation of hydroxyl groups at pHs close to that of human blood plasma, *i.e.*, 7.4
ii. Accumulation of calcium ions on the negatively charged surface, which leads to the formation of calcium titanate on the surface and the surface charge becoming positive
iii. Attraction of phosphate groups on the surface and formation of amorphous calcium phosphate on the surface
iv. Transformation of the amorphous calcium phosphate to the thermodynamically stable crystalline apatite

In fact, zeta potential measurements are presented by Kokubo *et al.* (12) to confirm this model. As shown in Figure 1.1, the zeta potential, starting at a negative value, becomes positive in about 40 h, and then becomes negative again. The authors suggest that adsorption of calcium ions on the surface in step ii is confirmed by the increase in the zeta potential, while adsorption of the phosphate groups at step iii is confirmed by the decrease in the zeta potential. One of the main questions, which can be raised to this model, is the role of other ions present in SBF solutions. Ions other than sodium, calcium and phosphate are not discussed in the model presented by Kokubo *et al.* (12). A very similar model to that described above is also proposed for the apatite formation on a polyethylene substrate (13).

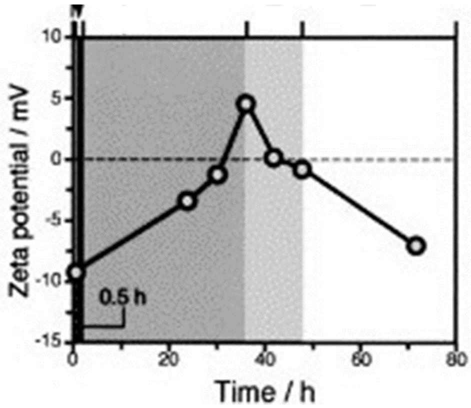

Figure 1.1 Variation of the zeta potential as a function of time for an alkali and heat treated titanium sodium surface soaked in SBF (12,14).

1.2.2 Interaction of organic residues and biomolecules with surfaces

Interactions of a biomaterial with the living tissue are via the surface. Immediately after the implantation of the biomaterial, water close to the surface changes its configuration based on the hydrophobicity or hydrophilicity of the surface. If the surface is hydrophobic, a loose water layer will form close to the surface. In the case of a hydrophilic surface, water adsorbs on the surface in a molecular or dissociative manner. The surface becomes hydroxylated in the case of dissociative water adsorption. In the next step, ions approach the surface in a manner, which is determined by surface properties but also ion-surface and ion-water interactions.

Biomolecules are the next species which approach the surface. First, initial adsorption of organic molecules on the surface takes place, which is mainly driven by smaller organic molecules since they can move faster. The adsorbed organic molecules might undergo conformational changes or be replaced by larger biomolecules, which have a higher affinity for the surface. Therefore, the organic layer on the surface is a mixture of those smaller biomolecules, which initially adsorb on the surface, and those larger ones, which have a higher affinity for the surface. The next step involves the interaction and adhesion of cells on the surface, which is covered by all other species adsorbed previously on the surface (3,15). Cells can be 100-10,000 times bigger than proteins (16). While human blood plasma contains many different components, *e.g.*, biomolecules and cells, current SBF solutions proposed for apatite-forming ability of Ti-based biomaterials are ionic solutions containing only tris as the buffering agent. Many of the adsorption events, which were just discussed, can occur in a matter of a few nano- to milliseconds; therefore, capturing the essence of what is happening to the surface of the biomaterial might, therefore, be very difficult experimentally.

1.3 The computational approach in the thesis

The use of *in silico* studies has emerged in many scientific fields including surface science. Keeping in mind the length-scale and time-scale, which should be considered for a problem related to surface science, quantum mechanics calculations and atomistic simulations are suitable for such studies. The practical limitation of these methods extends to nano- and micro- scales but recent studies, especially in biology, are expanding the sampling scale up to the milliseconds. Since quantum chemistry calculations are based on solving the Schrödinger equation, results obtained by such studies have a high accuracy and are well accepted by the scientific community. Larger and longer computational studies, than what quantum mechanical methods can afford, are achieved by a cost of decreased accuracy when moving to classical atomistic simulations. Molecular dynamics and Monte Carlo are both affected by the limitations of force field development. A systematic protocol to improve the force fields is yet to be widely accepted and used by the scientific community, and its absence can be considered as the main drawback of classical atomistic methods (17).

Nevertheless, certain positive points of molecular dynamics have encouraged its extensive use especially in biological systems among which one can point out the studies usually being carried out under the physiological conditions or using water as the solvent (17).

1.4 Objectives and structure of the thesis

The main questions, which have been tried to be addressed in this thesis, are the following:

i. Can one investigate the apatite formation model of Kokubo *et al.* (12) computationally and present details on the energetics and the kinetics of the system – especially with regard to the role of other ions which are not discussed in the current model?

ii. Can one go one step further on the current apatite formation model by considering the thermodynamics of the SBF solution and the ionic pairs which spontaneously form in the solution? And what roles can ionic pairs play in the apatite formation?

iii. Should one invest in introducing organic residues to the current SBF solutions used in AFA testing of Ti-based biomaterials? Can one expand the current apatite formation model of *in vitro* to *in vivo*, without considering any organic residue? Alternatively, is the absence of organic molecules in vitro a great obstacle for this purpose?

In this thesis, classical molecular dynamics have been used, accompanied by well-tempered metadynamics, to study and improve the current understanding of the events, which a titanium oxide (rutile) surface might experience in a simplified *in vitro*-like environment. Over the course of addressing the above questions, many parameters had to be improved or developed. In specific, force field parameters had to be transformed from their original form to another form to obtain cross-term interactions.

This thesis contains eight chapters. Here, main objectives of each chapter are presented.

Chapter 1 – This chapter aims to introduce the subject of the thesis to the reader.

Chapter 2 – The state of the art is reviewed in the second chapter as a review article prepared and published by the author of the thesis and her directors over the course of the Ph.D. thesis.

Chapter 3 – Computational methods used in the thesis are explained in this chapter. Different settings and parameters used in the simulations are also discussed and described.

Chapter 4 – Thermodynamic modelling is used to determine the ionic complexes and their distribution, which form under physiological conditions in an SBF solution. In this chapter, the interaction of most abundant single ions, under physiological conditions, and main ionic pairs of interest with the rutile surface is studied from an energetic point of view.

Chapter 5 – Adsorption conformation of several amino acids on a rutile surface is investigated in this chapter, using well-tempered metadynamics. Furthermore, the energetics of adsorption of amino acids are explained based on their adsorption conformation.

Chapter 6 – The competitive adsorption of ionic species and organic molecules on a rutile surface with pre-adsorbed species is studied, using well-tempered metadynamics.

Chapter 7 – The adsorption behavior of a polypeptide on a rutile surface is investigated. Two surfaces with different charge density and two different side groups of the polypeptide are studied.

Chapter 8 – The main findings and conclusions of the thesis are summarized in this chapter. Avenues which can be studied further are also discussed.

References

1. Patel, N. R. & Gohil, P. P. A review on biomaterials: scope, applications & human anatomy significance. *Int. J. Emerg. Technol. Adv. Eng.* **2,** 91–101 (2012).

2. Liu, X., Chu, P. K. & Ding, C. Surface modification of titanium, titanium alloys, and related materials for biomedical applications. *Mater. Sci. Eng. R Rep.* **47,** 49–121 (2004).

3. Roach, P., Eglin, D., Rohde, K. & Perry, C. C. Modern biomaterials: a review—bulk properties and implications of surface modifications. *J. Mater. Sci. Mater. Med.* **18,** 1263–1277 (2007).

4. Cao, W. & Hench, L. L. Bioactive materials. *Ceram. Int.* **22,** 493–507 (1996).

5. ISO 23317 - Implants for surgery —*In vitro* evaluation for apatite-forming ability of implant materials. (2007).

6. Badyal, D. K. & Desai, C. Animal use in pharmacology education and research: The changing scenario. *Indian J. Pharmacol.* **46,** 257–265 (2014).

7. Zadpoor, A. A. Relationship between *in vitro* apatite-forming ability measured using simulated body fluid and *in vivo* bioactivity of biomaterials. *Mater. Sci. Eng. C* **35,** 134–143 (2014).

8. Hulsart-Billström, G. *et al.* A surprisingly poor correlation between *in vitro* and *in vivo* testing of biomaterials for bone regeneration: results of a multicentre analysis. *Eur. Cell. Mater.* **31,** 312–322 (2016).

9. Roach, M. D., Williamson, R. S., Blakely, I. P. & Didier, L. M. Tuning anatase and rutile phase ratios and nanoscale surface features by anodization processing onto titanium substrate surfaces. *Mater. Sci. Eng. C* **58,** 213–223 (2016).

10. Kim, H-M., Miyaji, F., Kokubo, T. & Nakamura, T. Preparation of bioactive Ti and its alloys via simple chemical surface treatment. *J. Biomed. Mater. Res.* **32,** 409–417 (1996).

11. Nishiguchi, S. *et al.* The effect of heat treatment on bone-bonding ability of alkali-treated titanium. *Biomaterials* **20,** 491–500 (1999).

12. Kokubo, T., Kim, H.-M. & Kawashita, M. Novel bioactive materials with different mechanical properties. *Focus Biomater. Sci. Asia* **24,** 2161–2175 (2003).

13. Leonor, I. B. *et al.* Surface potential change in bioactive polymer during the process of biomimetic apatite formation in a simulated body fluid. *J. Mater. Chem.* **17,** 4057–4063 (2007).

14. Kim, H-M. *et al.* Surface potential change in bioactive titanium metal during the process of apatite formation in simulated body fluid. *J. Biomed. Mater. Res. A* **67A,** 1305–1309 (2003).

15. Kasemo, B. Biological surface science. *Surf. Sci.* **500,** 656–677 (2002).

16. Kasemo, B. & Gold, J. Implant surfaces and interface processes. *Adv. Dent. Res.* **13,** 8–20 (1999).

17. Maginn, E. J. From discovery to data: What must happen for molecular simulation to become a mainstream chemical engineering tool. *AIChE J.* **55,** 1304–1310 (2009).

Chapter 2 Literature review

This chapter reviews the current state of the art for the subjects addressed in this thesis in the form of a review paper, which was prepared and published by the author of the thesis and her two directors.

Understanding the response of a surface to the components that interact with it, is vital. In this thesis, the focus is on the interaction of the surface with ions, which are present in human blood plasma and SBF solutions, and biomolecules. Researchers have used experimental (1–5), as well as computational (6–13), methods to address this question.

An extensive literature review was carried out and a review paper was written by the author of the thesis (first author). It was revised extensively by both directors of the thesis. This review paper was published in the Journal of Colloids and Surfaces B: Biointerfaces 161 (2018) 563-577 (https://doi.org/10.1016/j.colsurfb.2017.11.004). The supplementary material of this article is presented in Appendix A.[1]

---

[1] The permission for reusing the figures from the literature is taken from the corresponding publishers. For any further use, the reader should refer to the corresponding publisher.

References

1. Kim, S. S., Kuang, Z., Ngo, Y. H., Farmer, B. L. & Naik, R. R. Biotic–Abiotic interactions: Factors that influence peptide–graphene interactions. *ACS Appl. Mater. Interfaces* **7,** 20447–20453 (2015).

2. Byrne, T. M., Lohstreter, L., Filiaggi, M. J., Bai, Z. & Dahn, J. R. Quantifying protein adsorption on combinatorially sputtered Al-, Nb-, Ta- and Ti-containing films with electron microprobe and spectroscopic ellipsometry. *Surf. Sci.* **603,** 992–1001 (2009).

3. Höök, F. *et al.* A comparative study of protein adsorption on titanium oxide surfaces using in situ ellipsometry, optical waveguide lightmode spectroscopy, and quartz crystal microbalance/dissipation. *Colloids Surf. B Biointerfaces* **24,** 155–170 (2002).

4. Ozhukil Kollath Vinayaraj *et al.* A modular approach to study protein adsorption on surface modified hydroxyapatite. *Chem. – Eur. J.* **21,** 10497–10505 (2015).

5. Bai Zhijun *et al.* Surface characteristics and protein adsorption on combinatorial binary Ti-M (Cr, Al, Ni) and Al-M (Ta, Zr) library films. *J. Biomed. Mater. Res. A* **92A,** 521–532 (2009).

6. Galmarini, S. & Bowen, P. Atomistic simulation of the adsorption of calcium and hydroxyl ions onto portlandite surfaces — towards crystal growth mechanisms. *Cem. Concr. Res.* **81,** 16–23 (2016).

7. Galmarini, S., Kunhi Mohamed, A. & Bowen, P. Atomistic simulations of silicate species interaction with portlandite surfaces. *J. Phys. Chem. C* **120,** 22407–22413 (2016).

8. Bouhadja, M. & Skelton, A. A. Dynamical properties of water and ions at the quartz (101)–water interface at a range of solution conditions: A classical molecular dynamics study. *J. Phys. Chem. C* **122,** 1535–1546 (2018).

9. Wright, L. B. & Walsh, T. R. First-principles molecular dynamics simulations of NH_4^+ and CH_3COO^- adsorption at the aqueous quartz interface. *J. Chem. Phys.* **137,** 224702 (2012).

10. Kubiak-Ossowska, K., Tokarczyk, K., Jachimska, B. & Mulheran, P. A. Bovine serum albumin adsorption at a silica surface explored by simulation and experiment. *J. Phys. Chem. B* **121,** 3975–3986 (2017).

11. Corno, M. *et al.* Computational study of acidic and basic functionalized crystalline silica surfaces as a model for biomaterial interfaces. *Langmuir* **31,** 6321–6331 (2015).

12. Hughes, Z. E., Wright, L. B. & Walsh, T. R. Biomolecular adsorption at aqueous silver interfaces: First-principles calculations, polarizable force-field simulations, and comparisons with gold. *Langmuir* **29,** 13217–13229 (2013).

13. Aschauer, U. & Selloni, A. Adsorption of biomedical coating molecules, amino acids, and short peptides on magnetite (110). *J. Chem. Phys.* **143,** 044705 (2015).

Colloids and Surfaces B: Biointerfaces 161 (2018) 563–577

Interaction of biologically relevant ions and organic molecules with titanium oxide (rutile) surfaces: A review on molecular dynamics studies

Azade YazdanYar[✦], *Ulrich Aschauer*[✦✦], *Paul Bowen*[✦]
[✦] Department of Materials Science and Engineering, École Polytechnique Fédérale de Lausanne (EPFL), Lausanne, Switzerland
[✦✦] Department of Chemistry and Biochemistry, University of Bern, Bern, Switzerland

Abstract

The surface of a biomaterial can play a major role in its biological fate since the surface is the primary pathway for its interaction with the body. As the natural response of the body to a foreign material is to encapsulate it with a fibrous material, the interactions between the body and the biomaterial are mediated by this fibrous layer. Initial interactions occur between the biomaterial surface, water, ionic species and organic molecules, which then mediate further interactions with body tissues. Surface engineering can influence these interactions and hence, improve the biocompatibility of the biomaterial. Therefore, both experimental and computational studies have been interested in phenomena happening at the solid-solution interface as their mechanisms and driving forces can point to new directions for biomaterial design and evaluation. In this review, we summarize the computational work on the interaction of titanium oxide surfaces (mainly rutile) with solvated ions and organic molecules by means of molecular dynamics, with a certain relevance to bioactivity testing protocols. The primary goal of this review is to present the current state of the art and draw attention to points where further investigations are required.

2.1 Introduction

Titanium alloys are nowadays extensively used for biomedical applications since they have proven to be biocompatible (the ability to exist in contact with human body tissue without causing an unacceptable degree of harm to the body[1]) for many biomedical applications (*e.g.*, artificial bones, joints and dental implants[2]). It is argued that they owe their biocompatibility for such applications to the oxide layer that forms when the metal is in contact with either oxygen or water.[2] The oxide layer on Ti implants that interacts with the surrounding environment is a mixture of amorphous and crystalline forms of titanium oxide (hereafter, titanium oxide will refer to both crystalline and amorphous states).[3] The three major crystalline polymorphs of titanium dioxide are rutile, anatase and brookite, rutile being the most abundant naturally occurring phase at ambient pressure, while anatase is stable in nanomaterials.[2,4–8] At high temperatures, anatase and brookite can irreversibly transform to rutile.[9,10] Chemical treatments are often used to render inert surfaces bioactive. For example, Kokubo *et al.* showed that a sodium titanate hydrogel layer forms on a titanium metal surface after its immersion in sodium hydroxide.[11] Heat treatment of this sodium titanate hydrogel layer-covered titanium showed that it transforms into a sodium titanate at 400-500 °C and crystalline sodium titanate and rutile at temperatures above 700 °C.[12] These chemically modified surfaces show an excellent biocompatibility for specific applications and are under clinical trials for artificial hip joints and spinal fusion devices.[13] This highlights the importance of rutile, which is the titanium oxide phase studied in most publications on this topic.

The biocompatibility of an implant with a given surface preparation can most reliably be evaluated by *in vivo* testing where the assessment is done with the implant inserted in a living body. However, for economic as well as ethical reasons it is desirable to perform reliable *in vitro* tests, in which samples are tested in laboratories and outside any living bodies. In the latter case, researchers try to achieve experimental conditions close to those found *in vivo*. While in some cases *in vitro* results agree with *in vivo* results, other studies have shown that there are unidentified factors during *in vitro* tests that cause discrepancies between the results obtained by these two methodologies.[14,15] In a recent study, eight different European universities carried out *in vivo* and *in vitro* studies on 93 different biomaterials, showing a weak correlation between *in vivo* and *in vitro* results.[16]

One of the sources of this discrepancy is the solution used for *in vitro* testing.[17,18] Depending on the purpose of the study, different aqueous *in vitro* solutions have been proposed, Simulated Body Fluid solutions (SBFs) being a popular category.[19,20] The ionic concentrations in different SBFs (Table 2.1) are very close to those in blood plasma. The variations say between the Kokubo and Bohner solutions have a minor effect on supersaturation[18] and it is the possible specific adsorption of ions onto different surfaces that should be of importance in the hydroxyapatite formation on implants. There are certainly differences between blood plasma and SBF solutions; for example, the buffer used to maintain the solution pH near the 7.4 found in human blood. The use of a carbonate buffer (*i.e.*, a P_{CO_2} of 5%) instead of an organic molecule such as Tris should render the *in vitro* test more representative. This can change the amount of carbonate or bicarbonate species in solution,[18] which may lead to modifications in the inorganic species adsorbed on implant surfaces. This, in turn, may influence the nucleation and growth of calcium phosphates on implant surfaces *in vitro*. Also, one of the most commonly used SBF solutions, proposed by Kokubo *et al.* and used in the ISO standard,[21] lacks the proteins present in the blood plasma.[17,22] In the human body proteins adsorb onto an implant surface in a variety of orientations and configurations shortly after implantation. Further interactions between the cells and the implant surface will occur through this organic layer.[2,23,24] Since cells recognize only a few specific proteins in well-defined orientations and configurations, the composition and structure of the adsorbed organic layer will influence the biocompatibility of the biomaterial.[25–28] Therefore, the absence of proteins during *in vitro* testing could be another reason for the discrepancies found between *in vivo* and *in vitro* testing.

Table 2.1 Ionic concentration [mM] of the human blood plasma and some Simulated Body Fluid solutions (SBFs). [18,21,22,29]

	Human blood plasma	ISO 23317 (pH 7.4)	Kokubo *et al.*	Bohner *et al.*
Na^+	142.00	142.00	142.00	142.00
K^+	5.00	5.00	5.00	-
Mg^{2+}	1.50	1.50	1.50	-
Ca^{2+}	2.50	2.50	2.50	2.31
Cl^-	103.00	147.80	148.80	109.90
HCO_3^-	27.00	4.20	4.20	34.88
HPO_4^{2-}	1.00	1.00	1.00	1.39
SO_4^{2-}	0.50	0.50	0.50	-

Understanding protein adsorption on biomaterial surfaces is therefore of great importance since, alongside water-surface interactions, it can significantly affect the performance of a biomaterial.[19,24,30] With this knowledge, it would be possible to design implants with surfaces that trigger or boost biocompatibility and bioactivity when in contact with blood-plasma proteins,[14,25] since "*there is a causal connection between the detailed properties of a native implant surface and the ultimate tissue response*".[31] It should be borne in mind that the extent and the manner of protein adsorption on surfaces are significantly influenced by certain properties of the surface[31,32] and the local environment such as wettability, hydrophobicity, surface charge, pH, the concentration of ions and temperature.[23,24,26,33,34] Also, the presence of organic molecules can control some surface features[33] such as step and edge formation and crystal growth.[35]

Despite steady advances in experimental methods and techniques, computational methods can be more suitable for answering certain questions.[27,36,37] Depending on the property under study, different computational methods can be used. Even though surface science aspects of titanium oxide have been extensively studied using density functional theory (DFT), investigation of surface-protein interactions is currently beyond the reach of this method. Due to the large number of atoms (simulation of even a single organic molecule via DFT can be impractical) and the extended timescales, classical molecular dynamics (MD) is better suited to these tasks. Reactive force fields can describe changes in bonding and charge transfer, but there are only a few MD studies using this type of force field at the moment[38–41] and hence, in this review we focus on studies done with non-reactive force fields.

To have a proper time average, as many configurations as possible must be sampled, which is hindered by high energy barriers, the crossing of which often occurs only on millisecond timescales (such as protein folding) as well as the finite sampling time.[42] Enhanced sampling methods, such as metadynamics, make it possible to overcome these barriers and to sample configurations inaccessible within the nanosecond time limit inherent to classical molecular dynamics (it is worth mentioning that affording even a few hundred picoseconds via DFT is impractical).[37] During metadynamics, the free energy of a system is biased to the point that the system can cross an energy barrier and explore neighboring energy wells. Currently, only a few groups have used enhanced sampling methods and we discuss their results in this review.

While some review papers have summarized the experimental work on the interaction of organic molecules with titanium oxide (alongside other materials),[2,24,43] to the knowledge of the authors, hardly any reviews exist for computational studies on bio-related titanium oxide systems.[44] Here, we assess what is known from classical and enhanced molecular dynamics about the interactions of ions and organic molecules with titanium oxide. The limited number of studies presented here on anatase, brookite and amorphous titanium oxide stems from the fact that most researchers have been conducting their studies on rutile (the most thermodynamically stable phase of titanium dioxide) and not because we have narrowed the scope of this review.

While we focus mainly on studies in aqueous solution, we do present computational studies in vacuum (in four instances) since they provide the fundamental knowledge required to investigate more complex systems. As it will be discussed later in this review, water plays a crucial role in the adsorption process of ions and organic molecules on the surface. We would like the reader to be cautious about studies carried out in vacuum and keep in mind that they ignore the irreplaceable role of the solvent in an adsorption event.

A concise discussion of the available force fields is presented in section 2.2. In section 2.3, we discuss the interaction of rutile surfaces with ions in aqueous solution. Section 2.4 covers different surface features which affect the organic-inorganic interactions. The effect of the initial orientation of the organic on its adsorption on the surface is also addressed in this section. The paper concludes with a summary section. The temperature of the simulations is in the range of 25 - 37 ℃ unless otherwise stated. We do not provide a description of the atomistic simulation methods, which are mentioned throughout the review but refer the reader to other sources for a detailed discussion.[27,37,45] A list of the abbreviations and the chemical representation of most of the organic molecules investigated in this review are presented in the Appendix A.

2.2 Force fields

The accuracy of any atomistic simulation depends highly on its underlying force field. Great care should, therefore, be taken in choosing the force field (range of validity) as well setting it up in a specific code. Moreover, determining undefined parameters should be done judiciously - for example, in case one has force field parameters for the interaction of atom type i with itself and for atom type j with itself, there are several ways to obtain parameters for the interactions between types i and j.

In molecular dynamics simulations, the force applied on atoms, which is described by the force field, is used in Newton's law of motion equation to propagate velocities and atomic coordinates using a timestep shorter than the fastest atomic vibrations in the system. The types of interaction between atoms can be divided into bonded and non-bonded or intramolecular and intermolecular interactions. The bonded interactions are defined for the atoms of the same molecule that are covalently bonded to each other. The non-bonded interactions include Coulombic and van der Waals interactions between the atoms of different molecules. Both bonded and non-bonded interactions are described by a variety of parametric functions of the atom coordinates and types, which we will not discuss in details here.

The system of an inorganic surface with organic molecules in an ionic solution includes the inorganic surface, the organic molecule, ions and water. Atomistic simulations of such systems require five primary groups of interaction parameters; the first four groups will be the potential sets of the inorganic, organic, ions and water; the last group contains the cross-term interactions between the components: inorganic-organic, inorganic-ions, inorganic-water, organic-ions, organic-water and ions-water.

Given that accurate force fields for the first four groups are known, deriving the cross-term interactions is the most challenging task. Where feasible, for example, when the organic molecule is relatively small, *ab initio* calculations can be carried out to extract cross-term interaction parameters.[42,46] However, this approach becomes impractical for more complex organic molecules.[47] Freeman *et al*.[48] proposed a methodology which uses the existing potential sets and generates only the cross-term interactions between different components of a system such as water-mineral, mineral-organic and mineral-ions. In this method, expensive fitting steps can be avoided. If we assume that atom A belongs to a different component than atom B, the fitting can be carried out on a mineral that contains both atoms A and B. For example, A can be the calcium in calcite ($CaCO_3$) and B can be the oxygen atom of the organic molecule and one can use $Ca - O$ interaction parameters of calcite to obtain the new cross-term interactions of $Ca_{mineral} - O_{organic}$.

Another method to obtain the cross-term interactions is via the Lorentz-Berthelot mixing rules. This method requires the Lennard-Jones parameters for atom i and atom j to generate the Lennard-Jones parameters for the interaction between atoms i and j.[49,50] Several studies presented in this review have used Lorentz-Berthelot mixing rules to obtain the organic-inorganic, organic-water and ion-water interactions.[51–53]

In the following, we will mention some of the force fields used for the components of the under-study system. Since caution should be taken when trying to use an existing force field for a particular system, we do not present the force field parameters in this review and refer the reader to the original manuscript for parameters and validation.

2.2.1 Titanium oxide

A broad range of titanium oxidation states for stoichiometries varying from Ti_2O to TiO_2 can be present in the surface oxide layer.[2] Several force fields have been suggested for modelling titanium oxide systems.[54–58] One of the most well-established force fields for titanium dioxide polymorphs was first developed by Matsui and Akaogi.[54] While this force field is not very successful at reproducing the anisotropic static relative permittivity of rutile, its simplicity and capability in reproducing the structures of titanium dioxide polymorphs have led to its extensive usage in molecular dynamics simulations.[59–61]

Kim *et al*. developed an alternative force field for rutile and tested the transferability of this force field to anatase and brookite.[55] Several properties such as the lattice constants, bulk modulus and heat capacity for titanium dioxide polymorphs were well reproduced.

The majority of studies on oxidized titanium surfaces assume a perfect crystalline structure. However, the force field developed by Schneider *et al*. is capable of modelling an amorphous oxidized titanium surface.[62,63] In this parameterization, the interface between titanium and TiO_x (surface oxide layer) was described using a Finnis-Sinclair form of a many-body potential. The parameters were chosen such that they reproduce the same atomic charges as the Matsui-Akaogi set when the TiO_x structure is bulk TiO_2 rutile. The amorphous oxidized titanium layer was modeled using electrostatic Coulomb interactions and short-range repulsive terms. Despite its simplicity, this force field is successful in describing the amorphous oxide layer.

2.2.2 Water and its interaction with titanium dioxide

At least 46 water models were developed between 1933 and 2002.[64] However, for titanium oxide in biological systems mainly simple three-site SPC/E and TIP3P (three-site transferable intermolecular potential) water models have been used.[65–67] Despite their simplicity, these models have been able to reproduce many properties of water accurately.[64,68–71] Although more evolved water models such as TIP4P (four-site transferable intermolecular potential)[72,73] might be able to present a better model of water and its interactions, adding just one more interaction site to the water model can significantly increase the computational cost in biologically-relevant studies.[70]

In both *in vivo* and *in vitro* conditions, titanium oxide is in contact with an aqueous environment which will lead to the hydroxylation of the surface via dissociative adsorption of water molecules.[74,75] The hydroxyl group on the rutile surface which forms as a consequence of the protonation of a surface oxygen atom is called the bridging hydroxyl while the hydroxyl which forms as a result of the attachment of an OH group to a surface Ti atom is called the terminal hydroxyl. The degree of hydroxylation, conventionally, refers to the fraction of the available surface O and Ti sites that carry bridging and terminal hydroxyl groups, respectively. Non-neutral pH, however, will lead to a selective protonation or deprotonation of surface sites, which affects both the degree of hydroxylation and the balance between the number of bridging and terminal hydroxyl groups and thus induces a surface charge. We will, in the following, use the term ‘partial hydroxylation’ to refer to the presence of unequal numbers of either type of hydroxyl groups. The experimentally observed negative surface charge at biologically relevant pHs above the isoelectric point of rutile can be achieved using two approaches. One possibility is to have a partial coverage of terminal hydroxyl groups with no bridging hydroxyl groups. Another possibility is to have a full coverage of terminal hydroxyl groups with a partial coverage of bridging hydroxyl groups.[66] Figure 2.1 is a schematic of the rutile (110) surface in the non-hydroxylated, fully hydroxylated and partially hydroxylated states; in the latter case, shown in Figure 2.1c, the surface charge is provided through partial coverage with only terminal hydroxyls and in Figure 2.1d, the surface charge is the result of partial coverage of bridging hydroxyls on a surface with a full coverage of terminal hydroxyls. This figure shows the surface in the unrelaxed state for the sake of clarity. Upon relaxation, the hydroxyl groups are tilted and hydrogen bonds form between adjacent groups.

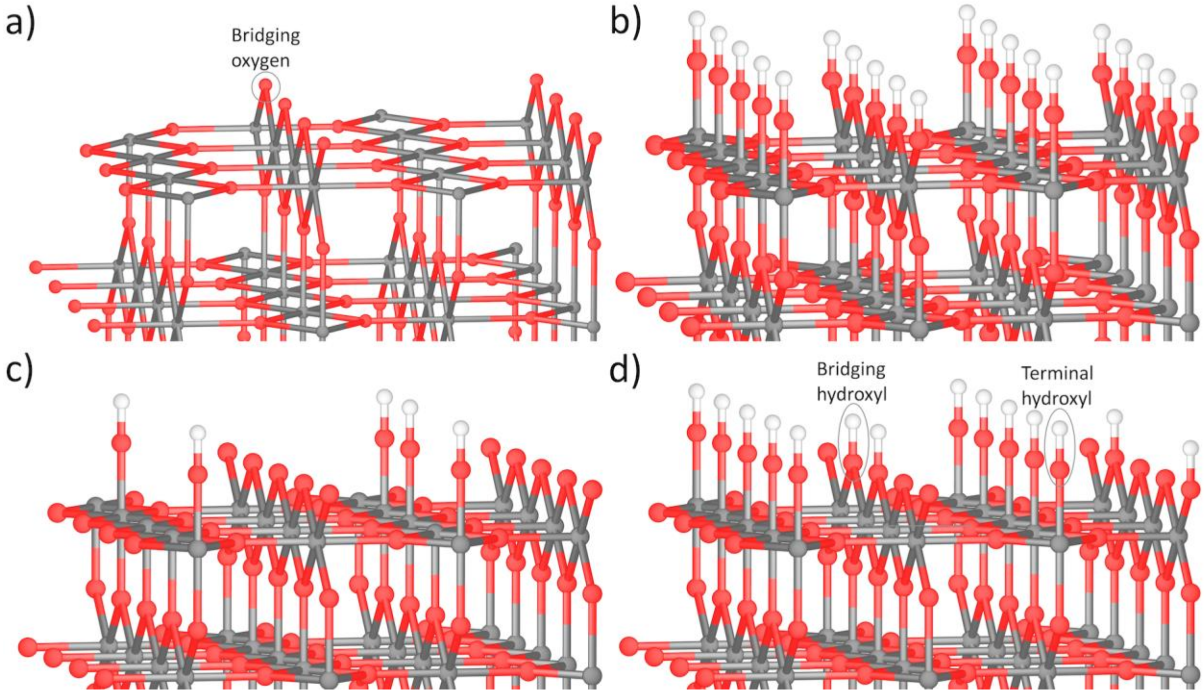

Figure 2.1 Unrelaxed rutile (110) surface: a) non-hydroxylated surface, b) fully hydroxylated surface highlighting the bridging and terminal hydroxyl groups, c) partial coverage of terminal hydroxyl groups on the surface and d) full coverage of terminal hydroxyl groups and partial coverage of bridging hydroxyl groups. Color code: Ti: grey, O: red and H: white. Adapted from Ref. 66. © 2004 American Chemical Society.

From *ab initio* calculations, Predota *et al*. found that surface Ti atoms and hydroxyl groups are variable-charge atoms.[66] Thus, Predota *et al*. developed slightly different charge schemes for the rutile surface in the neutral (non-hydroxylated or fully hydroxylated) and negatively charged (partially hydroxylated) states.[76]

The Matsui and Akaogi force field was amended by Bandura *et al*.[60] to include TiO_2-H_2O interactions. A*b initio* calculations were carried out to validate this force field for the interaction of the SPC/E (extended simple point charge) water model with the rutile (110) surface. In comparison to another titanium dioxide parameterization (developed by Kim *et al*.[55]), they observed that the Matsui and Akaogi force field yields better agreement with *ab initio* results. Predota *et al*. further adapted the force field derived by Bandura *et al*. to introduce different surface charges on the rutile (110) surface.[66]

Alimohammadi *et al*.[58] also modified the force field developed by Bandura *et al*.[60] to refine the interaction of water with rutile and anatase surfaces. This refined force field contains new cross-term interactions between titanium and oxygen atoms of titanium dioxide with oxygen of water. The binding energies and conformations obtained by using this refined force field yielded results which were in good agreement with first-principle DFT calculations and experiments.

Several computational studies have used implicit water instead of explicit water molecules,[6,77] in which no actual water molecule is present in the system and the solvent is modelled as a dielectric continuum.[78] While this can significantly reduce the computational cost, details of the interfacial structure might be ignored and the results should be interpreted cautiously.[47] The main problem with using an implicit water model is ignoring the competition of the water molecules and the organic residue for the surface and the incapacity of the implicit model to represent hydrophobic effects.[42]

Water is known to adopt a layered structure close to different rutile planes, as well as the amorphous titanium oxide.[65,67,79,80] By studying the water structure close to these two rutile surfaces, strongly structured water layers were observed close to both of them. The density distribution of water in the surface normal direction revealed that water is more strongly orientated on the (110) surface compared to the (001) surface.[79] An organic molecule often binds to the surface through the first layer of water molecules, which is known as indirect bonding.[52] Many studies have investigated the water structure close to the titanium oxide surfaces,[67,74,75,80–86] but we will not discuss them further in this review.

2.2.3 Ions and their interaction with rutile and water

Some of the proposed force fields for ions which are present in the human blood plasma and SBF solutions (Table 2.1) can be found in following references.[66,87–93]

Predota *et al*. defined the short-range van der Waals interaction between ions and rutile oxygen as being similar to the interaction between ions and the oxygen atom of water. Due to the lack of available force fields for the short-range interaction between the titanium atoms of rutile and ions, they ignored the short-range interactions and considered the Ti-ion interactions to be purely electrostatic.[66]

2.2.4 Organic molecules and their interaction with rutile and water

The force field for an organic residue can be established based on different force fields such as AMBER, CHARMM, GROMOS, etc.[42,94–96]

For investigating the interaction of a dipeptide with the rutile surface, Carravetta *et al*. used *ab initio* calculations on small sections of the organic residue and the inorganic surface to have a better approach to predicting the surface-dipeptide interactions.[46] Other groups have mainly used the Lorentz-Berthelot mixing rules to obtain the organic-inorganic or organic-water interactions. Since this requires having the force field of rutile in the Lennard-Jones scheme, several groups have fitted Lennard-Jones parameterizations to the original Matsui-Akaogi Buckingham set.[50,51,97,98]

2.3 Interactions of ions with rutile surfaces

Interaction of ionic species with surfaces can provide insight into the affinity of the ion for the surface, preferred adsorption sites, adsorption energy, etc. Interaction of some of the ions that are present in SBF solutions or human blood plasma (Table 2.1) with rutile surfaces has been studied.

In this section, the interaction of three monovalent (Na^{+}, Rb^{+}, K^{+}) and four divalent (Ca^{2+}, Sr^{2+}, Mg^{2+} and Zn^{2+}) cations with two rutile surfaces ((110) and (100)) is discussed. Different temperatures, surface charge densities and pH levels have been tested and it was shown that all these parameters, along with the ionic size, affect the adsorption energy as well as the adsorption site (adsorption geometry) on the surface.

Predota *et al*. studied the adsorption geometry and binding strength of several monovalent and divalent cations (Na^+, Rb^+, Ca^{2+}, Sr^{2+} and Zn^{2+}) solvated in water (SPC/E model) on neutral and negatively charged (partially hydroxylated) rutile (110) surfaces.[99] X-ray structure determinations were also carried out to compare the results of simulation and experiment.[100] The simulation box was electrically neutralized by adding a sufficient number of chlorine anions. It was seen by means of molecular dynamics simulations that smaller cations ($e.g.$, Na^+, Ca^{2+} and Zn^{2+}) adsorb closer to the surface compared to larger ones (*e.g.*, Rb^+ and Sr^{2+}). Zn^{2+}, the smallest cation in this study, adsorbed the closest to both neutral and negatively charged rutile surfaces. Its small size also makes it the only cation, which adsorbs in a bidentate site (between two terminal oxygens or between one terminal and one bridging oxygen), DFT calculations confirming this to be the energetically most favorable adsorption mode.[101] However, we want to note that in *ab initio* calculations[101] water hydrolysis was observed in the first hydration shell, which adds complexity to Zn^{2+} adsorption that cannot easily be captured by classical MD. Based on the X-ray results, all other cations adsorbed at tetradentate sites (between two terminal and two bridging oxygens).[100] During the molecular dynamics simulations, however, adsorption in both tetradentate and bidentate sites was observed for all cations with different occupation probabilities.[99] Different adsorption sites for Rb^+, Sr^{2+} and Zn^{2+} are shown in Figure A.1.

The binding between divalent cations and their hydration shell is stronger than for monovalent cations.[102] Therefore, divalent cations tend to retain their hydration shell and remain solvated, especially in the case of a neutral surface. For all of the studied cations, inner-sphere adsorption on the rutile surface was observed. Inner-sphere adsorption implies that the cation adsorbs directly on the surface. However, water molecules are involved in the indirect binding of the ion on the surface in the case of an outer-sphere adsorption. Outer-sphere adsorption was also observed for Ca^{2+} and Sr^{2+} but much less frequently than the inner-sphere adsorption. By developing a method to predict the adsorption geometry of the cations, Predota *et al*. found that the adsorption geometry depends on the cation size.[99] While using this method one can predict all the possible adsorption geometries, molecular dynamics simulations are still required to find the preferred adsorption site based on the probability of the occupation of the adsorption site.

In agreement with the work of Predota $et\ al.$,[99] Wu *et al*. also observed that the ionic size notably affects the adsorption geometry and adsorption mechanism on the surface.[102] By studying the adsorption of a group of monovalent (Na^+, K^+ and Rb^+) and divalent (Mg^{2+}, Ca^{2+} and Sr^{2+}) cations solvated in water (SPC/E model) on the negatively charged (partially hydroxylated) rutile (110) surface, they observed that the preferred adsorption mechanism for all cations except Mg^{2+} and Ca^{2+} is inner-sphere adsorption. Magnesium, due to its small size, adsorbs in an outer-sphere configuration. It was however observed that there is no significant preference between inner-sphere and outer-sphere adsorption on the surface for the calcium cation. The residence time of water in the hydration shell of cations is significantly shorter for monovalent cations (5-25 ps) compared to divalent cations (150 ps-∞; which is limited by simulation time of 6 ns). This shows that the binding between the monovalent cations and their surrounding water molecules is not permanent; occasionally, the cation is free to bind to the surface or a peptide, if present in the system. Among the three divalent cations, magnesium has the largest residence time of water within its hydration shell, which is due to its small ionic size. This suggests strong binding energetics for Mg ions, implying that SBF solutions for *in vitro* studies should contain Mg ions despite the slow kinetics of their binding.[15,17,18]

The effect of temperature and surface charge density on the adsorption frequency and adsorption site on the rutile (110) surface at 25, 150 and 250 °C were studied for Na^{+}, Rb^{+} and Sr^{2+}.[76] Water was modelled using the SPC/E model. Using experimental titration tests, the surface charge density was calculated for the three temperatures mentioned above at different pH values. Five surface charge densities of -0.416, -0.208, -0.104, 0.0 and +0.104 $C \cdot m^{-2}$ were studied. The negative surface charge densities were produced by a partial coverage of bridging hydroxyl groups while the positive surface charge density was achieved by replacing some terminal hydroxyl groups with water molecules. Four different adsorption sites were observed, which included three inner-sphere adsorption sites and one outer-sphere adsorption site. The inner-sphere adsorption sites are closer to the rutile surface and consist of i) the TD tetradentate site in which the ion interacts with two bridging and two terminal hydroxyl groups; ii) the BOTO bidentate site in which the ion interacts with one bridging and one terminal hydroxyl group and iii) the TOTO bidentate site in which two terminal hydroxyl groups interact with the ion. The proximity of the adsorption site to the rutile surface varies in the order of TD, BOTO and TOTO; from the closest site to the farthest one.[76] The frequency of outer-sphere adsorption for different ions is lower than inner-sphere adsorption for all temperatures and all surface charge densities.

Increasing the temperature enables the ions to overcome energy barriers and to adsorb on sites closer to the surface. The adsorption frequency decreases significantly on the non-charged and positively charged rutile surfaces (almost zero) at higher temperatures. For the surface charge densities of -0.208 and -0.104 $C \cdot m^{-2}$, the TOTO adsorption sites are favored by Na^{+} and Sr^{2+} while Rb^{+} adsorbs most frequently in the TD adsorption sites. This can be explained by the weaker binding of water molecules in the Rb^{+} hydration shell compared to the ones around the smaller Na^{+} ion. The water molecules around Rb^{+} can be removed more easily, which facilitates its adsorption to the tetradentate site.[76]

Koppen *et al*. studied the interaction of sodium and chlorine ions in solution (using TIP3P water model) with the rutile (100) surface at three pH values of 4.0, 7.4 and 9.0.[103] Considering the isoelectric point of rutile (~ 5.3 at 35 °C [104] and between 5 - 6.7,[105] in general), the rutile surface carried a positive charge at the first pH and negative charge at the latter two pH values. The pH was adjusted by adding protons or hydroxyl groups to the stoichiometric rutile surface. The density distribution of the structured water layers close to the surface was affected by the ionic solution. While ions with a charge opposite to that of the surface (counter-ions) like to approach the surface, the ions with the same charge as the surface prefer to diffuse into the aqueous solution.

From the above studies, it can be seen that the interaction of ions present in a simulated body fluid with the titanium surface remains incomplete. In most cases, chlorine is used as the counter-ion, whereas other anions such as sulphate, bicarbonate and hydrogen phosphate are also present in SBFs (Table 2.1). Despite the fact that rutile and anatase surfaces are negatively charged at the temperature and pH of *in vivo* condition, the interaction of other anions present in the simulated body fluid can also be interesting.

2.4 Interaction of organic molecules with titanium oxide surfaces

A summary of studies on protein adsorption on different substrates, using experimental and computational methods, can be found elsewhere.[24] Here we will discuss those that have applied computational methods to study the interaction of organic molecules with titanium oxide surfaces. The sub-sections are divided according to the type of the organic molecule.

Due to their simplicity, single amino acids or oligomers have been the first residues to be computationally studied. Among the many possible organic molecules that can be studied, the RGD (Arg-Gly-Asp) and RKLPDA sequences of amino acids are of great interest. After the placement of a Ti implant inside the body, integrin receptors at the cell membrane will search for specific ligands on the surface to bind to. If the ligand is present and its conformation on the surface is suitable, further interaction between the cell and the implant can occur. Protein ligands such as fibronectin, vitronectin and collagen are present in the extracellular matrix (ECM). The cellular response induced by these extracellular matrix proteins, however, is mainly through the Arg-Gly-Asp (RGD) sequence.[9,106] The RGD sequence is a polypeptide; in the zwitterion state, the Arg residue is positively charged and the Asp residue is negatively charged. It has been reported that RGD can mediate cell attachment onto several ECM proteins such as type I collagen and has a high specificity for integrin receptors.[107] Consequently, coating Ti implants with RGD can enhance its bioactivity and biocompatibility.[108]

The RKLPDA hexapeptide is also known as a titanium binding peptide (TBP) since it has shown high affinity towards surfaces such as Ti but little affinity towards other surfaces such as Au, Cr, Pt, Zn, etc.[109] In 2005, Sano *et al*. showed that TBP-1, a sequence containing 12 amino acids, where the very first six amino acids are RKLPDA (TBP), recognizes Ti, Si and Ag surfaces. Since the electronic and crystallographic structures of these three are not similar, they hypothesized that there is an unknown parameter which controls the surface recognition by TBP-1.[109] With the continuous increase of computational resources, it has been possible to study more complex organic units.

2.4.1 Surface crystal structure and phase

2.4.1.1 The RGD polypeptide

Zhang *et al*. compared the binding energy of the RGD sequence to non-hydroxylated rutile (110) and anatase (101) surfaces in three different initial configurations, both in vacuum and in water (TIP3P model).[110] It was shown that the effect of the crystal structure is more important than the initial configuration of RGD. The higher binding energy of RGD to the anatase surface compared to the rutile surface was attributed to the fact that the anatase (101) surface consists of O and Ti atoms (the vertical distance between them is about 1 Å), but the rutile (110) surface is oxygen terminated. It was concluded that the presence of Ti atoms influences the adsorption process of RGD on the surface.

The binding energy of RGD to the surface was significantly smaller in water compared to vacuum for both rutile and anatase. In fact, water molecules can affect the adsorption process via different mechanisms. Before the adsorption of RGD to the surface, structured water layers form close to the surface. Hydrogen bonds between the surface and the water molecules should be broken before RGD can bind to the surface. Also, the binding between RGD and water molecules could be stronger than that of RGD and the surface. In this case, RGD will not be able to interact with the surface strongly.[110]

2.4.1.2 An albumin subdomain and two fibronectin modules

In another study, the adsorption of an albumin subdomain and two connected fibronectin type I modules onto the non-hydroxylated rutile (001), anatase (100) and brookite (100) surfaces were compared using an implicit water model.[6] The interaction energy for both organic segments was the highest on anatase and the lowest for brookite. The binding strength between the surface and the organic molecules was not directly compared. During energy minimization, albumin showed a strong interaction with all three polymorph surfaces, while during the following molecular dynamics run, fibronectin modules had stronger interactions with the surfaces. Both organic segments showed structural changes to increase their interaction with the surface.

2.4.2 Surface hydrophobicity

2.4.2.1 Human lactoferrin and human bone morphogenetic protein-2

Surface characteristics like its chemical composition can affect the interaction between the surface and the protein. Sun *et al*. studied the effect of the hydrophobicity of the fully hydroxylated rutile (110) surface on the strength and the nature of the interaction of this surface with two proteins.[111] Human lactoferrin (LF), which has antibacterial activity and is a part of the immune system of the body, and human bone morphogenetic protein-2 (BMP2), which is important in the development of bones and cartilage (Protein data bank ID codes: 1CB6 and 3BMP, respectively) were chosen as the organic residues. The TIP3P model was used to describe water molecules. The charges of rutile Ti and O atoms were scaled by a factor of 0.5 and 1.4 to create a more hydrophobic and a more hydrophilic surface, respectively, when compared to the original surface. Results revealed that both proteins have a stronger interaction with the more hydrophobic surface. On approaching this surface, water molecules are displaced by the protein residues and the protein binds directly to the surface. On the more hydrophilic surface, water competes with the protein more strongly. This leads to indirect adsorption of the protein on the surface; instead of interacting directly with the surface, the protein mainly interacts with the water layer on the surface.

2.4.3 Surface charge

The isoelectric point of rutile and anatase is generally below 7.[105] In physiological conditions ($pH \sim$ 7.4), these surfaces are hence negatively charged, which is why the cases presented in this section are either on neutral or negatively charged surfaces (positively charged surfaces not being relevant in physiological conditions). A neutral rutile surface can either be non-hydroxylated or fully hydroxylated while exchanging some of the surface hydroxyl groups with surface atoms leads to a net negative charge on the surface.

2.4.3.1 Charge neutral surfaces

2.4.3.1.1 Simple organic residues

Nada *et al*. studied the adsorption of the glycolate anion ($CH_2(OH)COO^-$) in water to two non-hydroxylated rutile surface directions: (110) and (001).[79] The TIP3P model was used for water. Density distributions were studied for the two carbon atoms of the glycolate anion close to the rutile surfaces. The adsorption on the (110) surface was through the carboxylate carbon, while for the (001) surface, it was through the hydroxyl carbon. Bonding of the glycolate ion was shown to be more stable to the (110) surface compared to the (001) surface. Since strong bonding between an organic and the surface can hinder the crystal growth, it can be expected that the (001) surface should have a higher growth rate compared to the (110) surface in the presence of the glycolate ion, which was in agreement with experimental results.[79]

Metadynamics was used to assess the binding/unbinding process of the formate anion ($HCOO^-$) to the rutile (110) surface in water (TIP3P model).[112] The rutile surface was non-hydroxylated and charge neutral. The free energy landscape was measured in the two cases where the ion is closer to the surface than 4 Å and where it is farther than 4 Å. In the first instance, two collective variables were chosen: the distance of the ion from the surface in the surface normal direction and the coordination number of the binding site on the rutile surface. In the latter case where the ion is not close to the surface, only one collective variable (the ion-surface distance in the normal direction) was considered.

Three energy basins were detected when the formate ion is close to the surface. The basins include the doubly bound, singly bound and unbound states; in the singly bound state, the formate ion is bonded to the surface by one of its oxygens while in the doubly bound state both oxygens of the ion are involved in bonding. Doubly and singly bound states were in more favorable energy states compared to the unbound state, but it was also shown that the ion has to cross energy barriers to be able to leave the unbound state and undergo the transition to first, the singly bound state and then the doubly bound state.

In the case where the formate ion is farther than 4Å from the surface (in the unbound state), there is a local minimum around 4.5Å which corresponds to the point when the ion is moving into bulk water.

2.4.3.1.2 Oligopeptides

It has been shown previously that amino acids bind to surfaces through their side-chains.[113] Brandt *et al*. used molecular dynamics (unbiased sampling), umbrella sampling and adaptive well-tempered metadynamics (biased sampling) to study the adsorption of amino acid side-chain analogues (SCA) and a titanium-binding peptide (TBP; the RKLPDA hexapeptide) on a charge neutral (non-hydroxylated) rutile (100) surface.[53] The C_α of the amino acid (the backbone carbon to which the carbonyl carbon is attached) was replaced by a hydrogen in different amino acids to obtain 19 SCAs (Figure A.2). These SCAs can be divided into four groups of polar, charged, aromatic and hydrophobic residues. The organic residues were solvated in water (TIP3P model).[53] Umbrella sampling and adaptive well-tempered metadynamics are both known as enhanced sampling molecular dynamics methods.

Comparison of the results obtained from these two methods in this study showed that they are in good agreement with each other.

Among the SCAs, polar and aromatic residues showed stronger adsorption to the surface while hydrophobic groups showed less affinity for the titanium dioxide surface. A general statement could not be made for charged residues. In general, residues with oxygen or nitrogen in their terminal groups can bind to the surface through hydrogen bonding while residues with carbon or sulfur terminations have less favorable interaction with the surface. Serine and tyrosine have the strongest binding to the surface; they can displace water molecules and bind directly to the surface.

Histidine was considered in its two forms (HID and HIE) with protonation on two different nitrogen atoms on the side group. Still, this minor difference was found to affect the free energy of adsorption.

The free energy of adsorption for the side-chain analogues can be used to predict the adsorption behavior of proteins. For example, a protein is expected to bind to the surface in a way that a higher number of SCAs with more favorable interactions is exposed to the surface. The binding energy of TBP was significantly larger than the accumulative free energy of adsorption of its SCAs, meaning its adsorption is more favorable than that of its residues, pointing out that this hexapeptide must have a strong affinity for titanium dioxide surfaces.[65] Two binding modes for TBP to TiO_2 surface were observed. The first mode is a worm-like mode which has more mobility compared to the second binding mode (compact c-like mode). The second binding mode was energetically more favorable than the first binding mode. Figure 2.2 shows the two-dimensional free energy landscape of TBP binding to the rutile (100) surface with respect to the peptide end-to-end distance (EED) and its surface separation distance (SSD). The two adsorption modes are marked with crosses in this figure.

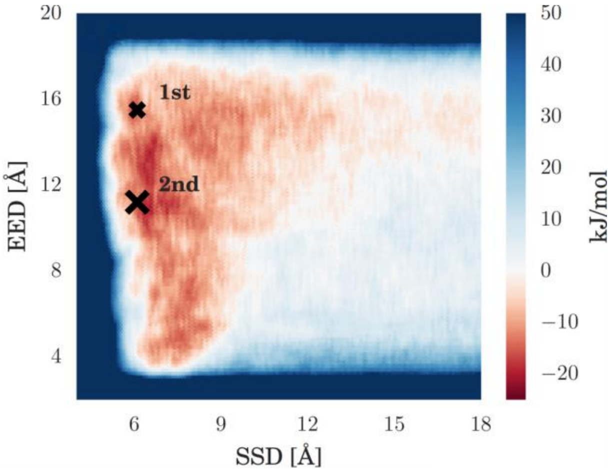

Figure 2.2 Two-dimensional free energy landscape of TBP based on its separation distance from the rutile (100) surface (SSD) and its end-to-end distance (EED). Crosses mark the two binding modes of the peptide on the surface. Reprinted with permission from Ref. 53. © 2015 American Chemical Society.

The interaction of C-terminated and N-terminated Ala amino acid (Ala-Ace and Ala-Nme, respectively) and Ala-Glu and Ala-Lys dipeptides (with -1 and +1 charges, respectively) with the non-hydroxylated rutile (110) surface was studied by Carravetta *et al*. .[46] The Ace blocking group which is added to the N-terminus, and the Nme blocking group which is added to the C-terminus, create peptide bonds for the Ala amino acid as it would appear in a protein. Water was described by the TIP3P model.

The radial distribution function revealed strong interactions between the carbonyl, carboxyl and amide groups of the Ala-Ace molecule and the water molecules (Figure A.3a). The amine group of the Ala-Nme molecule also showed a sharp peak in the radial distribution function with water molecules (Figure A.3b). The absence of a prominent peak between the Ala-Nme carbonyl oxygen and water can be explained by the direct interaction of this side group with the TiO_2 surface.

The trend of the interaction strength of different atom pairs in Ala-Glu and Ala-Lys with water molecules was similar. The interaction of Ala-Lys dipeptide with the surface is slightly more favorable than Ala-Glu dipeptide, which is also supported by the lower flexibility of the Ala-Lys dipeptide.

RAD (Arg-Ala-Asp) is similar to RGD and it can also be involved in cell attachment. Monti used molecular dynamics to study the interaction of a bilayer with the non-hydroxylated rutile (110) surface.[114] Each layer consisted of eight peptide chains. The bilayer was investigated in a parallel orientation and a perpendicular orientation towards the surface. Even though the water molecules (described by TIP3P model) between the bilayer and the surface were initially removed, some water molecules were found in this region at the end of the simulation. Thus, the water-surface interactions are in general more favorable than the bilayer-surface interaction and there is competitive adsorption between the organic and water on the surface. Nevertheless, the bilayer had direct and indirect interactions with the surface in both orientations; through direct bonds with the surface and hydrogen bonds with the adsorbed water molecules on the surface, respectively. The bilayer in the parallel orientation formed more bonds (95% through the Arg residue) with the surface compared to its perpendicular orientation. It was observed that in the perpendicular orientation, the bilayer is capable of significant conformational rearrangements to increase favorable interaction points with the surface. The reason for its higher mobility and flexibility was attributed to the smaller number of bonds with the surface compared to the parallel orientation.

2.4.3.1.3 An albumin subdomain

In order to study the effect of surface hydroxylation on protein adsorption, Kang *et al*. compared the adsorption of an albumin subdomain (HSA-IIIb made of 85 amino acids; Protein data bank ID code: 1AO6) on the non-hydroxylated and fully hydroxylated charge neutral rutile (110) surface in contact with water (SPC/E model).[51] The electrostatic interaction between albumin and the hydroxylated surface was found to be more favorable than with the non-hydroxylated surface. While on the hydroxylated surface some of the residues were able to displace water molecules and form hydrogen bonds with surface hydroxyls, the adsorbed residues could not perturb the first two water layers on the non-hydroxylated surface (Figure 2.3). This was the case even for the same amino acids in the albumin subdomain which were adsorbed onto the surface in both hydroxylated and non-hydroxylated states.

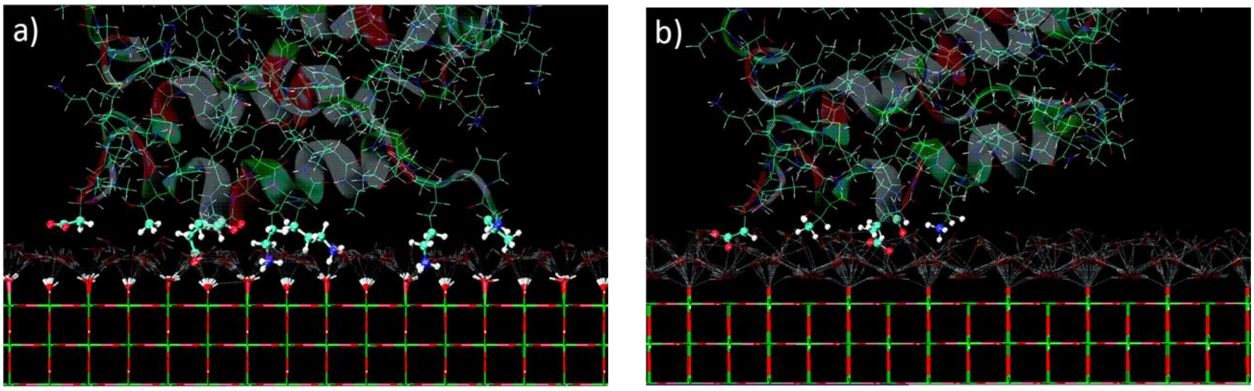

Figure 2.3 Adsorbed residues on a) fully hydroxylated and b) non-hydroxylated rutile (110) surfaces at 5 ns. Albumin atoms closer than 7 Å to the surface are shown using the ball-and-stick model. Water molecules except the interfacial water molecules have been removed for clarity. Hydrogen bonds are shown in white dashed lines. Color code: Ti: green, C: turquoise, O: red, N: blue and H: white. Reprinted with permission from Ref. 51. © 2010 American Chemical Society.

The first two water layers are bonded to each other via more hydrogen bonds on the non-hydroxylated surface compared to the number of hydrogen bonds between the surface hydroxyls and the first water layer on the hydroxylated surface, before and after adsorption of the protein. As a result, the movement of the albumin subdomain towards the non-hydroxylated rutile surface can be hindered by the stronger bonding between the water layers close to the surface.

2.4.3.1.4 The RGD polypeptide

Schneider *et al*. performed umbrella sampling to measure the desorption energy of RGD from an amorphous oxidized titanium surface.[63] The free energy of desorption of the RGD polypeptide solvated in water on a neutral amorphous titanium oxide surface was calculated to be -0.32 eV.[63] In the presence of external surfaces (substrates), adsorption of organic molecules on surface can be in competition with binding of integrin receptors to the surface, emphasizing the importance of surface modification and surface engineering. The interaction of RGD (Arg-Gly-Asp) with the oxidized titanium surface was through direct binding of the R residue (Arg) to the surface and indirect binding of the D residue (Asp).

2.4.3.2 Negatively charged surfaces

2.4.3.2.1 Simple organic residues

Sultan *et al*. considered six amino acid analogues rather than the complete amino acid.[115] There are numerous studies on the interaction of single amino acids with surfaces. Nevertheless, such results cannot be generalized to cases where the amino acid is part of a polypeptide or a protein because the exposed amine and carboxylate terminal groups of the non-bonded amino acids are absent in the polypeptide/protein.

The amino acid analogues covered nonpolar, uncharged polar and charged polar molecules. From the alanine, phenylalanine, serine, arginine, lysine and aspartic acid amino acids, the chosen analogues were methane, benzene, methanol, guanidinium cation, ammonium cation and methanoate anion, respectively. The first three analogues are neutral. The adsorption of these analogues was investigated in an aqueous environment (using a modified TIP3P water model), on a neutral non-hydroxylated rutile (110) surface using molecular dynamics and on a negatively charged (partially hydroxylated) rutile (110) surface using metadynamics.[115,116]

Among the neutral analogues, the two hydrophobic analogues, methane and benzene, revealed no attraction towards neither the neutral nor the charged surface. This suggests that the hydrophobic parts of peptides are expected to be found as far as possible from the hydrophilic titanium dioxide surface.[31,116] Methanol showed a weak binding to the negatively charged rutile surface.

Benzene and the guanidinium cation have relatively planar and rigid geometries. While benzene did not adsorb on either of the neutral or charged surfaces, the guanidinium cation showed the strongest binding to the charged rutile surface among all studied analogues (Figure 2.4a). The adsorption of the ammonium cation on the negatively charged rutile surface was similar to that of the guanidinium cation. Nevertheless, the methanoate anion also showed a favorable binding to the charged rutile surface. It was suggested that the binding of the anion to the negatively charged surface is due to the nanometer spatial variation of charges (missing bridging hydrogen) on the surface.[115,117]

In general, binding was always stronger and energetically more favorable on the charged surface compared to the neutral surface (Figure 2.4b). The free energy of adsorption was defined as the difference between the free energy of the system when the organic analogue is free in water and when it was adsorbed onto the surface. Since the adsorption of the organic analogue was possible on both faces of the solid slab, the free energy of the system in the adsorbed state was the average value of the adsorption on each face. The weak adsorption of the uncharged residues to the charged surface can even turn repulsive on the neutral surface.[115,116]

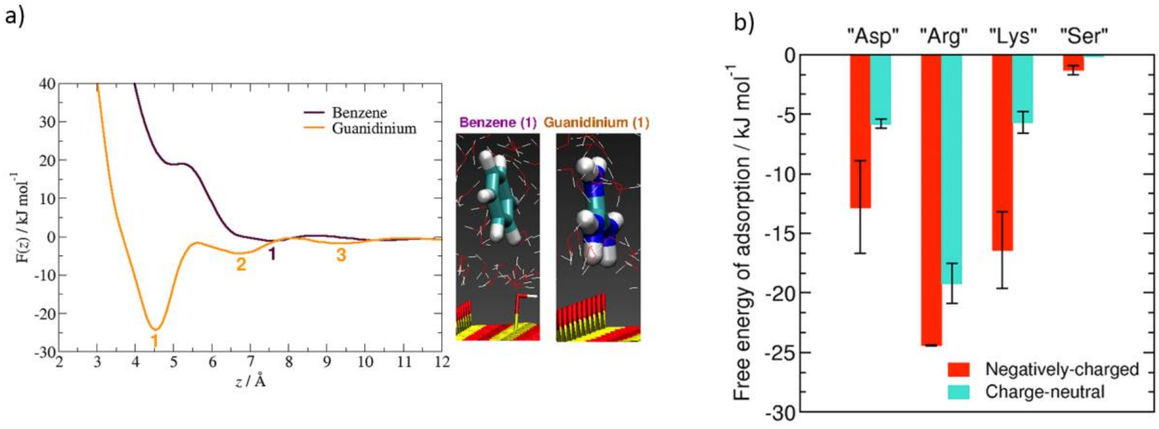

Figure 2.4 a) Variation of free energy of adsorption as a function of distance from the negatively charged rutile (110) surface for benzene and the guanidinium cation. The local (2 and 3) and global (1) energy minima are numbered. The lowest-energy configurations (1) are shown on the right. Color code: Ti: yellow, C: turquoise, N: blue, O: red and H: white. b) Free energy of adsorption for the adsorbed analogues on the charge neutral[116] and negatively charged rutile (110) surfaces. Reprinted with permission from Ref. 115. © 2014 American Chemical Society.

2.4.3.2.2 The RGD polypeptide:

Wu *et al*. studied the effect of the presence of Na^+ cations on the adsorption of the RGD polypeptide on the negatively charged (partially hydroxylated) rutile (110) surface in contact with water (SPC/E model).[118] In the absence of Na^+ cations, bonding between the negatively charged rutile surface and the positively charged Arg residue is expected. However, the presence of Na^+ cations in the solution forces RGD to change its conformation. Consequently, the Arg residue in RGD detaches from the rutile surface in the presence of Na^+ ions to reduce the repulsion between its amine group and the sodium cations. On the other hand, the Na^+ cations bridge the COO^- group to the rutile surface; making it possible for the negatively charged Asp residue to bind to the negatively charged rutile surface.

In order to see if monovalent and divalent cations mediate surface-organic bonding differently, Wu *et al*. studied the effect of different cations on the adsorption strength and conformation of RGD (the negatively charged Asp residue, in specific), onto the negatively charged (partially hydroxylated) rutile (110) surface.[102] Water molecules were described using the SPC/E water model. Monovalent cations, similar to sodium cations, help the COO^- group to form hydrogen bonds with the negatively charged rutile surface (Figure 2.5a).[118] If the number of these hydrogen bonds is sufficient to keep the RGD sequence attached to the surface, the monovalent cations are free to leave the surface. However, the adsorption of the peptide to the surface is quite different in the presence of divalent cations. In this case, the adsorption is through indirect binding between the surface and the divalent cation. This binding is robust enough to keep the peptide attached to the surface without the need to have direct hydrogen bonding between the rutile surface hydroxyl groups and the COO^- group of RGD (Figure 2.5b).

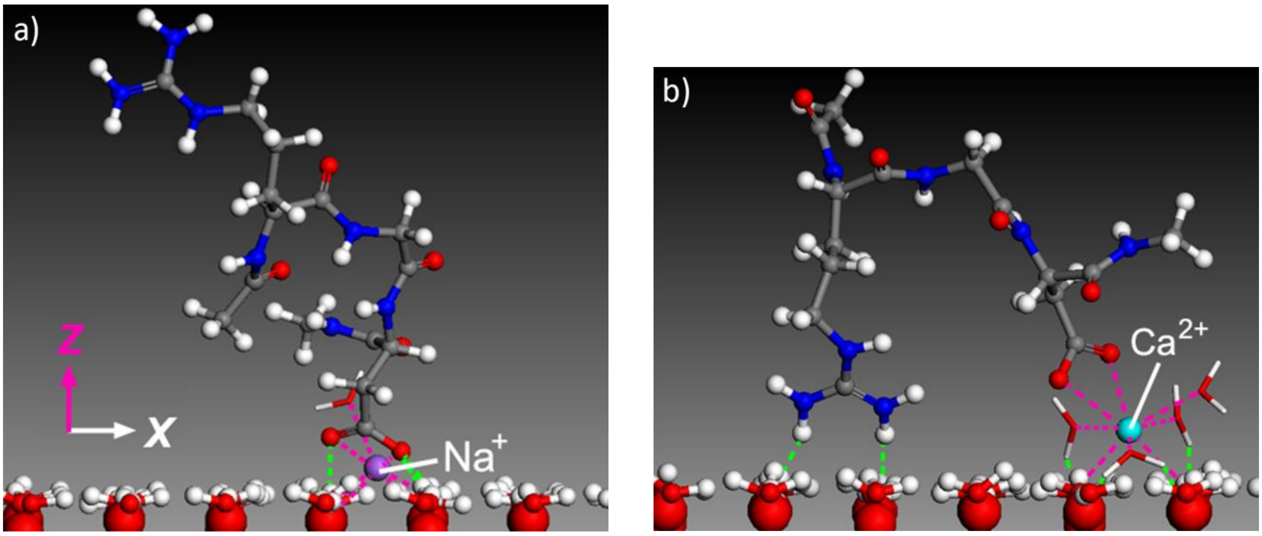

Figure 2.5 Adsorption configuration of RGD on the negatively charged (partially hydroxylated) rutile (110) surface in the presence of a) sodium and b) calcium cations. Color code: C: gray, N: blue, O: red, H: white, Na: purple and Ca: turquoise. Reprinted with permission from Ref. 102. © 2012 American Chemical Society.

2.4.3.2.3 Nucleotide bases:

Monti *et al*. studied the interaction of four nucleotide bases (adenine, thymine, guanine and cytosine) with the partially hydroxylated rutile (110) surface with a negative charge density of -0.104 $C \cdot m^{-2}$.[119] The total charge of the system was neutralized by adding Ca^{2+} and Cl^- ions to the solution. Ca^{2+} ions did not move freely in the solution and strongly adsorbed to surface terminal oxygens.

Since the surface carries a net negative charge, chlorine ions are expected to be far from the surface. However, a permanent interaction between calcium ions and chlorine ions was found (Figure A.4). It had been speculated that in the presence of multivalent cations, the chlorine ion could approach the surface up to small distances but not closer than the first water layer on the surface.[100,119] Although the surface was designed to mimic the charged titanium dioxide surface in the physiological pH, the presence of the calcium and chlorine ions close to the surface modifies the acid-base nature of the surface by compensating the surface charge.

The density distribution of the center of mass of the four nucleotide bases versus their distance from the surface showed that their preferred distance from the surface is between the structured water layers and the bulk water. This can be seen in Figure A.4 in which the density peak for the center of mass of the nucleotide bases is located farther than water peaks with respect to the rutile surface. The study of the variation of the free energy as a function of distance during the adsorption of these four nucleotide bases shows that the structured water layers close to the surface can postpone or significantly weaken the direct surface-nucleotide base interaction. In fact, none of the studied nucleotide bases showed a strong binding with the surface and their migration away from the surface was frequently seen.[119]

2.4.3.2.4 Lipids

The adsorption strength of three lipids solvated in water (TIP3P model) on the rutile (110) surface with different levels of hydroxylation was studied by Fortunelli *et al.* [120] The hydroxylation percentage of the partially hydroxylated surface was designed such that it will resemble the state of the surface in physiological conditions. The mobility and flexibility of the lipids decreased in the order of hydroxylated, partially hydroxylated and non-hydroxylated surface. Hence, the adsorption became more favorable in this order. Since pH affects the balance between the bridging and terminal hydroxyl groups on the surface, it will affect the attachment of organics on the surfaces.

2.4.3.2.5 Polypeptides

Sultan *et al*. used the Replica Exchange Solute Tempering (REST) method coupled with metadynamics to look at the adsorption mechanism and behavior of two polypeptides on a negatively charged rutile (110) surface.[117] The TIPS3P model was used to describe water. The surface charge density was set to -0.104 $C \cdot m^{-2}$. The two polypeptides were different in their total charge and the number of hydrophobic residues (Ti-1: QPYLFATDSLIK and Ti-2: GHTHYHAVRTQT). Despite their different building blocks, both residues showed a strong affinity for the rutile (110) surface. The free energy of adsorption was found to be -12.7 $\pm$ 0.4 $kJ \cdot mol^{-1}$ for Ti-1 and -16.34 $\pm$ 3.7 $kJ \cdot mol^{-1}$ for Ti-2. The same trend for the adsorption energy of two peptides was found using experimental methods. The absolute energy of the adsorption, however, was different from the experimental results which can be attributed to various parameters including the use of a non-reactive force field. Different characteristics of Ti-1 and Ti-2 and at the same time their similar adsorption energy on the titania surface indicate that the adsorption of these two residues should be via different mechanisms. The contribution of the entropy in the adsorption was estimated for the two residues. This parameter had a positive value for Ti-1 while it had a negative value for Ti-2. This indicates that the adsorption of Ti-1 on the rutile surface is driven by the entropy while Ti-2 adsorption is mainly driven by enthalpy.

2.4.3.2.6 The RKLPDA hexapeptide

The force field which was developed by Schneider *et al*. for amorphous oxidized titanium[63] was used to study the adsorption of the RKLPDA hexapeptide on the non-crystalline titanium oxidized surface in contact with water (TIP3P model) using the metadynamics method.[65] The surface carried a surface charge density of -0.123 $C \cdot m^{-2}$, which corresponds to the surface charge at physiological pH. The binding of the hexapeptide was through direct binding of the Arg residue to the surface.

2.4.4 Surface defects

Compared to defect-free surfaces, surfaces containing structural defects have a higher surface energy, which may enhance protein adsorption and cell attachment.[9,121] The strong interaction of the protein with surfaces containing structural defects might restrain the movement of the protein and affect further cell recognition and adhesion. Water density distribution close to the surface can also be affected by surface defects, which can provide more active interaction sites on the surface for the organic.[122]

2.4.4.1 Fibronectin module

Wu *et al*. compared the interaction of a fibronectin module (FN-III_{10}) with perfect and various defects on non-hydroxylated rutile (110) surfaces in vacuum. The surface defects included oxygen vacancies, steps and grooves.[123] While adsorption occurred on all surfaces, the binding strength differed for different surface topographies. Both side-chain and backbone atoms were involved in the adsorption process. The carbonyl and carboxylate groups showed dominant interaction with the surface while the interaction of the amine and amide groups were relatively weak. The surface with step defects showed the highest binding energy with the fibronectin module. The fibronectin module contains the RGD sequence. The adsorption of RGD, especially on the surface with steps, significantly reduced its mobility. While this can be beneficial in having stable protein adsorption on the surfaces, it should not hinder further cell recognition by the surface. Although these trends seem generally interesting, further work in the presence of water needs to be made to verify such findings in vacuum.

2.4.4.2 Collagen triple helix

Ebrahimi *et al*. studied the effect of the degree of surface roughness of the non-hydroxylated rutile (100) surface on the adhesive energy of type I collagen, consisting of a triple-helix, in vacuum.[124] Compared to the defect-free (100) surface, collagen experienced significant conformational changes while adsorbing on the surface defects and the surface-collagen equilibration distance was also relatively smaller. The interaction of the collagen segment to the rutile surface defects was much more favorable and the collagen bonded through more contact points to this surface.

2.4.4.3 The RGD polypeptide

Song *et al*. investigated the effect of surface defects, in the form of pits, on the adsorption of RGD solvated in water (TIP3P model) onto a non-hydroxylated rutile (110) surface.[9] Adsorption of RGD polypeptides onto a surface containing defects happened much faster compared to the defect-free surface and was more stable due to its stronger binding. The same trend for adsorption kinetics and adsorption strength was observed when the adsorption of RGD onto the non-hydroxylated (110) rutile surface in vacuum was compared between the defect-free surface and surfaces with grooves of different dimensions.[125]

Chen *et al*. compared the adsorption energy of RGD solvated in water (TIP3P model) on non-hydroxylated, defect-free and rutile (110) surfaces with defects represented by three different depths of grooves (3.25, 6.50 and 9.75 Å).[108] The binding state of RGD was initially through the carboxylate group. On the defect-free surface, RGD maintained this binding mode and the amine group was far from the rutile surface. On the grooved surfaces, however, RGD underwent significant conformational changes until the RGD long axis was parallel to the surface. RGD adsorption onto grooved surfaces was much more favorable than onto defect-free surfaces (almost 1.6 times, similar to Liang *et al*.[126]) which can be attributed to a higher number of active sites on the grooved surfaces.

2.4.4.4 Collagen segment

In another study, the effect of the width and the depth of surface grooves on the adsorption of a collagen segment (2KLW), solvated in water (SPC/E model), on the non-hydroxylated rutile (110) surface was investigated.[127] Adsorption was favored when the groove width matched well with the dimension of the collagen segment. This is in agreement with Kasemo's suggestion that topographical surface features with dimensions similar to those of the adsorbing protein can significantly affect its configuration, binding strength and activity.[31]

2.4.5 Surface contamination

2.4.5.1 Two peptides and the RKLPDA hexapeptide

Air-exposed titanium oxide surface can be contaminated with hydrocarbons and small alcohols, which are present in the ambient atmosphere. The adsorption of two peptides (TiOBP1: RPRGFGMSRERQ sequence and TiOBP2: WFCLLGCDAGCW sequence) and a hexapeptide (RKLPDA) on rutile (100) surfaces, with two different levels of contamination by pentanol, were compared to the partially hydroxylated clean surface in water (TIP3P model).[50]

Hydrophobicity of the peptide and the ratio of the hydrophobic to hydrophilic residues can affect its adsorption onto the surface. TiOBP1 has nine hydrophilic and three hydrophobic residues. As long as one of the faces of the slab was a clean surface, the adsorption of TiOBP1 on this surface was more favorable. When both surfaces of the slab were contaminated and no clean surface was present in the system, the adsorption occurred on the contaminated surface. Adsorption on both clean and contaminated surfaces was stable. In the case of the contaminated surface, the peptide underwent structural changes, during which it tried to expose more hydrophobic residues to the surface. Two of the residues with charged end groups penetrated the pentanol layer and bound directly to the titanium dioxide surface.

TiOBP2 has an equal number of hydrophobic and hydrophilic residues (6:6). In contrast to TiBP1, TiOBP2 did not adsorb on the clean surface while it quickly adsorbed on the contaminated surface. The hexapeptide (RKLPDA) is similar to TiOBP2 in terms of having the same ratio of the number of hydrophobic to hydrophilic residues (3:3). However, unlike TiOBP2, RKLPDA adsorbed on both clean and contaminated surfaces. It was concluded that the adsorption on different surfaces is driven by the ability of the organic molecule to undergo structural changes to rearrange its residues in a manner that allows more favorable interactions with the surrounding environment.

2.4.6 Initial orientation of the organic molecule

2.4.6.1 Ala dipeptides

Adsorption of two uncharged peptides (Ala-Lys (AK) and Ala-Glu (AE)) on the non-hydroxylated rutile (110) surface in the presence of water (TIP3P model) was studied.[128] Each peptide was studied in a separate system. In each system, nine different initial orientations of the peptide were simultaneously placed on top of the surface. In other words, each peptide was studied in the presence of eight other orientations of its own. This was done to investigate the perturbation effect resulting from the presence of neighboring peptides. During the equilibration step, one out of nine orientations of each peptide led to its detachment from the surface. Both peptides (AK and AE) interacted with the surface mainly through the oxygen atoms of their carboxylate groups and the nitrogen atoms of their amine groups. Further investigation revealed that the titanium dioxide surface constrains the movement of the peptides due to the surface-peptide binding.[129] It was shown that having several contact points between the backbone and the surface or even a single such contact point in addition to hydrogen bonding with other peptides that are strongly bonded to the surface can keep the peptide bonded to the surface throughout the simulation time of 6 ns.

2.4.6.2 The RGD polypeptide

The effect of the initial orientation of the RGD polypeptide on its adsorption to the non-hydroxylated rutile (110) surface was studied using two different water models (SPC/E and TIP3P).[106] In agreement with other studies, the initial orientation proved to be important since, for some orientations, the peptide moved away from the surface as its interaction with water was more favorable. The interaction of amine groups was dominant compared to the carboxylate groups and it was mainly through the Arg residue; this is in contrast with DFT results of adsorption of RGD on rutile (110) surface, albeit in vacuum, which occurs through the aspartic acid carboxyl groups and not the arginine side group.[130] The presence of the RGD polypeptide did not affect the water structure close to the hydrophilic rutile surface.

The results of surface-organic-water interactions using the two three-point rigid water models (SPC/E and TIP3P) showed that the SPC/E water model leads to slightly stronger interactions between the peptide and the surface oxygen atoms. Also, the peptide shows more flexibility while solvated in the SPC/E water model which helps it attain its equilibration state in a shorter time.

2.4.6.3 Collagen segment

While one of the most important segments of collagen is the RGD sequence, Monti studied the possibility of the adsorption of a collagen segment in the absence of any RGD sequence or charged amino acid to the non-hydroxylated rutile (110) surface.[131] The collagen segment was chosen to be a triple helical segment (THS) of collagen, consisting of 21 amino acids. Water molecules were modelled using the TIP3P model. The long axis of THS was orientated parallel to the rutile surface and its interactions with the surface were studied in six different rotations of THS around this axis. The attachment of the THS segment to the rutile surface was observed through hydrogen bonds.

The stability of the THS can be attributed to the stability of the hydrogen bonds between its helices. In proximity to the rutile surface, several residues in the helix will engage in bonding with the surface and will not be available for hydrogen bonding with the other two helices anymore. The other two helices, as a result, now have the possibility to interact with their surrounding solvent. The stronger the interaction of the helices far from the surface with their surrounding water molecules, the more likely the unfolding of the THS segment. In fact, in two out of six different initial orientations of THS, the helices started to expand over time to a point in which the initial THS orientation was completely lost and disrupted.

Even though the THS segment studied in this work lacks the carboxylate groups, it was seen that peptides rich in Hyp residues could also adsorb to the rutile surface but the binding stability depends on their initial orientation.

The adsorption of a collagen segment (2KLW) in three different orientations, solvated in water (SPC/E model), to the non-hydroxylated rutile (110) surface with defects has also been studied.[122] The initial orientation significantly affects the interaction frequency of the functional groups as well as the binding strength. No adsorption was observed in one out of three different orientations but in the other two orientations, the collagen segment adsorbed to the surface at the beginning of the simulation. Adsorption in these two cases occurred both indirectly through water molecules and directly through direct bonds between the collagen segment and the surface. The indirect bonding between the carboxylate group of the Asp residue was insufficient to keep the collagen segment bound to the surface and after some time it detached (Figure 2.6). On the other hand, direct binding between the amino group of Lys and the rutile surface was stable over the simulation time of 6 ns.

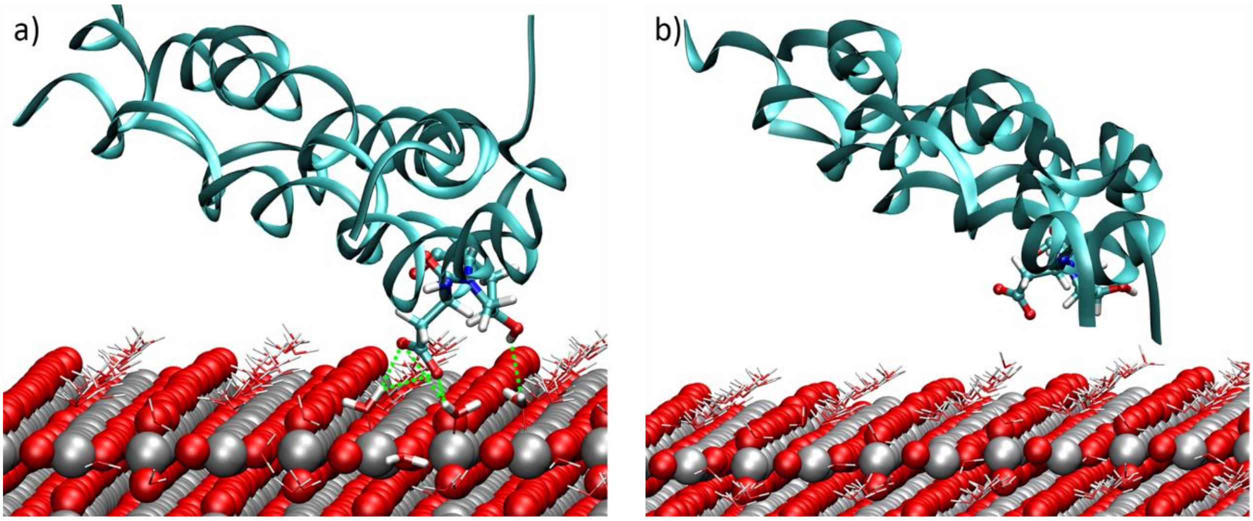

Figure 2.6 a) Collagen interaction with the non-hydroxylated rutile (110) surface at t = 3 ns and b) its detachment from the rutile surface at t = 6 ns. Color code: Ti: gray, C: turquoise, N: blue, O: red and H: white. Reprinted with permission from Ref. 122. ©2013 Elsevier.

2.4.6.4 Bone morphogenetic protein-2

The interaction of bone morphogenetic protein-2 (BMP-2) with the non-hydroxylated (001) rutile surface, solvated in water (TIP3P model), was investigated by Utesch *et al*. in six different initial orientations with respect to the surface.[132] The BMP-2 protein was placed on the surface in two end-on and four side-on orientations. Molecular dynamics and steered molecular dynamics methods were used. During steered molecular dynamics, an external force was applied on the biomolecule to accelerate its conformational changes and to observe its possible adsorption/desorption from the surface. Although the surface-biomolecule interaction was favorable, the adsorption of the BMP-2 molecule to the surface was loose and strongly hindered by the two structured water layers close to the hydrophilic TiO_2 surface. The force exerted by water molecules on BMP-2 was measured at different distances from the surface. At distances where the first water layer is located, this force was repulsive. At a distance close to the second water layer, this force was attractive and when far from the surface, the force was negligible. It was concluded that direct binding between BMP-2 and the surface is hindered by the repulsive force exerted on the biomolecule from the first water layer. Nevertheless, the attractive force between BMP-2 and the molecules of the second water layer was enough to keep the biomolecule loosely bonded to the surface. By applying an external force on BMP-2 to pull it towards the surface, BMP-2 penetrated the second water layer but not the first water layer close to the surface. Application of larger forces led to unrealistic conformational changes in BMP-2.

2.5 Summary

Here we present a summary of points which were made in different studies. Adsorption of ions and biologically relevant organic molecules readily take place on rutile surfaces at pHs near to physiological conditions and molecular dynamics studies have been able to shed significant light on the mechanisms involved. From these simulations, it can be concluded that surface characteristics (crystal structure, hydrophobicity, surface charge, surface defects and contamination) and organic molecule characteristics (its functional groups and orientation with respect to the surface) affect the organic-inorganic interactions as well as the conformational and structural changes that the organic molecule might experience during adsorption on the surface. Some other points include:

- There is competitive adsorption between water and the organic on the surface. Since water molecules cover the titanium oxide surface before organic molecules (on a non-coated surface), the organic residues have to displace the water molecules to bind directly to the surface.
- On a neutral surface, the interaction of functional groups containing oxygen or nitrogen with the titanium dioxide surface is more favorable than that of functional groups containing sulfur or carbon atoms. In general, adsorption onto a charged surface is more favorable than onto a neutral surface.
- Defect sites can provide additional binding sites for organic molecules. Their higher activity can lead to stronger binding. It should be noted that, in some cases, this strong binding can significantly restrict protein mobility and negatively affect cell recognition and attachment since cells recognize certain proteins in specific orientations and configurations.
- Surface contamination, like other surface characteristics, can control the arrangement of hydrophobic and hydrophilic residues of the organic unit before and during its adsorption on the surface.
- The initial orientation of the organic molecule affects its adsorption behavior. Several studies observed that for some orientations the molecule preferred to stay solvated while the same molecule bonded to the surface in other orientations. While this is not always problematic, caution should be taken when studying an organic molecule with several parts that are bonded to each other through hydrogen bonds. If some parts of the organic engage in surface binding, other sections might start compensating their missing hydrogen bonds through hydrogen bonding with surrounding water molecules. The unfolding of the initial conformation of the organic molecule, in this case, is probable.

There are still fundamental questions concerning the interaction of organic molecules with inorganic surfaces and research is still required on *in vitro* conditions. Computational methods are certainly useful in answering some of these questions. Some possible research points in this area are:

- The interaction of other SBF anions with titanium oxide surfaces, such as hydrogen phosphate, hydrogen carbonate and sulphate.
- The competitive adsorption of SBF ions and organics on titanium oxide surfaces.
- Enhanced sampling methods in line with molecular dynamics simulations to confirm adsorption energetics and kinetics at different sites both for SBF ions and organic molecules.

Ideally one should investigate the interaction of Ti surfaces with organic components solvated in a solution close to SBF - this could be computationally very expensive but it is an important next step in the realm of computational studies. Within the limitations of molecular dynamics modelling (limited timescale and no chemical reactions), some interesting and pertinent insights have already been gained. As outlined above, further work with well-defined systems (mimicking experimental conditions derived from thermodynamic modelling) will lead to a better understanding of the interaction of these complex solutions with solid surfaces. Further work on specific problems, where “reactive” situations are of high relevance, could then be carried out using first-principles molecular dynamics potentially combined with classical molecular dynamics for the non-reactive part (QM/MM scheme) or enhanced sampling methods to overcome timescale limitations.

References

(1) Patel, N. R.; Gohil, P. P. A Review on Biomaterials: Scope, Applications & Human Anatomy Significance. *Int. J. Emerg. Technol. Adv. Eng.* **2012**, *2* (4), 91–101.

(2) Liu, X.; Chu, P.; Ding, C. Surface Modification of Titanium, Titanium Alloys, and Related Materials for Biomedical Applications. *Mater. Sci. Eng. R Rep.* **2004**, *47* (3–4), 49–121.

(3) Lindahl, C.; Borchardt, P.; Lausmaa, J.; Xia, W.; Engqvist, H. Studies of Early Growth Mechanisms of Hydroxyapatite on Single Crystalline Rutile: A Model System for Bioactive Surfaces. *J. Mater. Sci. Mater. Med.* **2010**, *21* (10), 2743–2749.

(4) Diebold, U. The Surface Science of Titanium Dioxide. *Surf. Sci. Rep.* **2003**, *48*, 53–229.

(5) Swamy, V.; Gale, J. D.; Dubrovinsky, L. S. Atomistic Simulation of the Crystal Structures and Bulk Moduli of TiO_2 Polymorphs. *J. Phys. Chem. Solids* **2001**, *62* (5), 887–895.

(6) Raffaini, G.; Ganazzoli, F. Molecular Modelling of Protein Adsorption on the Surface of Titanium Dioxide Polymorphs. *Philos. Trans. R. Soc. Math. Phys. Eng. Sci.* **2012**, *370* (1963), 1444–1462.

(7) Hallil, A.; Tétot, R.; Berthier, F.; Braems, I.; Creuze, J. Use of a Variable-Charge Interatomic Potential for Atomistic Simulations of Bulk, Oxygen Vacancies, and Surfaces of Rutile TiO_2. *Phys. Rev. B* **2006**, *73* (16), 165406(1-10).

(8) Aschauer, U.; Selloni, A. Hydrogen Interaction with the Anatase TiO_2 (101) Surface. *Phys. Chem. Chem. Phys.* **2012**, *14* (48), 16595–16602.

(9) Song, D.-P.; Chen, M.-J.; Liang, Y.-C.; Bai, Q.-S.; Chen, J.-X.; Zheng, X.-F. Adsorption of Tripeptide RGD on Rutile TiO_2 Nanotopography Surface in Aqueous Solution. *Acta Biomater.* **2010**, *6* (2), 684–694.

(10) Diebold, U.; Ruzycki, N.; Herman, G. S.; Selloni, A. One Step towards Bridging the Materials Gap: Surface Studies of TiO_2 Anatase. *Catal. Today* **2003**, *85* (2–4), 93–100.

(11) Kokubo, T.; Miyaji, F.; Kim, H. M.; Nakamura, T. Spontaneous Formation of Bonelike Apatite Layer on Chemically Treated Titanium Metals. *J. Am. Ceram. Soc.* **1996**, *79*, 1127–1129.

(12) Kim, H. M.; Miyaji, F.; Kokubo, T.; Nakamura, T. Effect of Heat Treatment on Apatite-Forming Ability of Ti Metal Induced by Alkali Treatment. *J. Mater. Sci. Mater. Med.* **1997**, *8* (6), 341–347.

(13) Kokubo, T.; Yamaguchi, S. Novel Bioactive Materials Developed by Simulated Body Fluid Evaluation: Surface-Modified Ti Metal and Its Alloys. *Acta Biomater.* **2016**, *44*, 16–30.

(14) Castner, D. G.; Ratner, B. D. Biomedical Surface Science: Foundations to Frontiers. *Surf. Sci.* **2002**, *500* (1), 28–60.

(15) Zadpoor, A. A. Relationship between *in Vitro* Apatite-Forming Ability Measured Using Simulated Body Fluid and *in vivo* Bioactivity of Biomaterials. *Mater. Sci. Eng. C* **2014**, *35*, 134–143.

(16) Hulsart-Billström, G.; Dawson, J. I.; Hofmann, S.; Müller, R.; Stoddart, M. J.; Alini, M.; Redl, H.; El Haj, A.; Brown, R.; Salih, V.; others. A Surprisingly Poor Correlation between *in Vitro* and *in Vivo* Testing of Biomaterials for Bone Regeneration: Results of a Multicentre Analysis. *Eur. Cell. Mater.* **2016**, *31*, 312–322.

(17) Kokubo, T.; Takadama, H. How Useful Is SBF in Predicting *in Vivo* Bone Bioactivity? *Biomaterials* **2006**, *27* (15), 2907–2915.

(18) Bohner, M.; Lemaitre, J. Can Bioactivity Be Tested *in Vitro* with SBF Solution? *Biomaterials* **2009**, *30* (12), 2175–2179.

(19) Dorozhkin, S. V.; Dorozhkina, E. I. The Influence of Bovine Serum Albumin on the Crystallization of Calcium Phosphates from a Revised Simulated Body Fluid. *Colloids Surf A* **2003**, *215*, 191–199.

(20) Tas, A. C. The Use of Physiological Solutions or Media in Calcium Phosphate Synthesis and Processing. *Acta Biomater.* **2014**, *10* (5), 1771–1792.

(21) Implants for Surgery — *In Vitro* Evaluation for Apatite-Forming Ability of Implant Materials. ISO 2007.

(22) Kokubo, T.; Kushitani, H.; Sakka, S.; Kitsugi, T.; Yamamuro, T. Solutions Able to Reproduce *in Vivo* Surface-Structure Changes in Bioactive Glass-Ceramic A-W3. *J. Biomed. Mater. Res.* **1990**, *24* (6), 721–734.

(23) Kasemo, B. Biological Surface Science. *Surf. Sci.* **2002**, *500*, 656–677.

(24) Silva-Bermudez, P.; Rodil, S. E. An Overview of Protein Adsorption on Metal Oxide Coatings for Biomedical Implants. *Surf. Coat. Technol.* **2013**, *233*, 147–158.

(25) Ratner, B. D. The Engineering of Biomaterials Exhibiting Recognition and Specificity. *J Mol Recognit* **1996**, *9*, 617–625.

(26) Tang, L.; Thevenot, P.; Hu, W. Surface Chemistry Influences Implant Biocompatibility. *Curr. Top. Med. Chem.* **2008**, *8* (4), 270–280.

(27) Redondo, A.; LeSar, R. Modeling and Simulation of Biomaterials. *Annu. Rev. Mater. Res.* **2004**, *34* (1), 279–314.

(28) Roach, P.; Eglin, D.; Rohde, K.; Perry, C. C. Modern Biomaterials: A Review—bulk Properties and Implications of Surface Modifications. *J. Mater. Sci. Mater. Med.* **2007**, *18* (7), 1263–1277.

(29) Kokubo, T.; Kim, H.-M.; Kawashita, M. Novel Bioactive Materials with Different Mechanical Properties. *Biomaterials* **2003**, *24* (13), 2161–2175.

(30) Parhi, P.; Golas, A.; Vogler, E. A. Role of Proteins and Water in the Initial Attachment of Mammalian Cells to Biomedical Surfaces: A Review. *J. Adhes. Sci. Technol.* **2010**, *24* (5), 853–888.

(31) Kasemo, B.; Gold, J. Implant Surfaces and Interface Processes. *Adv. Dent. Res.* **1999**, *13* (1), 8–20.

(32) Carré, A.; Lacarrière, V. How Substrate Properties Control Cell Adhesion. A Physical–Chemical Approach. *J. Adhes. Sci. Technol.* **2010**, *24* (5), 815–830.

(33) Jäger, M.; Zilkens, C.; Zanger, K.; Krauspe, R. Significance of Nano- and Microtopography for Cell-Surface Interactions in Orthopaedic Implants. *J. Biomed. Biotechnol.* **2007**, *2007*, 1–19.

(34) Boyan, B. D.; Hummert, T. W.; Dean, D. D.; Schwartz, Z. Role of Material Surfaces in Regulating Bone and Cartilage Cell Response. *Biomaterials* **1996**, *17* (2), 137–146.

(35) Tang, R.; Darragh, M.; Orme, C. A.; Guan, X.; Hoyer, J. R.; Nancollas, G. H. Control of Biomineralization Dynamics by Interfacial Energies. *Angew. Chem. Int. Ed.* **2005**, *44* (24), 3698–3702.

(36) Latour Jr, R. A. Molecular Modeling of Biomaterial Surfaces. *Curr. Opin. Solid State Mater. Sci.* **1999**, *4* (4), 413–417.

(37) Deighan, M.; Pfaendtner, J. Exhaustively Sampling Peptide Adsorption with Metadynamics. *Langmuir* **2013**, *29* (25), 7999–8009.

(38) Monti, S.; van Duin, A. C. T.; Kim, S.-Y.; Barone, V. Exploration of the Conformational and Reactive Dynamics of Glycine and Diglycine on TiO_2: Computational Investigations in the Gas Phase and in Solution. *J. Phys. Chem. C* **2012**, *116* (8), 5141–5150.

(39) Monti, S.; Li, C.; Ågren, H.; Carravetta, V. Dropping a Droplet of Cysteine Molecules on a Rutile (110) Interface: Reactive versus Nonreactive Classical Molecular Dynamics Simulations. *J. Phys. Chem. C* **2015**, *119* (12), 6703–6712.

(40) Li, C.; Monti, S.; Carravetta, V. Journey toward the Surface: How Glycine Adsorbs on Titania in Water Solution. *J. Phys. Chem. C* **2012**, *116* (34), 18318–18326.

(41) Li, C.; Monti, S.; Ågren, H.; Carravetta, V. Cysteine on TiO_2 (110): A Theoretical Study by Reactive Dynamics and Photoemission Spectra Simulation. *Langmuir* **2014**, *30* (29), 8819–8828.

(42) Latour, R. A. Molecular Simulation of Protein-Surface Interactions: Benefits, Problems, Solutions, and Future Directions (Review). *Biointerphases* **2008**, *3* (3), FC2-FC12.

(43) Heinz, H.; Ramezani-Dakhel, H. Simulations of Inorganic–bioorganic Interfaces to Discover New Materials: Insights, Comparisons to Experiment, Challenges, and Opportunities. *Chem Soc Rev* **2016**, *45* (2), 412–448.

(44) De Nardo, L.; Raffaini, G.; Ebramzadeh, E.; Ganazzoli, F. Titanium Oxide Modeling and Design for Innovative Biomedical Surfaces: A Concise Review. *Int. J. Artif. Organs* **2012**, *35* (9), 629–641.

(45) Bussi, G.; Gervasio, F. L.; Laio, A.; Parrinello, M. Free-Energy Landscape for β Hairpin Folding from Combined Parallel Tempering and Metadynamics. *J. Am. Chem. Soc.* **2006**, *128* (41), 13435–13441.

(46) Carravetta, V.; Monti, S. Peptide−TiO_2 Surface Interaction in Solution by *Ab Initio* and Molecular Dynamics Simulations. *J. Phys. Chem. B* **2006**, *110* (12), 6160–6169.

(47) Harding, J. H.; Duffy, D. M. The Challenge of Biominerals to Simulations. *J Mater Chem* **2006**, *16* (12), 1105–1112.

(48) Freeman, C. L.; Harding, J. H.; Cooke, D. J.; Elliott, J. A.; Lardge, J. S.; Duffy, D. M. New Forcefields for Modeling Biomineralization Processes. *J. Phys. Chem. C* **2007**, *111* (32), 11943–11951.

(49) Griebel, M.; Knapek, S.; Zumbusch, G. W. Numerical Simulation in Molecular Dynamics: Numerics, Algorithms, Parallelization, Applications; Springer: Berlin, 2007.

(50) Friedrichs, W.; Langel, W. Atomistic Modeling of Peptide Adsorption on Rutile (100) in the Presence of Water and of Contamination by Low Molecular Weight Alcohols. *Biointerphases* **2014**, *9* (3), 031006(1-14).

(51) Kang, Y.; Li, X.; Tu, Y.; Wang, Q.; Ågren, H. On the Mechanism of Protein Adsorption onto Hydroxylated and Nonhydroxylated TiO_2 Surfaces. *J. Phys. Chem. C* **2010**, *114* (34), 14496–14502.

(52) Skelton, A. A.; Liang, T.; Walsh, T. R. Interplay of Sequence, Conformation, and Binding at the Peptide−Titania Interface as Mediated by Water. *ACS Appl. Mater. Interfaces* **2009**, *1* (7), 1482–1491.

(53) Brandt, E. G.; Lyubartsev, A. P. Molecular Dynamics Simulations of Adsorption of Amino Acid Side Chain Analogues and a Titanium Binding Peptide on the TiO_2 (100) Surface. *J. Phys. Chem. C* **2015**, *119* (32), 18126–18139.

(54) Matsui, M.; Akaogi, M. Molecular Dynamics Simulation of the Structural and Physical Properties of Four Polymorphs TiO_2. *Mol. Simul.* **1991**, *6*, 239–244.

(55) Kim, D. W.; Enomoto, N.; Nakagawa, Z.; Kawamura, K. Molecular Dynamics Simulation in Titanium Dioxide Polymorphs: Rutile, Brookite and Anatase. *J. Am. Ceram. Soc.* **1996**, *79*, 1095–1099.

(56) Swamy, V.; Gale, J. D. Transferable Variable-Charge Interatomic Potential for Atomistic Simulation of Titanium Oxides. *Phys. Rev. B* **2000**, *62* (9), 5406–5412.

(57) Ogata, S.; Lyetomi, H.; Tsuruta, K.; Shimojo, F.; Kalia, R. K.; Nakano, A.; Vashishta, P. Variable-Charge Interatomic Potentials for Molecular Dynamics Simulations of TiO_2. *J Appl Phys* **1999**, *86*, 3036–3041.

(58) Alimohammadi, M.; Fichthorn, K. A. A Force Field for the Interaction of Water with TiO_2 Surfaces. *J. Phys. Chem. C* **2011**, *115* (49), 24206–24214.

(59) Oliver, P. M.; Watson, G. W.; Kelsey, E. T.; Parker, S. C. Atomistic Simulation of the Surface Structure of the TiO_2 Polymorphs Rutile and Anatase. *J. Mater. Chem.* **1997**, *7* (3), 563–568.

(60) Bandura, A. V.; Kubicki, J. D. Derivation of Force Field Parameters for TiO_2 −H_2O Systems from *Ab Initio* Calculations. *J. Phys. Chem. B* **2003**, *107* (40), 11072–11081.

(61) Collins, D. R.; Smith, W.; Harrison, N. M.; Forester, T. R. Molecular Dynamics Study of TiO_2 Microclusters. *J. Mater. Chem.* **1996**, *6* (8), 1385–1390.

(62) Schneider, J.; Colombi Ciacchi, L. First Principles and Classical Modeling of the Oxidized Titanium (0001) Surface. *Surf. Sci.* **2010**, *604* (13–14), 1105–1115.

(63) Schneider, J.; Colombi Ciacchi, L. A Classical Potential to Model the Adsorption of Biological Molecules on Oxidized Titanium Surfaces. *J. Chem. Theory Comput.* **2011**, *7* (2), 473–484.

(64) Guillot, B. A. A Reappraisal of What We Have Learnt During Three Decades of Computer Simulations on Water. *J Mol Liq* **2002**, *101*, 219–260.

(65) Schneider, J.; Colombi Ciacchi, L. Specific Material Recognition by Small Peptides Mediated by the Interfacial Solvent Structure. *J. Am. Chem. Soc.* **2012**, *134* (4), 2407–2413.

(66) Předota, M.; Bandura, A. V.; Cummings, P. T.; Kubicki, J. D.; Wesolowski, D. J.; Chialvo, A. A.; Machesky, M. L. Electric Double Layer at the Rutile (110) Surface. 1. Structure of Surfaces and Interfacial Water from Molecular Dynamics by Use of *Ab Initio* Potentials. *J. Phys. Chem. B* **2004**, *108* (32), 12049–12060.

(67) Skelton, A. A.; Walsh, T. R. Interaction of Liquid Water with the Rutile TiO_2 (110) Surface. *Mol. Simul.* **2007**, *33* (4–5), 379–389.

(68) Mark, P.; Nilsson, L. Structure and Dynamics of the TIP3P, SPC, and SPC/E Water Models at 298 K. *J. Phys. Chem. A* **2001**, *105* (43), 9954–9960.

(69) Smith, P. E.; van Gunsteren, W. F. The Viscosity of SPC and SPC/E Water at 277 and 300 K. *Chem. Phys. Lett.* **1993**, *215* (4), 315–318.

(70) Wu, Y.; Tepper, H. L.; Voth, G. A. Flexible Simple Point-Charge Water Model with Improved Liquid-State Properties. *J. Chem. Phys.* **2006**, *124* (2), 024503(1-12).

(71) Mao, Y.; Zhang, Y. Thermal Conductivity, Shear Viscosity and Specific Heat of Rigid Water Models. *Chem. Phys. Lett.* **2012**, *542*, 37–41.

(72) Abascal, J. L. F.; Vega, C. A General Purpose Model for the Condensed Phases of Water: TIP4P/2005. *J. Chem. Phys.* **2005**, *123* (23), 234505(1-12).

(73) Jorgensen, W. L.; Chandrasekhar, J.; Madura, J. D.; Impey, R. W.; Klein, M. L. Comparison of Simple Potential Functions for Simulating Liquid Water. *J. Chem. Phys.* **1983**, *79* (2), 926–935.

(74) Lindan, P. J.; Harrison, N. M.; Gillan, M. J. Mixed Dissociative and Molecular Adsorption of Water on the Rutile (110) Surface. *Phys. Rev. Lett.* **1998**, *80* (4), 762–765.

(75) Beck, T. J.; Klust, A.; Batzill, M.; Diebold, U.; Di Valentin, C.; Tilocca, A.; Selloni, A. Mixed Dissociated/Molecular Monolayer of Water on the TiO_2 (011)-(2×1) Surface. *Surf. Sci.* **2005**, *591* (1–3), L267–L272.

(76) Předota, M.; Machesky, M. L.; Wesolowski, D. J.; Cummings, P. T. Electric Double Layer at the Rutile (110) Surface. 4. Effect of Temperature and pH on the Adsorption and Dynamics of Ions. *J. Phys. Chem. C* **2013**, *117* (44), 22852–22866.

(77) Ganazzoli, F.; Raffaini, G. Computer Simulation of Polypeptide Adsorption on Model Biomaterials. *Phys. Chem. Chem. Phys.* **2005**, *7* (21), 3651–3663.

(78) Feig, M.; Brooks, C. L. Recent Advances in the Development and Application of Implicit Solvent Models in Biomolecule Simulations. *Curr. Opin. Struct. Biol.* **2004**, *14* (2), 217–224.

(79) Nada, H.; Kobayashi, M.; Kakihana, M. Anisotropy in Conformation and Dynamics of a Glycolate Ion Near the Surface of a TiO_2 Rutile Crystal Between Its {001} and {110} Planes: A Molecular Dynamics Study. *J. Phys. Chem. C* **2016**, *120* (12), 6502–6514.

(80) Aschauer, U.; Selloni, A. Structure of the Rutile TiO_2 (011) Surface in an Aqueous Environment. *Phys. Rev. Lett.* **2011**, *106* (16), 166102(1-4).

(81) Kavathekar, R. S.; Dev, P.; English, N. J.; MacElroy, J. M. D. Molecular Dynamics Study of Water in Contact with the TiO_2 Rutile-110, 100, 101, 001 and Anatase-101, 001 Surface. *Mol. Phys.* **2011**, *109* (13), 1649–1656.

(82) Kornherr, A.; Vogtenhuber, D.; Ruckenbauer, M.; Podloucky, R.; Zifferer, G. Multilayer Adsorption of Water at a Rutile TiO_2 (110) Surface: Towards a Realistic Modeling by Molecular Dynamics. *J. Chem. Phys.* **2004**, *121* (8), 3722–3726.

(83) Bredow, T.; Jug, K. Theoretical Investigation of Water Adsorption at Rutile and Anatase Surfaces. *Surf. Sci.* **1995**, *327* (3), 398–408.

(84) Jug, K.; Nair, N. N.; Bredow, T. Molecular Dynamics Investigation of Water Adsorption on Rutile Surfaces. *Surf. Sci.* **2005**, *590* (1), 9–20.

(85) Fahmi, A.; Minot, C. A Theoretical Investigation of Water Adsorption on Titanium Dioxide Surfaces. *Surf. Sci.* **1994**, *304* (3), 343–359.

(86) Liu, L.-M.; Zhang, C.; Thornton, G.; Michaelides, A. Structure and Dynamics of Liquid Water on Rutile TiO_2 (110). *Phys. Rev. B* **2010**, *82* (16), 161415(1-4).

(87) Dang, L. X.; Rice, J. E.; Caldwell, J.; Kollman, P. A. Ion Solvation in Polarizable Water: Molecular Dynamics Simulations. *J. Am. Chem. Soc.* **1991**, *113* (7), 2481–2486.

(88) Lee, S. H.; Rasaiah, J. C. Molecular Dynamics Simulation of Ion Mobility. 2. Alkali Metal and Halide Ions Using the SPC/E Model for Water at 25 C. *J. Phys. Chem.* **1996**, *100* (4), 1420–1425.

(89) Demichelis, R.; Raiteri, P.; Gale, J. D.; Quigley, D.; Gebauer, D. Stable Prenucleation Mineral Clusters Are Liquid-like Ionic Polymers. *Nat. Commun.* **2011**, *2*, 590(1-8).

(90) Cannon, W. R.; Pettitt, B. M.; McCammon, J. A. Sulfate Anion in Water: Model Structural, Thermodynamics, and Dynamic Properties. *J Phys Chem* **1994**, *98*, 6225–6230.

(91) Wernersson, E.; Jungwirth, P. Effect of Water Polarizability on the Properties of Solutions of Polyvalent Ions: Simulations of Aqueous Sodium Sulfate with Different Force Fields. *J. Chem. Theory Comput.* **2010**, *6* (10), 3233–3240.

(92) Pegado, L.; Marsalek, O.; Jungwirth, P.; Wernersson, E. Solvation and Ion-Pairing Properties of the Aqueous Sulfate Anion: Explicit versus Effective Electronic Polarization. *Phys. Chem. Chem. Phys.* **2012**, *14* (29), 10248–10257.

(93) Zeebe, R. E. On the Molecular Diffusion Coefficients of Dissolved, and Their Dependence on Isotopic Mass. *Geochim. Cosmochim. Acta* **2011**, *75* (9), 2483–2498.

(94) Case, D. A.; Betz, R. M.; Cerutti, D. S.; Cheatham, T. E.; Darden, T. A.; *et al.* Amber. University of California, San Francisco 2016.

(95) Brooks, B. R.; Bruccoleri, R. E.; Olafson, B. D.; States, D. J.; Swaminathan, S.; Karplus, M. CHARMM: A Program for Macromolecular Energy, Minimization, and Dynamics Calculations. *J Comp Chem* **1983**, *4*, 187–217.

(96) Abraham, M. J.; van der Spoel, D.; Lindahl, E.; Hess, B.; and the GROMACS development team. GROMACS User Manual. 2014.

(97) Luan, B.; Huynh, T.; Zhou, R. Simplified TiO_2 Force Fields for Studies of Its Interaction with Biomolecules. *J. Chem. Phys.* **2015**, *142* (23), 234102(1-6).

(98) Brandt, E. G.; Lyubartsev, A. P. Systematic Optimization of a Force Field for Classical Simulations of TiO_2–Water Interfaces. *Phys. Chem. C* **2015**, *119*, 18110–18125.

(99) Předota, M.; Zhang, Z.; Fenter, P.; Wesolowski, D. J.; Cummings, P. T. Electric Double Layer at the Rutile (110) Surface. 2. Adsorption of Ions from Molecular Dynamics and X-Ray Experiments. *J. Phys. Chem. B* **2004**, *108* (32), 12061–12072.

(100) Zhang, Z.; Fenter, P.; Cheng, L.; Sturchio, N. C.; Bedzyk, M. J.; Předota, M.; Bandura, A.; Kubicki, J. D.; Lvov, S. N.; Cummings, P. T.; Chialvo, A. A.; Ridley, M. K.; Bénézeth, P.; Anovitz, L.; Palmer, D. A.; Machesky, M. L.; Wesolowski, D. J. Ion Adsorption at the Rutile−Water Interface: Linking Molecular and Macroscopic Properties. *Langmuir* **2004**, *20* (12), 4954–4969.

(101) Bandura, A. V.; Sofo, J. O.; Kubicki, J. D. Adsorption of Zn^{2+} on the (110) Surface of TiO_2 (Rutile): A Density Functional Molecular Dynamics Study. *Phys. Chem. C* **2011**, *115*, 9608–9614.

(102) Wu, C.; Skelton, A. A.; Chen, M.; Vlček, L.; Cummings, P. T. Modeling the Interaction between Integrin-Binding Peptide (RGD) and Rutile Surface: The Effect of Cation Mediation on Asp Adsorption. *Langmuir* **2012**, *28* (5), 2799–2811.

(103) Köppen, S.; Langel, W. Simulation of the Interface of (100) Rutile with Aqueous Ionic Solution. *Surf. Sci.* **2006**, *600* (10), 2040–2050.

(104) Ridley, M. K.; Machesky, M. L.; Palmer, D. A.; Wesolowski, D. J. Potentiometric Studies of the Rutile-Water Interface: Hydrogen-Electrode Concentration-Cell versus Glass-Electrode Titrations. *Colloids Surf.* **2002**, *204*, 295–308.

(105) Parks, G. A. The Isoelectric Points of Solid Oxides, Solid Hydroxides and Aqueous Hydroxo Complex Systems. *Chem Rev* **1965**, *65*, 177–198.

(106) Wu, C.; Chen, M.; Guo, C.; Zhao, X.; Yuan, C. Peptide−TiO_2 Interaction in Aqueous Solution: Conformational Dynamics of RGD Using Different Water Models. *J. Phys. Chem. B* **2010**, *114* (13), 4692–4701.

(107) Tirrell, M.; Kokkoli, E.; Biesalski, M. The Role of Surface Science in Bioengineered Materials. *Surf. Sci.* **2002**, *500* (1), 61–83.

(108) Chen, M.; Wu, C.; Song, D.; Li, K. RGD Tripeptide onto Perfect and Grooved Rutile Surfaces in Aqueous Solution: Adsorption Behaviors and Dynamics. *Phys Chem Chem Phys* **2010**, *12* (2), 406–415.

(109) Sano, K.-I.; Sasaki, H.; Shiba, K. Specificity and Biomineralization Activities of Ti-Binding Peptide-1 (TBP-1). *Langmuir* **2005**, *21* (7), 3090–3095.

(110) Zhang, H.; Lu, X.; Leng, Y.; Watari, F.; Weng, J.; Feng, B.; Qu, S. Effects of Aqueous Environment and Surface Defects on Arg-Gly-Asp Peptide Adsorption on Titanium Oxide Surfaces Investigated by Molecular Dynamics Simulation. *J. Biomed. Mater. Res. A* **2011**, *96A* (2), 466–476.

(111) Sun, T.; Han, G.; Lindgren, M.; Shen, Z.; Laaksonen, A. Adhesion of Lactoferrin and Bone Morphogenetic Protein-2 to a Rutile Surface: Dependence on the Surface Hydrophobicity. *Biomater. Sci.* **2014**, *2* (8), 1090–1099.

(112) Mori, T.; Hamers, R. J.; Pedersen, J. A.; Cui, Q. An Explicit Consideration of Desolvation Is Critical to Binding Free Energy Calculations of Charged Molecules at Ionic Surfaces. *J. Chem. Theory Comput.* **2013**, *9* (11), 5059–5069.

(113) Monti, S.; Alderighi, M.; Duce, C.; Solaro, R.; Tiné, M. R. Adsorption of Ionic Peptides on Inorganic Supports. *J. Phys. Chem. C* **2009**, *113* (6), 2433–2442.

(114) Monti, S. RAD16II β-Sheet Filaments onto Titanium Dioxide: Dynamics and Adsorption Properties. *J. Phys. Chem. C* **2007**, *111* (45), 16962–16973.

(115) Sultan, A. M.; Hughes, Z. E.; Walsh, T. R. Binding Affinities of Amino Acid Analogues at the Charged Aqueous Titania Interface: Implications for Titania-Binding Peptides. *Langmuir* **2014**, *30* (44), 13321–13329.

(116) Monti, S.; Walsh, T. R. Free Energy Calculations of the Adsorption of Amino Acid Analogues at the Aqueous Titania Interface. *J. Phys. Chem. C* **2010**, *114* (50), 22197–22206.

(117) Sultan, A. M.; Westcott, Z. C.; Hughes, Z. E.; Palafox-Hernandez, J. P.; Giesa, T.; Puddu, V.; Buehler, M. J.; Perry, C. C.; Walsh, T. R. Aqueous Peptide–TiO_2 Interfaces: Isoenergetic Binding via Either Entropically or Enthalpically Driven Mechanisms. *ACS Appl. Mater. Interfaces* **2016**, *8* (28), 18620–18630.

(118) Wu, C.; Skelton, A. A.; Chen, M.; Vlček, L.; Cummings, P. T. Modeling the Interaction between Integrin-Binding Peptide (RGD) and Rutile Surface: The Effect of Na^+ on Peptide Adsorption. *J. Phys. Chem. C* **2011**, *115* (45), 22375–22386.

(119) Monti, S.; Walsh, T. R. Molecular Dynamics Simulations of the Adsorption and Dynamical Behavior of Single DNA Components on TiO_2. *J. Phys. Chem. C* **2011**, *115* (49), 24238–24246.

(120) Fortunelli, A.; Monti, S. Simulations of Lipid Adsorption on TiO_2 Surfaces in Solution. *Langmuir* **2008**, *24* (18), 10145–10154.

(121) Song, D.-P.; Liang, Y.-C.; Chen, M.-J.; Bai, Q.-S. Molecular Dynamics Study on Surface Structure and Surface Energy of Rutile TiO_2 (110). *Appl. Surf. Sci.* **2009**, *255* (11), 5702–5708.

(122) Zheng, T.; Wu, C.; Chen, M. Early Adsorption of Collagen on the Reduced Rutile (110) Surface Mediated by Water: A Molecular Dynamics Study. *Surf. Sci.* **2013**, *616*, 51–59.

(123) Wu, C.; Chen, M.; Xing, C. Molecular Understanding of Conformational Dynamics of a Fibronectin Module on Rutile (110) Surface. *Langmuir* **2010**, *26* (20), 15972–15981.

(124) Ebrahimi, S.; Ghafoori-Tabrizi, K.; Rafii-Tabar, H. Molecular Dynamics Simulation of the Adhesive Behavior of Collagen on Smooth and Randomly Rough TiO_2 and Al_2O_3 Surfaces. *Comput. Mater. Sci.* **2013**, *71*, 172–178.

(125) Chen, M.; Wu, C.; Song, D.; Dong, W.; Li, K. Effect of Grooves on Adsorption of RGD Tripeptide onto Rutile TiO_2 (110) Surface. *J. Mater. Sci. Mater. Med.* **2009**, *20* (9), 1831–1838.

(126) Liang, Y.-C.; Song, D.-P.; Chen, M.-J.; Bai, Q.-S. Adsorption Mechanism of Arg-Gly-Asp on Rutile TiO_2 (110) Surface in Aqueous Solution. *J. Vac. Sci. Technol. B* **2009**, *27* (3), 1548–1554.

(127) Chen, M.; Zheng, T.; Wu, C.; Xing, C. Molecular Dynamics Simulations of Collagen Adsorption onto Grooved Rutile Surface: The Effects of Groove Width. *Colloids Surf. B Biointerfaces* **2014**, *121*, 150–157.

(128) Monti, S.; Carravetta, V.; Zhang, W.; Yang, J. Effects Due to Interadsorbate Interactions on the Dipeptide/TiO_2 Surface Binding Mechanism Investigated by Molecular Dynamics Simulations. *J. Phys. Chem. C* **2007**, *111* (21), 7765–7771.

(129) Monti, S.; Carravetta, V.; Battocchio, C.; Iucci, G.; Polzonetti, G. Peptide/TiO_2 Surface Interaction: A Theoretical and Experimental Study on the Structure of Adsorbed ALA-GLU and ALA-LYS. *Langmuir* **2008**, *24* (7), 3205–3214.

(130) Muir, J. M. R.; Costa, D.; Idriss, H. DFT Computational Study of the RGD Peptide Interaction with the Rutile TiO_2 (110) Surface. *Surf. Sci.* **2014**, *624*, 8–14.

(131) Monti, S. Molecular Dynamics Simulations of Collagen-like Peptide Adsorption on Titanium-Based Material Surfaces. *J. Phys. Chem. C* **2007**, *111* (16), 6086–6094.

(132) Utesch, T.; Daminelli, G.; Mroginski, M. A. Molecular Dynamics Simulations of the Adsorption of Bone Morphogenetic Protein-2 on Surfaces with Medical Relevance. *Langmuir* **2011**, *27* (21), 13144–13153.

Chapter 3 Computational methods and force fields

“The Greeks were the first to consider forces in a nonreligious way. They found that they needed only two fundamental forces to account for all natural phenomena: Love and Hate. The first brought things together, while the second caused them to part.” (1)

In this chapter, the types of intra- and intermolecular forces and how they contribute to a force field set, described in a classical level, are explained. Some key concepts on the treatment of long-range interactions and spatial conditions of a simulation box in atomistic modelling are given. Different simulation methods used in this thesis are introduced and finally, the force field parameters are discussed and presented.

3.1 The potential energy of a system from the classical point of view

Computational methods use different ways to describe a certain system. Quantum mechanics (QM) methods explicitly consider electrons and solve the time-independent Schrödinger’s equation to determine the wavefunction of a system and its electronic distribution. While results obtained by this method are well accepted by the scientific community due to the way they treat subatomic particles, sometimes it is essential to use other computational methods to overpass the limited time and length-scale of QM methods. Classical methods in the atomic level consider only nuclei and ignore electrons. Since the degrees of freedom of the system decrease in these methods, longer time-scales can be simulated and larger length scales can be studied. Similarly, coarse-grained methods, or other computational approaches such as finite element analysis, can be used, where more assumptions are made and degrees of freedom are reduced even further enabling macroscopic dimensions and properties to be studied. The method to be used for a specific question is chosen based on the time and length-scale of events, which are to occur.

Classical computational techniques use the data obtained either by experiment or quantum mechanics to describe the interactions between atoms in the system – known as the force field set. The accuracy of any result obtained by classical simulations depends mostly on the force field used (2). Computational methods used in this thesis are based on the classical description of the potential energy of the system and include energy minimization, molecular dynamics and well-tempered metadynamics. Therefore, in the following, only the types of interactions, present in a classical-level description of the potential energy, are discussed.

The potential energy of a system, at the classical level, is due to all the interactions present between its atoms. One common way to divide the type of these interactions into certain categories is via the definition of intramolecular and intermolecular interactions. By intramolecular, interactions between covalently-bonded atoms are addressed, while intermolecular includes the remaining interactions. Most of the interactions can be attributed to only one of the categories. Electrostatic interactions, however, are present in both categories. Therefore, in the following, first, intramolecular and intermolecular interactions are discussed and then, electrostatic interactions are presented separately.

3.1.1 Intramolecular interactions

Intramolecular interactions maintain and control molecular structures. It should be clarified that polyatomic ions are also treated as molecular units. The complexity of the molecular structure dictates the types of interactions, which are needed to describe such structure. To start with a diatomic ion, for example, OH^-, a single bond potential is sufficient to describe the intramolecular interactions in the molecule. The energy of a bond potential is a function of the bond length.

In molecules with more than two atoms, the angles between atoms should also be maintained, using an angle potential. For example, the $H-O-H$ angle in a water molecule is approximately $104°$ and this should be maintained using an angle potential in the force field parametrization. Dihedral angles are the angles between two planes, each one containing three out of four atoms. If all four atoms are part of the same molecule, the dihedral angle is referred to as the torsion angle. Torsion angles must be preserved in certain molecules such as the carbonate ion (CO_3^{2-}), which has a planar structure. Clearly, from bond potentials towards angle potentials and dihedral potentials, the degree of freedom of the molecular unit is decreasing.

Each one of the above intramolecular interactions can be described in several forms. Equation 3.1 to Equation 3.3 present only one common form for each type of interaction in the order of bond, angle and torsion angle (3).

$$U_{Morse}^{Bond}(r_{ij}) = E_0\left[1-\exp\left(-k(r_{ij}-r_0)\right)\right]^2 \qquad \textit{Equation 3.1}$$

$$U_{Harmonic}^{Angle}(\theta_{ijk}) = \frac{k_{ijk}}{2}\left(\theta_{ijk}-\theta_0\right)^2 \qquad \textit{Equation 3.2}$$

$$U_{Cosine}^{Torsion}(\phi_{ijkl}) = A[1+\cos(m\,\phi_{ijkl}-\delta)] \qquad \textit{Equation 3.3}$$

In Equation 3.1, E_0 is the depth of the potential energy well, k is a measure of the steepness of the potential well, r_{ij} is the distance between atoms i and j, and r_0 is the equilibrium bond length. In Equation 3.2, k_{ijk} is a spring constant, which acts when θ_{ijk} (the angle between atoms i, j and k) deviates from θ_0 (the equilibrium angle).

In Equation 3.3, A is a qualitative indication of the relative barrier to rotation, m is the multiplicity, *i.e.*, the number of minimum points in the function as the bond is rotated through 360°, and δ is the torsion angle where the potential is minimum (3).

3.1.2 Intermolecular interactions

Intermolecular interactions can also be defined as 2-body, 3-body, 4-body and so on. The type of the intermolecular interactions present in a system depends on the type of materials present in the system. Short-range 2-body (or pair) van der Waals interactions are the only intermolecular interaction considered in this thesis. Several forms exist for describing the potential energy acting between two species due to van der Waals interactions. Equation 3.4 and Equation 3.5 showcase two common forms.

$$U_{LJ}^{VdW}(r_{ij}) = 4\epsilon_{ij}\left[\left(\frac{\sigma_{ij}}{r_{ij}}\right)^{12} - \left(\frac{\sigma_{ij}}{r_{ij}}\right)^{6}\right] \quad \textit{Equation 3.4}$$

$$U_{Buckingham}^{VdW}(r_{ij}) = A_{ij}\exp\left(-\frac{r_{ij}}{\rho_{ij}}\right) - \frac{C_{ij}}{r_{ij}^{6}} \quad \textit{Equation 3.5}$$

Equation 3.4 is the well-known Lennard-Jones potential, containing a long-range attractive van der Waals interaction and a short-range (empirical) part which takes into account the Pauli repulsion. In this equation, ϵ_{ij} is the depth of the energy well for the interaction of atoms i and j, and σ_{ij} is the distance at which U_{ij} is zero. Figure 3.1a shows the short-range interactions between argon atoms based on the original work of Rahman (4).

The Buckingham potential (Equation 3.5) consists of a repulsive and an attractive term. The A_{ij}, ρ_{ij} and C_{ij} depend on the depth of the minimum energy and the minimum energy distance. Later in this chapter, the force field parameters for titanium oxide developed by Matsui and Akaogi are presented. In Figure 3.1b, the repulsive and attractive terms of Equation 3.5, as well as their sum, is plotted for the $Ti - O$ pair based on this parameterization (Table 3.1).

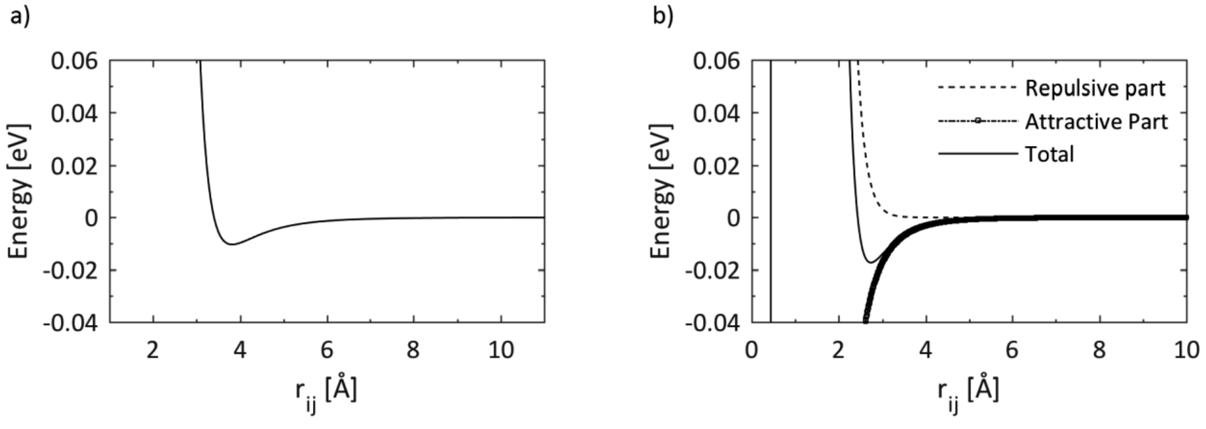

Figure 3.1 a) van der Waals interactions between atoms of argon, based on the previous work of Rahman (4) and b) the contribution of the attractive and repulsive terms to the Buckingham potential.

3.1.3 Electrostatic interactions

Long-range Coulombic forces, which act between two charged atoms known as ions, can be described via the following form.

$$U^{Coul}(r_{ij}) = \frac{1}{4\,\pi\,\epsilon_0}\,\frac{q_i q_j}{r_{ij}} \qquad \textit{Equation 3.6}$$

Where ϵ_0 is the permittivity constant of vacuum, q_i and q_j are the charges of the two particles and r_{ij} is the distance between them. Electrostatic interactions are long-range as they decay relative to r^{-1}. Since they do not converge to small values in the common sizes for a simulation box of MD (a few nanometers), one has to treat them with more caution as detailed in section 3.2.

Before describing the force field parameters used in this thesis, some details on the treatment of the simulation box, and main concepts of the simulation methods used in this thesis are presented. The detailed set of force field parameters is presented at the end of this chapter, section 3.8.

3.2 Treatment of short- and long-range interactions

For a system with N particles, even if all interactions are considered to be two-body, there are still $\frac{N(N-1)}{2}$ interactions to be computed in the system. Therefore, N implies an upper limit to the size of the system to be studied. In a simulation box with N atoms, some of the atoms are adjacent to the boundaries of the simulation box. This is similar to experimental conditions where some atoms are on boundaries and interfaces. However, the ratio of the number of atoms on boundaries to the total number of atoms in an atomistic simulation is much larger than experimental systems. This is one of the artefacts of n not always being comparable to experimental systems. This problem is addressed by using periodic boundary conditions (PBC). With using N such that the computational cost is affordable, and applying periodic boundary conditions, particles in the simulation box will experience conditions as if the simulation box was extended, and so the atoms adjacent to the boundaries of the simulation box will interact with images of the simulation cell. Periodic boundary conditions in one, two and three directions of the simulation box can be used for simulating a rod, plane or bulk-shape material.

To implement periodic boundary conditions, for example, in all three directions, the simulation box is replicated in all three directions. This is shown in Figure 3.2, in 2D. Under these conditions, atoms interact with atoms, which were originally in the simulation box, but also with those in all the periodic images.

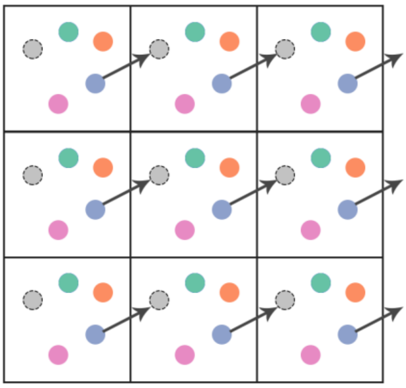

Figure 3.2 The central square is the original simulation box with four particles. It is replicated in all directions using PBC. If the blue particle crosses the simulation boundary in the direction of the arrow, it will re-appear as the grey particle in the original simulation box due to PBC.

Even with PBC that helps to avoid unwanted boundary effects, simulation cells describing realistic geometries still contain a large number of atoms. One technique to reduce the number of computations below N^2 is to limit the interactions between particles to distances smaller than a certain value, known as the cutoff distance. Short-range interactions decay to values very close to zero in small distances. Therefore, a cutoff distance, in the range of 8-12 Å, is usually set, beyond which all short-range interactions are set to zero. The error caused by this technique is negligible for short-range interactions but long-range interactions should be treated with more care. Long-range electrostatic interactions converge to zero very slowly. The total electrostatic energy in a system of N particles, in a cubic box of size L, and considering all periodic images, can be written by (5):

$$U_{Coul}^{Total} = \frac{1}{2}\frac{1}{4\pi\epsilon_0}\sum_{n}^{\prime}\sum_{i=1}^{N}\sum_{j=1}^{N}\frac{q_i q_j}{r_{ij,n}} \qquad \text{Equation 3.7}$$

Where the first summation over $n = 0{:}\infty$ insures considering all periodic images. q_i is the charge of particle i. n is the cell-coordinate vector ($n = (n_1, n_2, n_3) = n_1 L_x + n_2 L_y + n_3 L_z$). The original cell is located at $n = (0,0,0)$ and its images are located at Ln intervals as n goes to infinity. The first sum is primed to indicated that for $n = 0$, terms with $i = j$ are omitted. The $\frac{1}{2}$ constant is considered to cancel out double counting of $i - j$ and $j - i$ interactions. The distance between a particle in the original cell and an image cell is $r_{ij,n} = |r_{jn} - r_i| = |r_i - r_j + nL|$. Equation 3.7 decays very slowly and is only conditionally convergent meaning that the value to which it converges depends on the order of summation.

To treat long-range electrostatic interactions, Ewald (6) considered the total electrostatic energy as the sum of two quickly-converging series and a constant term (Equation 3.8).

$$U_{Coul}^{Total} = U^{real} + U^{reciprocal} + U^{correction} \qquad \text{Equation 3.8}$$

Where:

$$U^{real} = \frac{1}{2}\frac{1}{4\pi\epsilon_0}\sum_{n}^{\prime}\sum_{i=1}^{N}\sum_{j=1}^{N}\frac{q_i q_j}{|r_{ij,n}|}\, erfc\left(\frac{|r_{ij,n}|}{\sqrt{2}\sigma}\right) \qquad \textit{Equation 3.9}$$

$$U^{reciprocal} = \frac{1}{2}\frac{1}{V\epsilon_0}\sum_{k\neq 0}\sum_{i=1}^{N}\sum_{j=1}^{N}\frac{q_i q_j}{k^2}\exp\left(ik\cdot(r_i - r_j)\right)\exp\left(-\frac{\sigma^2 k^2}{2}\right) \qquad \textit{Equation 3.10}$$

$$U^{correction} = \frac{1}{4\pi\epsilon_0}\frac{1}{\sqrt{2\pi}\sigma}\sum_{i=1}^{N} q_i^2 \qquad \textit{Equation 3.11}$$

V is the volume of the simulation box. k is a vector in the reciprocal space given by $2\pi\left(\frac{n_1'}{L_x},\frac{n_2'}{L_y},\frac{n_3'}{L_z}\right)$, where n_1', n_2' and n_3' are integers. The first part in Equation 3.8 (U^{real}; Equation 3.9) is short-range and is treated in the real space since it decays rapidly as $n \to \infty$. The second part ($U^{reciprocal}$; Equation 3.10) is long-range and is treated in the reciprocal space and since it is a smooth function, its Fourier transform decays rapidly.

The correction term (Equation 3.11) is considered to account for the fact that, the summation presented for the electrostatic energy (Equation 3.7) is only conditionally convergent and cannot be described only by two converging series as Equation 3.9 and Equation 3.10.

From a physical point of view, in the Ewald sum, for every point charge, a Gaussian charge distribution of the same size but opposite sign is considered by the functional form given in Equation 3.12 (7).

$$\rho_i(r) = \frac{q_i\alpha^3}{\pi^{\frac{3}{2}}}\exp(-\alpha^2 r^2) \qquad \textit{Equation 3.12}$$

Where ρ_i is the Gaussian charge distribution for charge q_i, α is the width of the Gaussian distribution ($\alpha = \frac{1}{\sqrt{2}\sigma}$ where σ is the standard deviation of the Gaussian distribution) and r is the position relative to the center of distribution (5). The interaction of the charge points and the countercharge Gaussians in long-range is effectively neutralized, causing electrostatic interactions to become short-range in the real space. The width of the Gaussians should be chosen in a way that either only charges in the original cell are interacting with each other, or if there is a cutoff distance defined, only those interactions in this cutoff are included. The U^{real} summation decays faster for narrower Gaussians, *i.e.*, smaller σ s.

To cancel out the added Gaussian charge distributions, another set of them, with the same size but opposite charge to the first set (or similar charge to the original charge points), is added. Now, if the summation is performed in the reciprocal space using Fourier transformation, it will also rapidly converge to zero (5). The $U^{reciprocal}$ summation also depends on the size of σ and converges faster for larger values. Therefore, one should choose σ carefully, so both summations converge efficiently. From a physical point of view, $U^{correction}$ removes the interaction of each Gaussian function with itself, in the real-space.

Ewald summation is routinely used for periodic MD simulations. Several flavors have been proposed based on the standard Ewald summation. In this thesis, the standard Ewald summation has been used to treat the long-range electrostatic interactions.

3.3 Unit cells and supercells

The most simple way to describe the structure and symmetry of a crystalline material is through its unit cell. However, applying the periodic boundary condition on a single unit cell might be questionable. This is mainly because lattice parameters may fail to provide the condition of $> 2 * r_{cutoff}$ in all three directions; which is important since it assures one that all the interactions, which are at a similar distance from a certain atom, are considered. Before applying the PBC conditions, the original simulation space should be expanded. This can be achieved by using a supercell. A supercell is a replicate of a unit cell in one, two or three directions. The orthorhombic box (3) was used for the simulations performed in this thesis.

3.4 Surface slab

Surfaces have an important significance in many applications where they control the behavior, performance and interaction of one or more components. In Chapter 1, the basis of general interest in interactions happening on surfaces was discussed. A supercell, which contains several unit cells replicated in all directions, can be cleaved in the direction of lattice planes to resemble a surface. In the direction of a certain lattice plane, one can also cleave the structure at different depths resulting in different terminations of the surface.

Here, construction of a surface from a supercell is explained (8,9). Let's imagine that a supercell, as shown in Figure 3.3a, is to be cleaved in a certain direction (shown by the red dashed lines). The supercell should be cleaved and transformed according to Figure 3.3b and the excess sections at 1, 2, 3 and 4 should be moved to their new positions shown by $1'$, $2'$, $3'$ and $4'$, respectively. The final product is a slab (Figure 3.3c), with a surface cleaved in the desired direction (shown by the red dashed line).

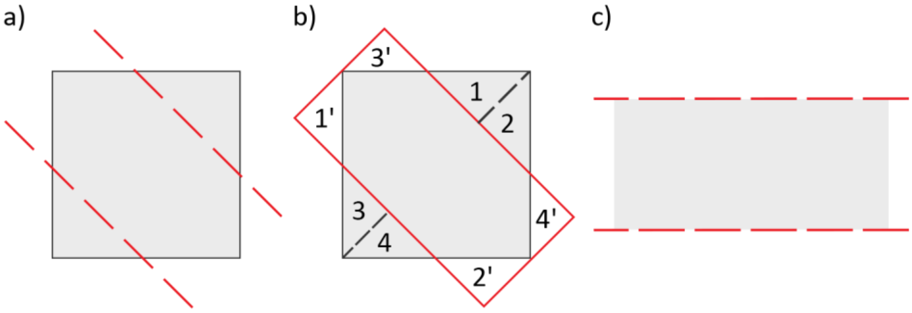

Figure 3.3 The schematic of cleaving a supercell in a certain direction and constructing a slab. a) A supercell, which is to be cleaved in a certain direction, e.g., the red dashed line, b) the required transformation and c) final slab in the desired direction.

Some points should be considered in simulation boxes containing surfaces.

i. A slab has a finite thickness. This thickness should be chosen in a way that does not allow strong interactions between the upper and lower faces of the slab.

ii. The thickness of the slab also should be chosen in a way that the material in the central part of the slab behaves similarly to the bulk.

At this point, the simulation box is periodic in the lateral directions but not in the direction normal to the surface. As previously mentioned, the Ewald summation is applicable to systems periodic in all three directions. To resolve the missing periodicity in the slab surface, and to implement the Ewald summation, another step should be taken for preparing a surface slab to be used in atomistic simulations. In this step, a vacuum gap is added to the surface slab in the z-direction which prevents image-image interactions in this direction. Furthermore, all or part of the vacuum gap can be filled by a solvent, to study interactions with the surface.

3.5 Energy minimization

Mountains are a very good metaphor for the potential energy surface of a system, also known as hypersurfaces. The hypersurface represents the change of potential energy of the system as a function of the internal coordinates of atoms. Due to the complexity of potential energy, being a function of $3N$ variables (internal coordinates of the system), for a constant volume calculation, energy minimization (EM) methods use numerical methods to locate the minimum point; they change the coordinates of the system while trying to spot the set of coordinates, which yields the minimum potential energy. In atomistic simulations, it is advised to start a simulation from a configuration close to equilibration (or at a local minimum); this configuration can be achieved by performing energy minimization on the initial structure.

EM methods can be categorized based on the highest degree of derivatives of the energy, which is used by their algorithm. Common EM algorithms use the first or the second derivatives with respect to the coordinates, which are gradients and the Hessian matrix, respectively.

EM methods differ in how quickly an energy minimum can be found, which also varies based on how close or far the initial configuration is from the minimized energy configuration. Thus, usually, a combination of minimization methods are used to have the advantages of different methods. Here, some of the energy minimization methods are briefly explained.

3.5.1 The steepest descent method

Starting from an initial configuration (x_k), a step will be taken in the direction with the steepest descent ($-\vec{g}_0$), which is also parallel to the direction of the net force. The length of this step (γ) is obtained by performing a line search in which, the minimum along $-\vec{g}_0$ is found (x_{k+1}). The same procedure will be repeated at configuration x_{k+1}, where the steepest descent is now orthogonal to the steepest descent in the previous step. Therefore, approaching the minimum of the energy is over a zig-zag route (8).

3.5.2 The conjugate gradient method

In the steepest descent method, both the gradients and directions of successive steps are orthogonal. However, in the conjugate gradient method (10), at any two points of i and j, the gradients are orthogonal ($\vec{g}_i \cdot \vec{g}_j = 0$) while the directions are conjugate ($\vec{v}_i \cdot H_{ij} \cdot \vec{v}_j = 0,$ where H_{ij} is the Hessian matrix) (3). The advantage of the conjugate gradient method over the steepest descent method is that for a system with exactly one minimum, and a function of M variables, the minimum will be found in maximum M steps. The number of steps will be higher in realistic cases with usually more than one minimum (8).

3.5.3 The Newton-Raphson method

Taylor series expansion of the first derivative of function $V(x)$ about point $x_k$can be written as (3):

$$V'(x) = x\,V'(x_k) + (x - x_k)\,V''(x_k) \qquad \textit{Equation 3.13}$$

At the minimum ($x_k = x^*$), the first derivative of the function $V(x)$ equals to zero ($V'(x^*) = 0$). Therefore, x^* can be found using the following equation.

$$x^* = x_k - \frac{V'(x_k)}{V''(x_k)} \qquad \textit{Equation 3.14}$$

In the above equation, the inverse of the Hessian matrix has to be calculated ($\frac{1}{V''(x_k)} = H^{-1}(x_k)$). While the Hessian matrix gives useful information on the curvature of the hypersurface, the calculation of the inverse of the Hessian matrix can be cumbersome.

Here, for energy minimization, namely GULP (the General Utility Lattice Program) (11) and METADISE (12) were used.

3.6 Molecular dynamics

Force field parameters obtained either empirically or through quantum mechanics methods are the basis of classical molecular dynamics simulations and any result obtained by these methods, first and foremost, is affected by the accuracy of the underlying force field.

To initiate an MD simulation, the initial positions and velocities of all the atoms should be defined. The initial positions are determined based on the atomic structure of the system under certain conditions; for a crystalline material, for example, one can use lattice positions to define the initial simulation box. The initial velocities are attributed to atoms based on a Maxwell-Boltzmann distribution at the desired temperature.

The Newton's equation of motion (Equation 3.15) is used to link the force on each atom in the system, which can be obtained using Equation 3.16, to its velocity and acceleration. In these equations, $\vec{f_i}$ is the force on atom i, m_i is the mass and a_i the acceleration of atom i, U is the potential energy of the system and $\vec{r_i}$ is the coordinates of the atom. Once the forces are obtained using Equation 3.16, integration of equation of motion over time will give the evolution of the atomic positions and velocities.

$$\vec{f_i} = m_i \, \vec{a}_i \qquad \text{Equation 3.15}$$

$$\vec{f_i} = -\frac{\partial U_i}{\partial \vec{r_i}} \qquad \text{Equation 3.16}$$

Different algorithms have been presented to integrate the equation of motion which all assume that the positions, velocities, accelerations, etc. can be approximated using Taylor series expansions. The evolution of the system is determined every timestep (dt). Here, three such algorithms are explained; Verlet, velocity Verlet and leapfrog Verlet.

The Verlet algorithm uses $\vec{r}(t-dt)$, $\vec{r}(t)$ and $\vec{a}(t)$ to approximate the positions at $t+dt$ using Taylor series expansions (Equation 3.17 to Equation 3.19) (13). This is done by adding equations for $\vec{r}(t-dt)$ and $\vec{r}(t+dt)$ (Equation 3.17 and Equation 3.18) as shown in the following.

$$\vec{r}(t+dt) = \vec{r}(t) + \vec{v}(t)\,dt + \frac{1}{2}\vec{a}(t)\,dt^2 \qquad \text{Equation 3.17}$$

$$\vec{r}(t-dt) = \vec{r}(t) - \vec{v}(t)\,dt + \frac{1}{2}\vec{a}(t)\,dt^2 \qquad \text{Equation 3.18}$$

$$\begin{aligned} &\vec{r}(t+dt) + \vec{r}(t-dt) = 2\,\vec{r}(t) + \vec{a}(t)\,dt^2 \implies \\ &\vec{r}(t+dt) = 2\,\vec{r}(t) - \vec{r}(t-dt) + \vec{a}(t)\,dt^2 \end{aligned} \qquad \text{Equation 3.19}$$

$$\vec{v}(t) = \frac{\vec{r}(t+dt) - \vec{r}(t-dt)}{2\,dt} \qquad \text{Equation 3.20}$$

Although subtracting Equation 3.17 and Equation 3.18 will result in $v(t)$ as shown in Equation 3.20, but it is subject to errors of order dt^2 compared to $\vec{r}(t+dt)$, which is subject to an error in the order of dt^4. Another drawback of the Verlet algorithm is that velocities at time t are unknown until the positions at time $t+dt$ are known (7).

The velocity Verlet algorithm (14) determines the positions, velocities and accelerations in the same timestep, but evolves every half of timestep. First, velocities at $t+\frac{1}{2}dt$ are calculated using Equation 3.21. Then, the velocities at $t+\frac{1}{2}dt$ are used to calculate positions at the next full timestep ($t+dt$), as shown in Equation 3.22. Newton's equation of motion at the timestep of $t+dt$ will result in $a(t+dt)$. Finally, velocities at $t+dt$ will be calculated as shown in Equation 3.23.

$$\vec{v}\left(t+\frac{1}{2}dt\right) = \vec{v}(t) + \frac{1}{2}\vec{a}(t)\,dt \qquad \text{Equation 3.21}$$

$$\vec{r}(t+dt) = \vec{r}(t) + \vec{v}(t)\,dt + \frac{1}{2}\vec{a}(t)dt^2 \Rightarrow$$
$$\vec{r}(t+dt) = \vec{r}(t) + \vec{v}\left(t+\frac{1}{2}dt\right)\,dt$$

Equation 3.22

$$\vec{v}(t+dt) = \vec{v}\left(t+\tfrac{1}{2}dt\right) + \tfrac{1}{2}\vec{a}(t+dt)\,dt = \vec{v}(t) + \tfrac{1}{2}\big(\vec{a}(t)+\vec{a}(t+dt)\big)\,dt$$

Equation 3.23

Another algorithm similar to velocity Verlet is the Verlet leapfrog algorithm, which is used throughout this thesis. Verlet leapfrog is different from velocity Verlet in the sense that velocities are never explicitly calculated in the full timesteps. First, velocities at $t+\frac{1}{2}dt$ are calculated based on those at $t-\frac{1}{2}dt$ (Equation 3.24). Using these values, next coordinates are calculated using Equation 3.22. Finally, velocities at the current timestep (t) will be calculated using Equation 3.25.

$$\vec{v}\left(t+\frac{1}{2}dt\right) = \vec{v}\left(t-\frac{1}{2}dt\right) + \vec{a}(t)\,dt$$

Equation 3.24

$$\vec{v}(t) = \frac{1}{2}\left[\vec{v}\left(t-\frac{1}{2}dt\right) + \vec{v}\left(t+\frac{1}{2}dt\right)\right]$$

Equation 3.25

Here, the DL_POLY Classic package (15) v1.9 has been used for performing molecular dynamics simulations.

3.6.1 Time average and ensemble average

Macroscopic properties are the average of properties over a long period of time. For a system with N particles, the instantaneous value of the property A is a function of the positions and momenta of the particles and can be written as $A\big(p^N(t), r^N(t)\big)$, where p is the momentum and r is the coordinate. The time average of A can be then described by (3):

$$A_{avr} = \lim_{\tau\to\infty}\frac{1}{\tau}\int_{t=0}^{\tau} A\big(p^N(t), r^N(t)\big)dt$$

Equation 3.26

However, the averages obtained by unbiased atomistic simulations is a time average of very limited time length, since the studied time and length-scales are much smaller than experimental measurements. The theorem of ergodicity replaces the time average of a physical quantity in a macroscopic experimental system with the ensemble average of the same property for many smaller and independent simulations, in the probability space:

$$\langle A\rangle = \int\int dp^N dr^N A(p^N, r^N)\rho(p^N, r^N)$$

Equation 3.27

Although this equation is written as a double integral, there are indeed $6N$ integrals, which should be performed (corresponding to the $6N$ positions and momenta of the particles in the system). $\rho(p^N, r^N)$ is the probability density of the ensemble, which obeys the Boltzmann distribution, and depends on the energy of the configuration (p^N, r^N).

3.6.2 Thermostat

In experimental conditions, the temperature of a system can be controlled by coupling it to a large heat source with the desired temperature. In atomistic simulations, different approaches have been proposed for controlling the temperature. In this thesis, the Nosé-Hoover thermostat (16) has been used, in which the equation of motion is modified as (17):

$$\frac{d^2\vec{r}_i}{dt^2} = \frac{\vec{f}_i}{m_i} - \chi(t)\frac{d\vec{r}_i}{dt} \qquad \textit{Equation 3.28}$$

Where $\chi(t)$ is the friction coefficient of the thermal bath to the velocity of the particles ($\frac{dr_i}{dt}$ in Equation 3.28) and depends on the properties of the thermal bath and the strength of the coupling between the system and the bath. For a system with the instantaneous temperature of $T(t)$ coupled with a bath with a temperature of T_{ext}, the friction coefficient varies over time, directly depending on the difference between the temperature of the bath and the system (Equation 3.29). τ determines how often the temperature of the system is pushed back to the temperature of the bath (9).

$$\frac{d\chi(t)}{dt} = \frac{1}{T_{ext}\tau^2}(T(t) - T_{ext}) \qquad \textit{Equation 3.29}$$

3.6.3 Barostat

Controlling the size and volume of the simulation box in atomistic simulations is undertaken by coupling the system to a barostat. Similar to the Nosé-Hoover thermostat, the Nosé-Hoover barostat applies a time-dependent friction coefficient ($\eta(t)$) to the positions, velocities and simulation box volume. Since temperature and pressure cannot be varied independently, the friction coefficient of the thermostat and the barostat are related to each other – and both time-dependent.

For applying an isotropic pressure, the friction coefficient of the barostat is the same for all components. However, a tensor of friction coefficients can be used if one prefers to apply anisotropic pressure on the system. Here, for the sake of simplicity, the modified equations of motion, due to the thermostat and barostat, are presented for an isotropic pressure (9,15):

$$\frac{d\vec{r}_i(t)}{dt} = \vec{v}_i(t) + \eta(t)\big(\vec{r}_i(t) - \vec{R}_0\big) \qquad \textit{Equation 3.30}$$

$$\frac{d^2\vec{r}_i(t)}{dt^2} = \frac{\vec{f}_i}{m_i} - [\chi(t) + \eta(t)]\,\frac{d\vec{r}_i}{dt} \qquad \textit{Equation 3.31}$$

$$\frac{dV(t)}{dt} = \left(3\,\eta(t)\right) V(t) \qquad \textit{Equation 3.32}$$

$$\frac{d\chi(t)}{dt} = \frac{1}{T_{ext}\tau^2}\left(T(t) - T_{ext}\right) + \frac{1}{\tau^2}\left(\tau'^2 \eta(t)^2 - \frac{1}{N_f}\right) \qquad \textit{Equation 3.33}$$

$$\frac{d\eta(t)}{dt} = 3\,\frac{V(t)}{N_f k_B T_{ext}\tau'^2}\left(P(t) - P_{ext}\right) - \chi(t)\,\eta(t) \qquad \textit{Equation 3.34}$$

Where $\vec{R}_0$ is the center of mass of the system, $V(t)$ is the volume, T_{ext} and P_{ext} are the temperature and pressure of the thermostat and barostat, $T(t)$ and $P(t)$ are the instantaneous temperature and pressure of the system, τ and τ' are the time constant for oscillations of the system with the thermostat and barostat, N_f is the number of degrees of freedom and k_B is the Boltzmann constant.

3.7 Well-tempered Metadynamics

Proper sampling is essential in molecular dynamics simulations and one should be aware of the phase space over which the averaging is done. The timestep in a classical molecular dynamics simulation should be small enough to capture the fastest motions in an atomistic system, which is in the order of a few femtoseconds (18–20); thus also assures that between the timesteps when the integration is performed, the acceleration is constant. According to the transition state theory, the rate of a transition depends on the size of the energy barrier associated with the transition. The relatively small time-scale accessible by MD makes the observation of those transitions with relatively large energy barriers (larger than a few kT) even less frequent; hence the naming of rare events.

Therefore, it is important to acknowledge that results obtained by molecular dynamics simulations correspond to one or a few energy minima in the system but not all the possible configurations and/or high energy regions. In other words, Monte Carlo and molecular dynamics mostly sample lower-energy regions of the phase space (3) as opposed to an ergodic system where all energetically-relevant configurations are visited by the system (19).

To resolve this issue, several approaches have been suggested for accelerating rare events and can be placed into different groups (18). In one category, the probability distribution of one or several degrees of freedom is modified over time. In another category, reconstruction of the potential energy surface is undertaken (18). Among different enhanced sampling methods, which are supposed to facilitate and accelerate the sampling of high-energy regions of the phase space, here, the focus is on one of the flavors of metadynamics: the well-tempered metadynamics method. Metadynamics biases the potential energy of the system over time, along one or a few degrees of freedom, known as collective variables or reaction coordinates. Eventually, the biased potential energy will be large enough to cancel out the energy barrier. This will cause the system to move to the next minimum energy well. This is shown in Figure 3.4. One of the advantages of metadynamics, in addition to accelerating rare events, is that it allows one to use the added bias to reconstruct the free energy surface and to determine the free energy associated with energy barriers (18).

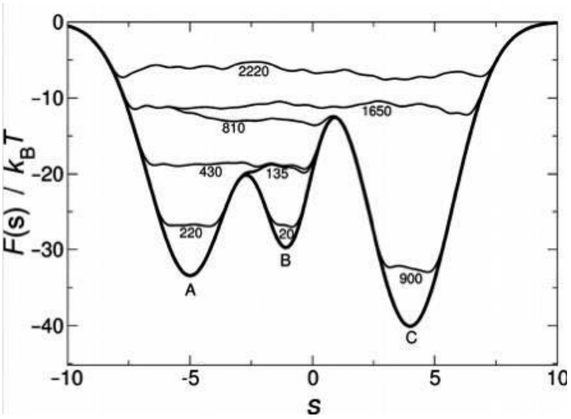

Figure 3.4 Free energy profile of a system as a function of a single collective variable (s). The numbers on the energy profile correspond to the number of deposited Gaussians. Biasing of the free energy starts from well B and continues to well A (after approximately 135 deposition of Gaussians) and finally, to well C after the deposition of 810 Gaussians (19).

Let's consider d collective variables, where each collective variable is a function of the microscopic coordinates $\vec{x}$ of the system (19). One can refer to the sets of collective variables as:

$$\vec{S}(\vec{x}) = \left(S_1(\vec{x}), S_2(\vec{x}), \dots, S_d(\vec{x})\right) \qquad \textit{Equation 3.35}$$

The equilibrium probability distribution of these variables can be defined by (18):

$$P(\vec{s}) = \frac{\exp\left(-\left(\frac{1}{T}\right)F(\vec{s})\right)}{\int d\vec{s}\,\exp\left(-\left(\frac{1}{T}\right)F(\vec{s})\right)} \qquad \textit{Equation 3.36}$$

And the free energy ($F(s)$), of the system under the potential $V(x)$ and at temperature T, is given by:

$$F(\vec{s}) = -T\ln\left(\int d\vec{x}\,\exp\left(-\frac{1}{T}\,V(\vec{x})\right)\,\delta\left(\vec{s} - S(\vec{x})\right)\right) \qquad \textit{Equation 3.37}$$

If the potential energy of the system is biased using Gaussians with a width of σ_i (for the i^{th} collective variable), a height of W and a deposition frequency of τ_G, at time t the bias potential can be calculated by:

$$V_G(S(\vec{x}), t) = \int_0^t dt'\,\omega\,\exp\left(-\sum_{i=1}^{d}\frac{\left(\vec{S}_i(\vec{x}) - \vec{s}_i(\vec{x}(t'))\right)^2}{2\,\sigma_i^2}\right) \qquad \textit{Equation 3.38}$$

Where ω is the energy rate and is the height of the Gaussians divided by the deposition frequency ($\frac{W}{\tau_G}$). The prime notation over t is to emphasize that $t' = \tau_G, 2\tau_G, \dots$. The characteristics of Gaussians and their deposition frequency should be chosen carefully so, the computational power is used efficiently (18). Adding very small Gaussians will slow down the sampling and adding very large Gaussians might under- or overestimate the energy barriers.

The name of metadynamics refers to the action of a dynamic over another dynamic. In fact, every τ_G timesteps, the derivative of Equation 3.38 with respect to collective variables is calculated and added to forces acting on atoms, biasing the dynamics of the system (Equation 3.39) (18).

$$\left(\frac{\partial}{\partial \vec{x}}\right) V_G(S(\vec{x}), t) = \left(\frac{\partial V_G(\vec{s}, t)}{\partial \vec{s}}\right)\left(\frac{\partial S(\vec{x})}{\partial \vec{x}}\right) \qquad \text{Equation 3.39}$$

If biasing is performed for a relatively long time, one can assume:

$$V_G(\vec{s}, t \rightarrow \infty) = -F(\vec{s}) + C \qquad \text{Equation 3.40}$$

Where $F(\vec{s})$ is the free energy of the system and C is a constant. The presence of C in Equation 3.40 is one of the drawbacks of conventional metadynamics. This is because using this approach, at large t, the biased potential will oscillate around $F(\vec{s})$ and will not converge to it. This also makes it difficult to know when sufficient sampling has been done and whether one can terminate the simulation.

In well-tempered metadynamics (WT-MTD), the biased potential will converge to $F(\vec{s})$ modulo a constant. In this approach, the Gaussian height is rescaled as shown in Equation 3.41 (19):

$$W = \omega\, \tau_G \exp\left(-\frac{V_G(\vec{s}, t)}{k_B \Delta T}\right) \qquad \text{Equation 3.41}$$

Where the bias potential ($V_G(\vec{s}, t)$) is formulated differently (19):

$$V_G(\vec{s}, t) = k_B\, \Delta T \ln\left(\frac{1 + \omega\, N(\vec{s}, t)}{k_B\, \Delta T}\right) \qquad \text{Equation 3.42}$$

$N(\vec{s}, t)$ in the equation above is the histogram of the $\vec{S}$ collective variables during the biased simulation. ΔT is a temperature difference, which facilitates the exploration of the phase space (21). In a molecular dynamics simulation, $\Delta T \rightarrow 0$; in a conventional metadynamics simulation, ΔT would constantly increase with time ($\Delta T \rightarrow \infty$). However, in a well-tempered metadynamics simulation, this parameter is defined as input and limits the phase space available to be explored to an energy range of $T + \Delta T$, which is one of the advantages of the well-tempered metadynamics since it limits sampling only to the physically meaningful space (21). The concept of well-tempered metadynamics can also be explained by the bias factor $\gamma = {T'}/{T}$, where $T' = T + \Delta T$. The bias factor of γ performs the sampling in an effective temperature of $T' = \gamma\, T$.

It should be noted that for WT-MTD, the bias potential does not oscillate around $-F(\vec{s})$ similar to Equation 3.40, but rather converges to $-\frac{\Delta T}{T+\Delta T}\, F(\vec{s}) + C$.

The choice of a CV is crucial in metadynamics simulations and depends on the system and the purpose of the study. Collective variables should have certain features (18,19):

i. As a reaction coordinate, they should distinguish reagents, intermediate products and final products.

ii. They should represent rare events related to the process under study.
iii. They should be a few and not too many.

Many different collective variables have been used in metadynamics simulations; some are simpler such as the distance between two atoms and some are more complex such as a dihedral angle or the coordination number. Point (iii) is one of the limitations of metadynamics, but also one of its advantages as it allows one to simultaneously bias more than one collective variable (18).

It is important to note that if the entire phase space were to be explored, the choice of CV would not be so important anymore (20). This is why reweighting methods have been developed where the reconstructed free energy obtained by biasing a certain set of collective variables can be reweighted to extract the free energy associated with any other collective variable. In this thesis, the reweighting method developed by Tiwary *et al.* (22) and implemented within the PLUMED plugin has been used as a post-processing tool.

All well-tempered metadynamics simulations were performed using the PLUMED plugin (v2.2) (23) on the DL_POLY Classic MD package.

3.8 Force field set

A force field set should describe all the components, which are present in the system, and their interactions with each other. Systems studied in this thesis include all or some of the following: titanium oxide in the form of rutile, water, ions, organic molecules. In Chapter 2, general force field sets for these components were mentioned and briefly explained. In the following, the exact set of parameters, which were used in this thesis, how they were obtained and how they were verified will be explained in detail. Further details can be found in Appendix C and Appendix D.

It is important to mention that all the force field parameters used in this thesis are non-polarizable. The polarizability effect in molecular dynamics simulations can be induced by the so-called core-shell model. In this model, every polarizable species is defined to have a core, where the mass of the species is present, and a shell, where the charge of the species is located. A spring constant acts between the core and the shell. The downside of the core-shell model is that since the shell is almost mass-less, the timestep used for integrating the equation of motion should be decreased further to capture the movements of the shell. Mainly for this reason, polarizability has not been considered in the present work and all the parameters are non-polarisable.

3.8.1 Rutile

The force field set proposed by Matsui and Akaogi for titanium oxide polymorphs has been extensively used in computational studies (24). Their original parameters are in the Buckingham form. Bandura *et al.* (25) modified the parameters proposed by Matsui and Akaogi using density functional theory calculations to adopt them for surfaces and interactions with water. Predota *et al.* (26) developed force field parameters to be used for atomistic simulations based on those of Bandura *et al.* (25), which are also used in this study for rutile (Table 3.1).

Table 3.1 Force field parameters used for rutile (25,26).

Buckingham potential parameters ($U(r) = A_{ij} \exp\left(\frac{-r}{\rho_{ij}}\right) - \frac{C_{ij}}{r^6}$)			
$i - j$	$A_{ij}\ [eV]$	$\rho_{ij}\ [\text{Å}]$	$C_{ij}\ [eV \cdot \text{Å}^6]$
$Ti - Ti$	31120.1336	0.1540	5.2500
$Ti - O$	16957.4923	0.1940	12.5900
$O - O$	11782.7328	0.2340	30.2199

$q_{Ti} = +2.196\ [e], q_O = -1.098\ [e]$

The Matsui-Akaogi potential for rutile was verified by comparing lattice parameters and elastic constants obtained by energy minimizing the rutile unit cell with those reported in the literature (Table 3.2). Here, values from three different computational studies are reported.

The first study (variable-charge model), proposed by Swamy and Gale (27), allows the charge of atoms to vary depending on the local environment of the atom in the lattice. The second study by Kerisit *et al.* (28) uses the core-shell model to induce polarizability in the Matsui-Akaogi parameters. This core-shell model successfully reproduced the electronic distribution of rutile and anatase. The third study (MA-like), developed by Schneider and Colombi Ciacchi (29), does not modify the original parameters of Matsui and Akaogi. However, the cutoff used in the Buckingham equation is a function of a few variables and varies if i and j are both titanium atoms, or are titanium and oxygen atoms, with the purpose of modelling the interface of titanium and titanium oxide. Compared to other computational results in Table 3.2, the difference of the obtained energy minimized values with the experimental data is acceptable, especially with those of the MA-like study.

Table 3.2 Lattice constants, bulk modulus and elastic constants of rutile reported based on previous experimental and computational data and those obtained in this work by energy minimization of the unit cell. The values in the parentheses are the difference of the reported calculated value with the experimental data [%].

	Exp.	Variable-charge model[c]	Core-Shell model[d]	Matsui-Akaogi [MA] like[e]	EM (This work)
a [Å]	4.59[a]	4.59 (-0.07)	4.51 (-1.83)	4.50 (-1.96)	4.49 (-2.18)
c [Å]	2.96[a]	2.96 (-0.07)	3.01 (+1.59)	3.01 (+1.69)	3.01 (+1.69)
$B\ [GPa]$	212.3[b]	229.0 (+7.87)	236.0 (+11.16)	235.9 (+11.12)	236.85 (+11.56)
$C_{11}\ [GPa]$	268.0[b]	293.8 (+9.63)	316.2 (+18.0)	321.2 (+19.85)	321.95 (+20.13)
$C_{33}\ [GPa]$	484.2[b]	422.7 (-12.70)	438.3 (-9.48)	443.2 (-8.47)	444.08 (-8.29)
$C_{44}\ [GPa]$	123.8[b]	96.04 (-22.42)	117.5 (-5.09)	122.4 (-1.13)	122.58 (-0.99)
$C_{66}\ [GPa]$	190.2[b]	189.5 (-0.37)	222.1 (+16.77)	224.7 (+18.14)	226.01 (+18.83)
$C_{12}\ [GPa]$	174.9[b]	201.9 (+15.44)	226.6 (+29.56)	227.8 (+30.25)	229.32 (+31.11)
$C_{23}\ [GPa]$	147.4[b]	168.3 (+14.18)	151.7 (+2.92)	146.3 (-0.75)	147.21 (-0.13)

a and c are lattice constants and $b = a$; B is the bulk modulus; C_{xx}s are the elastic constants.
[a]Bauer *et al.* (30), [b]Isaak *et al.* (31), [c]Swamy and Gale (27), [d]Kerisit *et al.* (28), [e]Schneider and Colombi Ciacchi (29)

3.8.1.1 The (110) surface of rutile

Among all the possible crystallographic surfaces of rutile, the (110) surface was chosen. This surface is of interest for two aspects. The first one is that this surface has the lowest surface energy compared to other crystallographic surfaces, making it the thermodynamically most stable surface of rutile (32,33). The second aspect is the broad range of studies on this surface, which makes the current understanding of this surface more extensive, compared to other surfaces.

The (110) surface of rutile is terminated by oxygens (32) (Figure 3.5a). This surface was prepared by METADISE (12). In the presence of water, the (110) surface is hydroxylated due to the dissociative adsorption of water molecules on the surface (34) (Figure 3.5). Two types of hydroxyl groups form on the surface (26). The first one is a hydroxyl group from a water molecule attaching to a Ti atom – this is known as the terminal hydroxyl. The second type of hydroxyl group, which is called the bridging hydroxyl group, is due to the protonation of an oxygen atom on the rutile surface, given from a water molecule. Atomic species of hydroxyl groups, in this thesis, are labelled as OT, HT, OB and HB for the oxygen and hydrogen of terminal and bridging hydroxyl groups, respectively. If all the hydroxyl groups are present, the net surface charge is zero. Protonation (formation of associated water) of a terminal group will lead to a net positive charge on the surface while for a bridging hydroxyl, this will lead to a net negative charge on the surface – the de-protonated oxygen, in this case, is referred to as OS. Since dissociation cannot take place in an MD simulation, here, the extent of surface hydroxylation is used as a mean to induce a non-zero net charge on the surface, which can be then associated to a specific pH and surface charge density estimated from experimental data (35–37).

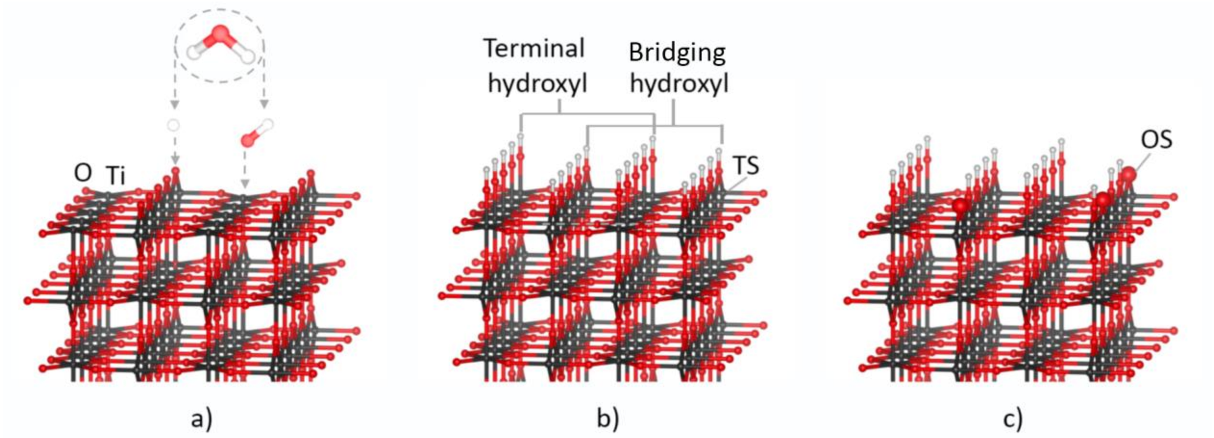

Figure 3.5 Atomic representation of the rutile (110) surface. a) The surface before hydroxylation and dissociation of a water molecule on the surface, b) formation of surface hydroxyl groups and c) de-protonation of some of the bridging hydroxyl groups leading to a net negative charge on the surface.

The isoelectric point of rutile, in ambient conditions, is generally smaller than 7.0 (38). Herein, the physiological condition ($T = 37$ ℃ and $pH \sim 7.4$) is of interest, in which the rutile surface is negatively charged. The surface charge density of rutile at the pH of 7.4 is reported to be approximately $-0.1\ C.m^{-2}$ (36,39).

Predota *et al.* (26) studied different levels of hydroxylation on the rutile (110) surface and observed that the partial charges of the hydroxyl groups, and the titanium atoms bound to them (referred to by TS), varies with the surface charge density. They calculated the partial charges of these species for a few surface charge densities. Here, three different surface charge densities were used. The partial charge of rutile species for these surface charge densities was either taken (chapters 6 and 7) or calculated based on the work of Predota *et al.* (37) (chapters 4 and 5), and will be explained in more detail in the corresponding chapters.

3.8.2 Water

In spite of the extensive efforts made to model liquid water, no computational water model can yet completely mimic water properties. Since different water models provide different properties, it is important that one choose the appropriate water model based on the simulation system and desired properties. Literature survey shows that for biological systems, mostly, TIP3P (40) and SPC/E (41) water models are used. Some key parameters and properties of these two water models and the liquid water are presented in Table 3.3. The SPC/E model was used in this thesis.

Table 3.3 Some properties and parameters of two different water models.

Property	Liquid water	TIP3P	SPC/E
$q_O\ [e]$	-	-0.834[c]	-0.8476[e]
$q_H\ [e]$	-	+0.417[c]	+0.4238[e]
$d_{OH}\ [\text{Å}]$	0.9572[a]	0.9572[c]	1.00[e]
$H-O-H$ angle [°]	104.52[a]	104.52[c]	109.47[e]
$\epsilon_{ow-ow}\ [eV]$	-	0.00659[c]	0.00674[e]
$\sigma_{ow-ow}\ [\text{Å}]$	-	3.1507[c]	3.166[e]
$D\ [10^{-9}\ m^2.s^{-1}]$	2.3[b]	5.670[d]	2.5 (300 K)[e]
$\rho\ [g.cm^{-3}]$	0.9965[b]	0.982[c]	0.998[e]
$C_p\ [cal \cdot mol^{-1} \cdot °]$	17.99[c]	16.80[c]	19.433[f]

q is the charge, d is the bond length, ϵ and σ are Lennard-Jones parameters (Equation 3.4), D is the diffusion coefficient, ρ is density and C_p is the heat capacity.

[a]Hoy and Bunker (42), [b]Spoel *et al.* (43), [c]Jorgensen *et al.* (40), [d]Mark and Nilsson (44), [e]Berendsen *et al.* (41), [f]Mao and Zhang (45)

3.8.3 Ions

Here, ions present and relevant to those found in human blood plasma and SBFs, are of interest: K^+, Na^+, Ca^{2+}, Mg^{2+}, Cl^-, CO_3^{2-}, HCO_3^-, and PO_4^{3-} (Table 2.1). The force field parameters of most of the ions were taken from those previously reported in the literature (46–48), and are summarized in Table 3.4. The force field parameters of carbonate, bicarbonate and phosphate had to be modified mainly to obtain the interaction of those species with other components of the system. This is discussed and explained in detail in Appendix C, where the performance of the force field parameters are also extensively tested.

Table 3.4 Force field parameters for some of the ions studied in this work.

Species	Charge $[e]$	$\epsilon\ [eV]$	$\sigma\ [\text{Å}]$
K^+	+1	0.004336	3.332
Na^+	+1	0.004336	2.583
Ca^{2+}	+2	0.004336	2.895
Mg^{2+}	+2	0.0379436	1.398
Cl^-	-1	0.004336	4.401

3.8.4 Organic molecules

In this thesis, a few single amino acids (Ala, Arg, Asp, Gly, Leu, Lys and Ser) and a polypeptide were studied. For both types of organic residues, the DL_FIELD package (49) was used. The amino acids were described using the CHARMM force field (50) while for the polypeptide the Amber force field (51) was used. Both Amber and CHARMM force fields, in their initial development, did not explicitly consider all hydrogen atoms; Amber considered those bonded to carbon atoms united atoms while CHARMM also treated those bonded to sulfur, similarly. This was soon abandoned and an all-atom description was favored.

3.8.5 Cross-interactions

Cross-term interactions should be carefully defined. In this thesis, the following cross-term interactions were taken into account:

i. Rutile-Ion
ii. Rutile-Organic
iii. Rutile-Water
iv. Ion-Organic, Ion-Water, Organic-Water

Here, the treatment of cross-term interactions of each of the above categories is briefly explained. Further details are presented in corresponding chapters.

i. *Rutile-Ion*. Similar to the work of Predota *et al.* (26), the interactions of ions with the titanium of rutile were considered to be purely electrostatic. Those between ions and oxygen of rutile were defined similarly to that of ions-OW (oxygen of water) – see iv, below.

ii. *Rutile-Organic.* For defining these type of interactions, the Lorentz-Berthelot mixing rules (7,52,53) were used. To use this rule, one needs the force field parameters of components i and j in the Lennard-Jones form (Equation 3.4). Cross-term interactions can then be obtained as:

$$\sigma_{ij} = \frac{(\sigma_{ii} + \sigma_{jj})}{2}$$ *Equation 3.43*

$$\epsilon_{ij} = \sqrt{\epsilon_{ii}\epsilon_{jj}}$$ *Equation 3.44*

The force field parameters describing organic molecules, as explained in section 3.8.4 above, were originally in the Lennard-Jones form. However, the parameters of rutile had to be transformed from their original Buckingham form to the Lennard-Jones form. The procedure and its verification are explained in detail in Appendix D, but the final parameters are summarized in Table 3.5. It should be noted that the Lennard-Jones parameters were only used to obtain the cross-term interactions and that rutile was described by the original parameterization of Matsui and Akaogi (Table 3.1) (24).

iii. *Rutile-Water*. For the interactions of rutile species with water, the parameters developed by Bandura *et al.* based on *ab initio* calculations and verified by Predota *et al.* (25,26) were used.

iv. For the other three groups (Ion-Organic, Ion-Water and Organic-Water) all cross-term interactions were obtained using the mixing rules (Equation 3.43 and Equation 3.44), which is a common practice (47,54,55).

Table 3.5 Fitted LJ parameters for the atomic species of rutile.

Atomic species	$\epsilon\ [eV]$	$\sigma\ [\text{Å}]$
Ti	0.0384	1.799
O	0.0059	2.922
O of the hydroxyl groups De-protonated oxygen	0.0059	2.922

References

1. Israelachvili, J. N. *Intermolecular and Surface Forces*. (Elsevier Science, 2015).

2. Maginn, E. J. From discovery to data: What must happen for molecular simulation to become a mainstream chemical engineering tool. *AIChE J.* **55,** 1304–1310 (2009).

3. Leach, A. R. *Molecular Modelling: Principles and Applications*. (Prentice Hall, 2001).

4. Rahman, A. Correlations in the Motion of Atoms in Liquid Argon. *Phys. Rev.* **136,** A405–A411 (1964).

5. Toukmaji, A. Y. & Board, J. A. Ewald summation techniques in perspective: a survey. *Comput. Phys. Commun.* **95,** 73–92 (1996).

6. Ewald P. P. Die Berechnung optischer und elektrostatischer Gitterpotentiale. *Ann. Phys.* **369,** 253–287 (1921).

7. Allen, M. P., Allen, M. P., Tildesley, D. J. & Tildesley, D. J. *Computer Simulation of Liquids*. (Clarendon Press, 1989).

8. Aschauer, U. & Bowen, P. Atomistic Simulation in Powder Technology - from Growth Control and Dispersion Stabilization to Segregation at Doped Interfaces - Ph.D. Thesis - EPFL. (2008).

9. Galmarini, S. & Bowen, P. Atomistic Simulation of Cementitious Systems - Ph.D. Thesis - EPFL. (2013).

10. Hestenes, M. & Stiefel, E. Methods of Conjugate Gradients for Solving Linear Systems. *J. Res. Natl. Bur. Stand.* **49,** 409–436 (1952).

11. Gale, J. D. & Rohl, A. L. The General Utility Lattice Program (GULP). *Mol. Simul.* **29,** 291–341 (2003).

12. Watson, G. W., Kelsey, E. T., de Leeuw, N. H., Harris, D. J. & Parker, S. C. Atomistic simulation of dislocations, surfaces and interfaces in MgO. *J. Chem. Soc. Faraday Trans.* **92,** 433–438 (1996).

13. Verlet, L. Computer 'Experiments' on Classical Fluids. I. Thermodynamical Properties of Lennard-Jones Molecules. *Phys. Rev.* **159,** 98–103 (1967).

14. Swope, W. C. & Andersen, H. C. ${10}^{6}$-particle molecular-dynamics study of homogeneous nucleation of crystals in a supercooled atomic liquid. *Phys. Rev. B* **41,** 7042–7054 (1990).

15. Smith, W., Forester, T. R. & Todorov, I. T. The DL POLY Classic User Manual. (2012).

16. Hoover, W. G. Canonical dynamics: Equilibrium phase-space distributions. *Phys. Rev. A* **31,** 1695–1697 (1985).

17. Thijssen, J. M. *Computational Physics*. (Cambridge University Press, 1999).

18. Laio, A. & Gervasio, F. L. Metadynamics: a method to simulate rare events and reconstruct the free energy in biophysics, chemistry and material science. *Rep. Prog. Phys.* **71,** 126601 (2008).

19. Barducci Alessandro, Bonomi Massimiliano & Parrinello Michele. Metadynamics. *Wiley Interdiscip. Rev. Comput. Mol. Sci.* **1,** 826–843 (2011).

20. Valsson, O., Tiwary, P. & Parrinello, M. Enhancing Important Fluctuations: Rare Events and Metadynamics from a Conceptual Viewpoint. *Annu. Rev. Phys. Chem.* **67,** 159–184 (2016).

21. Barducci, A., Bussi, G. & Parrinello, M. Well-Tempered Metadynamics: A Smoothly Converging and Tunable Free-Energy Method. *Phys. Rev. Lett.* **100,** 020603 (2008).

22. Tiwary, P. & Parrinello, M. A Time-Independent Free Energy Estimator for Metadynamics. *J. Phys. Chem. B* **119,** 736–742 (2015).

23. Tribello, G. A., Bonomi, M., Branduardi, D., Camilloni, C. & Bussi, G. PLUMED 2: New feathers for an old bird. *Comput. Phys. Commun.* **185,** 604–613 (2014).

24. Matsui, M. & Akaogi, M. Molecular Dynamics Simulation of the Structural and Physical Properties of the Four Polymorphs of TiO_2. *Mol. Simul.* **6,** 239–244 (1991).

25. Bandura, A. V. & Kubicki, J. D. Derivation of Force Field Parameters for TiO_2−H_2O Systems from *ab Initio* Calculations. *J. Phys. Chem. B* **107,** 11072–11081 (2003).

26. Předota, M. *et al.* Electric Double Layer at the Rutile (110) Surface. 1. Structure of Surfaces and Interfacial Water from Molecular Dynamics by Use of *ab Initio* Potentials. *J. Phys. Chem. B* **108,** 12049–12060 (2004).

27. Swamy, V. & Gale, J. D. Transferable variable-charge interatomic potential for atomistic simulation of titanium oxides. *Phys. Rev. B* **62,** 5406–5412 (2000).

28. Kerisit, S., Deskins, N. A., Rosso, K. M. & Dupuis, M. A Shell Model for Atomistic Simulation of Charge Transfer in Titania. *J. Phys. Chem. C* **112,** 7678–7688 (2008).

29. Schneider, J. & Ciacchi, L. C. First principles and classical modeling of the oxidized titanium (0001) surface. *Surf. Sci.* **604,** 1105–1115 (2010).

30. Baur, W. H. & Khan, A. A. Rutile-type compounds. IV. SiO2, GeO2 and a comparison with other rutile-type structures. *Acta Crystallogr. Sect. B* **27,** 2133–2139 (1971).

31. Isaak, D. G., Carnes, J. D., Anderson, O. L., Cynn, H. & Hake, E. Elasticity of TiO_2 rutile to 1800 K. *Phys. Chem. Miner.* **26,** 31–43 (1998).

32. Diebold, U. The surface science of titanium dioxide. *Surf. Sci. Rep.* **48,** 53–229 (2003).

33. Oliver, P. M., Watson, G. W., Toby Kelsey, E. & Parker, S. C. Atomistic simulation of the surface structure of the TiO_2 polymorphs rutileand anatase. *J. Mater. Chem.* **7,** 563–568 (1997).

34. Fahmi, A. & Minot, C. A theoretical investigation of water adsorption on titanium dioxide surfaces. *Surf. Sci.* **304,** 343–359 (1994).

35. Zhang, Z. *et al.* Ion Adsorption at the Rutile−Water Interface: Linking Molecular and Macroscopic Properties. *Langmuir* **20,** 4954–4969 (2004).

36. Machesky, M. L. *et al.* Chapter 12 Ion adsorption into the hydrothermal regime. *Interface Sci. Technol.* **11,** 324–358 (2006).

37. Předota, M., Machesky, M. L., Wesolowski, D. J. & Cummings, P. T. Electric Double Layer at the Rutile (110) Surface. 4. Effect of Temperature and pH on the Adsorption and Dynamics of Ions. *J. Phys. Chem. C* **117,** 22852–22866 (2013).

38. Parks, G. A. The Isoelectric Points of Solid Oxides, Solid Hydroxides, and Aqueous Hydroxo Complex Systems. *Chem. Rev.* **65,** 177–198 (1965).

39. Takahashi, K. & Fukuzaki, S. Cleanability of Titanium and Stainless Steel Particles in Relation to Surface Charge Aspects. *Biocontrol Sci.* **13,** 9–16 (2008).

40. Jorgensen, W. L., Chandrasekhar, J., Madura, J. D., Impey, R. W. & Klein, M. L. Comparison of simple potential functions for simulating liquid water. *J. Chem. Phys.* **79,** 926–935 (1983).

41. Berendsen, H. J. C., Grigera, J. R. & Straatsma, T. P. The missing term in effective pair potentials. *J. Phys. Chem.* **91,** 6269–6271 (1987).

42. Hoy, A. R. & Bunker, P. R. A precise solution of the rotation bending Schrödinger equation for a triatomic molecule with application to the water molecule. *J. Mol. Spectrosc.* **74,** 1–8 (1979).

43. van der Spoel, D., van Maaren, P. J. & Berendsen, H. J. C. A systematic study of water models for molecular simulation: Derivation of water models optimized for use with a reaction field. *J. Chem. Phys.* **108,** 10220–10230 (1998).

44. Mark, P. & Nilsson, L. Structure and Dynamics of the TIP3P, SPC, and SPC/E Water Models at 298 K. *J. Phys. Chem. A* **105,** 9954–9960 (2001).

45. Mao, Y. & Zhang, Y. Thermal conductivity, shear viscosity and specific heat of rigid water models. *Chem. Phys. Lett.* **542,** 37–41 (2012).

46. Dang, L. X. Mechanism and Thermodynamics of Ion Selectivity in Aqueous Solutions of 18-Crown-6 Ether: A Molecular Dynamics Study. *J. Am. Chem. Soc.* **117,** 6954–6960 (1995).

47. Předota, M., Zhang, Z., Fenter, P., Wesolowski, D. J. & Cummings, P. T. Electric Double Layer at the Rutile (110) Surface. 2. Adsorption of Ions from Molecular Dynamics and X-ray Experiments. *J. Phys. Chem. B* **108,** 12061–12072 (2004).

48. Gavryushov, S. Mediating Role of Multivalent Cations in DNA Electrostatics: An Epsilon-Modified Poisson−Boltzmann Study of B-DNA−B-DNA Interactions in Mixture of NaCl and MgCl2 Solutions. *J. Phys. Chem. B* **113,** 2160–2169 (2009).

49. Yong, C. W. Descriptions and Implementations of DL_F Notation: A Natural Chemical Expression System of Atom Types for Molecular Simulations. *J. Chem. Inf. Model.* **56,** 1405–1409 (2016).

50. MacKerell, A. D. *et al.* All-Atom Empirical Potential for Molecular Modeling and Dynamics Studies of Proteins. *J. Phys. Chem. B* **102,** 3586–3616 (1998).

51. Ponder, J. W. & Case, D. A. in *Adv. Protein Chem.* **66,** 27–85 (Academic Press, 2003).

52. Lorentz H. A. Ueber die Anwendung des Satzes vom Virial in der kinetischen Theorie der Gase. *Ann. Phys.* **248,** 127–136 (1881).

53. Wisniak, J. Daniel Berthelot. Part I. Contribution to thermodynamics. *Educ. Quím.* **21,** 155–162 (2010).

54. Almora-Barrios, N. & De Leeuw, N. H. Molecular Dynamics Simulation of the Early Stages of Nucleation of Hydroxyapatite at a Collagen Template. *Cryst. Growth Des.* **12,** 756–763 (2012).

55. Larentzos, J. P. & Criscenti, L. J. A Molecular Dynamics Study of Alkaline Earth Metal−Chloride Complexation in Aqueous Solution. *J. Phys. Chem. B* **112,** 14243–14250 (2008).

Chapter 4 Interaction of ionic species with the rutile (110) surface

In this chapter, the interaction of different forms of ionic species with a rutile surface is studied. The main purpose of this chapter is to present insights on events, which happen on a rutile surface in an ionic solution – similar to blood plasma or SBF. While these events might not be directly responsible for apatite nucleation and growth on the surface, hopefully, they can help one to understand events that affect this process.

Apatite forms *in vivo* or *in vitro* due to the supersaturation of the blood plasma or the SBF solution with respect to ionic species. In this chapter, the interaction of ionic species with the rutile (110) surface from different aspects and under different conditions is studied. As it will be presented, thermodynamic modelling shows that under physiological conditions ($T \sim 37$ ℃ and $pH \sim 7.4$), ions in an SBF solution exist mainly in their free form except for the phosphate and carbonate, which are more abundant in their protonated forms.

The model previously proposed by Kokubo *et al.* (1), and explained in Chapter 1, describes the apatite formation via the adsorption of calcium and phosphate ions on the alkali and heat treated sodium titanate surface. To verify and expand this model on rutile and understand whether other ions can aid or hinder the adsorption of these ions on the surface, or whether they do not interact with the surface at all, different questions are addressed in this chapter.

First, the interaction of the most abundant ionic species in blood plasma (or SBF), in their free form, with a rutile surface, which has only one negative charge point on its surface, is investigated. For this part, the adsorption and desorption of ions found in SBF and human blood plasma on the rutile (110) surface are presented in the form of an article to be submitted to a peer-reviewed international journal. The simulations and analyses were performed by the first author (also, author of this thesis). The article was also written by her and was revised by her two thesis directors.

In the second part of this chapter, the interaction of two cations (sodium and calcium) with the rutile (110) surface, this time with two negative charge points on the surface, is investigated. This will allow one to get an idea of the effect of surface charge density on the adsorption behavior of ions on the rutile surface.

Thermodynamic modelling also reveals that many ionic complexes, although with a lower probability compared to the free form ions, also form in an SBF solution. For the third and fourth sections of this chapter, three of the most relevant and interesting ionic pairs are chosen. In the third section, the free energy of formation of these pairs is studied while in the fourth section, the adsorption behavior of these pairs on the rutile (110) surface is investigated.

4.1 Interaction of single ions with the negatively charged rutile (110) surface

A well-tempered metadynamics study on the interactions of simulated body fluid ions with the rutile (110) surface

Azade YazdanYar✦*, Ulrich Aschauer*✦✦*, Paul Bowen*✦
✦ Department of Materials Science and Engineering, École Polytechnique Fédérale de Lausanne (EPFL), Route Cantonale, Lausanne 1015, Switzerland
✦✦ Department of Chemistry and Biochemistry, University of Bern, Freiestrasse 3, Bern 3012, Switzerland

Abstract

Apatite formation on a surface, *in vivo* or *in vitro*, is considered to be closely related to the bioactivity of the material. In both testing conditions, apatite forms from the ions in solution. In this study, we have used well-tempered metadynamics to study the adsorption behavior of ions, present in human blood plasma as well as the *in vitro* solutions, on a prototypical rutile surface. Based on the adsorption and desorption energies from our calculations, we used transition state theory to compare the kinetics of adsorption and desorption of different ions for the surface. We explain the relative adsorption energy and the activation energy for adsorption and desorption of nine different ions. Our findings suggest that among the studied ions, Na^+, K^+, Ca^{2+}, CO_3^{2-} and PO_4^{3-} have a favorable adsorption on the surface. Therefore, a model for apatite formation should address the contribution of these ions. Other ions are expected to transiently affect the surface composition as their adsorption barrier is small but their desorption barrier is even smaller.

4.1.1 Introduction

The bioactivity of new biomaterials can be evaluated by both *in vivo* and *in vitro* testing. Kokubo *et al.*[1] proposed that a biomaterial will be able to bond to the bone provided that *in vivo*, an apatite layer (a calcium-phosphate phase containing chlorine, fluorine or hydroxyl) forms at the interface between the bone and the biomaterial. They also suggested that this apatite formation on the surface can be reproduced *in vitro* and interpreted as a sign of bioactivity.[1] Apatite formation *in vivo* is the result of a series of complex and unknown chemical events, which happen in the biological environment at the interface of the biomaterial and the body fluid[2] but *in vitro*, apatite forms directly from the aqueous solution in which the sample is immersed.

In this work, we are interested in apatite formation on a rutile surface, which is present in the passivation layer formed on Ti-based implants.[3] One of the well-known *in vitro* solutions proposed for titanium-based samples are the Simulated Body Fluid (SBF) solutions. SBFs have an ionic composition similar to human blood plasma; for their ionic concentration see Table C.1. They are rich in Na^+ and Cl^- but they also contain small, but nevertheless essential, quantities of K^+, Mg^{2+}, Ca^{2+}, HCO_3^-, HPO_4^{2-} and SO_4^{2-}.[1] The proposed SBF solutions for Ti-based biomaterials to date, do not contain any organic components (although the common practice is to use tris(hydroxymethyl-aminomethane) as the buffering agent),[1,4-6] in particular the *in vitro* method standardized by the International Organization for Standardization (ISO 23317) in 2007,[7] which has been widely used to evaluate the bioactivity of various materials over the past decade. The lack of organic components has only very recently started to be investigated experimentally.[8]

While apatite formation is still not understood thoroughly, one of the current models, proposed by Kokubo and Kim *et al.*,[9] suggests that the alkaline ($NaOH$) and heat treatment of a titanium metal surface cause the formation of a $Na_2O - TiO_2$ layer on the surface. After soaking the surface in the SBF solution, sodium ions are exchanged for hydronium ions (H_3O^+), which leads to the formation of $TiOH$ groups on the surface. As the titanium oxide surface is negatively charged under physiological conditions ($T = 37$ °C and $pH{\sim}7.4$),[10] it attracts Ca^{2+} ions. The accumulated calcium ions on the surface increase the supersaturation of the solution close to the surface and can trigger apatite nucleation[11] by attracting phosphate ions, which leads to the formation of an amorphous apatite layer.[3] As amorphous apatite is thermodynamically metastable, it will eventually transform to crystalline apatite.[6,9,12,13]

There are still further details, which need to be considered and investigated, to gain a better understanding of the apatite formation. For example, the model proposed by Kokubo and Kim *et al.*[9] only discusses the role of calcium and phosphate adsorption on the surface in the apatite formation and not that of other ionic species. If the adsorption of ionic species other than calcium and phosphate is comparable to that of these two ions in terms of energetics or kinetics, they can hinder adsorption of calcium and phosphate on the surface and affect apatite formation.

While in a solution, ions can exist in their free form or as ionic complexes depending on the pH, temperature and ionic strength (as shown for SBF under physiological conditions in Table C.2), in this study we focus only on the free form of ions as a first step of studying the apatite formation on the rutile surface. We choose to study the adsorption energetics and kinetics of several ions found in the ISO standard SBF solution used for apatite-forming ability testing[7] except for the hydrogen phosphate and sulphate components, namely: K^+, Na^+, Ca^{2+}, Mg^{2+}, Cl^-, CO_3^{2-}, HCO_3^- and PO_4^{3-} on the rutile (110) surface. The chosen ions include the most abundant ions found in human blood plasma or SBF solutions. The (110) surface is of particular interest as it is the thermodynamically most stable surface of rutile.[14]

Compared to molecular dynamics (MD), enhanced sampling methods allow the system to explore the sampling space more extensively. Continuous biasing of the potential energy of the system eventually provides it with sufficient energy to overcome barriers associated with rare events inaccessible on an MD timescale. In this paper, we use well-tempered metadynamics (WT-MTD) to study the adsorption energetics and kinetics of several ions (K^+, Na^+, Ca^{2+}, Mg^{2+}, Cl^-, CO_3^{2-}, HCO_3^-, and PO_4^{3-}) on the rutile (110) surface. We then use transition rate theory to compute adsorption and desorption transition rate constants of different ions from the WT-MTD results. This allows us to discuss the relative effects of different ions at the solid-water interface.

4.1.2 Simulation methods

4.1.2.1 Rutile slab

The rutile (110) surface was modelled as a slab with lateral dimension of 35.5×38.9 Å^2. In the direction perpendicular to the surface, the simulation box consisted of the rutile slab, a water layer and a vacuum gap with a thickness of 70, 90 and 100 Å, respectively. These relatively large thicknesses were chosen to ensure that bulk properties are recovered in the center of both the rutile slab in terms of inter-layer distances, and the water layer in terms of the density and the plane-averaged dipole moment of water molecules (Figure C.1). Periodic boundary conditions were applied in three directions. The vacuum gap in the direction normal to the surface was used to reduce the slab-slab interactions in the periodic images. Both the upper and lower surface of the inorganic slab were fully hydroxylated. As rutile is negatively charged under physiological conditions (with an approximate charge density of -0.1 $C \cdot m^{-2}$,[15,16] one of the bridging hydroxyl groups on the surface (which was in contact with water) was de-protonated (hereafter referred to as the charge point) to create a slightly negatively charged rutile surface. The surface charge density, in this case, is -0.012 $C \cdot m^{-2}$ and was chosen to avoid complications related to the distribution of de-protonated groups for higher surface charges. Hereafter, this scheme is referred to as the singly deprotonated surface. The charge distribution of atomic species is explained in detail elsewhere.[17]

4.1.2.2 Force fields

Classical atomistic force fields were used in this study. Parameters for rutile were taken from Predota *et al.*[18] The SPC/E model was used to describe water.[19] The ions studied here are: K^+, Na^+, Ca^{2+}, Mg^{2+}, Cl^-, CO_3^{2-}, HCO_3^-, and PO_4^{3-}. Force field parameters for Na^+, K^+ and Cl^- were taken from Dang[20] and parameters for Ca^{2+} and Mg^{2+} were taken from Predota *et al.*[21] and Gavryushov[22], respectively. Detailed description of species charges and force field parameters can be found in C.2. All the species and interactions are non-polarizable. Force field parameters for CO_3^{2-} and PO_4^{3-} were initially taken from de Leeuw *et al.*[23] and de Leeuw[24], respectively, and then modified as explained in C.3. The force field parameters for HCO_3^- were developed based on DFT structures as described in section C.3. Even though carbonate and phosphate ions are not among the major ions in the initial composition of SBF, we study their interaction with the surface since a) we used the force field of carbonate to obtain the force field parameters for bicarbonate and b) phosphate plays an important role in the apatite formation model. Moreover, apatite formation is believed to occur via adsorption of calcium and phosphate ions from the solution.[25]

Cross-interactions between rutile, ions and water were defined as by Predota *et al.*[21] Interactions between O_{rutile} and O_{water} were described as for the interactions between oxygen atoms of water molecules. Interactions between Ti and O_{water} atoms were formulated by Predota *et al.*[21] Interactions between Ti and ions were considered to be purely electrostatic. Interactions between O_{rutile} and ions were set with the same parameters as the interactions between O_{water} and ions, which were described using Lorentz-Berthelot mixing rules. Long-range electrostatic interactions were calculated by 3D Ewald summation with automatic parameter optimization for a relative error smaller than 10^{-6}. A cutoff of 12 Å was considered for short-range van der Waals interactions as well as the real space part of the electrostatic interactions.

4.1.2.3 Simulation details

Well-tempered metadynamics[26] were used to enhance sampling and to obtain the free energy landscape as an ion approaches the rutile (110) surface. Two collective variables (CV) were chosen. The first one was the perpendicular distance of the ion from the surface (by surface we mean the average position of the oxygen atoms of hydroxyl groups in the z-direction). The second CV was the distance of the ion from the charge point on the surface in the xy-plane. The role of this collective variable is to assure that the ion explores the area around the charge point. In both collective variables, the center of mass was considered for polyatomic ions. Hereafter, the two collective variables will be referred to as the distance CV and the radius CV, respectively. A virtual upper wall at a distance of 20 Å was applied to the distance CV. The restraining potential of the upper wall acts on the CV when the value of CV is larger than the limit of the wall (here, 20 Å) or in other words it limits the sampling space in the direction of the distance CV to a distance of 20 Å from the surface. Such limitation of the phase space will allow one to focus on that part of the phase space which is more interesting, important or physically more relevant. We expect to observe two extreme scenarios as a function of the radius CV. The first one is when the ion adsorbs close to the charge point and the second one is when it adsorbs far from the charge point. Exploring the entire configuration space between these two extremes would significantly increase the computational cost. Consequently, we used an alternative approach for which an upper wall at 4 Å was applied to the radius CV. To sample both aforementioned scenarios, we studied adsorption of all ions in the vicinity of the charge point (close scenario) and for calcium and phosphate, we also studied the adsorption far from the charge point (far scenario) in order to be able to compare the results of these two cases. The center of the radius CV in the far scenario was a hydroxyl group (hereafter referred to as the central hydroxyl); the distance between the centers of the radius CV for the close and far scenario (the charge point and the central hydroxyl) was approximately 25 Å. Upper walls on both collective variables were applied using the following parameters; an energy constant of 10000.0 $kJ \cdot mol^{-1}$, an offset of 0, a rescaling factor of 1.0 and a power of 2.0. A schematic of the simulation box and CV setup is presented in Figure C.5.

Verlet leapfrog was used as the integration algorithm. A Nosé-Hoover thermostat (with a relaxation time of 0.5 ps) was used for the NVT ensemble. All simulations were performed at 310 K with a timestep of 0.7 fs for mono-atomic and 0.6 fs for polyatomic ions. Atomic positions were stored every 25,000 timesteps. Each simulation box contained only one type of ion, therefore, there are no ion-ion interactions present in our study and the solution is thus very dilute, with an ionic concentration of about 13 mM. The total charge was compensated with a uniform background charge, which will, however, not affect the relative energetics we are interested in. Before production runs, each system was equilibrated for 200 ps during which the ion was kept fixed at a distance of 10 Å from the surface. During the equilibration and production runs, the solid slab was kept fixed and only the hydroxyl groups and the titanium atoms they are bound to were able to move. Sampling during the production runs was performed for 20 ns. The width of Gaussian for the distance CV and the radius CV was 0.05 and 0.1 Å, respectively. The initial height of the Gaussians was set to 1.0 $kJ \cdot mol^{-1}$ and the bias factor was 15. Gaussians were deposited every 2,000 steps. The reduction in the Gaussian height over time can be seen in Figure C.6. The DL_POLY Classic v1.9 package[27] with the PLUMED plugin[28] v2.2.2 was used to perform both MD and WT-MTD simulations. Quantum ESPRESSO[29] v5.3.0 was used to carry out DFT calculations needed to determine potential parameters for CO_3^{2-}, HCO_3^-, and PO_4^{3-} polyatomic anions, details can be found in the supporting information, C.3.

4.1.3 Results and Discussion

Before we present and discuss results, it is necessary to briefly discuss the types of interactions, which affect the adsorption behavior of ions, solvated in water, on a surface.

Adsorption of an ion on an inorganic surface depends on three types of interactions: i) ion-water interactions: since the ion has to lose some of the water molecules in its hydration shell,[3] ii) surface-water interactions: since some of the water molecules close to the surface have to be displaced, at least around the adsorption site,[30] and finally iii) ion-surface interactions, *i.e.,* how favorable the ion-surface interactions are. In the following, we will briefly discuss each type of interaction as they are the basis for the discussion of our results.

I. *Ion-water interaction.* The ion-water interaction depends on the ionic charge and the ionic radius, which eventually determines the coordination number of the ion.[31] For ions with the same valence, those with a smaller radius have a stronger interaction with their coordinated water molecules and there are also fewer water molecules coordinated with them. Therefore, water molecules in the hydration shell of a smaller ion have a higher residence time compared to an ion with a larger radius. The same is true for ions with a higher valence compared to those with a lower valence. A stronger interaction between the water molecules and a small ion can result in the adsorption event on the surface to require more energy as it is more difficult to disrupt the hydration shell of the ion. However, this is not always true since ion-surface and surface-water interactions also affect the adsorption behavior (see below). This was shown by Wu *et al.*[32] using unbiased MD, where the adsorption strength on a negatively charged rutile (110) surface increased, for monovalent cations (K^+, Na^+ and Rb^+) in decreasing order of radius, but for divalent cations (Ca^{2+}, Mg^{2+}, and Sr^{2+}) in increasing order of radius.

II. *Surface-water interaction.* Similar to other studies, the water density in the normal direction to the rutile (110) surface reveals two notable peaks with water density higher than bulk water, at distances of 2.35 and 4.60 Å from the surface (Figure C.1), which make the adsorption of ions on the surface difficult. However, since we study the adsorption of all ions on the same surface, the surface-water interaction is similar in all cases studied here and in the following, we will not discuss the effect of surface-water interactions on the adsorption behavior of ions.

III. *Ion-surface interaction.* Ions can adsorb in inner- and outer-sphere configurations. In the inner-sphere adsorption, there are no intermediate water molecules between the ion and the surface. In the case where the ion is adsorbed on the surface enclosed in its hydration shell, water molecules are present between the ion and the surface, which is considered as the outer-sphere adsorption mode.

4.1.3.1 Free energy in 2D CV space

As we use two collective variables for our well-tempered metadynamics, the obtained free energy profile is two-dimensional (Figure 4.1). Several observations can be made based on this figure. We can see that all the cations except magnesium have an energy minimum in the adsorbed state (small distance CV) as well as an energy minimum when solvated in water. For Mg^{2+}, the energy minimum is when the ion is solvated in water and not when it is close to the surface.

For anions, the energy minima are either further from the surface (larger distance CVs) or further from the charge point (larger radius CVs) compared to the cations. Phosphate, especially in the far scenario, has a notable energy minimum close to the surface. Based on the position of the energy minima in the direction of the radius CV, we see that cations adsorb closer to the charge point compared to the anions, which indicates the electrostatic interactions are dominating here.

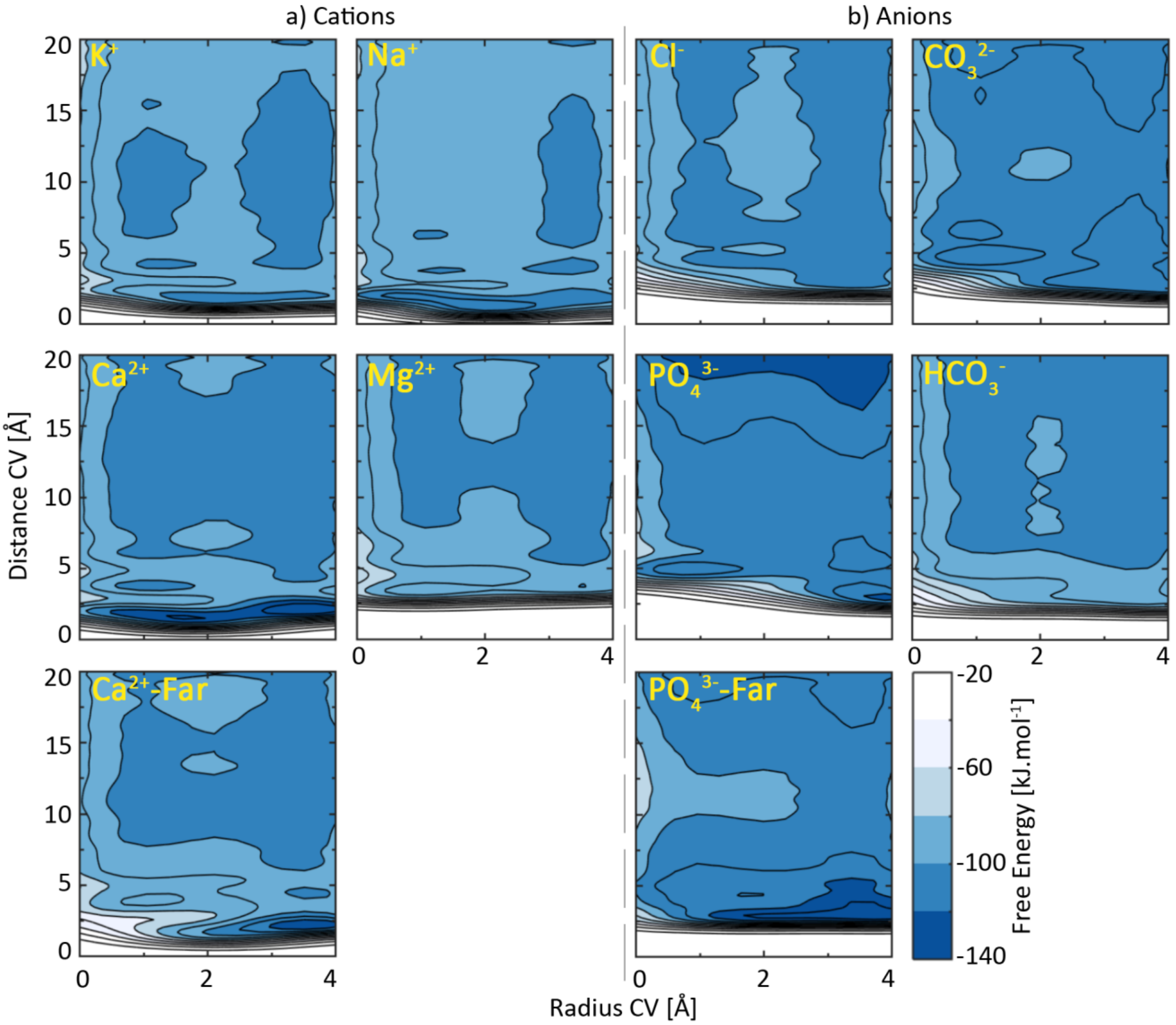

Figure 4.1 Free energy as a function of the radius CV and distance CV for the various cations (a) and anions (b) studied. Darker colors represent regions lower in free energy.

4.1.3.2 Free energy along the distance CV

The distance CV (Figure C.7) shows that all the ions approach the surface several times during the simulation. For some ions, the adsorption is strong and prevents rapid desorption while for others, the adsorption is transient. In order to be able to characterize the affinity of different ions for the rutile (110) surface, in the following, we will discuss the free energy along the distance CV, presented in Figure 4.2. Based on Figure 4.2, we define three characteristics. The ***desorption barrier*** is considered as the difference between the free energy maximum and minimum closest to the surface. The ***adsorption barrier*** is defined as the difference between the closest maximum and the second closest minimum of the free energy. Finally, the ***adsorption energy*** is defined as the difference between the closest minimum and the second closest minimum. We choose this quantity as it is not always easy to extract the formally correct difference between the first minimum and the free energy far from the surface (see, e.*g.*, PO_4^{3-}). The desorption and adsorption barriers characterize the kinetics while the adsorption energy characterizes the thermodynamics.

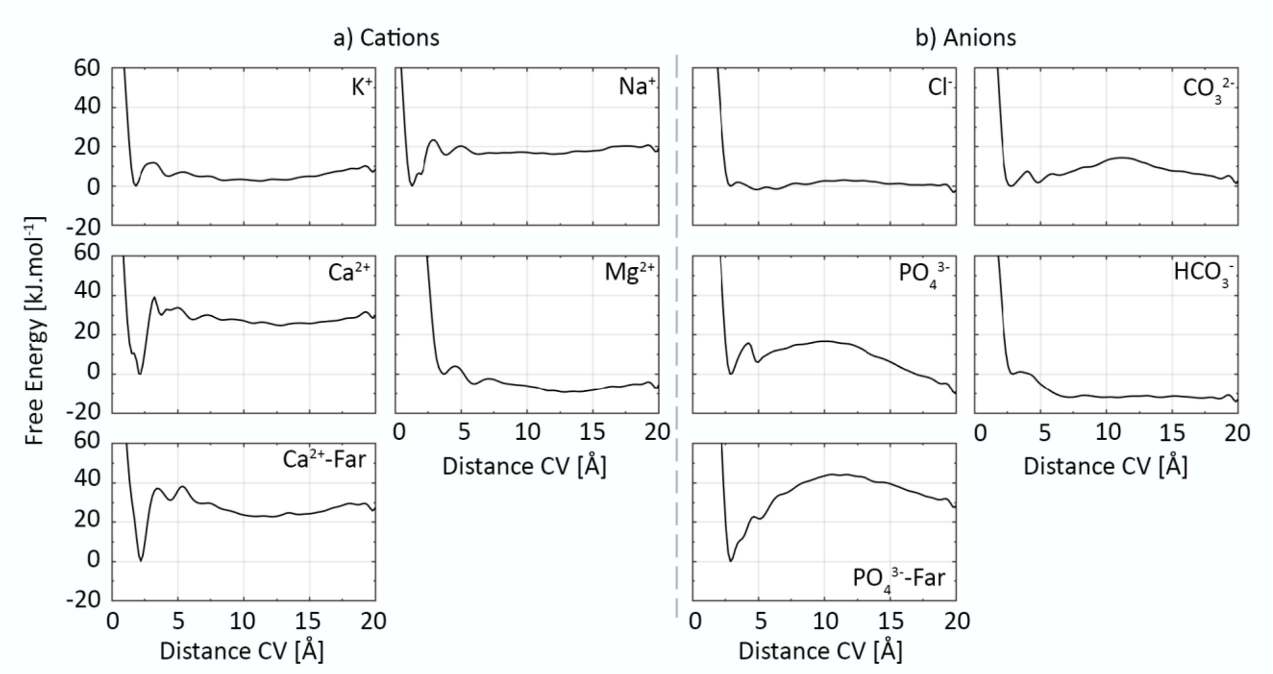

Figure 4.2 Free energy of adsorption along the distance collective variable for a) cations and b) anions. The free energy of the closest minimum to the surface for all ions is normalized to 0 $kJ \cdot mol^{-1}$.

Regarding the three defined characteristics, we consider the ion-water and surface-water interactions to control the adsorption barrier and the ion-surface interactions to control the desorption barrier. The adsorption energy is the difference between the two barriers and therefore, depends on all three types of interactions. Adsorption energies, as well as adsorption and desorption barriers for different ions, are shown in Figure 4.3, and later summarized in Table 4.2. In the following, we discuss results in the order of cations and anions in the close scenario and then, we compare the close and far scenarios for calcium and phosphate ions.

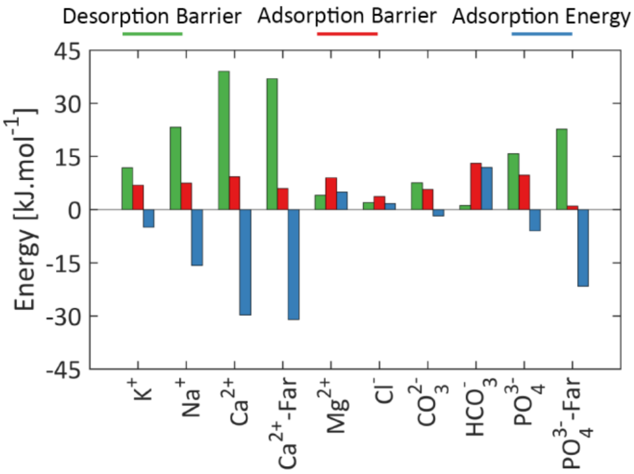

Figure 4.3 Adsorption energy, adsorption barrier and desorption barrier calculated for all the ions based on the free energy along the distance collective variable.

4.1.3.2.1 Cations in the close scenario

If we compare the adsorption barrier of ions with the same valence in Figure 4.3, the adsorption barrier of sodium is slightly larger than that of potassium; the smaller size of sodium and stronger interaction with its hydration shell make it more difficult for sodium to lose some of its coordinated water molecules and to adsorb on the surface.

However, the same is not true for calcium and magnesium. We observe that the adsorption barrier of magnesium is slightly smaller than that of calcium despite its smaller ionic radius. We can also see from Figure 4.2 that the distance of the closest energy minimum to the surface for magnesium is the largest among cations, which is interesting as it has the smallest ionic radius among the cations studied here. To understand the reason behind this behavior, we present the position of the closest minimum of the free energy along the distance CV to the surface, the ionic radius and the radius of the hydrated ion in Table 4.1.

Table 4.1 The position of the closest minimum of the free energy along the distance collective variable to the surface, ionic radii and hydrated ionic radii.

Ion	First minimum [Å]	Ionic radius [Å]	Hydrated ionic radius [Å]
K^+	1.83	1.38[a] 1.41 ± 0.08[b]	2.12[a]
Na^+	1.29	0.97 ± 0.06[b] 1.02[a]	2.28[a]
Ca^{2+}	2.22	1.00[a] 1.03 ± 0.05[b] 1.26[c]	2.71[a]
Ca^{2+}-Far	2.22		
Mg^{2+}	3.71	0.70 ± 0.04[b] 0.72[a] 0.86[c]	2.99[a]
Cl^-	2.92	1.67[c] 1.80 ± 0.07[b] 1.81[a]	2.24[a]
CO_3^{2-}	2.79	1.78[a]	2.54[a]
HCO_3^-	2.95	1.56[a]	2.15[a]
PO_4^{3-}	2.89	2.38[a]	2.92[a]
PO_4^{3-}-Far	2.93		

[a]Marcus[33], [b]Marcus[34], [c]Larentzos *et al.*[35]

We can determine the nature of ion adsorption on the surface (inner- or outer-sphere mode) in two ways. The first way is to compare the position of the first energy minimum of the ion with the un-hydrated and hydrated ionic radii (Table 4.1). We can consider the adsorption mode to be inner-sphere if the position of the first minimum of the free energy along the distance collective variable is close to the ionic radius and outer-sphere if it is closer to the hydrated ionic radius. This method has uncertainty due to the definition of the surface. We define the surface to be the average position of the oxygen atoms of the surface hydroxyls since the OH bonds of the hydroxyl groups do not stand perpendicular to the surface but are tilted due to interaction with their neighboring hydroxyl groups. Therefore, the first atomic layer of the surface might extend up to 1 Å (an $O-H$ bond) further than the defined position of the surface. Thus, we use another method to assure that the nature of ion adsorption on the surface is determined correctly. In the second method, we look at the water axial distribution in the surface normal direction (Figure C.1). Since the closest water layer to the surface is at a distance of 2.35 Å from the surface (Figure C.1), we consider the adsorption to be of inner-sphere mode if the position of the first minimum of the free energy along the distance collective variable is smaller than the first high-density water layer at 2.35 Å and outer-sphere, otherwise. Both these methods for determining the adsorption mode yield the same results, which is inner-sphere adsorption for potassium, sodium and calcium and outer-sphere adsorption for magnesium and thus, the delicacy of the definition of the surface is resolved.

Among the cations, only magnesium adsorbs on the surface in an outer-sphere fashion. This can also be seen in the variation of the coordination number of the ion (or the central atom for polyatomic ions) with respect to the water molecules in the adsorbed and solvated states (Figure C.7). For all cations, except magnesium, adsorption on the surface is accompanied by a reduction in the coordination number. However, for magnesium, no notable change in the number of water molecules can be observed when the ion approaches the surface (Figure C.7). The atomistic snapshots of cations in the inner-sphere mode are shown in Figure 4.4.

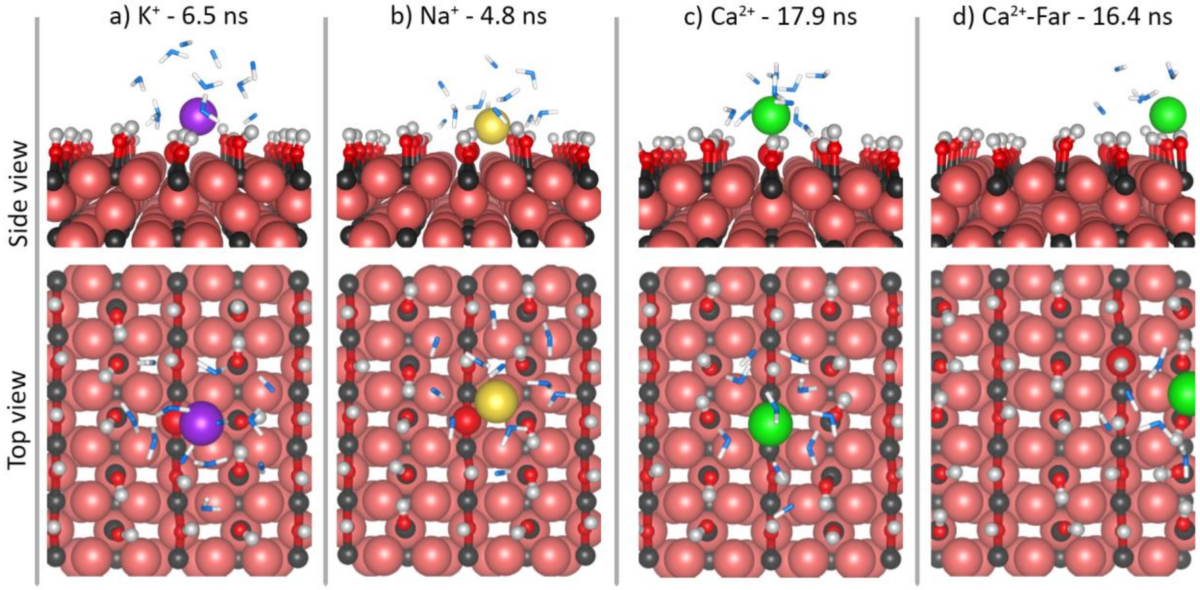

Figure 4.4 Atomic snapshots of a) K^+, b) Na^+ and c) Ca^{2+} and d) Ca^{2+}-Far in their inner-sphere adsorption mode on the surface. The un-protonated oxygen of the charge point in the close scenario and the protonated oxygen of the central hydroxyl in the far scenario are shown slightly larger compared to the oxygen atoms of the surface hydroxyl groups. Only water molecules closer than 5 Å to the cations are shown. Ti: grey, bulk rutile O: bright red, surface rutile O: red, water O: blue, H: white, K: purple, Na: yellow, Ca: green. Vesta[36] was used for visualization.

The outer-sphere adsorption mode of magnesium on rutile has already been reported; Wu *et al.*[32] performed MD simulations and reported that among Na^+, K^+, Rb^+, Ca^{2+}, Mg^{2+} and Sr^{2+}, magnesium always adsorbs on the surface in an outer-sphere fashion. They also tested the stability of the adsorption mode for magnesium. From the inner-sphere mode, the ion did not move to the outer-sphere mode. In the outer-sphere mode, the ion did not change its position either to the inner-sphere mode nor the solvated state in water. This confirms that the energy barrier, which the ion needs to cross to change its adsorption mode from outer-sphere to inner-sphere (or vice versa), has to be sizable.

We would like to emphasize here that our biased simulations were not able to force magnesium to adsorb in an inner-sphere mode (Figure C.7), within the simulated time frame. If we compare the adsorption behavior of calcium and magnesium, considering that both ions are interacting with the rutile (110) surface and, as mentioned before surface-water interactions are similar in both cases, we can conclude that ion-water and ion-surface interactions are the two that differentiate the adsorption behavior of these two ions. The fact that calcium adsorbs on the rutile surface via the inner-sphere adsorption mode may be due to either its lower solvation energy compared to magnesium (Table C.5), which makes it easier for the ion to escape its hydration shell or its higher affinity for the rutile surface.

The desorption barrier of cations increases in the order of Mg^{2+}, K^{+}, Na^{+} and Ca^{2+}. For magnesium, the outer-sphere adsorption mode and the strong coordination of the ion with water molecules weaken the electrostatic interactions between the charge point on the surface and the ion, and hence the smaller desorption barrier. For the other cations, we conclude that the affinity of the ion for the surface increases in the same order (of the increase in the desorption barrier). In fact, the difference between the adsorption barrier and desorption barrier (*i.e.,* adsorption energy) reveals that for all the cations, except magnesium, their interaction with the surface is more favorable than their interaction with water. The affinity of the magnesium ion for the surface is only sufficient to bring it close to the surface but is not strong enough to compensate the energy cost of losing the water molecules in the hydration shell of this ion.

4.1.3.2.2 Anions in the close scenario

Determining the adsorption mode in the free energy minimum for anionic species needs some explanation since except Cl^{-}, all anionic species are polyatomic ions. For chlorine, the free energy minimum in Table 4.1 is further than the first water layer and it is also larger than the radius of the hydrated ion, so we can conclude that the adsorption mode is the outer-sphere. The polyatomic anions are larger in size compared to monoatomic ions. For example, the size of the phosphate ion (2.38 Å) is larger than the distance of the closest water layer to the surface (2.35 Å); therefore, comparing the position of the first minimum in Table 4.1 with the position of the closest water layer to the surface, as it was done for cations, cannot be used as a way to determine the adsorption mode of the polyatomic anions. Thus, to decide the adsorption mode in the minimum free energy state for polyatomic anions, we compare the position of the first energy minimum with the radius of the hydrated ion. According to Table 4.1, all the anions are, in their free energy minimum, at a distance from the surface that is comparable to or larger than the radius of the hydrated ion, which means their adsorption mode is outer-sphere.

Based on Figure 4.3, we will discuss the adsorption energetics only for those anions, which show a favorable adsorption on the surface, *i.e.*, the ones which have a negative adsorption energy, which are carbonate and phosphate ions. For these anions, we observe that the adsorption barrier is larger for phosphate compared to carbonate. Since the adsorption mode for these ions is the outer-sphere mode, the ions are surrounded by water molecules in their adsorbed state. If we compare the radius of the hydrated ion and the distance of the first energy minimum in Table 4.1, we observe that the difference between these two values is 0.25 and 0.03 Å for carbonate and phosphate, respectively. This implies that the distance of the center of mass of the phosphate ion is at a distance from the surface equivalent to the radius of the hydrated ion; while the center of mass of carbonate is further from the surface, *i.e.*, phosphate has been able to displace more water molecules to approach the surface (but not those of its hydration shell) compared to carbonate. Consequently, we conclude that the larger adsorption barrier of phosphate is due to its adsorption closer to the surface compared to carbonate. Since this study is conducted close to a negative charge point, and repulsive electrostatic interactions exist between anions and the adsorption site, this behavior of phosphate reveals its higher affinity for the surface compared to carbonate. The desorption barrier shows a similar trend to the adsorption barrier. The adsorption of these two anionic species, as well as phosphate ion in the far scenario, on the surface is shown in Figure 4.5.

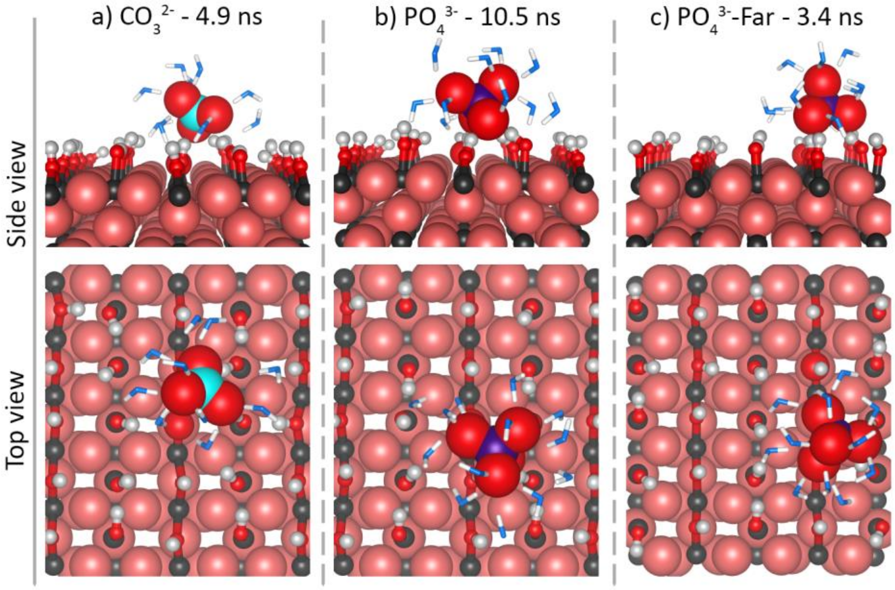

Figure 4.5 Atomic snapshots of those anions which show a favorable adsorption on the surface a) CO_3^{2-}, b) PO_4^{3-} as well as c) PO_4^{3-}-Far. The un-protonated oxygen of the charge point in the close scenario and the protonated oxygen of the central hydroxyl in the far scenario are shown slightly larger compared to the oxygen atoms of the surface hydroxyl groups. Only water molecules closer than 5 Å to the central atom of the polyatomic anions are shown. Ti: grey, bulk rutile O: bright red, surface rutile O and O_{ion}: red, water O: blue, H: white, C: turquoise, P: purple. Vesta[36] was used for visualization.

4.1.3.2.3 Comparison of close and far scenarios

In the far scenario, attractive or repulsive electrostatics between the ion and the oxygen of the central hydroxyl, around which we are studying the adsorption, are weaker. By comparing the energetics of adsorption far from the charge point (the far scenario) and close to it (the close scenario), we observe that adsorption of calcium is very similar in both cases (Figure 4.3). However, from Figure 4.1 one can observe that the Ca^{2+} adsorption site is further from the central hydroxyl in the far scenario than the charge point in the close scenario, which can also be seen in Figure 4.4c and d (top views). Since the adsorption of phosphate on the surface in the close scenario is energetically favorable, where the electrostatic repulsions are stronger, we can only expect its adsorption to become more favorable in the far scenario, which is the case.

4.1.3.3 Transition rate constants

We can use the transition state theory to obtain the rate constants for the adsorption and desorption events. The rate constants can be expressed in an Arrhenius form of $\kappa A \exp(-E_b/k_B T)$; where κ is the transmission coefficient, A is the pre-exponential attempt rate, $k_b$is the Boltzmann constant, T is the temperature and E_b is the activation energy for an event.[37,38] We assume a value of 1 for the transmission coefficient; we acknowledge that this assumption affects our results in the same way, and they are still comparable. The coefficient A is determined by the vibrational properties of the ion close to the surface and is typically in the range of 10^{13}-10^{14}

s^{-1}. To avoid ambiguities with the determination of this coefficient, since we are mainly interested in the order of magnitude of the rate constants, here we compare the rate constants for adsorption and desorption normalized by the coefficient A.

Adsorption and desorption barriers (explained in section 4.1.3.2) are summarized in Table 4.2. These values were used to obtain the rate constants of adsorption and desorption for different ions, normalized by A (Table 4.2); r/A is unit-less. For K^+, Na^+, Ca^{2+}, CO_3^{2-}, and PO_4^{3-}, the adsorption rate constant is larger than the desorption rate constant, which means that there will be a net amount of these ions on the surface. In addition to the apatite-forming ions, we see that K^+, Na^+ and CO_3^{2-} also have extended residence times on the surface. Therefore, compared to the proposed model for apatite formation on the alkali and heat treated sodium titanate surface,[9] we believe that sodium, potassium and carbonate could also affect apatite formation on the rutile surface. Other ions, although not stable on the surface, might also play an important role in the apatite formation as the surface composition is constantly modified by their rapid adsorption and desorption on the surface.

We want to underline that the adsorption and desorption barriers, which we have computed cannot directly be used in the case of *in vitro* testing; in our calculations, we only consider one kind of ion in each system while *in vitro*, several types of ions and many ionic complexes (although usually low in concentration – Table C.2) are present in the solution. The adsorption behavior of ionic complexes could be significantly different from that of a free ion, which is not taken into account here. Thermodynamic modelling, as one of the avenues to understand the formation of ionic complexes in the SBF solution and to study their affinity for the surface, will hence be needed to better understand the apatite formation on the surface more comprehensively. Moreover, the concentration of some ions, in specific sodium and chlorine, in blood plasma or SBF, is much higher compared to the others; this should be considered along with the transition rate of adsorption and desorption events to determine how much different ions control or affect the apatite formation on the surface.

Table 4.2 Adsorption and desorption barriers and the transition rate constants normalized by A.

Ion	Adsorption barrier $[kJ \cdot mol^{-1}]$	$\left({}^{r_{Adsorption}}/_{A}\right)$	Desorption barrier $[kJ \cdot mol^{-1}]$	$\left({}^{r_{Desorption}}/_{A}\right)$
K^+	6.87	7.0 * 10^{-2}	11.85	1.0 * 10^{-2}
Na^+	7.53	5.4 * 10^{-2}	23.30	1.2 * 10^{-4}
Ca^{2+}	9.29	2.7 * 10^{-2}	39.03	2.6 * 10^{-7}
Mg^{2+}	9.02	3.0 * 10^{-2}	4.06	2.1 * 10^{-1}
Cl^-	3.74	2.3 * 10^{-1}	1.99	4.6 * 10^{-1}
CO_3^{2-}	5.76	1.1 * 10^{-1}	7.56	5.3 * 10^{-2}
HCO_3^-	13.13	6.1 * 10^{-3}	1.21	6.3 * 10^{-1}
PO_4^{3-}	9.79	2.2 * 10^{-2}	15.75	* 10^{-3}

4.1.4 Conclusion

In this study, we use well-tempered metadynamics to study the adsorption behavior of several ions, present in the simulated body fluid solution, close to a negative charge point on the rutile (110) surface, as well as far from the charge point. Three characteristics (adsorption barrier, desorption barrier and adsorption energy) are extracted for all ions from their free energy profile as a function of the distance of the ion from the surface. Among the cations, only magnesium adsorbs in an outer-sphere mode while the other cations adsorb inner-sphere. This is because the solvation of magnesium in water is very favorable and it is very difficult for the ion to escape its hydration shell. Calcium only has a slightly smaller water affinity, compared to magnesium, but due to its very favorable interaction with the surface, it adsorbs in the inner-sphere mode. All anions adsorb in an outer-sphere mode; carbonate and phosphate having an energetically favorable adsorption on the surface.

For calcium and phosphate, we also study the adsorption when far from the charge point on the surface. The reduced attractive and repulsive electrostatic interactions between the ions and the surface, in the far compared to the close scenario, are directly reflected in the decreased and increased adsorption strength for calcium and phosphate, respectively. These two ions, specifically, show a high affinity for the surface, which is not merely driven by electrostatic interactions.

While all our simulations were carried out in very simplified conditions, where all ions were studied individually, we used the adsorption and desorption barriers to gain insights into the surface composition. Since the adsorption transition rate constants for Na^+, K^+, Ca^{2+}, CO_3^{2-} and PO_4^{3-} are larger than their desorption rate constants, these ions should primarily be involved in the apatite formation model on the rutile surface. The high desorption rate constant of other ions points out that the composition of the surface is constantly changing, which implies that these ions should also be considered in the proposed models for apatite formation.

This work is a very simplified model of the experimental condition of *in vitro*; nevertheless, this is an essential step in verifying the current models on apatite formation. Future work will be based on increasing the complexity of the system by considering additional ionic species and complexes in the system as well as studying the adsorption behavior of ions on a surface, which has already been exposed to the SBF solution and thus, its composition has been modified by prior adsorption events, to some extent.

Supplementary material

See Appendix C for the thermodynamic modelling on SBF, water distribution close to the surface, force field parameters and re-parametrization for polyatomic anions, schematic of the simulation box, hills height, and sampling space explored by the collective variables.

References

1. T. Kokubo, H. Takadama, Biomaterials. **27**, 2907 (2006).
2. N. L. D’Elia, N. Gravina, J. M. Ruso, J. L. Marco-brown, J. M. Sieben, P. V. Messina, J. Colloid Interface Sci. **494**, 345 (2017).
3. M. Svetina, L. Colombi Ciacchi, O. Sbaizero, S. Meriani, A. De Vita, Acta Mater. **49**, 2169 (2001).
4. M. Bohner, J. Lemaitre, Biomaterials. **30**, 2175 (2009).
5. A. Oyane, H.-M. Kim, T. Furuya, T. Kokubo, T. Miyazaki, T. Nakamura, J. Biomed. Mater. Res. **65A**, 188 (2003).

6. T. Kokubo, S. Yamaguchi, Acta Biomater. **44**, 16 (2016).

7. ISO 23317. Implants for surgery – *In Vitro* Evaluation for Apatite-forming Ability of Implant Materials. (2007).

8. W. Zhao, J. Lemaitre, P. Bowen, Acta Biomater. **53**, 506 (2017).

9. H.-M. Kim, T. Himeno, M. Kawashita, J.-H. Lee, T. Kokubo, T. Nakamura, J. Biomed. Mater. Res. A **67A**, 1305 (2003).

10. X. Liu, P. Chu, C. Ding, Mater. Sci. Eng. R. **47**, 49 (2004).

11. P. Zhu, Y. Masuda, K. Koumoto, Biomaterials. **25**, 3915 (2004).

12. T. Kokubo, Acta Mater. **46**, 2519 (1998).

13. H. Takadama, H. M. Kim, T. Kokubo, T. Nakamura, J. Biomed. Mater. Res. **57**, 441 (2001).

14. U. Diebold, Surf. Sci. Rep. **48**, 53 (2003).

15. M. L. Machesky, D. J. Wesolowski, D. A. Palmer, M. K. Ridley, P. Bénézeth, S. N. Lvov, M. V. Fedkin, Interface Sci. Technol. **11**, 324 (2006).

16. K. Takahashi, F. Satoshi, Biocontrol Sci. **13**, 9 (2008).

17. A. YazdanYar, U. Aschauer, P. Bowen, J. Phys. Chem. C. **122**, 11355 (2018).

18. M. Predota, A. V. Bandura, P. T. Cummings, J. D. Kubicki, D. J. Wesolowski, A. A. Chialvo, M. L. Machesky, J. Phys. Chem. B **108**, 12049 (2004).

19. H. J. C. Berendsen, J. R. Grigera, T. P. Straatsma, J. Phys. Chem. **91**, 6269 (1987).

20. L. X. Dang, J. Am. Chem. Soc. **117**, 6954 (1995).

21. M. Predota, Z. Zhang, P. Fenter, D. J. Wesolowski, P. T. Cummings, J. Phys. Chem. B **108**, 12061 (2004).

22. S. Gavryushov, J. Phys. Chem. B **113**, 2160 (2009).

23. N. H. de Leeuw, J. R. Bowe, J. A. Rabone, L. Faraday Discuss. **134**, 195 (2007).

24. N. H. de Leeuw, Phys. Chem. Chem. Phys. **6**, 1860 (2004).

25. C. Lindahl, P. Borchardt, J. Lausmaa, W. Xia, H. J. Engqvist, Mater. Sci. Mater. Med. **21**, 2743 (2010).

26. A. Barducci, G. Bussi, M. Parrinello, Phys. Rev. Lett. **100**, 020603 (2008).

27. W. Smith, T. R. Forester, I. T. Todorov, The DL_POLY Classic User Manual. SFTC Daresbury Laboratory. (2012).

28. G. A. Tribello, M. Bonomi, D. Branduardi, C. Camilloni, G. Bussio, Comput. Phys. Commun. **185**, 604 (2014).

29. P. Giannozzi, S. Baroni, N. Bonini, M. Calandra, R. Car, C. Cavazzoni, D. Ceresoli, G. L. Chiarotti, M. Cococcioni, I. Dabo, A. D. Corso, S. de Gironcoli, S. Fabris, G. Fratesi, R. Gebauer, U. Gerstmann, C. Gougoussis, A. Kokalj, M. Lazzeri, L. Martin-Samos, N. Marzari, F. Mauri, R. Mazzarello, S. Paolini, A. Pasquarello, L. Paulatto, C. Sbraccia, S. Scandolo, G. Sclauzero, A. P. Seitsonen, A. Smogunov, P. Umari, R. M. Wentzcovitch, J. Phys. Condens. Matter. **21**, 395502 (2009).

30. S. Galmarini, P. Bowen, Cem. Concr. Res. **81**, 16 (2016).

31. F. David, V. Vokhminz, G. Ionova, J. Mol. Liq. **90**, 45 (2001).

32. C. Wu, A. A. Skelton, M. Chen, L. Vlček, P.T. Cummings, Langmuir **28**, 2799 (2012).

33. Y. Marcus, J. Chem. Soc. Faraday Trans. **87**, 2995 (1991).

34. Y. Marcus, J. Solution Chem. **88**, 1475 (1988).

35. J. P. Larentzos, L. J. Criscenti, J. Phys. Chem. B **112**, 14243 (2008).

36. K. Momma, F. Izumi, VESTA: A Three-Dimensional Visualization System for Electronic and Structural Analysis. (2014).

37. P. Hanggi, P. Talkner, M. Borkovec, Rev. Mod. Phys. **62**, 251 (1990).

38. K. J. Laidler, M. C. King, J. Phys. Chem. **87**, 2657 (1983).

4.1.5 Outlook and reservations

Despite the analyses and discussions made earlier in section 4.1, this study can be improved upon in several aspects. Also, certain points should be investigated in more detail before publishing the presented results. In the following, some of these points are listed.

4.1.5.1 Improvement of simulation setup and settings

- With the available computational facilities and the simulation code used, every half nano-second of simulation time took one day of wall time. One effective way to accelerate the computation is to reduce the thickness of the water layer. As it can be seen in Figure C.1, bulk water density is recovered at a distance of 20 Å from the surface, while the orientation of water molecules reverts to its random distribution at a distance smaller than 50 Å from the surface. Therefore, a smaller thickness for water (50 Å) is suggested.

- As this study includes ions with different valences, a different number of counterions is necessary for each system to neutralize the overall charge of the simulation box. Since the type of the counterion (sodium for anions and chlorine for cations, for example) and their number affect the final free energy profile in a complex manner, it was decided not to neutralize the simulation boxes, explicitly. However, it seems that the non-zero explicit charge in the simulation box has affected the behavior of ions. As the ions move away from the surface, the free energy profile should converge and become approximately flat. However, convergence is hardly achieved in the free energy profile for a few ions in Figure 4.2, *e.g.*, sodium and calcium. Thus, it is essential to address this issue and try the tests in neutralized boxes to see whether the convergence of the free energy profiles can be achieved.

- The collective variables can be modified. In Figure 4.1, the ions seem to approach the surface once in small radius CV (<2 Å) and once in larger radius CV (>2 Å). When the free energy profile is projected along the distance CV, the free energy regions for radius CV < 2 Å and > 2 Å are added to each other. Since the free energy of adsorption in these two cases are different, when they are added to each other, they lead to double energy minima, which can be seen for example, in case of sodium and calcium (Figure 4.2). In section 4.2 the radius CV is limited to 1.5 Å, and the free energy profile, before and after projection along the distance CV, is smoother; therefore, a smaller radius CV can be used, but this should be tested carefully to make sure that the dynamics of the ion are not unexpectedly modified.

The radius CV was used to identify the adsorption site of ions around the charge point. However, all ions showed a similar trend, where cations adsorbed in the space between the charge point, one bridging hydroxyl and two terminal hydroxyl groups, and anions further away, close to the upper limit of the radius CV. Therefore, using a single collective variable (the distance CV, in specific) can be just as fine.

- As explained in Chapter 3, a bias factor of γ in well-tempered metadynamics simulations samples the CVs in the effective temperature of $\gamma \cdot T$, where T is the temperature input for the simulation. Here, a bias factor of 15 was used, which compared to the common practice (5 - 10) is larger. The use of smaller bias factors and their effect on the final free energy profile should be considered.

4.1.5.2 Further studies

- Similar to phosphate, force field parameters were also modified, based on previous work, to be able to model to cross-interactions between hydrogen phosphate and rutile. Very recently, an extensive effort was made to develop force field parameters for some phosphate species (phosphate, hydrogen phosphate and dihydrogen phosphate) based on *ab initio* QM calculations (2). The comparison of the modified parameters with those reported by Demichelis *et al.* (2) showed that the interactions between the hydrogen of water and hydrogen phosphate are not properly captured, because in the modified parameters, no such interactions were considered. Therefore, results relevant to hydrogen phosphate are not presented in this section but also not in the next chapters. However, results should be tested to understand to what extent the $HW - HPO_4^{2-}$ interaction is important in governing the overall adsorption behaviour of hydrogen phosphate on the surface and whether results are valid to some extent or not. Also, the modified force field parameters developed in this thesis should be compared with the recently developed parameters and the performance of the force field should be verified. Considering the high probability distribution of HPO_4^{2-} and $H_2PO_4^{-}$ species (Table C.2), it is very interesting also to include these species in the study performed in section 4.1. Cross-term interaction parameters of these species with rutile, though, are missing and should be developed.
- The solvation behavior of ions, and how well this is reproduced via the simulation, significantly affects the accuracy of the results. Currently, the solvation energy of ions in water is calculated, with rather a simplistic approach, in Table C.5. Although values obtained are relatively comparable to those previously reported in the literature, the solvation energy should be re-calculated to assure the accuracy of the force field in reproducing the ionic behavior in the solution.
- The transition state theory in section 4.1.3.3 is used to compare the adsorption/desorption kinetics of different ions. As explained in this section, the rate constant depends on the pre-factor A which has various definitions and is difficult to be estimated for different species. Therefore, results were presented normalized by this pre-factor, to avoid further complications.

  A very rough estimation of A can be using the Hertz-Knudsen equation – this equation is for the gas phase, and here the displacement of water from the adsorption site is neglected. This equation states that sticking of a gas molecule on a surface is proportional to $1/\sqrt{m}$ where m is the mass of the atom. If one compares

$1/\sqrt{m}$ for the lightest (Na^+) and heaviest ion (PO_4^{3-}) among the ions, $1/\sqrt{m}$ has a value of 0.213 and 0.102, respectively. Even though this is a very rough analogy, one can say that the largest difference between the prefactors of studied ions can be a factor of 2, and still would not affect the discussion made in this section. Nevertheless, as mentioned, this is a very rough analogy and it would be much better if the pre-factor for each ion is estimated.

4.2 Interaction of sodium and calcium ions with two charge points on the rutile (110) surface

To compare the effect of the surface charge density on the adsorption energetics of single ions on the surface, the adsorption of sodium and calcium ions was studied on the rutile (110) surface with two charge points on the surface. The surface charge density, in this case, is -0.024 $C \cdot m^{-2}$.

4.2.1 Approach

The simulations carried out in this section are similar to those in section 4.1.2 in many aspects. Here, the similarities are mentioned and the differences are explained.

Similarities

- Simulation box dimensions and the thickness of the rutile slab, water and vacuum gap
- Constraining the rutile slab atomic species except for the surface hydroxyl groups
- Periodic boundary conditions and implementation of the Ewald summation
- Force field set and its cutoff
- Integration algorithm and the timestep
- The Nosé-Hoover thermostat in the NVT ensemble at 310 K
- Collective variables used in WT-MTD and the parameters used for upper walls limiting the collective variables
- The width, height and frequency of deposition of Gaussians in WT-MTD

Differences

- There were two de-protonated oxygens (from bridging hydroxyls) on the surface, which led to a surface charge density of -0.024 $C \cdot m^{-2}$ on the surface. The two charge points on the surface are positioned next to each other (Figure 4.6).
- The partial charge of the atomic species of rutile for this charge density was obtained using the procedure explained in D.2. The values can be seen in Table 4.3.
- Here, the simulation box was maintained charge neutral. Therefore, for the system containing sodium, two sodium ions were considered in the simulation box while for the system containing calcium, only one cation

was considered in the box. In the former box, to avoid interaction between both sodium ions with the surface, one of the sodium ions was kept restrained at a distance of 50 Å from the surface over the total simulation time. All collective variables were applied to the other sodium ion. This sodium ion and the calcium ion were initially put at a distance of 5 Å from the rutile surface.

- The distance CV was defined as the perpendicular distance of the ion from the rutile surface. Similar to the section 4.1.2.3, the surface was considered as the average position of the oxygen atoms of the hydroxyl groups on the surface and the distance CV was limited to a distance of 20 Å from the surface.
- The radius CV was defined as the in-plane distance of the ion from a virtual point, which was the center of mass of the two charge points on the surface. This CV was limited to a very narrow upper wall at 1.5 Å around the virtual point (Figure 4.6). It should be noted that this value for the radius CV is too small and it may prevent possible adsorption sites.
- Both systems were first equilibrated for 175 ps during which the ions were kept fixed. Afterwards, the ions were unrestrained and the production step was performed for 25 ns.

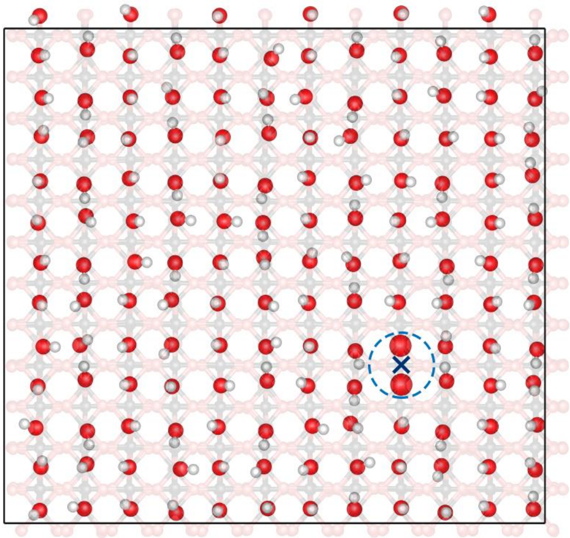

Figure 4.6 Schematic of the surface – top view. Atoms in the bulk of rutile are shown transparent and only the surface hydroxyl groups and charge points are visible (O: red, H: white). The two de-protonated oxygens are shown slightly larger. They are positioned next to each other. The radius CV is restrained around the center of mass of these two oxygens (shown by the blue cross) to a distance of 1.5 Å (shown by the dashed circle).

Table 4.3 Charge distribution of rutile variable-charge species for a surface charge density of -0.024 $C \cdot m^{-2}$.

Atomic species	TS	OT	HT	OB	HB	OS
Partial charge $[e]$	2.1524	-0.9394	0.4306	-0.9630	0.4542	-1.0179

TS: Ti atoms bound to the hydroxyl groups.
OT and OB: oxygen of terminal and bridging hydroxyl groups, respectively; HT and HB: their hydrogen atoms.
OS: de-protonated oxygen atoms from the hydroxyl groups.
See section 3.8.1.1 for the explanation of atomic labels.

4.2.2 Results and discussion

The water density, in the direction normal to the surface, was very similar to Figure C.1a. The 2D free energy profiles are shown in Figure 4.7. Compared to Figure 4.1, it can be seen that restraining the phase space, which the ions can explore in the direction of the radius CV to 1.5 Å, narrows down the free energy profile.

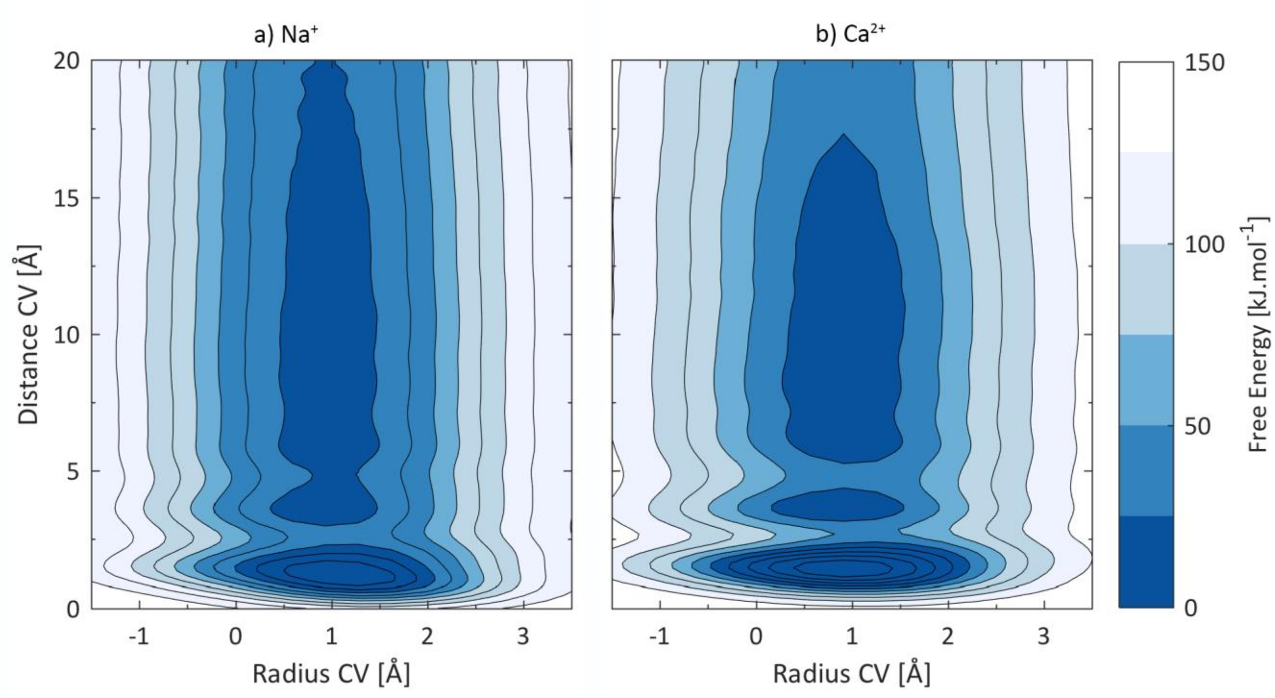

Figure 4.7 Free energy profile as a function of radius and distance CVs for the interaction of a) sodium and b) calcium ions with the rutile surface with a surface charge density of -0.024 $C \cdot m^{-2}$.

The free energy along the distance CV can be seen in Figure 4.8a for adsorption of both ions on the surface. The general form of the free energy profile for the adsorption of sodium and calcium ions on a surface with two charge points (Figure 4.8a) is very similar to that of the surface with one charge point (Figure 4.2 – replotted here with dashed line). However, the free energy difference between the adsorbed state and the solvated state is much larger on the surface with two charge points compared to that with only one charge point. This can be seen in Figure 4.8b, where the adsorption/desorption barriers and adsorption energy are summarized and can be compared with results already obtained in section 4.1.3.2 (shown by dashed lines in this figure). These parameters are defined the same as those previously described in section 4.1.3.2 and are shown schematically in Figure 4.9. Similar to the surface with a smaller charge density, the adsorption of calcium on the surface is more favorable than the adsorption of sodium.

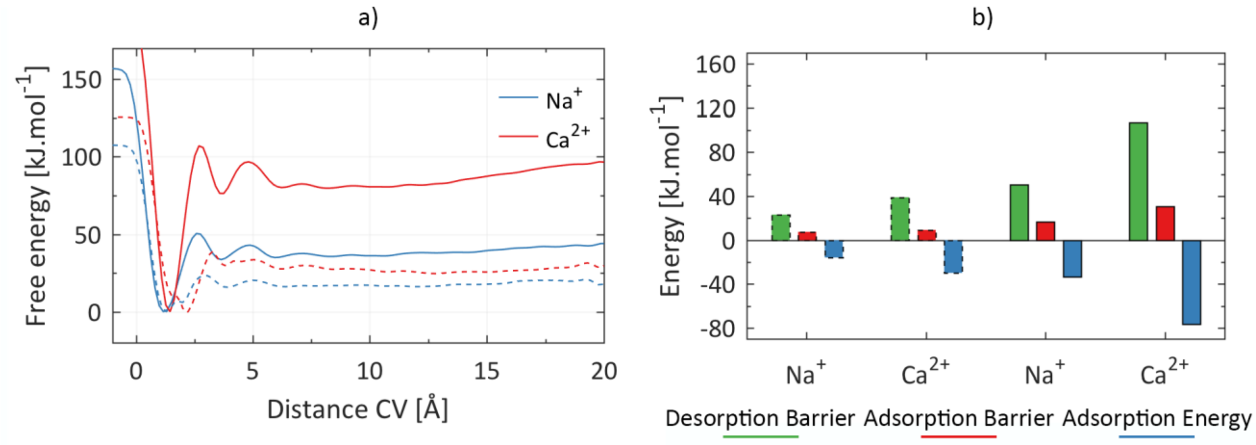

Figure 4.8 a) Free energy profile of ions adsorption and desorption on the rutile surface with two charge points and b) energy parameters defined similarly to those in section 4.1.3.2 and explained in Figure 4.9. The dashed lines show results previously obtained in section 4.1.3.2, for the surface with a single charge point. The solid lines are for the present section, where the interaction is with two charge points on the surface.

The distance of the global minimum energy at Figure 4.8a from the surface is 1.16 and 1.45 Å for sodium and calcium ions, respectively, which implies inner-sphere adsorption for both cations again. In comparison with Table 4.1, it can be seen that the position of the first minimum in the free energy profile along the distance CV is now closer to the surface where the absolute surface charge density is larger; the reason being the stronger electrostatic interactions between the ions and the two charge points on the surface.

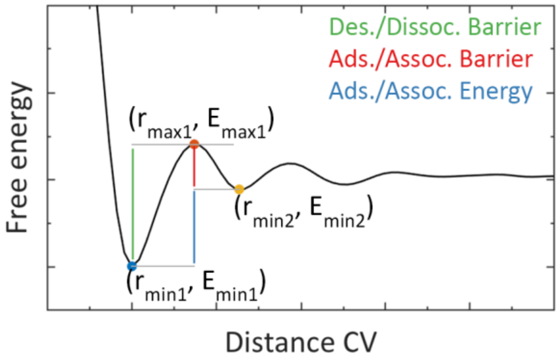

Figure 4.9 Schematic representation of defined parameters as (desorption or dissociation) barrier, (adsorption or association) barrier and (adsorption or association) energy. Adsorption and desorption are used for describing the interaction of an ion with a surface while association and dissociation are used to discuss the formation of ionic pairs, as discussed in section 4.3.

4.2.3 Conclusion

Experimentally, it has been shown that a negative charge on the surface, promotes hydroxyapatite nucleation since it leads to a higher accumulation of the calcium ions on the surface, which itself increases the supersaturation of the solution close to the surface (3). Comparison of sections 4.1 and 4.2 reveals that electrostatic interactions between ions and the rutile surface directly control the adsorption behavior of ions. As expected, a larger surface charge density leads to stronger attractive forces between cations and the surface. Therefore, under physiological conditions, where the absolute values of rutile surface charge density are much larger than those studied in sections 4.1 and 4.2, favorable adsorptions will become more favorable and unfavorable ones will become even more unfavorable. Revisiting Figure 4.3 and adsorption/desorption rates in Table 4.2, the modification of surface compositions by those ions which have a transient adsorption on the surface with a single charge point (magnesium, chlorine and bicarbonate) will be much less frequent on the surface with a higher charge density and contribution of other ions, potassium, sodium and calcium, in specific, with favorable adsorption energetics to apatite formation will be more.

4.3 Formation of ionic pairs

Thermodynamic modelling, as shown in Table C.2, reveals that many ionic pairs are present in an SBF solution. Among all the possible ionic pairs, which one can study, three ionic pairs were chosen. First, the $[CaPO_4]^-$ pair was chosen as it contains the main building blocks of HAp; Ca^{2+} and PO_4^{3-}. In fact, HAp is speculated to form from amorphous calcium phosphate, which itself forms from Posner's clusters ($Ca_9(PO_4)_6$) (4,5). Figure 4.10 shows the unit cell of hydroxyapatite (HAp - $Ca_{10}(PO_4)_6(OH)_2$ - $Ca/P \sim 1.66$), as well as Posner's clusters, which can be defined in the structure of HAp. These concepts are discussed in more detail at the end of this chapter (section 4.5).

The second chosen ionic pair was $[NaCl]^0$ since Na^+ and Cl^- are the most abundant ions in the SBF (and human blood plasma - Table C.1). Therefore, although chlorine does not show a strong affinity for the rutile surface (Figure 4.3), its high concentration in the solution can control the events, which occur in the interface of rutile and solution. The third ionic pair was chosen to be $[CaHCO_3]^+$ since among the ionic pairs, which form between Ca^{2+} and other anions, this pair has the next highest probability after $[CaHPO_4]^0$; since $[CaPO_4]^-$ is already chosen, the calcium-bicarbonate seems more interesting than calcium-hydrogen phosphate. In this section, the association and dissociation of these ionic pairs are studied.

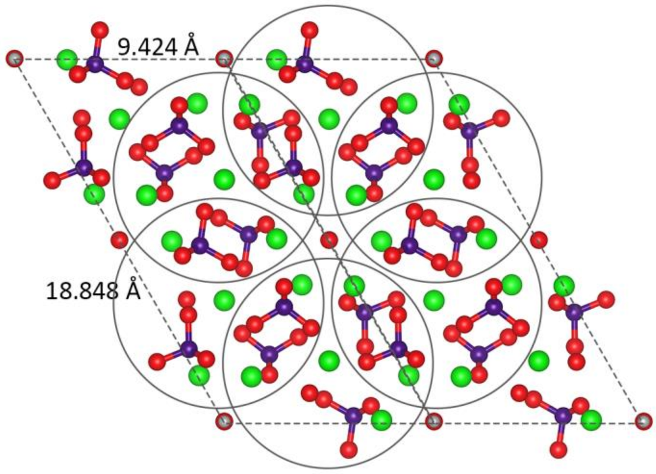

Figure 4.10 Top view of the unit cell of hydroxyapatite (dashed line). Posner's clusters ($Ca_9(PO_4)_6$) are shown via circles. Ca: green, P: Purple, O: red and H: white.

4.3.1 Approach

To study the free energy of formation of an ionic pair in water, well-tempered metadynamics simulations were performed. All the simulations were performed at 310 K in a box of water, which contained one type of cation and one type of anion. Gaussians with an initial height of 1.0 $kJ \cdot mol^{-1}$ and a bias factor of 15 were deposited every 2,000 steps. Details of the simulation box for different ionic pairs are presented in Table 4.4.

Table 4.4 Simulation details for studying the formation of ionic pairs.

Ionic pair	Box dimension [$Å^3$]	Timestep [fs]	Cutoff [Å]	t_{Total} [ns]	CV type
$[NaCl]^0$	24×24×24	0.7	12	10	Distance
$[CaPO_4]^-$	20×20×20	0.7	9	100	Distance and angle
$[CaHCO_3]^+$	20×20×20	0.6	9	60	Distance, angle and height

Various collective variables were used depending on the complexity of the ionic pair which were to form. For the $[NaCl]^0$ ionic pair, only the distance between the two ions was used as the collective variable (distance CV). An upper wall limited the ions to explore distances further than 7 Å from each other.

For the $[CaPO_4]^-$ ionic pair, in addition to the distance CV (between the calcium atom and the phosphorous atom and limited to 7 Å), an angle CV was defined between calcium, phosphorus and one of the oxygens of the phosphate anion (O^*), as shown in Figure 4.11a.

Consideration of the distance and angle CVs for the ionic pair of $[CaHCO_3]^+$ proved to be insufficient. Further investigations revealed that this is due to the planar structure of the bicarbonate ion. As in this case, a cation around the carbon atom will not show any significant affinity for it unless it is close or inside the plane of the bicarbonate anion. Consequently, for this pair, three collective variables were used (Figure 4.11b):

- Radius CV: The in-plane distance of calcium from the carbon atom, limited to 4 Å
- Angle CV: The angle between calcium, carbon and the protonated oxygen (O^*) of bicarbonate, spanning π
- Height CV: The perpendicular distance of calcium from the plane of the anion, limited to 5 Å

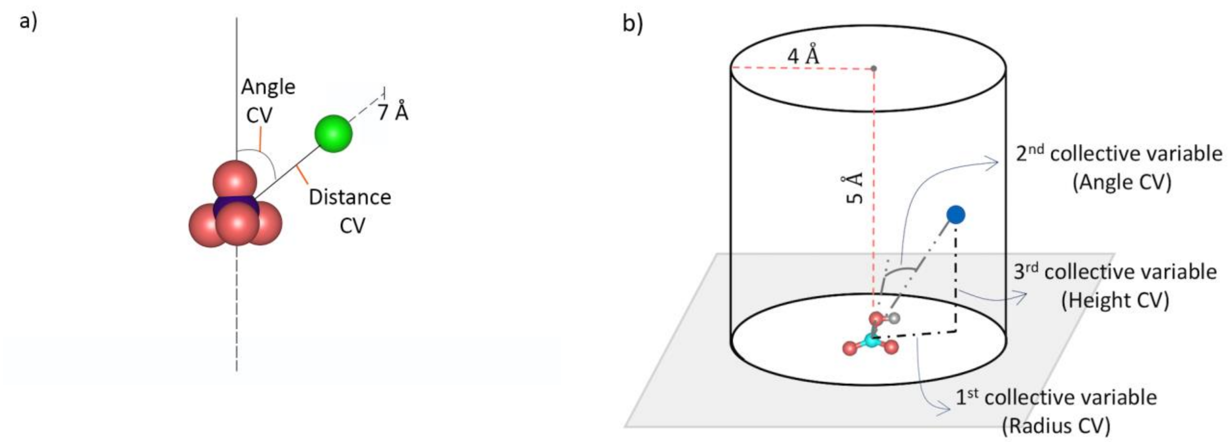

Figure 4.11 Collective variables used for studying the formation of a) $[CaPO_4]^-$ and b) $[CaHCO_3]^+$ pairs.

For all the ionic pairs, the width of the Gaussians for distance-based CVs was 0.5 Å and for angle-based CVs, it was 0.2 R (=11.46°).

4.3.2 Results and discussion

Similar to the parameters defined in section 4.1.3.2, here the difference in the free energy of the first energy minimum and the first energy maximum is considered as the dissociation barrier, the difference between the first energy maximum and second energy minimum as the association barrier and the difference between the first and second energy minima as the association energy. These parameters were explained schematically in Figure 4.9 and will be summarized in Table 4.5 for the three ionic pairs.

Based on the number of collective variables, which were used in the metadynamics simulations, the free energy landscape obtained for the formation of ionic pairs is 1D, 2D or 3D. The free energy profile of $[NaCl]^0$ formation is 1D and is shown in Figure 4.12. The equilibrium distance between sodium and chlorine in the ionic pair is 3.03 Å. Before reaching this minimum energy point, the ions have to cross an energy barrier of 12.21 $kJ \cdot mol^{-1}$ at a distance of 3.74 Å from each other. The associated state of the ions is more favorable than the dissociated state with an energy difference of -3.23 $kJ \cdot mol^{-1}$ (Table 4.5).

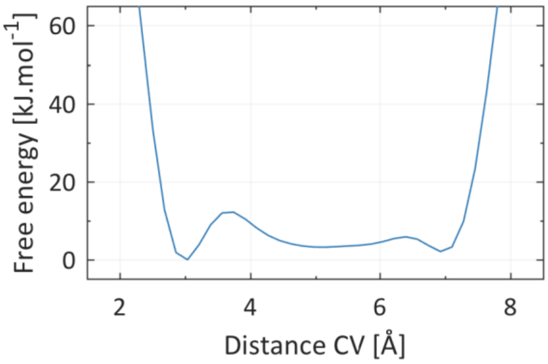

Figure 4.12 Free energy of the $[NaCl]^0$ ionic pair formation.

The angle-based collective variables control the favorable pathways for the cation to approach the anion. For the calcium-phosphate pair, the 2D free energy profile for the formation of this ionic pair is shown in Figure 4.13a. The phosphorous atom in the phosphate ion is surrounded by four oxygen atoms, where the $O-P-O$ angles are similar ($\sim$ 109.5°). The symmetrical geometry of phosphate (Figure 4.11a) dictates the most favorable coordination of the calcium ion with phosphate to be when the cation is shared between three oxygens.

The angle CV is the $Ca-P-O^*$ angle, O^* one of the oxygen atoms of phosphate. In Figure 4.13a, the angle CV affects the free energy profile mainly in three regions. For values less than 45°, the association of the ions is not favorable, the reason being calcium is mainly coordinated with a single oxygen (O^*). For values between 45 to 80°, the association seems the most favorable as in this region, the calcium ion is coordinated with three oxygen atoms. For the values larger than 80°, the calcium ion is coordinated with two oxygen atoms and as it can be seen the free energy is more favorable than when calcium is coordinated with only O^*, but less favorable than when it is coordinated with three oxygen atoms. If one assumes that calcium is approaching the phosphate ion along the most favorable pathway (being coordinated with three oxygens), the free energy can be estimated as a function of the distance of the ions. Consequently, the free energy profile was projected along the distance CV for the range of 45 to 80° of the angle CV, and then averaged (Figure 4.13b). In this figure, the projection of the free energy along the distance CV in the entire range of the angle CV is also shown by the dashed line for the sake of comparison. As it can be seen, the equilibrium distance of calcium and phosphorus in the ionic pair is 2.71 Å. The averaged free energy profile, in the range of 45 to 80° of the angle CV, shows an energy barrier of 4.50 $kJ \cdot mol^{-1}$. The energy difference between the associated and dissociated states is notable (49.28 $kJ \cdot mol^{-1}$). Compared to $[NaCl]^0$ with the association energy of -3.23 $kJ \cdot mol^{-1}$, the formation of $[CaPO_4]^-$ is much more energetically favorable.

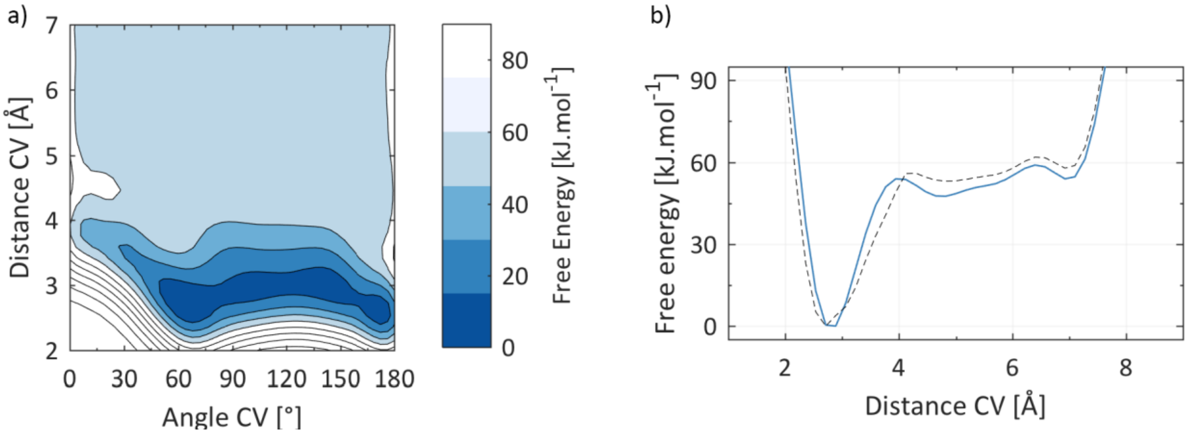

Figure 4.13 Free energy profile of interaction of calcium with phosphate a) in the 2D phase space and b) projected along the distance CV; blue line is for the angle CV range of 45-80 ° and the dashed line is for the full range of the angle CV.

As explained before, for the formation of $[CaHCO_3]^+$, due to the planar structure of bicarbonate, it is essential to consider a third collective variable in addition to distance and angle CVs. Thus, the free energy profile becomes 3D. However, it is difficult to discuss the free energy as a function of all three collective variables; consequently, first, the free energy profile in the 3D space was carefully examined and then two pathways, via which the cation may approach the anion, were chosen and will be discussed in the following.

In the first pathway, the free energy profile was examined, for a constant value of height CV of 0.13 Å (approximately in the plane of the bicarbonate ion). For this value, the free energy was plotted as a function of the radius CV, for each value of the angle CV, as shown in Figure 4.14. The free energy profiles are shifted downward for the sake of clarity.

Among the three oxygen atoms in the bicarbonate ion, the protonated oxygen (O^*), with which the angle CV is also defined (Figure 4.11), is less electronegative than the other two oxygen atoms (O). Therefore, it is expected that calcium will be in a lower energy state when it is positioned between the two oxygen atoms, compared to when it is shared between one of the oxygens and the protonated oxygen. The $O^* - C - O$ angle, based on force field parameters, is 113.9°. This is also reflected in Figure 4.14, where a local minimum in the free energy starts to form for angles larger than ~113°; *i.e.*, when calcium is positioned between the two un-protonated oxygens. This local energy minimum is at an equilibrium distance of calcium and carbon of 2.92 Å. To reach this equilibrium distance, calcium has to cross an energy barrier at a distance of 3.44 Å. The free energy between these two points, or the dissociation barrier, was calculated for each angle and averaged to be 15.8 $\pm$ 5.4 $kJ \cdot mol^{-1}$. Since at large radius CVs, the free energy does not entirely converge, probably due to the small upper limit for the radius CV, it is very difficult to estimate the association energy (the difference between the associated and dissociated states). However, it can be mentioned that largest difference between the free energy at the equilibrium distance of 2.92 Å and 3.96 Å is -7.11 $kJ \cdot mol^{-1}$.

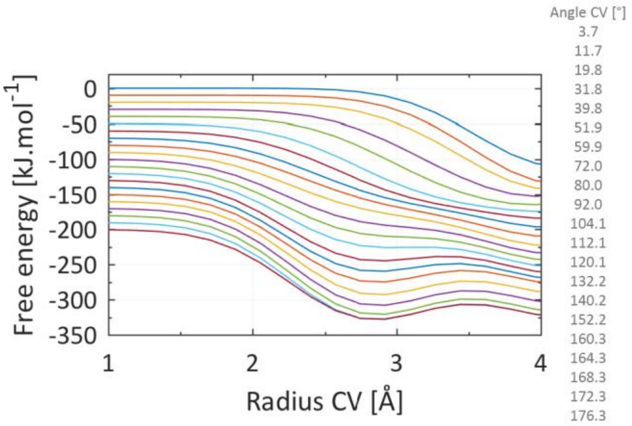

Figure 4.14 Free energy profile as a function of the radius CV, for different values of angle CV and h = 0.13 Å. From top to bottom the value of angle CV for each curve is written on the right. The free energy profiles are shifted downward for the sake of clarity.

The second chosen pathway was for a constant value of the radius CV at 2.92 Å, which is the equilibrium distance of calcium and carbonate in the ionic pair, based on above discussion. For this value, free energy was plotted for each angle CV, as a function of the height CV (Figure 4.15); again the free energy profiles are shifted downward. As it can be seen in this figure, for many values of the angle CV, there is no significant dependence of free energy to the height CV. Similar to what was observed just before, the dependence of the free energy on the height CV appears for angles larger than ~113°. For these angles, there is a notable decrease in the free energy as the cation approaches the plane of the anion, on average 125.01 $\pm$ 20.43 $kJ \cdot mol^{-1}$.

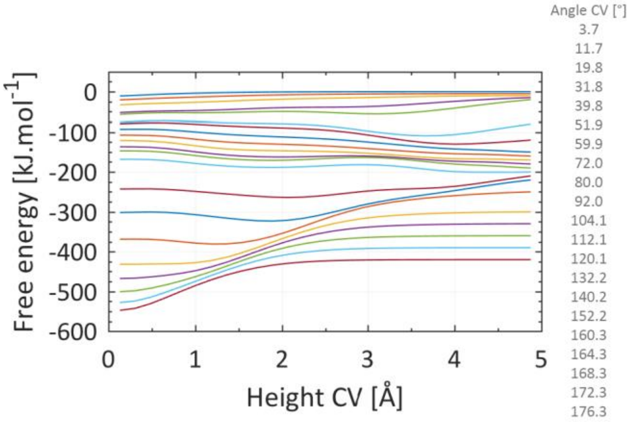

Figure 4.15 Free energy profile as a function of the height CV, for different values of angle CV and r = 2.92 Å. From top to bottom the value of angle CV for each curve is written on the right.

So, if calcium would want to dissociate from the bicarbonate ion by moving away from the anion but in the plane of the anion, it has to cross an energy barrier of $15.8 \pm 5.4\ kJ \cdot mol^{-1}$. However, if calcium would try to first get out from the plane of the bicarbonate anion, when at the equilibrium distance from carbon, the energy cost would be $125.01 \pm 20.43\ kJ \cdot mol^{-1}$. Since the energy of dissociation is much larger in the second case, dissociation is expected to occur first via calcium moving away from bicarbonate, in the same plane, and then out of the plane. Consequently, the dissociation barrier for this ionic pair will be considered the minimum of the two values, meaning $15.8 \pm 5.4\ kJ \cdot mol^{-1}$. It should be noted that due to the complexity of the free energy profile for the formation of $[CaHCO_3]^+$, conclusions made are only rough estimates.

4.3.3 Conclusion

The equilibrium distance of ions in their associated form, as well as the energetics of the ionic pair formation, are summarized in Table 4.5. As mentioned in the previous section, due to the complexity of the free energy surface for the formation of the $[CaHCO_3]^+$ pair, not all the parameters could be obtained, and the one reported here is only a rough estimate based on specific pathways of ions approaching each other.

Nonetheless, in general, dissociation barrier of $[CaPO_4]^-$ is much larger than the other two ionic pairs. The association energy also is notable for this ionic pair, implying that formation of this pair is very favorable. The dissociation barrier of $[NaCl]^0$ and $[CaHCO_3]^+$ seems to be energetically similar, considering that in the $[CaHCO_3]^+$, dissociation occurs first via calcium moving away from bicarbonate and then out of the plane of the anion.

Table 4.5 Energetics of formation of ionic pairs.

Ionic pair	r_{min1} [Å]	Association energy $[kJ \cdot mol^{-1}]$	Association barrier $[kJ \cdot mol^{-1}]$	Dissociation barrier $[kJ \cdot mol^{-1}]$
$[NaCl]^0$	3.03	-3.23	8.97	12.21
$[CaPO_4]^-$	2.71	-49.28	4.50	53.70
$[CaHCO_3]^+$	2.92	-	-	(15.8 ± 5.4)

4.4 Interaction of ionic pairs with a single charge point on the surface

The interaction of the three ionic pairs, chosen in section 4.3, with the rutile (110) surface is investigated in this section. As it was shown in section 4.1, the adsorption of calcium on the surface is more favorable than other single ionic species. Also, in section 4.3, it was shown that calcium and phosphate ions have a very high affinity for each other; their ionic pair can form very easily and the dissociation barrier is large enough to make this ionic pair very stable. Therefore, for these ions, another adsorption scenario was also studied. In this scenario, a calcium ion is already adsorbed on a negative charge point on the surface (hereafter referred to as the pre-adsorbed calcium) and the adsorption of the phosphate ion on this pre-adsorbed calcium will be studied.

4.4.1 Approach

Simulation details are similar to those explained in section 4.1.2. Again, only one of the surface hydroxyl groups was de-protonated, which led to a surface charge density of -0.012 $C.m^{-2}$ (the singly deprotonated surface) and in each simulation box, only one ionic pair was studied. The interaction of the ionic pair with the surface was studied only close to the charge point (*i.e.*, close scenario). Only the following points were different from section 4.1.2.

- Distance and radius CVs were defined to the center of the mass of the ionic pair for section 4.4.2.1, and to the center of mass of the phosphate ion for section 4.4.2.2 (in section 4.1, these CVs were defined to the central atom for polyatomic ions). The distance CV was limited to a distance of 12.5 Å while the radius CV was limited to a distance of 5 Å from the charge point. Similar to previous sections, the surface was defined as the average positions of the oxygen atoms of the surface hydroxyl groups over the simulation time.
- The equilibration step was performed for 170 ps.
- Data production step was performed for 50 ns.
- For the ionic pairs, the same pairs, which were chosen in section 4.3, were studied: $[NaCl]^0$, $[CaPO_4]^-$ and $[CaHCO_3]^+$.
- For the adsorption of a phosphate ion on a pre-adsorbed calcium, first, the calcium ion was not restrained in its adsorbed state on the surface. However, after the first adsorption of the phosphate ion on the surface, the calcium ion left the surface with the phosphate ion. Therefore, it was necessary to keep the pre-adsorbed calcium ion restrained on the surface. Based on the findings of section 4.1, since the adsorption of calcium close to the surface charge point was very favorable, the pre-adsorbed calcium was positioned next to the charge point, and then restrained.

In the following, first, the adsorption of ionic pairs and then, the adsorption of a phosphate ion on a pre-adsorbed calcium, on the surface will be discussed.

4.4.2 Results and discussion

4.4.2.1 Adsorption of ionic pairs on the rutile surface

As mentioned in section 4.4.1, the bias during the well-tempered metadynamics simulations was applied to the center of mass of the ionic pair and no restraint was applied to keep the ionic pair together. In other words, the ionic pairs were allowed to dissociate, if their energetics dictate so. Among the three chosen ionic pairs, it was observed that the $[NaCl]^0$ and $[CaHCO_3]^+$ ionic pairs dissociated in less than 5 ns. This can be seen in Figure 4.16, where the ion-ion distance for different ionic pairs is shown. As shown earlier in Table 4.5, the dissociation barrier for the $[NaCl]^0$ and $[CaHCO_3]^+$ ionic pairs is relatively smaller than that for $[CaPO_4]^-$. The $[CaPO_4]^-$ ionic pair did not dissociate over the simulation time of 50 ns. Since the $[NaCl]^0$ and $[CaHCO_3]^+$ dissociated in less than 5 ns, their simulations were terminated and only the adsorption behavior of $[CaPO_4]^-$ on the surface was further investigated.

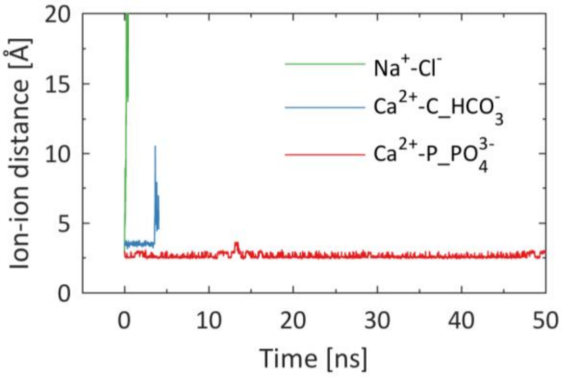

Figure 4.16 Ion-ion distance, when applying a bias on the distance of the ionic pair, from the rutile (110) surface.

The 2D free energy profile and its projection along the distance CV are shown in Figure 4.17. Based on this figure, the adsorption energy, which is the difference in the energy between the adsorbed and solvated states, is estimated to be -25.89 $kJ \cdot mol^{-1}$. Since no notable barrier can be identified during the adsorption of the ionic pair, the adsorption and desorption barriers cannot be estimated. The stability of this ionic pair in their adsorbed state on the surface was studied via classical MD for 2 ns during which, the ionic pair preserved its adsorbed state and did not desorb into water.

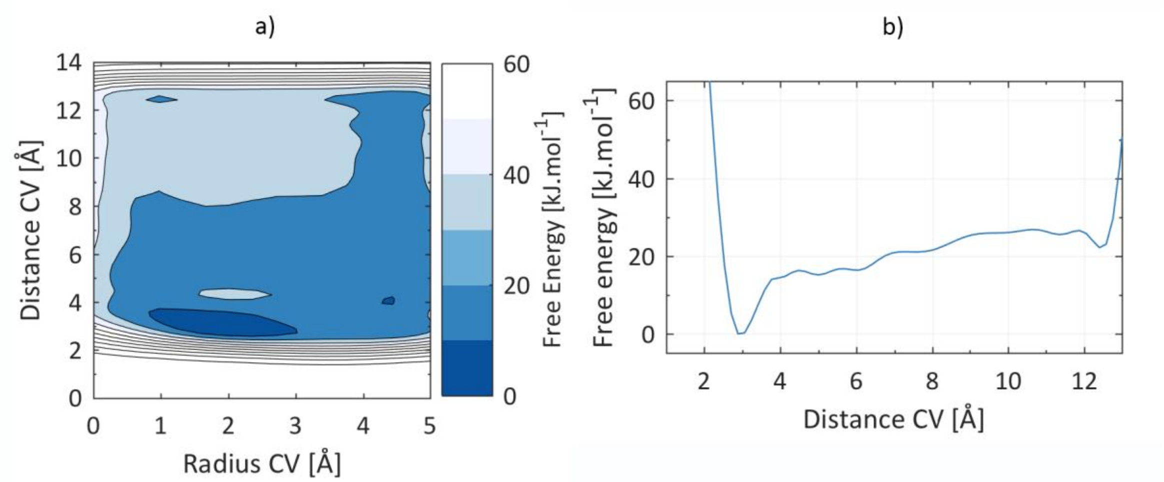

Figure 4.17 a) 2D free energy profile and b) its projection along the distance CV during the interaction of $[CaPO_4]^-$ with the rutile surface.

4.4.2.2 Adsorption of phosphate on a pre-adsorbed calcium

As briefly mentioned in section 4.4.1, first, the pre-adsorbed calcium was not restrained on the surface. Figure 4.18 shows the distance of the phosphorus atom of the phosphate ion, and the pre-adsorbed calcium from the rutile (110) surface over the simulation time of 10 ns. As it can be seen in this figure, the phosphate ion, under the applied bias, adsorbs rapidly on the pre-adsorbed calcium. Thereafter, the phosphate ion does not leave the surface and the pre-adsorbed calcium (till $t = 3\ ns$), until the bias is strong enough to take the anion away. However, now, the phosphate ion may either leave the surface in its free form, for which the dissociation of the $[CaPO_4]^-$ should occur, or may either leave the surface as the $[CaPO_4]^-$ ionic pair, along with the pre-adsorbed calcium, for which the desorption of this pair from the surface should occur. In Table 4.5, it was shown that the dissociation barrier for the $[CaPO_4]^-$ ionic pair is 53.70 $kJ \cdot mol^{-1}$. On the other hand, in section 4.4.2.1, it was shown that desorption of the $[CaPO_4]^-$ ionic pair from the rutile surface requires 25.89 $kJ \cdot mol^{-1}$. Since the latter requires a smaller amount of energy, the pre-adsorbed calcium ion leaves the surface along with the phosphate ion, in the form of an ionic pair.

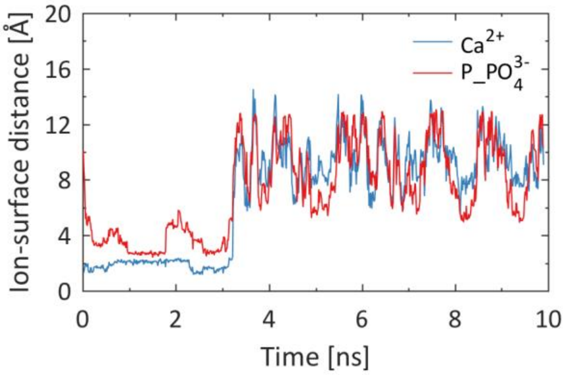

Figure 4.18 Distance of a calcium ion from the rutile (110) surface as the distance of the phosphate ion from the surface is biased. As it can be seen, after 3 ns the calcium ion leaves the surface due to the formation of an ionic pair with the phosphate ion.

Therefore, to compare the adsorption behavior of a phosphate ion on a pre-adsorbed calcium, it was essential to restrain the calcium ion in its adsorbed state on the surface. The 2D free energy profile and its projection along the distance CV are shown in Figure 4.19. The position of the pre-adsorbed calcium is marked by a red star in Figure 4.19a. Similar to the adsorption of the calcium-phosphate pair on the surface, the adsorption of phosphate on the pre-adsorbed calcium does not show an energy barrier. The adsorption energy, as the difference of the energy of the adsorbed and solvated states is significant and more than 100 $kJ \cdot mol^{-1}$.

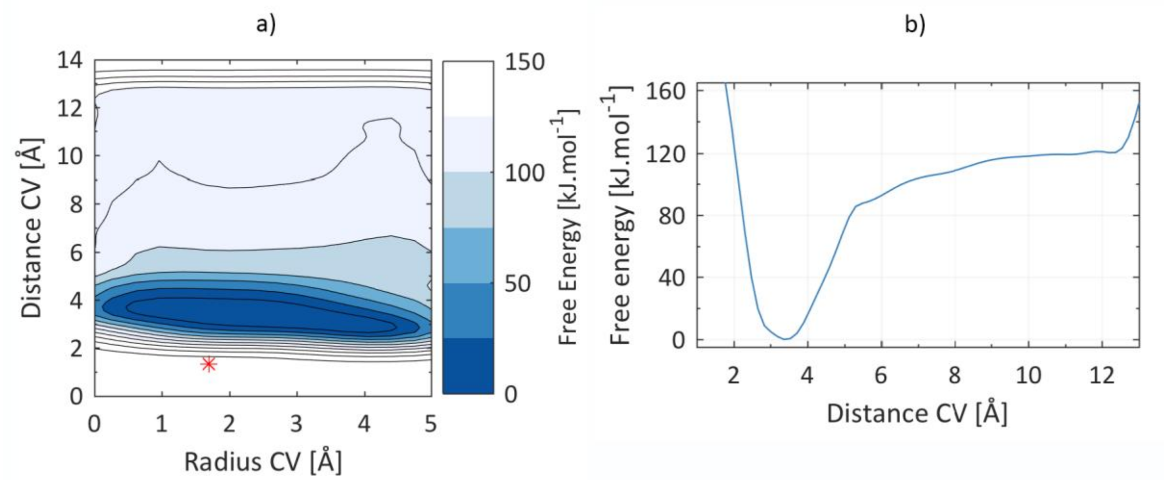

Figure 4.19 a) 2D energy profile of the adsorption of a phosphate ion on a pre-adsorbed calcium ion on the rutile surface; the calcium ion is kept fixed on the surface and its position is shown by the red star and b) the projection of the free energy along the distance CV.

4.4.3 Conclusion

In this section, the adsorption of three ionic pairs on the rutile (110) surface was envisaged. However, two of the ionic pairs ($[NaCl]^-$ and $[CaHCO_3]^+$) dissociated under the applied bias, since their dissociation barrier is not significant. Therefore, only the adsorption behavior of $[CaPO_4]^-$ on the surface was investigated further. It was seen that there is no significant adsorption barrier for the adsorption of this pair on the surface.

The adsorption of a phosphate ion on a pre-adsorbed calcium was also studied on the surface. The pre-adsorbed calcium had to be restrained on the surface since otherwise, it would leave the surface with the phosphate ion in the form of an ionic pair, since the affinity of calcium for the surface is less than its affinity for phosphate. The adsorption of phosphate on the pre-adsorbed calcium proved to be very favorable. No energy barrier was observed for the adsorption of this ion. The large adsorption energy is believed to be due to the affinity of this ion for the rutile surface but also its affinity for the calcium ion.

4.5 Discussion and summary

In this chapter, the interaction of some ionic pairs, either with a rutile surface, or either with other ions, was studied to understand the initial events, which may lead to apatite formation. Ions were considered mainly in their most probable thermodynamic form in an SBF under physiological conditions (their free form); some of the ions were also studied in the form of an ionic pair. Similar to the apatite-forming model previously proposed by Kokubo *et al.* for the alkali and heat treated sodium titanate surface (1), it was seen that calcium and phosphate have favorable adsorption on the rutile surface. In addition, it was seen that other ions (sodium, potassium and carbonate) also have a favorable adsorption energy on the surface. While the adsorption of these ions on rutile may not be as stable as calcium, these ions should also be considered in the apatite-forming model as their adsorption on the surface, even if transient, will continuously modify the surface composition and will affect the available nucleation sites for apatite.

The adsorption of sodium and calcium, on a rutile surface with a higher surface charge density, proved to become more favorable. Since electrostatic forces seem to affect the ion-surface interactions, under physiological conditions where the surface charge density is more negative than those studied in this chapter, one expects the favorable adsorptions become more favorable. Therefore, the contribution of potassium, sodium and calcium, which in the first part of this chapter showed a favorable adsorption on the rutile surface, to the apatite formation will be even more important.

The adsorption of ionic pairs on the surface seems both interesting and relevant. First, the formation of $[NaCl]^0$, $[CaPO_4]^-$ and $[CaHCO_3]^+$ was studied. The dimension of the sampling space varied based on the complexity of the ionic pair which were to form. For $[NaCl]^0$ and $[CaPO_4]^-$, the energy of formation of the ionic pair was calculated. For $[CaHCO_3]^+$, the sampling space was three-dimensional. The complexity of the sampling space caused difficulty to the interpretation of the energetics of formation of the ionic pair, and the analysis was done only for two specific pathways. Comparison of the energetics of the three ionic pairs showed that the formation of $[CaPO_4]^-$ is energetically much more favorable than the other two pairs.

The adsorption behavior of these three ionic pairs on the rutile (110) surface was studied. Since no restraint was applied to keep the ionic pair together, two of them dissociated not long after the beginning of the simulations. The calcium-phosphate ionic pair, however, proved to be very stable and it was possible to study its adsorption on the surface in the form of a pair.

In Table 4.6, the adsorption energetics of calcium and phosphate on the singly deprotonated rutile (110) surface, as well as the energetics of formation of the $[CaPO_4]^-$ pair, are summarized, which were obtained in this chapter. From this table, it can be seen that while the adsorption of calcium and phosphate, in their single form, on the surface is associated with an energy barrier, this is not the case when phosphate adsorbs on the pre-adsorbed calcium or when these ions adsorb on the surface in the form on an ionic pair.

Table 4.6 Adsorption energetics of calcium and phosphate on the rutile (110) surface.

Ionic pair	Detail	r_{min1} [Å]	Assoc./Ads. energy $[kJ \cdot mol^{-1}]$	Assoc./Ads. barrier $[kJ \cdot mol^{-1}]$	Dissoc./Des. barrier $[kJ \cdot mol^{-1}]$
$[CaPO_4]^-$	Formation of the pair	2.71	-49.28	4.50	53.70
Ca^{2+}	Ads. on rutile	2.22	-29.74	9.29	39.03
PO_4^{3-}	Ads. on rutile	2.89	-5.96	9.79	15.75
$[CaPO_4]^-$	Ads. on rutile	2.88	-25.89	-	-
PO_4^{3-}	Ads. on pre-adsorbed Ca^{2+} on rutile	3.36	-117.83	-	-

Ignoring the ions which are present in SBF except calcium and phosphate, and also all the ionic pairs which can form, let's assume that apatite is to form only from the adsorption of calcium and phosphate. If one also assumes that the hydroxyl groups of hydroxyapatite will be provided by water, and not hydrated species, the initial nuclei of hydroxyapatite has to form either in water, or on the surface. In the former case, first the $[CaPO_4]^-$ pair has to form in water with an energy barrier of 4.50 $kJ \cdot mol^{-1}$ and an energy gain of -49.28 $kJ \cdot mol^{-1}$; then this pair has to adsorb on the surface, with no notable energy barrier but an energy gain of -25.89 $kJ \cdot mol^{-1}$. In the latter case, first calcium adsorbs on the surface, as it is much more favorable than phosphate, and then phosphate adsorbs on the pre-adsorbed calcium. There is an energy barrier of 9.29 $kJ \cdot mol^{-1}$ to the adsorption of calcium, but an energy gain of -29.74 and -117.83 $kJ \cdot mol^{-1}$, to the adsorption of calcium on the surface and the following adsorption of phosphate on the pre-adsorbed calcium. Since the energy gain of these two scenarios should be path-independent, but this is not what the energy values reveal here, one should consider the energy difference between the solvated and adsorbed states, instead of the adsorbed state and the second closest minimum to the surface.

The following directions are suggested for future work on the investigation of apatite formation.

1. The findings of this chapter predict the adsorption of potassium, sodium and calcium on the rutile surface under the physiological condition to be very favorable. Compared to potassium and calcium, the concentration of sodium in the blood plasma and SBF solutions is much higher. Therefore, the amount of

sodium on the rutile surface may be much more than that of calcium and potassium. Hence, the interaction of other ions with pre-adsorbed sodium ions, similar to section 4.4, is interesting.

2. Thermodynamic modelling (C.1) suggests that the probability of different pairs is especially high for phosphate species. Investigation of formation of these pairs and their adsorption behavior on the surface can be very insightful.
3. Experimentally, apatite formation is speculated to be due to the formation of Posner's clusters ($Ca_9(PO_4)_6$ - Figure 4.10) and different amorphous calcium phosphate phases. Posner and Betts (4) hypothesized that ACP (amorphous calcium phosphate) forms from Posner's clusters. Molecular dynamics studies also observed the formation of Posner-like clusters in supersaturated solutions, in a time-scale smaller than 5 ns (6). This was also recently shown by means of thermodynamic modelling which suggested that Posner's clusters might engage in primary and secondary nucleation by dehydration and incorporation of phosphate ions (7). An interesting next step is therefore to study the interaction and adsorption behavior of Posner's clusters on the rutile surface and to estimate the extent to which they govern the apatite formation.

References

1. Kokubo, T., Kim, H.-M. & Kawashita, M. Novel bioactive materials with different mechanical properties. *Focus Biomater. Sci. Asia* **24,** 2161–2175 (2003).

2. Demichelis, R. *et al.* Simulation of calcium phosphate species in aqueous solution: Force field derivation. *J. Phys. Chem. B* **122,** 1471–1483 (2018).

3. Zhu, P., Masuda, Y. & Koumoto, K. The effect of surface charge on hydroxyapatite nucleation. *Biomaterials* **25,** 3915–3921 (2004).

4. Posner, A. S. & Betts, F. Synthetic amorphous calcium phosphate and its relation to bone mineral structure. *Acc. Chem. Res.* **8,** 273–281 (1975).

5. Dorozhkin, S. V. Amorphous calcium (ortho)phosphates. *Acta Biomater.* **6,** 4457–4475 (2010).

6. Mancardi, G., Hernandez Tamargo, C. E., Di Tommaso, D. & de Leeuw, N. H. Detection of Posner's clusters during calcium phosphate nucleation: A molecular dynamics study. *J. Mater. Chem. B* **5,** 7274–7284 (2017).

7. Carino, A., Ludwig, C., Cervellino, A., Müller, E. & Testino, A. Formation and transformation of calcium phosphate phases under biologically relevant conditions: Experiments and modelling. *Acta Biomater.* (2018).

Chapter 5 Interaction of single amino acids with the rutile (110) surface

T*o understand if the absence of organic molecules in the current protocols of apatite formation in SBF solutions should be re-considered, the interaction of several amino acids with a rutile surface is studied in this chapter. The adsorption of amino acids proved to be more favorable than what was observed previously in chapter 4 for most ionic species.*

As mentioned in Chapter 1, the current international standard for the apatite-forming ability of Ti-based biomaterials does not contain any organic residue except tris (tris(hydroxymethyl)aminomethane (see Table A.2), which is used as the buffering agent (1). The objective of this chapter is to quantify the affinity of adsorption of a few amino acids on a rutile surface to understand the importance of considering organic residues in the apatite-forming ability testing of biomaterials in an SBF solution. Amino acids were chosen based on a few criteria.

First, even though they are relatively small compared to the most of biomolecules, *e.g.*, polypeptides and proteins, they are still good representatives since they are the building blocks of larger biomolecules. Their small size is of interest for two reasons. First, due to their smaller size, they have faster kinetics compared to larger biomolecules; therefore, there is a high probability that they reach the surface in the first stages after the implantation of the biomaterial. Consequently, amino acids may have an important role in the composition and conformation of the organic layer, which forms on the surface of the biomaterial, immediately after the implantation. Second, for computational methods, a smaller organic molecule means that the number of interactions in the system is smaller. Therefore, with a certain computational resource, longer time-scales can be simulated and studied and the sampling of the phase space will generally be much better for smaller molecules compared to larger ones.

The second criterium for choosing amino acids is their presence in biological conditions. Around 8$\%$ of the body weight of an adult person is due to blood ($\sim$ 4 - 6 l). 55$\%$ of the blood volume is the blood plasma; red blood cells, white blood cells and platelets form the remaining 45$\%$. Blood plasma can be described as the medium in which the red blood cells, white blood cells and platelets flow. Blood plasma is mainly water ($\sim$ 90%). 8% of the plasma is due to proteins (with a concentration of 60-80 g/l) and other organic residues; the remaining 1-2% is nutrients, gases, hormones, wastes and products of cell activity and ions (2). Although the concentration of amino acids in plasma is much smaller than proteins - a recent study reports the average concentration of amino acids in the blood plasma, based on different diets, to be 0.5 g/l (3). Amino acids *in vivo* can interact with the surface of Ti-based biomaterials, for example, used for orthopedic applications. Another instance, where amino acids can interact with a Ti-based biomaterial, is dental applications since human saliva also contains free amino acids with a concentration of 0.03 g/l (4).

In the following, this chapter is presented in the form of an article. All the calculations were performed by the first author (the author of this thesis) and the manuscript was also written by her; it was revised by her two directors. The article was published in the Journal of Physical Chemistry C (JPCC 122 (2018) 11355-11363 DOI: 10.1021/acs.jpcc.7b12614). The supporting information of this article can be found in Appendix D.

Journal of Physical Chemistry C 122 (2018) 11355-11363

Adsorption Free Energy of Single Amino Acids at the Rutile (110)/Water Interface Studied by Well-tempered Metadynamics

Azade YazdanYar✦, *Ulrich Aschauer*✦✦, *Paul Bowen*✦
✦ Department of Materials Science and Engineering, École Polytechnique Fédérale de Lausanne (EPFL), Lausanne 1015, Switzerland
✦✦ Department of Chemistry and Biochemistry, University of Bern, Bern 3012, Switzerland

Abstract

Single amino acids are present in blood plasma and are the building blocks of larger organic residues. Their interaction with surfaces is therefore crucial for biomedical applications in contact with blood. In this work, we use well-tempered metadynamics to study the adsorption of six amino acids, with non-polar (Ala and Leu), polar (Ser), positively charged (Arg and Lys) and negatively charged (Asp) side groups, on a negatively charged rutile (110) surface. The free energy of adsorption and the desorption barriers were determined for all amino acids under different adsorption conformations. When using the center of mass as the collective variable in well-tempered metadynamics, results for different amino acids were difficult to interpret due to different adsorption conformations on the surface overlapping in collective-variable space. After projecting onto separate collective variables for the backbone and the side group much clearer trends were observable. We show that, on the negatively charged surface of rutile, adsorption via the backbone occurs for all the amino acids irrespective of their side group. Adsorption driven via the side group only occurs for polar and charged side groups as opposed to the non-polar side groups. This points to the importance of interactions of the side group with the strongly structured water layer rather than direct side group-surface interactions in determining the adsorption behavior.

5.1 Introduction

A thin oxide layer forms on titanium surfaces in the presence of air or water and it is reported that titanium biomaterials owe their biocompatibility to this oxide layer.[1–2] Inorganic surfaces, such as the titanium oxide layer on an implant, are covered by organic residues rapidly after their implantation in the body;[3–5] this can be favorable, in the case of biosensors and drug delivery systems;[6] or unfavorable, where interactions of the surface with ions and cells in the blood plasma, are hindered or prevented by this organic layer.[7]

Alongside experimental studies, computational work can provide insights on the underlying interaction mechanism. Molecular dynamics (MD) is one of the atomistic tools for performing computational studies on the interactions of molecules with surfaces.[8] In the equilibrium state, the system spends a significant portion of time within stable states,[9] which are local energy minima; rare events move the system from one stable state to the other.[10] Rare events occur very infrequently, due to the large energy barriers associated with them, but rather quickly once the barrier has been surpassed.[9] Observation of rare events in a standard molecular dynamics simulation is unlikely due to the still relatively short timescales accessible using current hardware and software.[10–13] Enhanced sampling methods, such as metadynamics, which we use here, bias the potential energy of the system to promote rare events. In metadynamics, Gaussians bias potentials are deposited in a space defined by one or a few collective variables (CVs).[14,15] The free energy can be derived from the deposited bias potential. In well-tempered metadynamics, which is one of the flavors of metadynamics, the deposition rate and bias height of these Gaussians decrease over the simulation time.[15,16]

Free amino acids represent one group of the many different biomolecules present in blood plasma[17] and they also build up larger organic residues such as peptides and proteins. Each amino acid consists of an amine group, a carboxyl group and a C_α which carries a hydrogen and a side group. The different side groups determine specific properties of amino acids. The small size of single amino acids makes their adsorption on a biomaterial surface more probable in the initial steps after implantation since they are expected to have faster kinetics compared to other (larger) biomolecules. Both experimental, as well as computational studies, have investigated the interaction of amino acids, in forms of single residues or sequences, with inorganic surfaces.[5,18–20] One of the main debates on this topic is whether the nature of such interaction is entirely electrostatic.[21] For example, adsorption of positively charged Lys to the titanium oxide with a negative charge is reported to be purely electrostatic at neutral pH.[22] Tentorio *et al.*[23] also observed that adsorption of Glu and Lys on amorphous titanium oxide nanoparticles always happens in the pH range where attractive Coulomb interaction exists but it also occasionally occurs in the pH range where the Coulomb interaction is repulsive. Notman *et al.*[19] compared the free energy of adsorption of methane (as the side chain of Ala) and methanol (as the side chain of Ser) on a quartz (100) surface using MD simulations. The free energy landscape for both moieties was similar, which is not expected as the two analogues are different (hydrophobic and polar, respectively). It was argued that the surface shields the hydrophobic residue (methane) from water, favoring the adsorption of the hydrophobic side chain on the quartz surface.

It is also still unclear whether the adsorption and interaction of a single amino acid with an inorganic surface is fully determined by the side group as it has been reported that in a zwitterion, the three potential binding groups (the amine group, the carboxyl group and the side group) compete to interact with the surface.[24,25] Schmidt studied the adsorption of different amino acids on the titanium oxide surface in different pH ranges.[25] Side groups from similar categories (either non-polar, polar or charged) did not lead to similar adsorption behavior in the same pH range. While some non-polar amino acids adsorbed, others did not; the same behavior was observed for amino acids with polar side groups. However, amino acids with charged side groups (either positive or negative) always adsorbed on the surface.

In much computational work, the side group of the amino acids has often been studied because in a peptide chain, both the carboxyl group and amine group are engaged in peptide bonds with the neighboring amino acids and the interaction with the surface is mainly via the side group. Sultan *et al.*[26] used metadynamics to study the energetics of adsorption of the end part of the side chain (side chain analogues) of some amino acids on the rutile (110) surface with a surface charge density of -0.104 $C \cdot m^{-2}$. The non-polar side groups showed weak interaction with the surface while polar and charged side groups showed strong interaction; the side groups with an opposite charge to the surface adsorbing the strongest. For the polar and charged side chain analogues, they noted that the adsorption affinity increased in the order of Ser, Asp, Lys and Arg.

Brandt *et al.*[27] used umbrella sampling and metadynamics to look at the same question but on a non-hydroxylated and charge neutral rutile (100) surface. They looked at analogues of the side group for all 20 naturally occurring amino acids. The results of both methods were consistent and showed that polar and aromatic side groups had strong interactions with the surface while the non-polar (and non-aromatic) side groups had a weak affinity for the surface. Ser showed the strongest adsorption on the neutral rutile (100) surface and the free energy of adsorption increased in the order of Ala, Lys, Leu, Asp, Arg and Ser. They observed that positively charged Lys had a lower adsorption energy than the non-polar Leu; in fact, the authors mention that a trend for the charged side chains could not be generalized and the reason was that the strongly bound water on the surface shields the interactions between the surface and charged functional groups.

The free energy of adsorption of full amino acids using well-tempered metadynamics was studied on gold and silver surfaces.[28] While the adsorption behavior on a metallic substrate should be different from an inorganic surface, this study seems to be the closest study to ours, which considers the entire unit of amino acids and not just the side group. The authors observed different trends for different substrates. The adsorption free energy increased in the order of Leu, Ala, Lys, Asp, Arg and Ser on the silver substrate and in the order of Lys, Ala, Asp, Ser, Leu and Arg on the gold substrate.

Here, we use well-tempered metadynamics to investigate the adsorption conformation and behavior of different amino acids on a rutile surface from the viewpoint of the free energy. In considering the full amino acid, we would like to explore whether it is the side group or backbone which mainly drives the adsorption. Six amino acids are chosen to cover those with polar, non-polar and charged side groups. All the simulations are performed on the rutile (110) surface which carries a small negative charge. This surface has the lowest surface energy among other rutile surfaces and therefore, it is the most stable surface of rutile.[2] The well-tempered metadynamics simulations were carried out using a single collective variable (center of mass of the amino acid) followed by projection of the results onto two collective variables (center of mass of side group and backbone) for further analysis.

5.2 Simulation methods

5.2.1 Rutile surface

We study the (110) surface of rutile which is hydroxylated in presence of air or water. Two types of hydroxyl groups form on this surface: the bridging and the terminal hydroxyl.[29] Under physiological conditions ($T \sim 37$ °C and $pH \sim 7.4$), rutile is negatively charged with a surface charge density of approximately -0.1 $C \cdot m^{-2}$,[30,31] which stems from a partial deprotonation of bridging hydroxyl groups. Predota *et al.* showed that surface groups of rutile (surface Ti and the hydroxyl groups) are variable-charge atoms[29] and presented the partial charges of these groups for different surface charge densities.[32] In the current work, we are concerned with the interaction of the amino acids with a single charged site on the surface, mainly to avoid complications related to the distribution of charged sites and the complexities which it can add to draw conclusions. Therefore, in this paper, we deprotonate only one bridging hydroxyl group on the rutile surface, which has 72 bridging and 72 terminal hydroxyl groups. This single deprotonated hydroxyl results in a surface charge density of -0.011 $C \cdot m^{-2}$ on our rutile (110) surface. The surface, the hydroxyl groups on the surface, and the single charge point on the surface are shown in Figure D.1. The partial charges of the surface groups at this surface charge density were calculated as explained in section D.2.

The surface dimensions of the rutile slab were 35.51×38.98 Å^2 with a thickness of 70 Å. A water layer with a thickness of 90 Å was added on one side of the solid slab in the z-direction. The thickness of the solid slab was selected such that interactions between the upper and lower faces of the slab were avoided. Also, the thickness of the water layer assured bulk water properties when far from the solid-liquid interface or the liquid-vacuum surface. Periodic boundary conditions were applied in all directions. Along the z-direction, the periodic images were separated from each other by a vacuum gap of 100 Å to prevent interaction between periodic images of the simulation box.

5.2.2 Amino Acids

Six amino acids were chosen (Figure 5.1): alanine and leucine (Ala and Leu; both with a non-polar side group), serine (Ser; with a polar side group), aspartic acid (Asp; with a negatively charged side group), and arginine and lysine (Arg and Lys; both with positively charged side groups). The selection of amino acids was made in a way to consider amino acids with different side groups. Also, the amino acids were chosen similar to those present in the titanium-binding peptide sequence which consists of Arg-Lys-Leu-Pro-Asp-Ala amino acids. This hexapeptide has proven to have a high affinity for several surfaces, including titanium. In our choice of amino acids, we replaced the aromatic and non-polar Pro with the polar Ser. pK_a and pK_b for all amino acids are less than 3.0 and more than 8.0.[33] In the pH range between these two values (*e.g.*, the physiological pH of 7.4 at 37 °C), the carboxylate group is deprotonated and the amine group is protonated. The charging state of the side groups of each amino acid was chosen based on its pK. Therefore, with a pK of 12.48 and 10.53, for the amine side groups of Arg and Lys,[33,34] respectively, their side groups are protonated. With a pK of 3.65 for the carboxyl side group of Asp, [33,34] its side group is deprotonated. Ala, Leu and Ser have non-polar and polar side groups which do not protonate or deprotonate.

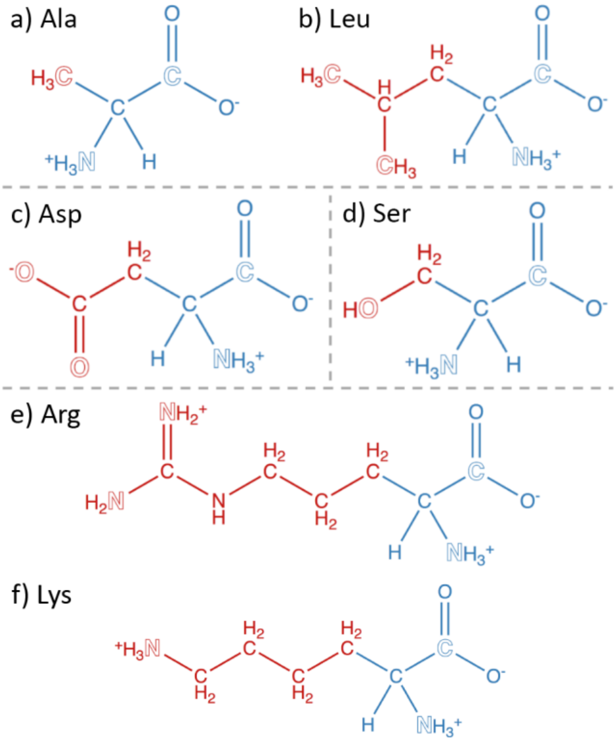

Figure 5.1 Amino acids studied in this work; a) alanine, b) leucine, c) aspartic acid, d) serine, e) arginine and f) lysine. Amino acids are labelled using their abbreviations in the figure. The atoms in blue are considered as the backbone and the atoms in red are the side group. Some of the analyses, as stated in the text, are based on the atoms shown with outline font.

5.2.3 Force fields

The classical force field developed by Predota *et al.*[29] was used to define interaction parameters of rutile. Water was modelled using the SPC/E model.[35] Rutile-water interactions were described by the parameters proposed by Predota *et al.*[29] which are based on previous *ab initio* studies.[36] The force field input files for the amino acids were prepared by the DL_FIELD package.[37] The CHARMM force field[38] was used in this package to obtain the interaction parameters. Parameters for cross-interactions between water and the amino acids, and between rutile and the amino acids were all obtained using the mixing rules of Lorentz-Berthelot.[39] Since the parameters in the Lennard-Jones form are required to use these mixing rules, fitting of the Lennard-Jones form to the force field parameters of rutile to the Buckingham form was carried out (see D.3). It should be noted that for describing rutile, we used the force field developed by Predota *et al.*[29] in the Buckingham form and the Lennard-Jones parameters were used only for rutile-amino acid interactions. The cutoff for the short-range van der Waals interactions as well as the real space part of the electrostatic calculations was 12 Å. Long-range electrostatics were treated by an Ewald summation. A Nosé-Hoover thermostat with a relaxation time of 0.5 ps was used to impose a temperature of 37

°C in the NVT ensemble. The equations of motion were integrated with a timestep of 0.7 fs. The integration algorithm was Verlet leapfrog.

5.2.4 Simulation details

Well-tempered metadynamics simulations[16] were performed using DL_Classic v1.9[40] with the Plumed plugin v2.2.2.[41] Gaussian hills with an initial height of 1 $kJ \cdot mol^{-1}$ and a width of 0.5 Å were deposited every 2,000 timesteps (1.4 ps) with a bias factor of 15. Before production runs, each system was equilibrated for 200-250 ps during which the C_α atom of the amino acid was kept fixed at a distance of 15 Å from the surface. All atoms of the rutile slab, except the hydroxyl groups on the surface, were kept frozen during the equilibration and production runs to speed up the computation. The perpendicular distance of the center of mass of the amino acids from the surface was considered as the collective variable ($\mathrm{CV_{COM}}$) and it was limited to a distance of 12 Å from the surface in the z-direction. The surface position was defined to be the average z component of the oxygen atoms of all the hydroxyl groups. In the XY plane, the center of mass of the amino acid was confined to move within a radius of 4 Å around the charge point on the surface (Figure D.1).

To be able to better differentiate the role of the backbone and the side group of an amino acid in its adsorption behavior, we projected the results obtained in the $\mathrm{CV_{COM}}$ space into a two- dimensional space that allows us to differentiate between adsorption of the backbone and the side chain. The validity of this so-called reweighting approach,[42] in particular in combination with well-tempered metadynamics, was previously shown for projections onto two dihedral angles after having biased the dynamics of only a third dihedral in an alanine dipeptide.[42] Plumed analysis tools were used for post-processing. The 'reweight_metad' functionality of Plumed was first used to cancel out the bias applied to the system due to the usage of $\mathrm{CV_{COM}}$. This functionality implements the Tiwary-Parrinello reweighting method[42] to an already biased trajectory. Then, the 'histogram' functionality was used to accumulate the average probability density of the two new collective variables. Finally, 'convert_to_fes' was used to obtain the free energy profile.

The two-dimensional space we project into is spanned by the collective variables $\mathrm{CV_{Backbone}}$ and $\mathrm{CV_{Side}}$. Both collective variables represent the distance from the surface in the z-direction for the center of mass of a part of the amino acid. The $\mathrm{CV_{Backbone}}$ takes into account the amine group, the carboxyl group, the C_α and its hydrogen. The $\mathrm{CV_{Side}}$ includes the rest of the amino acid which we refer to as the side group. The groups of atoms considered for the backbone and the side group are shown in Figure 5.1 in blue and red, respectively. The free energy landscape as a function of these two collective variables helped us to detect favorable adsorption conformations. We will also be able to see if an amino acid prefers to approach the surface mainly via the backbone, the side group or both.

All simulations were carried out for 20 ns, corresponding to 31-44 days per calculation on our available HPC resources. Using the block analysis method, the average error of the calculations was estimated for different block sizes. Figure A.3 shows the error corresponding to each amino acid as the block size increases. As the convergence of the error value can be a proper criterion for sufficient sampling, we can say that the simulation length is acceptable. The estimated error associated with our calculations (performing well-tempered metadynamics using the CV_{COM}) is less than 1.6 $kJ \cdot mol^{-1}$.

5.3 Results and Discussion

5.3.1 Water-Surface interactions and adsorption mode of amino acids

It has been shown that close to rutile surfaces, independent of surface charge, water is orientated in a few layers with a higher density than bulk water.[26,29,43] The water density in the normal direction to the surface is plotted in Figure D.4. As it can be seen in this figure, there are high-density water layers at distances of 2.35 and 4.6 Å from the surface, which is in agreement with previous studies.[29,44,45] We define direct binding when a group binds directly to the surface without the presence of intermediate water molecules. During this binding mode, the binding group has to lose some of its associated water molecules. Unlike direct binding, indirect binding involves the presence of water molecules between the binding group and the surface. Many studies have emphasized the competition between water and the adsorbate during the adsorption of organic residues on the surface. In many cases, the indirect binding can have a long residence time and can be the primary binding mode of the adsorbate.[27,46,47] The stability or residence time of a bound configuration depends on the energy required to distort the bond. If such energy is not negligible, the bond will have a longer residence time. For the sake of simplicity, in our study we have considered the adsorption mode to be indirect if the bonding distance from the surface is further than the water layer closest to the surface (at 2.35 Å) since in such a case, water molecules are present between the adsorbate and the surface. We consider the bonding mode to be direct if the adsorption distance from the surface is closer than this water layer to the surface mainly because in such a case, the adsorbate has a high affinity for the surface which has allowed it to pass the closest water layer to the surface, reach the surface and have a direct interaction with it.

The distance of the main atom of each group (outline fonts in Figure 5.1) from the surface is shown in Figure 5.2 (for those with two end atoms in the side group, the average value is plotted); we also present some atomic snapshots over the simulation time in this figure. Close observation of this figure for different amino acids reveals that in the adsorbed state, most of the time, one of the potential binding groups is closer to the surface than the first water layer (shown as the horizontal dashed line in Figure 5.2) meaning that the adsorption is driven by direct binding with at least one of the groups. For the cases where the adsorption is mainly via the carboxyl group (*e.g.*, Figure 5.2b in the time interval of 16-18 ns) or a negatively charged side group (Figure 5.2c in the time interval of 12-12.5 ns), the repulsive electrostatics between the negative charge point on the surface and the negatively charged binding group of the amino acid (the carboxyl group in the backbone or the side group of Asp) causes the adsorption to take place slightly farther from the surface (Figure 5.2c-ii). Nonetheless, since there is no water molecule between the binding group and the surface, this adsorption mode is still considered to be direct (Figure 5.2b-ii). In fact, based on Figure 5.2, we do not observe any indirect yet stable binding of the amino acid to the surface, *i.e.*, there is no clear stable adsorption in which the distance of the binding group from the surface is more than the first water layer while water molecules can be seen in the atomic snapshot between the binding group and the surface.

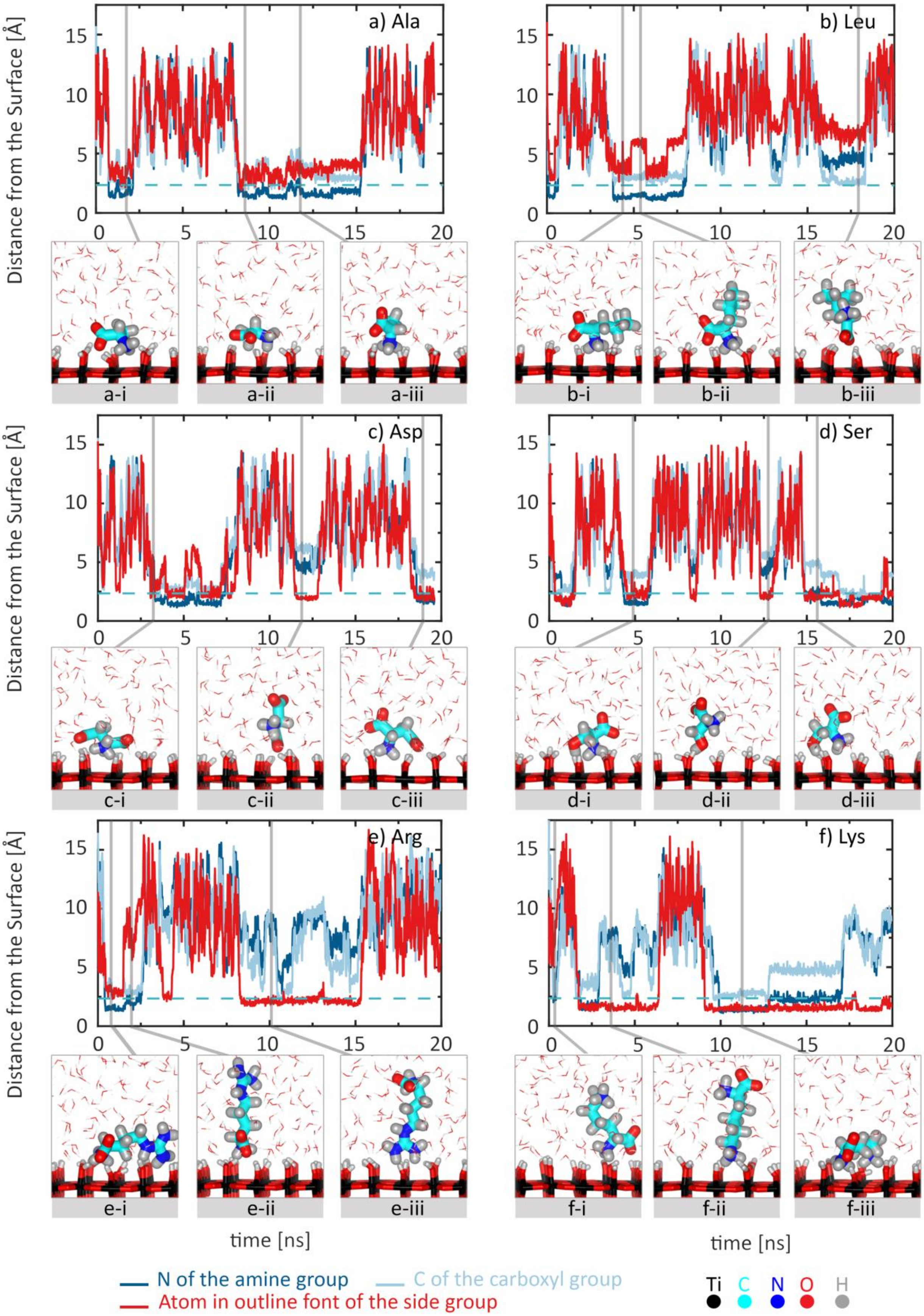

Figure 5.2 Distance from the surface of outlined atoms Figure 5.1, for a) Ala, b) Leu, c) Asp, d) Ser e) Arg and f) Lys. For Leu, Asp and Arg the red plot corresponds to the average of two outlined atoms of the side group in Figure 5.1. The dashed horizontal line shows the position of the first water layer. Atomistic snapshots (labelled by i, ii and iii) were visualized by Vesta[48] and correspond to the time points shown by grey lines.

5.3.2 Free energy profile using CV_{COM}

The free energy as a function of the center of mass of the amino acid from the surface (collective variable CV_{COM}), is shown in Figure 5.3. This CV allows the amino acid to approach the surface in different orientations and conformations of the backbone and the side group. In previous studies by other groups, the center of mass was used to examine the energetics of the adsorption;[26,27] since these studies investigate only side group analogues of the amino acid, the use of this collective variable can be sufficient in obtaining proper free energy profiles of the adsorption. Here, however, we observe that using only CV_{COM} fails to provide sufficient details with respect to the adsorption behavior; for example, in Figure 5.3, it is unclear why Ala and Ser have similar energy landscapes and what causes a single-well landscape for these two amino acids but not for the others. Even Arg and Lys, which have similar positively charged side groups, show different energy states in their multi-well energy profiles. Consequently, we use the so-called reweighting method[42], so that we could extract more details from the atomistic trajectories.

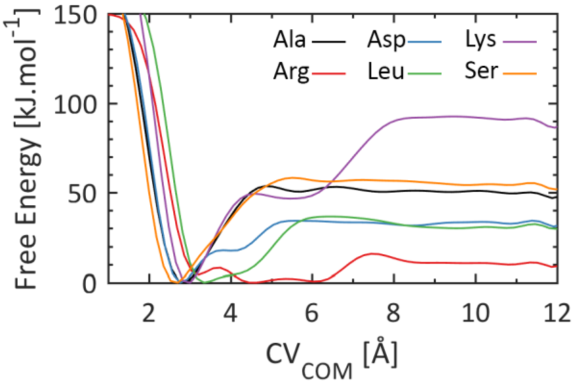

Figure 5.3 Free energy profile as a function of the CV_{COM} (distance of the center of mass of amino acid from the surface).

5.3.3 Free energy profile after reweighting

The nature of the adsorption mode can be further understood by reconstructing the free energy of adsorption with respect to the backbone and the side group using a reweighting method[42] as explained in the following. It is important to note that increasing the dimensionality of the CV space during reweighting can lead to limitations and that directly performing well-tempered metadynamics using $CV_{Backbone}$ and CV_{Side} would be preferable, although computationally much more intensive. We hence use reweighting here, as a means of projecting results of CV_{COM} into the two-dimensional space of $CV_{Backbone}$ and $CV_{Side.}$ It should also be noted that we tried reweighting using two separate collective variables for the amine and the carboxyl group but the small and almost constant distance between these two groups makes these two collective variables correlated. As the collective variables in metadynamics should be independent, the amine and carboxyl groups, along with C_α and its hydrogen, were considered as the backbone group while the remaining part of the amino acid was considered as the side group (see blue and red coloring in Figure 5.1, respectively).

The free energy landscape as a function of the $CV_{Backbone}$ and the CV_{Side} is shown in Figure 5.4. All the amino acids show an energy minimum where both the $CV_{Backbone}$ and the CV_{Side} are small (point A). In such a conformation, both the backbone and the side group are involved in the adsorption of the amino acid on the surface. An energy minimum at point S (small CV_{Side} and large $CV_{Backbone}$) represents adsorption of the amino acid via only its side group while an energy minimum at point B (small $CV_{Backbone}$ and large CV_{Side}) represents the adsorption of the amino acid only via the backbone.

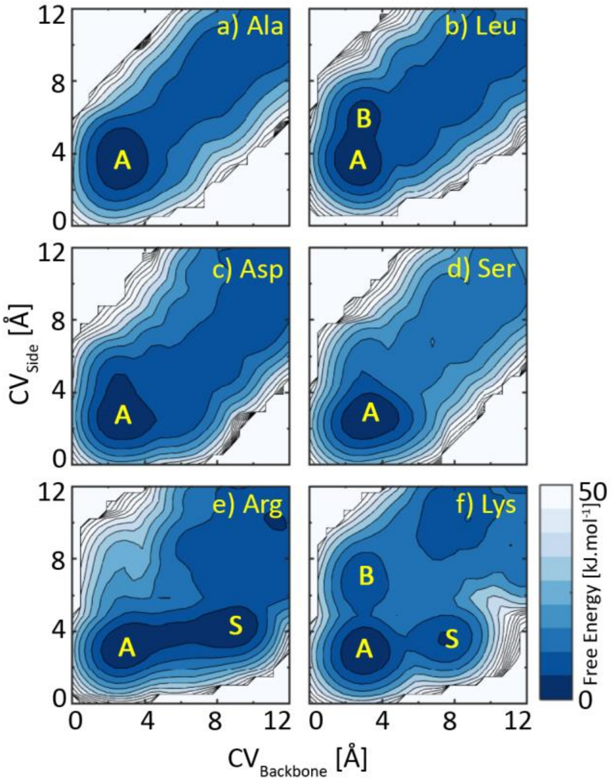

Figure 5.4 Free energy landscape as a function of $CV_{Backbone}$ and CV_{Side}, which are the distance of the center of mass of the backbone and the side group from the surface, respectively for a) Ala, b) Leu, c) Asp, d) Ser e) Arg and f) Lys. Points A, B and S are adsorption via A: both backbone and side group, B: backbone and S: side group.

The free energy map in 2D (Figure 5.4) can be further clarified by using the radius of gyration (R_g) of the individual amino acids (Figure D.5a). Here, we discuss the adsorption behavior of amino acids in increasing order of R_g which is Ala, Ser, Asp, Leu, Lys and Arg; the values are reported in Table 5.1 and are obtained from performing molecular dynamics simulations on a box of water containing single amino acids (Figure D.5b). Ala, as the amino acid with the smallest R_g, shows a single energy well at point A in which the adsorption seems to be via both the backbone and the side group (Figure 5.2a-i and ii). However, close observation of Figure 5.2a reveals that in the adsorbed state, most of the time, the adsorption is directly driven by the amine group (Figure 5.2a-iii). We can also see in Figure 5.4a that the energy minimum of Ala at point A is extended vertically, which shows that in this adsorption conformation, the side group is further from the surface than the backbone. So, the dominant adsorption mode of Ala is rather with the amine group in the backbone than the backbone and side groups together.

Table 5.1 Radius of gyration, adsorption energy on the surface and normalized desorption rates for the amino acids.

Amino acid	R_g [Å]	ΔE_{ads} $[kJ \cdot mol^{-1}]$	${r_{des}}/{A}$
Ala	1.87 ± 0.02	50.14	3.53 * 10-9
Leu	2.40 ± 0.03	30.92	6.13 * 10-6
Asp	2.08 ± 0.02	32.83	2.92 * 10-6
Ser	1.99 ± 0.03	54.92	5.52 * 10-10
Arg	3.18 ± 0.10	< 4 Å: 3.89 4-8 Å: 10.52	2.21 * 10-1 1.68 * 10-2
Lys	2.90 ± 0.07	91.06	4.46 * 10-16

Ser has a slightly larger R_g compared to Ala and as seen in Figure 5.2d-i, ii, iii, it can adsorb either via the side group or the side group and the backbone. The fact that we observe only one energy minimum for Ser at point A, similar to Ala, is due to its small size, which does not allow us to resolve other possible energy minima such as B and S. For Asp, we observe that the energy minimum at point A is extended both vertically towards the region of adsorption via the backbone and horizontally towards the region of adsorption via the side group. However, it seems that the size of Asp is still too small for the energy minimum to be separated from each other. In summary, for smaller amino acids (Ala, Asp and Ser), in our setup, the small R_g prevents the formation of a noticeable energy minimum other than point A even if either of the side group or the backbone are mainly driving the adsorption.

Leu exhibits a similar behavior to Ala; in the adsorbed state, the adsorption is direct via the backbone (Figure 5.2b-i, ii and iii). The larger size of Leu allows the formation of the energy minimum at point B. Arg and Lys exhibit several energy minima, as well. One would expect similar free energy landscapes for Arg and Lys due to their similarity in having a positively charged side group but the minimum at point B does not appear for Arg. One explanation could be that since Arg has a larger R_g than Lys (Figure D.5), in cases where the backbone is adsorbed on the surface, the larger R_g of Arg (or eventually its longer chain) provides it with more flexibility, which makes it possible for the side group to undergo conformational changes and find a second adsorption site on the surface (Figure 5.2e-i). Consequently, we believe that the adsorption via the backbone generally leads to the concurrent adsorption of the side group on the surface and so, point B is not present for Arg. Nevertheless, Figure 5.2e-ii represents adsorption of Arg via the backbone, which is transient as it eventually is accompanied by the adsorption of the side group. For Lys, on the other hand, the side group is slightly shorter which reduces its flexibility compared to Arg. As a result, we observe adsorption via a single group (backbone or side group) and both these groups for this amino acid (Figure 5.2f-i, ii, iii), which is reflected by the presence of three distinct energy minima.

Figure 5.4 also helps us to understand different free energy landscapes, which were observed in Figure 5.3. As already mentioned, we see that for small amino acids, separate energy minima do not form and consequently, Ala, Ser and Asp show one major energy well in Figure 5.3. Similarly, we can now explain why the other three amino acids show multiple or broader energy wells in Figure 5.3. Thus, we show that using only $\mathrm{CV}_{\mathrm{COM}}$ is not sufficient in studying the detailed adsorption behavior of amino acids especially with a larger size.

To compare the adsorption conformation of different amino acids more quantitatively and discuss the adsorption conformations in more details, we replot Figure 5.4 in 1D, where the free energy is projected along each collective variable (Figure 5.5). In Figure 5.5, the deep well at distances less than 5 Å from the surface, for all amino acids, points to the energy minimum at point A in Figure 5.4. For Ala, Asp and Ser, free energy along the CV$_{\text{Backbone}}$ is very similar to the free energy along the CV$_{\text{Side}}$ which is due to their small R_g which causes them to possess one major energy well (Figure 5.3 and Figure 5.4). For Ala, we observe that the deep energy well of the backbone (Figure 5.5a in blue) is closer to the surface than that of the side group (Figure 5.5a in red) which is the other way around for Ser. This again shows that in the adsorbed state, the backbone is closer to the surface than the side group for Ala, but the side group is closer than the backbone for Ser (Figure 5.2a-iii and 2-d-ii). This is attributed to the non-polar and polar nature of the Ala and Ser side group, respectively.

The energy wells along the collective variables are labeled in Figure 5.5 in accordance with Figure 5.4. As mentioned before, Arg is slightly longer than Lys and this can be seen in Figure 5.5 where the distance of the energy minimum at point S for Lys is closer to the surface compared to Arg. For Lys side-group adsorption is more favorable than backbone adsorption with an energy difference of 1.72 $kJ \cdot mol^{-1}$ and is less favorable than the double adsorption with an energy difference of 7.87 $kJ \cdot mol^{-1}$.

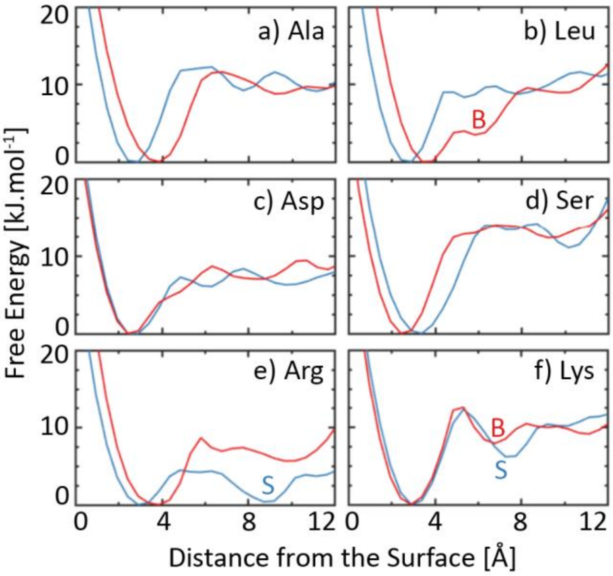

Figure 5.5 Free energy profile projected along only one collective variable (CV$_{Backbone}$: blue: and CV$_{Side}$: red). 'B' is the energy minimum along CV$_{Side}$ and 'S' is the energy minimum along CV$_{Backbone}$, for a) Ala, b) Leu, c) Asp, d) Ser e) Arg and f) Lys.

5.3.4 Desorption rate from the surface

In Table 5.1, we also report the energy gain of amino acids during the adsorption (ΔE_{ads}), which is the difference between the solvated state (distances larger than 8 Å from the surface) and the global energy minimum (normalized to 0 $kJ \cdot mol^{-1}$ for all the amino acids) in Figure 5.3. Only for Arg, adsorption and desorption seem to be separated by an intermediate energy barrier close to 4 Å (Figure 5.3). Therefore, for Arg, we mention the depth of energy well at two regions: before 4 Å and between 4 and 8 Å. From Table 5.1, we see that ΔE_{ads} for Ala and Ser is similar. For Asp, we only observe an energy minimum at point A in Figure 5.4. However, ΔE_{ads} of Asp on the surface is smaller than for Ala and Ser, the reason for which we think is the repulsive electrostatics between the charge point on the surface and the side group of Asp, which make the adsorption less favorable.

The smaller $\Delta E_{ads}$of Leu compared to Ala, which both have non-polar side groups, might be because the Ala side group contains one methyl group (CH_3) while Leu contains two. The non-polar side groups might be trying to avoid the well-defined water structure close to the rutile surface more in the case of Leu with two methyl groups compared to Ala. Even though both Arg and Lys have a side group with a +1 e charge, they are different in their functional groups; Arg ends with two NH_2 groups while Lys has one NH_3 group (Figure 5.1). While the Lennard-Jones interactions, which describe the interaction of these group with other atoms, are similar for both Arg and Lys, the nitrogen and hydrogen atoms are more negative and positive, respectively, in Arg compared to Lys.

ΔE_{ads} for Lys is larger than for all other amino acids. Since this amino acid has a stable adsorption via the side group or via the backbone, the addition of these two results in a larger energy gain when we study the adsorption using CV_{COM}.

Given the barrier-less adsorption profiles, we can use ΔE_{ads} and the transition state theory to have an insight into the desorption rate of amino acids from the surface. The rate constant of a transition with an activation energy of ΔE can be described as $A\exp(-\Delta E/_{k_B T})$; where A is a pre-exponential factor describing the attempt rate, and k_B and T are the Boltzmann constant and temperature, respectively.[49] The coefficient A is the temperature-dependent rate prefactor and is typically in the range of 10^{13}-10^{14} $[1/s]$. In order to avoid the problem of choosing a specific value for the pre-exponential factor, we present the desorption rate of amino acids from the surface, normalized by A, in Table 5.1 which is unit-less. If we were to consider a value for A, it will be the same value for all rate constants of amino acids.

5.3.5 Amino acid-Water interactions

During the adsorption process, the binding groups of the amino acids have to lose some of their associated water molecules. To see which amino acids have a stronger association with water, we can look at the radial distribution function of the amine, carboxyl and side groups with respect to the oxygen of water. For this analysis, we performed unbiased molecular dynamics simulation of the individual amino acids solvated in water. The radial distribution functions between the amine group and the carboxyl group with the oxygen of water (shown in Figure D.6) are similar for all the amino acids. Figure 5.6 shows the radial distribution function between the side group (atoms with outline fonts in Figure 5.1) and oxygen of water. For Arg, Asp and Leu, the radial distribution function is plotted only for one of the atoms of the side group shown with outline font (Figure 5.1). The absence of a significant peak for Ala and Leu, at distances closer than 4 Å, is due to their hydrophobic nature. The polar and charged amino acids show strong interaction with water molecules. Asp shows the strongest interaction with water molecules which is due to the side group consisting of bare oxygens while in Arg, Lys and Ser functional groups, the oxygens are bonded to hydrogen atoms. The difficulty for the side group to lose some of its associated water is related to the energy difference between the maximum and the local minimum in Figure 5.5 (on the CV_{Side} plot). This increases in the order of Ser, Arg, Lys, Asp which is in agreement with Figure 5.6. This can help us also explain the trend of ΔE_{ads} in Table 5.1 where, we see that for example, the adsorption of Asp on the surface is accompanied with a larger energy compared to that of Arg.

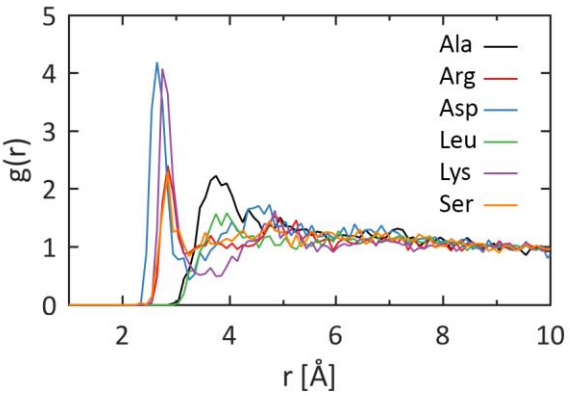

Figure 5.6 Radial distribution function of the side group with water (OW).

5.4 Summary

As mentioned in the introduction, to the knowledge of authors, most of the computational work on the adsorption of amino acids on surfaces only considers the side group. Thus, it is difficult to directly compare our results with those in the literature. Nevertheless, in general based on the literature, it seems that on a charge neutral surface, Ser has a high affinity for the surface and on a charged surface, amino acids with an opposite charge to the surface show higher affinity. The non-polar amino acids show a low affinity for surfaces. Our results are in agreement with these observations thus validating the use of the reweighting method for our system. Using this method, we were able to extract more information from our well-tempered metadynamics simulations and to explain the free energy changes associated with the adsorption of amino acids on the rutile (110) surface.

Compared to the results of Sultan *et al.*[26] and Brandt *et al.*[27] (the latter being for the (100) surface and not the (110) surface), which show that non-polar side chain analogues have a very weak or even repulsive interaction with the surface, we argue that when considering the entire amino acid, the adsorption can occur even for these amino acids, which is in agreement with the work of Tran *et al.*[24] where the adsorption of Ala on the titanium oxide surface was observed. To address the questions posed in the introduction, on whether the interaction of amino acids with the surface is thoroughly electrostatic, or is driven only via the side group, we believe that the electrostatic interactions are important since they can lead to the adsorption of the backbone of the amino acid even if the side group is non-polar. We also show that the adsorption of an amino acid on a charged surface can be via the backbone, as it contains charged amine and carboxyl groups. There is a competitive adsorption between water and the amino acids on the surface. The high hydrophilicity of the surface leads to strongly structured water layers to an extent where only polar and charged side groups but not non-polar side groups are able to traverse the water layer and directly bind to the surface.

5.5 Conclusion

We have studied the adsorption of six amino acids – covering polar, non-polar and charged side groups – onto a negatively charged rutile (110) surface using metadynamics in the presence of water. Our metadynamics simulations reveal that if we consider only the distance of the center of mass of an amino acid to the surface as the collective variable, it does not provide sufficient details on the adsorption conformation to allow us to differentiate between different adsorption modes. Using the reweighting method, we project the free energy into a space of two collective variables, the distances of the backbone (carboxyl, amine, C_α and its hydrogen) and the side group to the surface, and show that the adsorption in the vicinity of a negative charge point can always happen via the backbone (mainly the amine group) irrespective of the type of the side group. This explains why adsorption of amino acids on surfaces was previously reported, even for repulsive or weak interaction of the side group with the surface. The adsorption of amino acids with non-polar side groups is shown to be mainly via their backbone. For polar and charged amino acids, both the backbone and the side group can engage in the binding process and adsorption is robust when the side group has an opposite charge to the surface. Since the rutile surface is hydrophilic, a potential binding site has to lose the strongly orientated water molecules close to the surface to be able to directly bond the amino acid. We observe that only direct binding is stable and no indirect yet stable binding was observed. From the computed energy profiles, relative adsorption strengths and adsorption-desorption kinetics can be estimated via transition state theory to further enhance our understanding of the kinetics of amino acid interactions with surfaces. Experimental studies are currently being undertaken in our laboratory to further validate our results using zeta potential measurements and TGA by obtaining adsorption isotherms.

Supporting Information (Appendix D)

Atomic partial charges of the rutile surface; Lennard-Jones force field parameters for rutile; Error estimation; Water density close to the surface; Radius of gyration of amino acids; Radial distribution functions with water.

References

1. Liu, X.; Chu, P.; Ding, C. Surface Modification of Titanium, Titanium Alloys, and Related Materials for Biomedical Applications. Mater. Sci. Eng. R. 2004, 47, 49–121 DOI: 10.1016/j.mser.2004.11.001.
2. Diebold, U. The Surface Science of Titanium Dioxide. Surf. Sci. Rep. 2003, 48, 53–229 DOI: 10.1016/S0167-5729(02)00100-0.
3. Kasemo, B.; Gold, J. Implant Surfaces and Interface Processes. Adv. Dent. Res. 1999, 13, 8–20 10.1177/08959374990130011901.
4. Kasemo, B. Biological Surface Science. Surf. Sci. 2002, 500, 656–677 DOI: 10.1016/S1359-0286(98)80006-5.
5. Silva-Bermudez, P.; Rodil, S. E. An Overview of Protein Adsorption on Metal Oxide Coatings for Biomedical Implants. Surf. Coat. Technol. 2013, 233, 147–158 DOI: 10.1016/j.surfcoat.2013.04.028.

6. Gertler, G.; Fleminger, G.; Rapaport, H. Characterizing the Adsorption of Peptides to TiO_2 in Aqueous Solutions by Liquid Chromatography. Langmuir 2010, 26, 6457–6463 DOI: 10.1021/la903490v.

7. Zhao, W.; Lemaitre, J.; Bowen, P. A Comparative Study of Simulated Body Fluids in the Presence of Proteins. Acta Biomater. 2017, 53, 506–514 DOI: 10.1016/j.actbio.2017.02.006.

8. Yazdanyar, A.; Aschauer, U.; Bowen, P. Interaction of biologically relevant ions and organic molecules with titanium oxide (rutile) surfaces: A review on molecular dynamics studies. Colloids Surf B Biointerfaces 2018, 161, 563–577 DOI: 10.1016/j.colsurfb.2017.11.004.

9. Dellago, C.; Bolhuis, P. G.; Geissler, P. L. Transition Path Sampling Methods. Lect. Notes Phys. 2006, 703, 349–391 DOI: 10.1007/3-540-35273-2_10.

10. Latour, R. A. Molecular Simulation of Protein-Surface Interactions: Benefits, Problems, Solutions, and Future Directions (Review). Biointerphases 2008, 3, FC2-FC12 DOI: 10.1116/1.2965132.

11. Valsson, O.; Tiwary, P.; Parrinello, M. Enhancing Important Fluctuations: Rare Events and Metadynamics from a Conceptual Viewpoint. Annu. Rev. Phys. Chem. 2016, 67, 159–184 DOI: 10.1146/annurev-physchem-040215-112229.

12. Sutto, L.; Marsili, S.; Gervasio, F. L. G. New Advances in Metadynamics. WIREs Comput. Mol. Sci. 2012, 2012, 2, 771–779 DOI: 10.1002/wcms.1103.

13. Deighan, M.; Pfaendtner, J. Exhaustively Sampling Peptide Adsorption with Metadynamics. Langmuir 2013, 29, 7999–8009 DOI: 10.1021/la4010664.

14. Laio, A.; Gervasio, F. L. Metadynamics: A Method to Simulate Rare Events and Reconstruct the Free Energy in Biophysics, Chemistry and Material Science. Rep. Prog. Phys. 2008, 71, 126601–1:22 DOI: 10.1088/0034-4885/71/12/126601.

15. Barducci, A.; Bonomi, M.; Parrinello, M. Metadynamics. Comput. Mol. Sci. 2011, 1, 826–843 DOI: 10.1002/wcms.31.

16. Barducci, A.; Bussi, G.; Parrinello, M. Well-Tempered Metadynamics: A Smoothly Converging and Tunable Free-Energy Method. Phys. Rev. Lett. 2008, 100, 020603–1:4.

17. Stein, W.; Moore S. The Free Amino Acids of Human Blood Plasma. J. Biol. Chem. 1954, 211, 915–926.

18. Kubiak-Ossowska, K.; Tokarczyk, K.; Jachimska, B.; Mulheran, P. A. Bovine Serum Albumin Adsorption at a Silica Surface Explored by Simulation and Experiment. J. Phys. Chem. B 2017, 121, 3975−3986 DOI: 10.1021/acs.jpcb.7b01637.

19. Notman, R.; Walsh, T. R. Molecular Dynamics Studies of the Interactions of Water and Amino Acid Analogues with Quartz Surfaces. Langmuir 2009, 25, 1638–1644 DOI: 10.1021/la803324x.

20. Hook, F.; Voros, J.; Rodahl, M.; Boni, P.; Ramsden, J. J.; Textor, M.; Spencer, N. D.; Tengvall, P.; Gold, J.; Kasemo, B. A Comparative Study of Protein Adsorption on Titanium Oxide Surfaces Using in Situ Ellipsometry, Optical Waveguide Lightmode Spectroscopy, and Quartz Crystal Microbalance/Dissipation. Colloids Surf. B Biointerfaces 2002, 24, 155–170 DOI: 10.1016/S0927-7765(01)00236-3.

21. Roddick-Lanzilotta, A.; McQuillan, A. J. An in Situ Infrared Spectroscopic Study of Glutamic Acid and of Aspartic Acid Adsorbed on TiO_2: Implications for the Biocompatibility of Titanium. Colloid Interface Sci. 2000, 227, 48–54 DOI: 10.1006/jcis.2000.6864.

22. Roddick-Lanzilotta, A. D.; Connor, P. A.; Mcquillan, A. J. An In Situ Infrared Spectroscopic Study of the Adsorption of Lysine to TiO_2 from an Aqueous Solution. Langmuir 1998, 14, 6479–6484 DOI: 10.1021/la980425n.

23. Tentorio, A.; Canova, L. Adsorption of Alpha-Amino Acids on Spherical TiO_2 Particles. Colloids Surf. 1989, 39, 311–319 DOI: 10.1016/0166-6622(89)80282-3.

24. Tran, T. H.; Nosaka, A. Y.; Nosaka, Y. Adsorption and Photocatalytic Decomposition of Amino Acids in TiO_2 Photocatalytic Systems. J. Phys. Chem. B 2006, 110, 25525–25531 DOI: 10.1021/jp065255z.

25. Schmidt, M. X-Ray Photoelectron Spectroscopy Studies on Adsorption of Amino Acids from Aqueous Solutions onto Oxidised Titanium Surfaces. Arch. Orthop. Trauma Surg. 2001, 121, 403–410.

26. Sultan, A. M.; Hughes, Z. E.; Walsh, T. R. Binding Affinities of Amino Acid Analogues at the Charged Aqueous Titania Interface: Implications for Titania-Binding Peptides. Langmuir 2014, 30, 13321–13329 DOI: 10.1021/la503312d.

27. Brandt, E. G.; Lyubartsev, A. P. Molecular Dynamics Simulations of Adsorption of Amino Acid Side Chain Analogues and a Titanium Binding Peptide on the TiO_2 (100) Surface. J. Phys. Chem. C 2015, 119, 18126–18139 DOI: 10.1021/acs.jpcc.5b02670.

28. Palafox-Hernandez, J. P.; Tang, Z.; Hughes, Z. E.; Li, Y.; Swihart, M. T.; Prasad, P. N.; Walsh, T. R.; Knecht, M. R. Comparative Study of Materials-Binding Peptide Interactions with Gold and Silver Surfaces and Nanostructures: A Thermodynamic Basis for Biological Selectivity of Inorganic Materials. Chem. Mater. 2014, 26, 4960−4969 DOI: 10.1021/cm501529u.

29. Predota, M.; Bandura, A. V.; Cummings, P. T.; Kubicki, J. D.; Wesolowski, D. J.; Chialvo, A. A.; Machesky, M. L.; Pr, M. Electric Double Layer at the Rutile (110) Surface. 1. Structure of Surfaces and Interfacial Water from Molecular Dynamics by Use of *ab Initio* Potentials. J. Phys. Chem. B 2004, 108, 12049–12060 DOI: 10.1021/jp037197c.

30. Machesky, M. L.; Wesolowski, D. J.; Palmer, D. A.; Ridley, M. K.; Bénézeth, P.; Lvov, S. N.; Fedkin, M. V. Chapter 12 Ion Adsorption into the Hydrothermal Regime: Experimental and Modeling Approaches. Interface Sci. Technol. 2006, 11, 324–358 DOI: 10.1016/S1573-4285(06)80056-6.

31. Takahashi, K.; Satoshi, F. Cleanability of Titanium and Stainless Steel Particles in Relation to Surface Charge Aspects. Biocontrol Sci. 2008, 13, 9–16 DOI: 10.4265/bio.13.9.

32. Predota, M.; Machesky, M. L.; Wesolowski, D. J.; Cummings, P. T. Electric Double Layer at the Rutile (110) Surface. 4. Effect of Temperature and pH on the Adsorption and Dynamics of Ions. J. Phys. Chem. C 2013, 117, 22852–22866 DOI: 10.1021/jp407124p.

33. Lundblad, R.; Macdonald, F. Handbook of Biochemistry and Molecular Biology, Fourth Edition. CRC Press 2010.

34. Harris, T. K.; Turner, G. J. Structural Basis of Perturbed pK a Values of Catalytic Groups in Enzyme Active Sites. IUBMB Life 2002, 53, 85–98 DOI: 10.1080/10399710290038972.

35. Berendsen, H. J. C.; Grigera, J. R.; Straatsma, T. P. The Missing Term in Effective Pair Potentials. J. Phys. Chem. 1987, 91, 6269–6271 DOI: 10.1021/j100308a038.

36. Bandura, A. V; Kubicki, J. D. Derivation of Force Field Parameters for TiO_2-H_2O Systems from *ab Initio* Calculations. J. Phys. Chem. B 2003, 107, 11072–11081 DOI: 10.1021/jp034093t.

37. Yong, C. W. Descriptions and Implementations of DL_F Notation: A Natural Chemical Expression System of Atom Types for Molecular Simulations. J. Chem. Inf. Model 2016, 56, 1405–1409.

38. MacKarell, A. D.; Bashford, D.; Bellott, M.; Dunbrack, R. L.; Evanseck, J. D.; Field, M. J.; Fischer, S.; Gao, J.; Guo, H.; Ha, S.; *et al.* All-Atom Empirical Potential for Molecular Modeling and Dynamics Studies of Proteins. J. Phys. Chem. B 1998, 102, 3586–3616 DOI: 10.1021/jp973084f.

39. Allen, M. P.; Tildesley, D. J. Computer Simulation of Liquids. Clarendon Press 1987.

40. Smith, W.; Forester, T. R.; Todorov, I. T. The DL_POLY Classic User Manual. SFTC Daresbury Laboratory; 2012.

41. Tribello, G. A.; Bonomi, M.; Branduardi, D.; Camilloni, C.; Bussio, G. PLUMED 2: New Feathers for an Old Bird. Comput. Phys. Commun. 2014, 185, 604–613 DOI: 10.1016/j.cpc.2013.09.018.

42. Tiwary, P.; Parrinello, M. A Time-Independent Free Energy Estimator for Metadynamics. J. Phys. Chem. B 2015, 119, 736–742 DOI: 10.1021/jp504920s.

43. Skelton, A. A.; Walsh, T. R. Interaction of Liquid Water with the Rutile TiO_2 (110) Surface. Mol. Simul. 2007, 33, 379–389 DOI: 10.1080/17441690701191693.

44. Kavathekar, R. S.; Dev, P.; English, N. J.; MacElroy, J. M. D. Molecular dynamics study of water in contact with the TiO 2 rutile-110, 100, 101, 001 and anatase-101, 001 surface. Mol. Phys. 2011, 109, 1649–1656 DOI: 10.1080/00268976.2011.582051.

45. Liu, L.-M.; Zhang, C.; Thornton, G.; Michaelides, A. Structure and dynamics of liquid water on rutile TiO_2 (110). Phys. Rev. B 2010, 82, 161415(1–4) DOI: 10.1103/PhysRevB.82.161415.

46. Skelton, A. A.; Liang, T.; Walsh, T. R. Interplay of Sequence, Conformation, and Binding at the Peptide−Titania Interface as Mediated by Water. ACS Appl. Mater. Interfaces 2009, 1, 1482–1491 DOI: 10.1021/am9001666.

47. Schneider, J.; Colombi Ciacchi, L. Specific Material Recognition by Small Peptides Mediated by the Interfacial Solvent Structure. J. Am. Chem. Soc. 2012, 134, 2407–2413 DOI: 10.1021/ja210744g.

48. Momma, K.; Izumi, F. VESTA: A Three-Dimensional Visualization System for Electronic and Structural Analysis; 2014.

49. Hanggi, P.; Talkner, P.; Borkovec, M. Reaction-Rate Theory: Fifty Years after Kramers. Rev. Mod. Phys. 1990, 62, 251–342 DOI: 10.1103/RevModPhys.62.251.

5.6 Comparison with the previous chapter

Figure 5.7 summarizes the energetics of interaction of ions and amino acids with a partially negatively charged rutile (110) surface, from results obtained in chapters 4 and 5. In this figure, only the energy gained via the adsorption (adsorption energy) is shown. It is important to note, however, that results presented here are for systems where each ionic or organic species was studied individually and the energetics shown in Figure 5.7, in a system with different species will be affected by the presence of other species. In the systems studied here and in the previous chapter, in general, the adsorption energy of amino acids is more compared to ions (Figure 5.7). In certain cases, for example, when there is already a calcium ion on the surface, the adsorption of another species on the surface, here phosphate, becomes comparable to that of the amino acids. The comparable energetics of adsorption of ionic and organic species on the rutile surface in Figure 5.7, therefore, highlights the importance of considering organic residues in current SBF solution compositions. This is, however, not simple since the effect of the organic species on apatite formation is still not fully understood and controversial observations have been made. The observations strongly suggest that if the organic content were to be introduced to SBF solutions, the necessity and relevance of which is shown by results obtained in this chapter, they should be examined based on their chemical structure, but also their concentration in the SBF solution since:

1. It has been shown that in the presence of albumin the most abundant protein in human blood plasma, the formation of apatite is inhibited. The extent of the inhibition depends on the concentration of albumin in the SBF solution (5).
2. Current SBF solutions contain a high concentration of tris ($NH_2C(CH_2OH)_3$) as the buffering agent (1). Tris is comparable to amino acids in size and molecular weight and under physiological conditions, is positively charged. While preliminary in-house experiments showed that tris adsorbs on the rutile surface and inhibits further adsorption of amino acids on the surface. Still, many *in vitro* tests report apatite formation using the current international standard, in the presence of tris. This suggests that the current concentration of tris in SBF, despite being high, either does not entirely inhibit apatite formation, or there are other parameters affecting the interaction and adsorption of tris on the surface, and the apatite formation. As a first step, the interaction of tris with the surface can be studied using computational methods, similar to the study in this chapter, to understand the affinity of this molecule for the surface better. This will allow one, to compare the affinity of tris for the surface with those of amino acids (this chapter), and to confirm experimental observations, further.

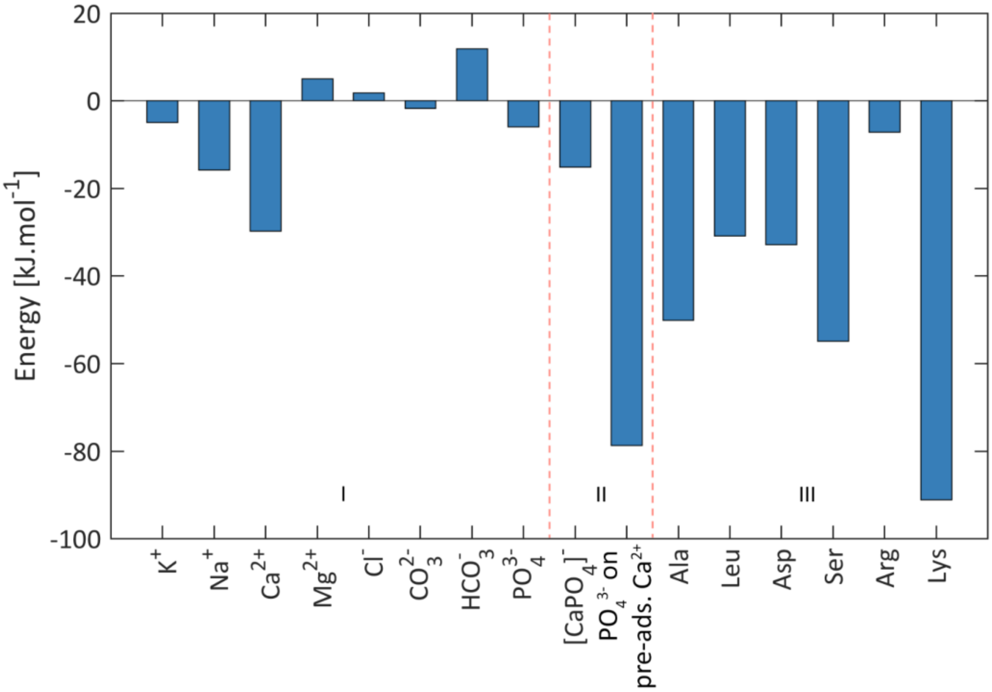

Figure 5.7 The adsorption energy of different ionic species and amino acids on a negatively charged rutile (110) surface with a single charge point. Single ions are shown in section I, the $[CaPO_4]^-$ *ionic pair and phosphate on pre-adsorbed calcium are shown in section II, and amino acids are shown in section III.*

References

1. ISO 23317 - Implants for surgery —*In vitro* evaluation for apatite-forming ability of implant materials. (2007).

2. Marieb, E. N. & Hoehn, K. *Human Anatomy & Physiology: Pearson New International Edition*. (Pearson Education Limited, 2013).

3. Schmidt, J. A. *et al.* Plasma concentrations and intakes of amino acids in male meat-eaters, fish-eaters, vegetarians and vegans: A cross-sectional analysis in the EPIC-Oxford cohort. *Eur. J. Clin. Nutr.* **70,** 306 (2015).

4. Masoudi Rad, H. *et al.* Free amino acids in stimulated and unstimulated whole saliva: Advantages or disadvantages. *J. Oral Rehabil.* **41,** 759–767 (2014).

5. Zhao, W., Lemaître, J. & Bowen, P. A comparative study of simulated body fluids in the presence of proteins. *Acta Biomater.* **53,** 506–514 (2017).

Chapter 6 Competitive adsorption of ions and amino acids on the rutile surface with two different charge densities

This chapter studies the effect of presence of pre-adsorbed species on the interaction of other species with the rutile (110) surface.

In this chapter, the idea is to investigate to what extent an amino acid (or an ion) can influence the interaction or adsorption behavior of an ion (or an amino acid) on the surface. For this purpose, findings of chapters 4 and 5 were used as starting hypotheses to be tested in sections 6.1 and 6.2.

Section 6.1 – In Chapter 5, it was shown that the adsorption of amino acids on a negative charge point on the rutile surface is driven electrostatically. Amino acids with different side groups showed possible adsorption conformation on the surface charge point via their backbone, while only charged and polar amino acids were able to compete with the water layer on the hydrophilic charged rutile surface. Also, results from chapters 4 and 5 revealed that between a single ion and a single amino acid, the energy gain on the rutile surface is usually larger for the adsorption of the amino acid. Based on these findings, the first hypothesis tested was the following. An amino acid has already adsorbed on a negative charge point on the surface via either its backbone or its side group – the favorable adsorption conformation was chosen from Chapter 5 – and the other end of the amino acid is free to interact with ions in the solution. How do the amino acid-surface and ion-surface interactions change if the ion-amino acid interactions are biased? Does the ion compete for the charge point on the surface occupied by the pre-adsorbed amino acid?

Section 6.2 – In Chapter 4, it was shown that the adsorption of calcium ions on the rutile surface is the most favorable among the ions investigated. Based on these findings, a second hypothesis was tested where pre-adsorbed calcium ions occupied the negative charge points on the surface while the distance of several amino acids with the surface was biased. Now, can the incoming amino acid desorb the pre-adsorbed calcium ions from the surface? Or does the presence of calcium ions affect the interaction of the amino acids with the surface and their adsorption behavior?

The simulations performed are explained in detail in sections 6.1 and 6.2 but are also summarized in Figure 6.1. As it can be seen in this figure, two different surface charge densities were tested, one with a single charge point (Figure 6.1a), similar to those used in previous chapters (-0.012 $C \cdot m^{-2}$ – the singly deprotonated surface), and one with 18 charge points (Figure 6.1b), similar to the physiological surface charge density of rutile (-0.104 $C \cdot m^{-2}$). The initial state of the simulation system, and the collective variables used in each section are shown schematically in Figure 6.1. As the tests proceeded, it was seen that some used setups were causing artefacts in the system (section 6.2, in specific), which will be discussed in detail later in this chapter. Therefore, the results in this chapter are preliminary and should be interpreted with care while they suggest future directions.

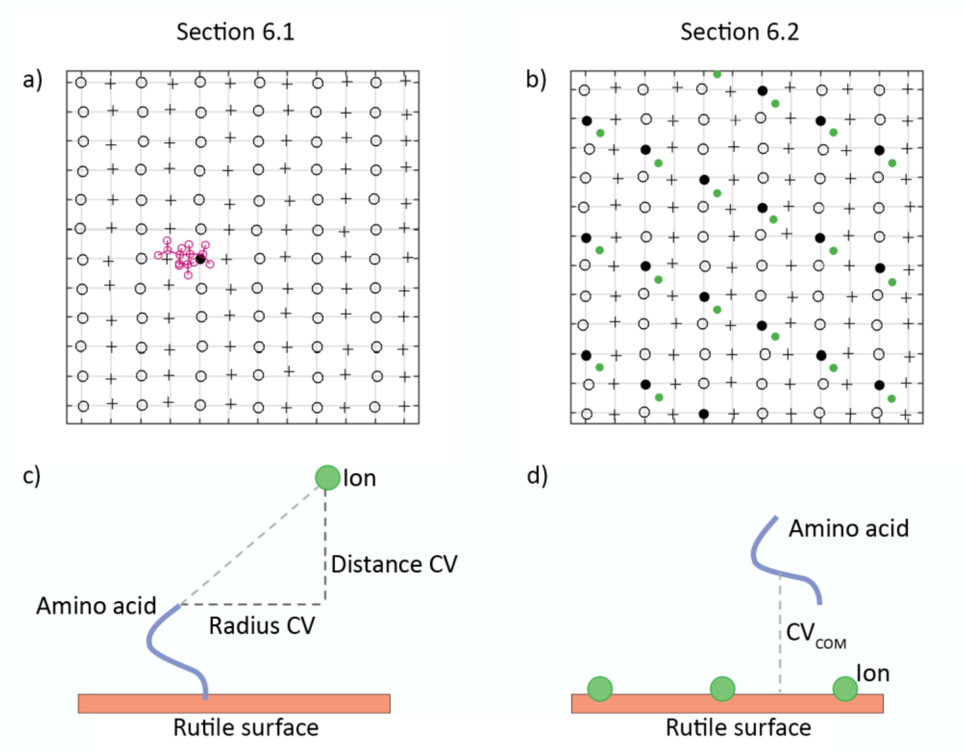

Figure 6.1 Top view of the rutile surface and the position of the pre-adsorbed species on the surface (a and b). Terminal hydroxyls are shown via plus signs, bridging hydroxyl via circles, and deprotonated bridging hydroxyls via filled black circles. In (a) an amino acid is pre-adsorbed on the surface (pink) where in (b) calcium ions are pre-adsorbed on the surface (green). Initial state of the simulation box and the collective variables used (c and d).

6.1 Interaction of ions with amino acids pre-adsorbed on a rutile surface

6.1.1 Approach

6.1.1.1 Initial configuration of the simulation box and choice of amino acids

Arg (with the positive side group) and Asp (with the negative side group) were used as the pre-adsorbed amino acids. Based on Chapter 5, the preferable adsorption conformation of these amino acids in the vicinity of a negative charge point, is via the side group for Arg, and via the backbone for Asp.

The initial configuration of the simulation box was taken from the trajectories of Chapter 5, with the singly deprotonated surface; for Arg, the simulation box was taken from snapshot shown in Figure 5.2e-iii, and for Asp, it was taken from the snapshot shown in Figure 5.2c-i, which are shown later in Figure 6.4.

6.1.1.2 Choice of ions

To decide between which ions to investigate, initially, Na^{+}, Cl^{-}, Ca^{2+} and PO_4^{3-} were chosen as relevant; the first two, due to their high concentration in SBF solutions, and the other two, due to their relevance to hydroxyapatite. However, the interaction of all these four ions with the pre-adsorbed amino acid was not studied. Instead, to reduce the number of simulations and investigate only those system where the interactions between ions and amino acids are relatively strong, first, the interaction of these ions with the backbone of Gly (glycine) (Table A.1) was studied. Glycine is the smallest amino acid with a single hydrogen atom as its side group. Well-tempered metadynamics simulations were performed to understand the interaction of cations (sodium and calcium) with the carboxyl group and the anions (chlorine and phosphate) with amine group of Gly. The force field parameters of Gly are given in Appendix B. The ion-amino acid interaction parameters were defined using the Lorentz-Berthelot mixing rules.

Four simulations were performed, as summarized in Table 6.1. In each simulation, the ion and the amino acid were solvated in a box of water with a dimension of 30×30×30 $Å^3$. Simulation boxes were first equilibrated for 450 ps at 310 K during which no bias was applied and the ion and the C_α atom of Gly were restrained. The restraints were then removed and well-tempered metadynamics simulations were performed for 20 ns during which the distance between the ion and either the nitrogen atom of the amine group or one of the oxygen atoms of the carboxyl group was biased (Distance CV).

Table 6.1 The collective variable, the equilibrium association distance, and the association energy of ions with the carboxyl group and the amine group of Gly.

System	Collective variable (Distance CV)	Equilibrium association distance [Å]	Association energy $[kJ \cdot mol^{-1}]$
Gly - Ca^{2+}	O_{BB} - Ca^{2+}	2.46	-19.96
Gly - Na^{+}	O_{BB} - Na^{+}	2.55	-7.88
Gly - Cl^{-}	N_{BB} - Cl^{-}	3.33	-4.25
Gly - PO_4^{3-}	N_{BB} - $P_{PO_4^{3-}}$	3.06	-32.24

BB represents the backbone.

The variation of the distance CV for the four systems is shown in Figure 6.2 and the free energy profile as a function of this CV is shown in Figure 6.3. The distance CV at the point of the minimum free energy, or the equilibrium association distance of calcium and sodium with one of the oxygen atoms of the carboxyl group, is 2.46 and 2.55 Å, and for the association of chlorine and phosphate with the nitrogen atom of the amine group is 3.33 and 3.06 Å, respectively.

Compared to sodium, calcium shows a longer residence time when it associates with the carboxyl group of Gly (Figure 6.2a and b). This is due to the larger dissociation barrier of calcium compared to sodium (19.96 and 12.13 $kJ \cdot mol^{-1}$, respectively, based on Figure 6.3), driven by its higher ionic charge. Association of chlorine and phosphate ions is studied via the protonated nitrogen atom of the amine group, while calcium and sodium associate with the bare oxygen in the carboxyl group.

The energy difference between the associated and dissociated states of ions with the backbone groups, or the association energy, is summarized in Table 6.1. Calcium and phosphate are found to have a larger association free energy compared to sodium and chlorine with the backbone groups of Gly. Therefore, these two ions were selected to be studied with pre-adsorbed amino acids on the rutile surface. Nevertheless, sodium and chlorine are much more abundant than calcium and phosphate, under physiological conditions. Although their association may not be as long-lasting as calcium and phosphate, in total, they may associate with the AA (amino acid) for a larger amount of time, simply since there are more in number.

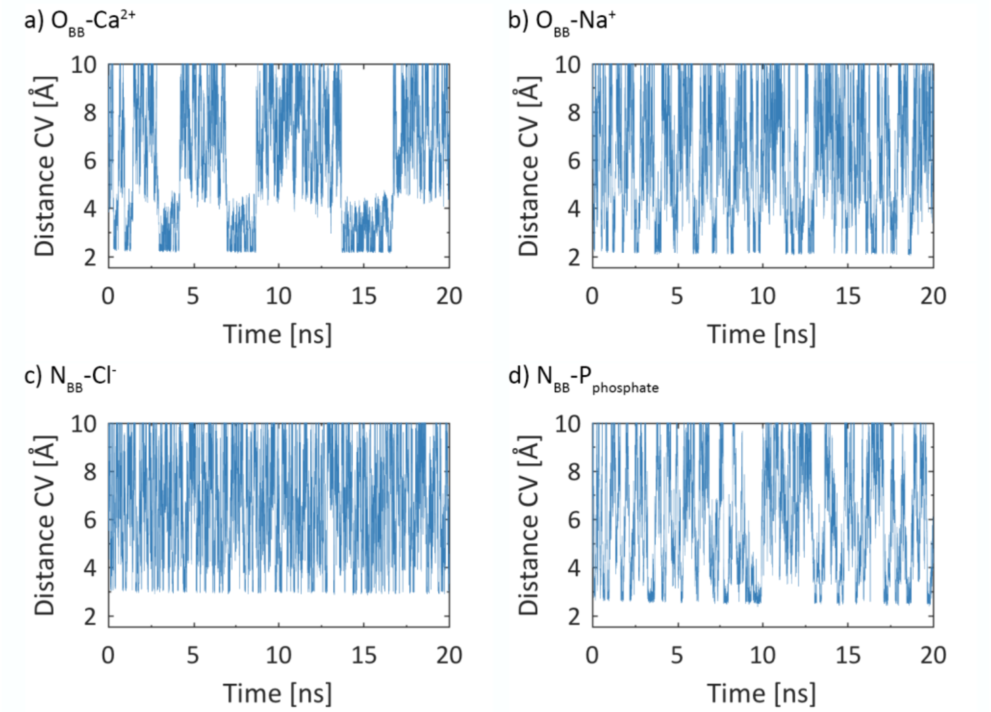

Figure 6.2 Distance CV over the simulation time for a) calcium, b) sodium, c) chlorine and d) phosphate associating with the backbone of Gly.

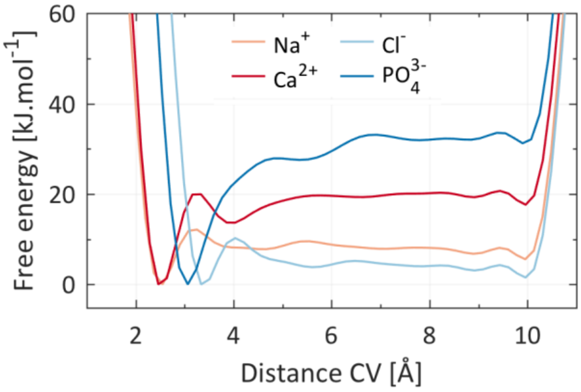

Figure 6.3 Free energy profile of the interaction of sodium and calcium with the Gly carboxyl group, and chlorine and phosphate with the Gly amine group.

6.1.1.3 Choice of amino acid-ion systems

Based on the initial adsorption conformation of amino acids on the surface (Figure 6.4), and the fact that the negatively charged group of Asp, and the amine and carboxyl group of Arg are free for interaction, the following three systems, were considered:

i. Arg $- Ca^{2+}$
ii. Arg $- PO_4^{3-}$
iii. Asp $- Ca^{2+}$

As already mentioned, in these three systems, the amino acids were pre-adsorbed on the surface close to the negative charge point. The ion was initially at a distance of 10 Å from the amino acid. Each simulation box contains one ion and one amino acid which leads to a concentration of 13.8 mM. The total concentration of free amino acids in blood plasma is reported to be 3.7 mM, and for Arg and Asp is 0.051 and 0.066 mM, in specific for meat-eaters (1). The concentration of all calcium and phosphate species in blood plasma is 2.5 and 1.00 mM (table C.1); for free calcium and PO_4^{3-} species, the concentration is 2.4 and 0.000006 mM. Therefore, the simulation box has a higher concentration of species compared to physiological conditions.

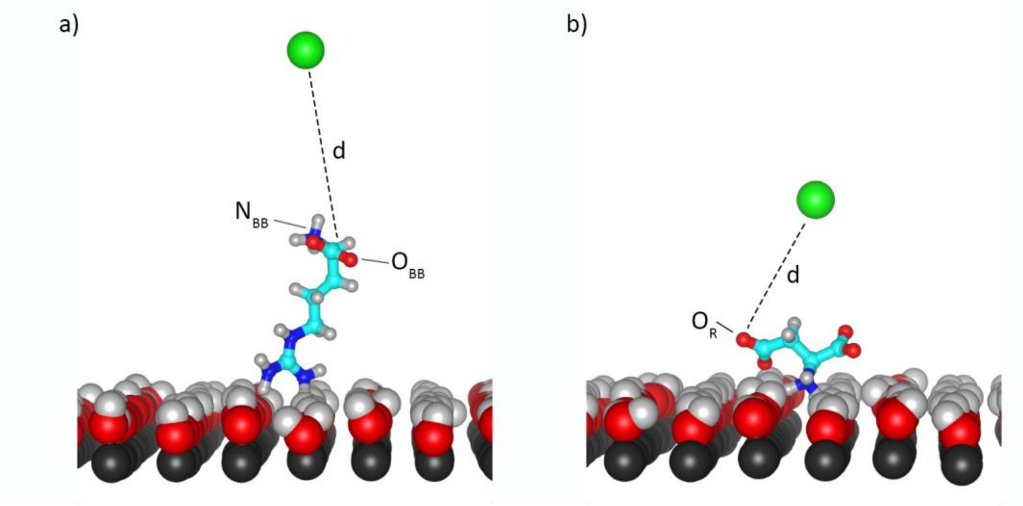

Figure 6.4 Initial conformation of a) Arg and b) Asp, pre-adsorbed on the rutile surface close to surface charge point. The ion was initially put at a distance of 10 Å from the amino acid.

6.1.1.4 Choice of collective variables and simulation details

As shown in Figure 6.1, neither the distance of the ion from the surface nor the distance of the amino acid from the surface were biased, but rather the distance between the ion and the amino acid (as shown in Figure 6.1c). Two collective variables were chosen for the well-tempered metadynamics simulation (Figure 6.1). Upper limits were applied to the collective variables as specified in Table 6.2. The atoms on the amino acids to which the collective variables are defined, are summarized in Table 6.2 and specified in Figure 6.4. Contrary to chapters 4 and 5, none of the ions or atoms of the amino acids were confined in a cylinder around the charge point since the bias is applied between the ion and the amino acid and does not involve the surface.

Table 6.2 Collective variables used for the interaction of ions with pre-adsorbed amino acids.

System	Biased distance (d)	1st CV (Distance CV)	2nd CV (Radius CV)
Arg – Ca^{2+}	$O_{BB} - Ca^{2+}$		
Arg – PO_4^{3-}	$N_{BB} - PO_4^{3-}{}_{COM}$	d_z < 12 Å	$\sqrt{d_x^2 + d_y^2}$ < 8 Å
Asp – Ca^{2+}	$O_R - Ca^{2+}$		

BB: Backbone, R: Side group

Systems were equilibrated for a total time of 300 ps during which no bias was applied. The ion and C_α of amino acids were restrained during the equilibration period. The amino acids preserved their adsorbed conformation during equilibration. Simulations were performed for 30 ns at 310 K. The initial height of Gaussians was 1.0 $kJ \cdot mol^{-1}$ and were deposited every 2,000 steps (1.2 ps for the system with phosphate and 1.4 ps for systems with calcium) with a bias factor of 15. The width of Gaussians was 0.5 and 1 Å for the distance CV and radius CV, respectively.

6.1.2 Results and discussion

In the following, results are discussed in the order of: Arg-Ca^{2+}, Arg- PO_4^{3-} and Asp- Ca^{2+} systems. Here, the biased distance (d in Table 6.2) is shown for all the three systems in Figure 6.5. Based on Figure 6.3 and Table 6.1, the equilibrium association distance of ions with amino acid groups, in their minimum free energy point, is also plotted (dashed line) in Figure 6.5. As it can be seen in this figure, phosphate approaches the amine group more frequently than calcium approaching the carboxyl groups. This is in agreement with Figure 6.3, where the former does not show any specific energy barrier of association while the latter requires an energy barrier of $\sim 6\, kJ \cdot mol^{-1}$ to be crossed. However, many of the attempts of phosphate to associate with the amine group are transient, while associations of calcium with the carboxyl group last longer. This can be due to the fact that phosphate approaches the fully protonated nitrogen atom of the amine group while calcium interacts with the bare oxygen in the carboxyl group.

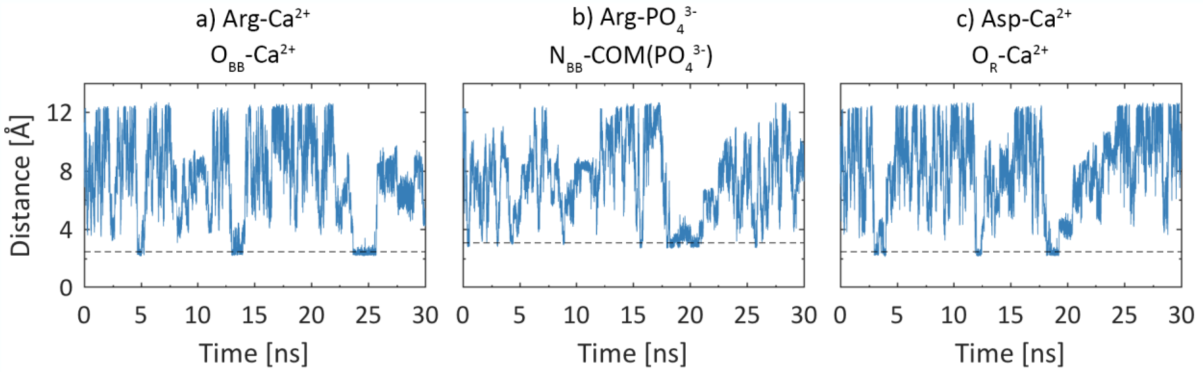

Figure 6.5 Biased distance for the three systems studied in this section. For each system, the distance between the atoms written on the figure, is plotted. The dashed lines for Arg-Ca^{2+} and Asp- Ca^{2+} system correspond to the O_{BB}-Ca^{2+} distance at the energy minimum in Figure 6.3, and for the Arg-$P_{PO_4^{3-}}$ system correspond to the N_{BB}-$P_{PO_4^{3-}}$ distance at the energy minimum in Figure 6.3.

In the following, the ion-AA, ion-surface and AA-distances, are shown and will be discussed. Since it is easier to analyze results with the surface as a reference point, the ion-AA distance (Figure 6.5) will be shown using a color map, where smaller biased distances will be shown with darker colors (panel b in Figure 6.6 to Figure 6.8).

Considering that the closest water layer to the surface is at a distance of approximately 2.3 Å, the ions were considered to be directly adsorbed on the surface, with no intermediate water molecule, if the ion (calcium) or any of its atoms (phosphate) were closer than 2.5 Å to the surface. For the amino acids, the distances of the following atoms are considered: nitrogen atom of the backbone, average of the oxygen atoms of the backbone, average of the nitrogen atoms or the oxygen atoms of the side group, for Arg and Asp, respectively. Since the nitrogen atoms of the amine group are bound to hydrogen, and for the carboxyl groups and side groups, average values are considered, for the sake of consistency, a group of an amino acid was considered adsorbed if it was closer than 4 Å to the surface.

6.1.2.1 Interaction of Ca^{2+} with pre-adsorbed Arg

The distance of main atoms of the backbone and side group of Arg, and calcium, from the surface, as well as the color map showing the calcium-amino acid distances, are shown in Figure 6.6, in a, c and b, respectively.

During the simulation time, the ion and the amino acid can be either adsorbed on the surface or solvated in water. Therefore, at any given point in time, the system is in one of the following states:

i. Only the AA is adsorbed
ii. Both ion and AA are adsorbed, irrespective of their relative adsorption site to each other
iii. Only the ion is adsorbed
iv. Neither the AA nor the ion are adsorbed

Since, in this section, initially the AA is pre-adsorbed on the surface and the ion is at a distance of 10-15 Å from the surface, all simulations are initially in state i. Thereafter, the bias will be acting on the ion-AA distance until it can change the state of the system from i.

Based on the states defined above, the simulation time was divided to different states, as shown with grey lines in Figure 6.6. The prime notion in this figure is used to distinguish between same states, occurring again (for example, i and i'). Since in this chapter, the competitive adsorption of species on the surface is of interest, the top view of the adsorption of the ion and AA on the surface, over the simulation time, is also shown in Figure 6.6. If any of the atoms of interest of the amino acid (nitrogen of the amine group, oxygens of the carboxyl group, or the side group) were in the adsorbed state, then the position of center of mass of the amino acid is plotted in this figure.

During state i, Arg stays close to the charged site on the surface (OS) (Figure 6.6i). The transition between states i and ii, occurs after around 9 ns. As it can be seen in Figure 6.6ii, calcium does not adsorb close to OS but rather far from it. This means that calcium does not compete with Arg for the charged site on the surface (OS).

During state ii, Arg stays adsorbed on the surface but as it can be seen, the center of mass of the molecule is displaced on the surface towards calcium (Figure 6.6ii). This is due the bias acting on $O_{BB} - Ca^{2+}$. Interestingly, the bias is able to move the adsorbed amino acid around on the surface, but not the adsorbed calcium ion. From state ii, the system can either transition to state i by desorbing the ion, which has a desorption barrier of 39.03 $kJ \cdot mol^{-1}$, as measured in Chapter 4, or to state iii, by desorbing the amino acid, which for Arg is 15.82 $kJ \cdot mol^{-1}$, as measured in Chapter 5. For the Arg $- Ca^{2+}$ system, the bias was able to desorb Arg from the surface, from its preferable adsorption conformation (via the side group, as seen in Chapter 5) at $t \sim 16\, ns$, in agreement with its lower desorption barrier estimated in previous chapters. During state iii, the bias is able to bring Arg close to the surface where Arg attempts adsorption on the surface a few times (Figure 6.6iii-right side). These attempts, although close to calcium, are not successful and result in Arg being solvated in water.

Eventually, at $t \sim 22.5\, ns$, Arg is able to re-adsorb on the surface; since the bias is applied between the backbone of Arg and the calcium ion, which is on the surface, the initial adsorption in this stage occurs via the backbone. The adsorption is now stable and the adsorption site is between OS and calcium. During state ii′, Arg walks on the surface, initially by its backbone close to the surface but eventually, Arg is able to change its conformation to the more favorable conformation, which is by its side group on the surface (Chapter 5). Before changing its conformation, the bias is able to displace calcium on the xy-plane (to the left; Figure 6.6ii') but calcium eventually returns to its original adsorption site.

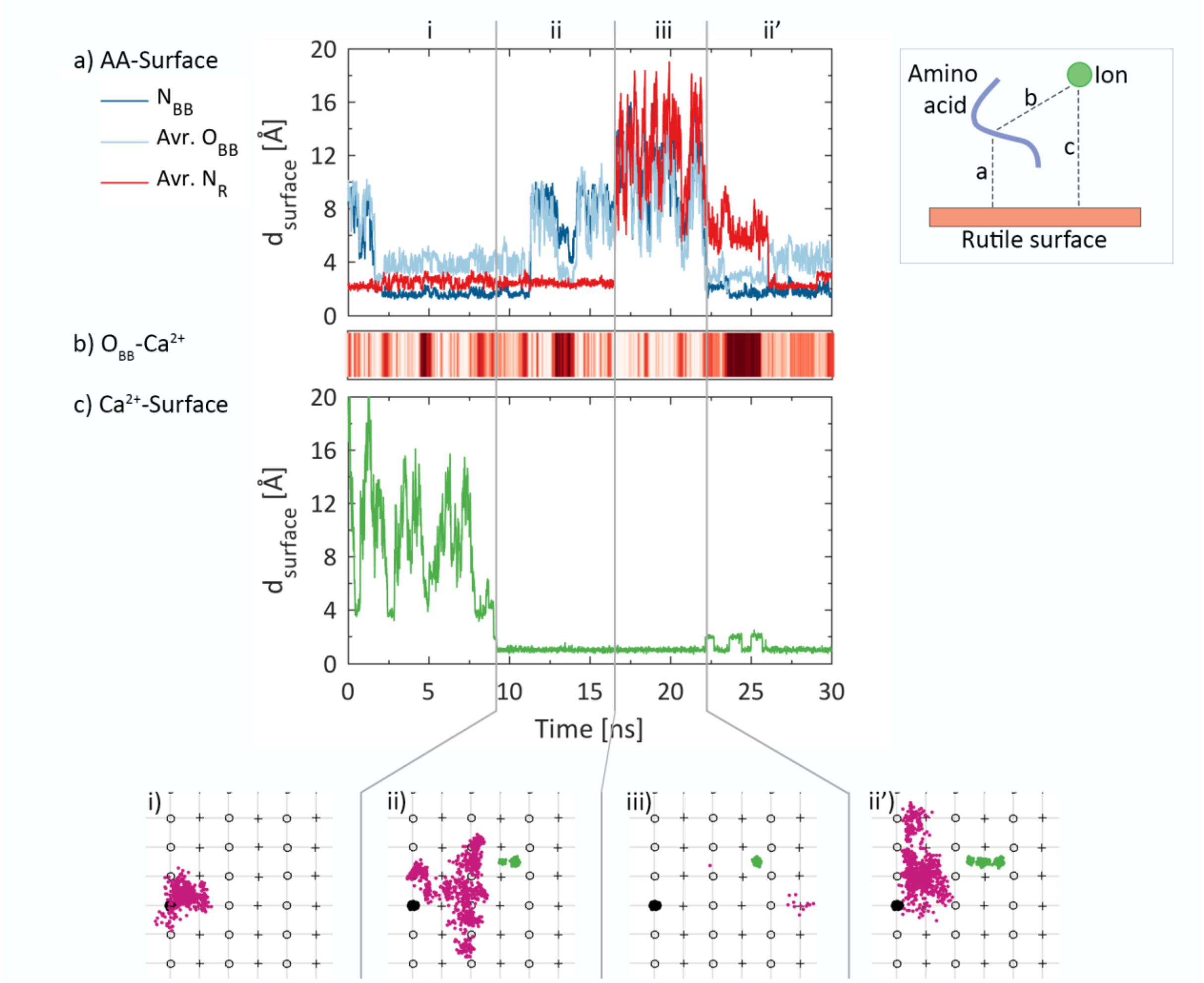

Figure 6.6 Distance of a) Arg from the surface, b) Arg atom from calcium (biased distance), darker color corresponds to a smaller value, and c) calcium from the surface. Different states are divided by grey lines. Top view distribution of Arg$_{COM}$ (pink) and calcium (green), in the xy-plane, when adsorbed on the surface in each state are also shown. The average in-plane position of the oxygen atoms of the bridging and terminal hydroxyl groups are shown via circle and plus signs, respectively. The negative charge point is shown via the filled black circle.

6.1.2.2 Interaction of PO_4^{3-} with pre-adsorbed Arg

The distances of Arg and phosphate from the surface, the biased distance (d in Table 6.2) as well as their distribution on the surface in their adsorbed states, are shown in Figure 6.7, in a, c and b, respectively. The adsorption of phosphate on the surface occurs very quickly (t = 0.65 n) (Figure 6.7c). The adsorption site is relatively close to OS (Figure 6.7ii) which is in agreement with the findings of Chapter 4, where the adsorption of phosphate was favorable even close to OS.

In contrast to calcium, the bias on the $N_{BB} - PO_4^{3-}{}_{COM}$ distance is able to desorb the ion from the surface during state i' (Figure 6.7i'). In fact, the desorption barrier measured for phosphate in Chapter 4 was 15.75 $kJ \cdot mol^{-1}$, which is well comparable with that of Arg, measured in Chapter 5 to be 15.82 $kJ \cdot mol^{-1}$. There are a few attempts for adsorption by phosphate during state i'. Due to the bias, the adsorption sites of phosphate in this state (i') is closer to OS but the ion cannot find a stable adsorption site. The adsorption of phosphate in state ii', where it is stable, compared to the attempts in the previous state, where it did not succeed, is further from OS. Similar to the Arg $- Ca^{2+}$, when the system is in state iii, where the ion is adsorbed and amino acid is not, the adsorption of amino acid (which can be seen in states ii'' and ii''') occurs somewhere close to the ion due to the bias, and close to the OS due to the attractive electrostatics between the positive side group of Arg and the negative charge point on the surface. Arg is mobile in states ii (ii, ii', ii'', ii''') since its adsorption is driven by the backbone and at the same time, carboxyl group-phosphate distance is being biased.

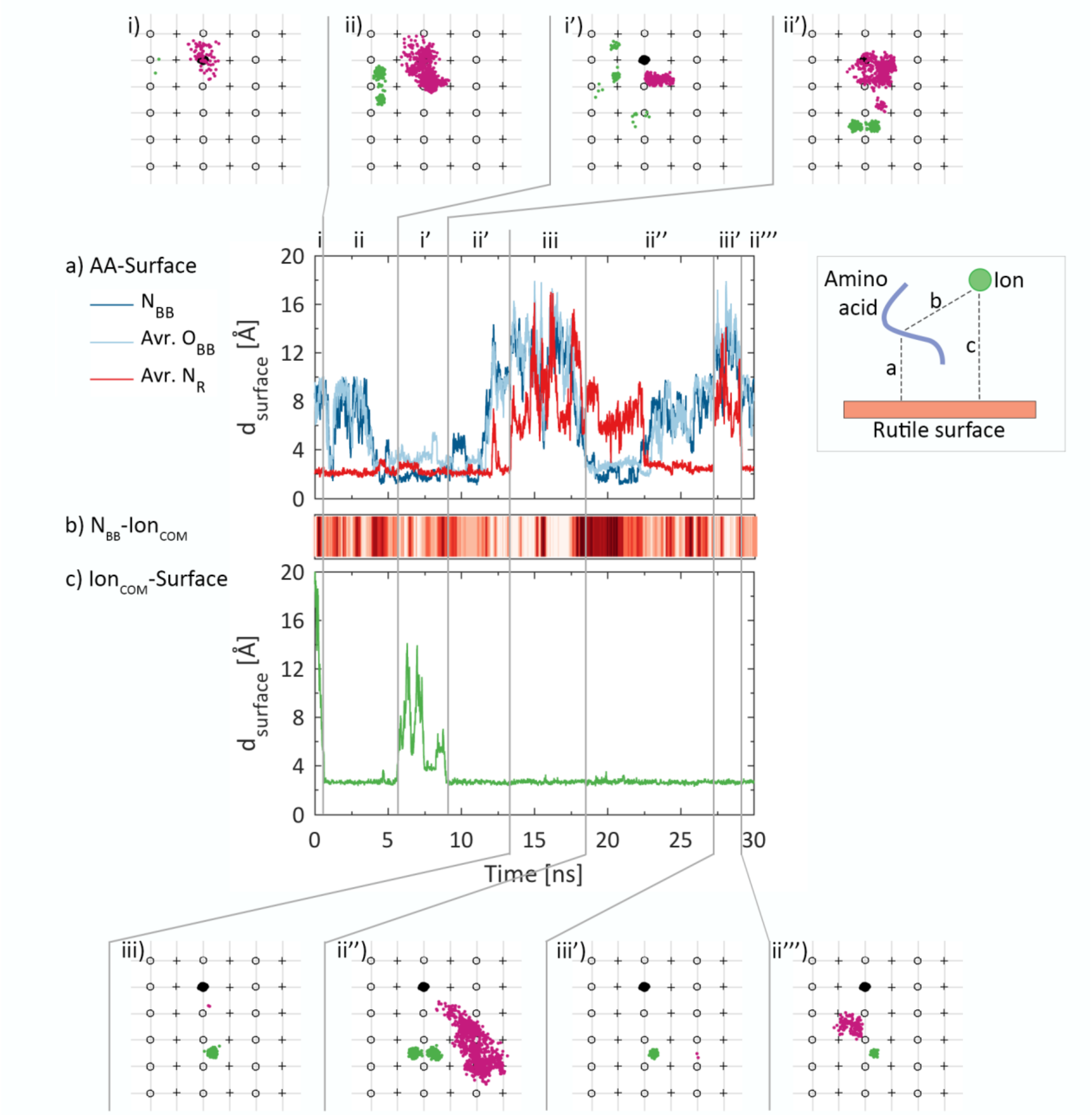

Figure 6.7 Distance of a) Arg from the surface, b) Arg atom from the center of mass of phosphate (biased distance), darker color corresponds to a smaller value, and c) center of mass of phosphate from the surface. Different states are divided by grey lines. Top view distribution of Arg$_{COM}$ (pink) and phosphate$_{COM}$ (green), in the xy-plane, when adsorbed on the surface in each state are also shown. The average in-plane position of the oxygen atoms of the bridging and terminal hydroxyl groups are shown via circle and plus signs, respectively. The negative charge point is shown via the filled black circle.

6.1.2.3 Interaction of Ca^{2+} with pre-adsorbed Asp

Similar plots to those in previous sections are shown for the Asp $-$ Ca^{2+} system in Figure 6.8. During state i, as the system is trying to change the Asp $-$ Ca^{2+} distance, Asp is displaced on the surface. This is due to the less favorable interaction of the surface negative charge point with Asp, with its net negative charge and a relatively small size.

Similar to Arg $-$ Ca^{2+} system, the first adsorption event of calcium on the surface takes some time to occur (at t = 12.4 ns). However, unlike the Arg $-$ Ca^{2+} system, the adsorption site of calcium is next to OS (Figure 6.8ii). Calcium preserves this adsorption site over the simulation time, despite the applied bias. The bias causes Asp, with a desorption barrier 6.2 $kJ \cdot mol^{-1}$ smaller than that of calcium (based on results from chapters 4 and 5 – -32.83 $kJ \cdot mol^{-1}$, in specific) to desorb from the surface during states iii and iii'.

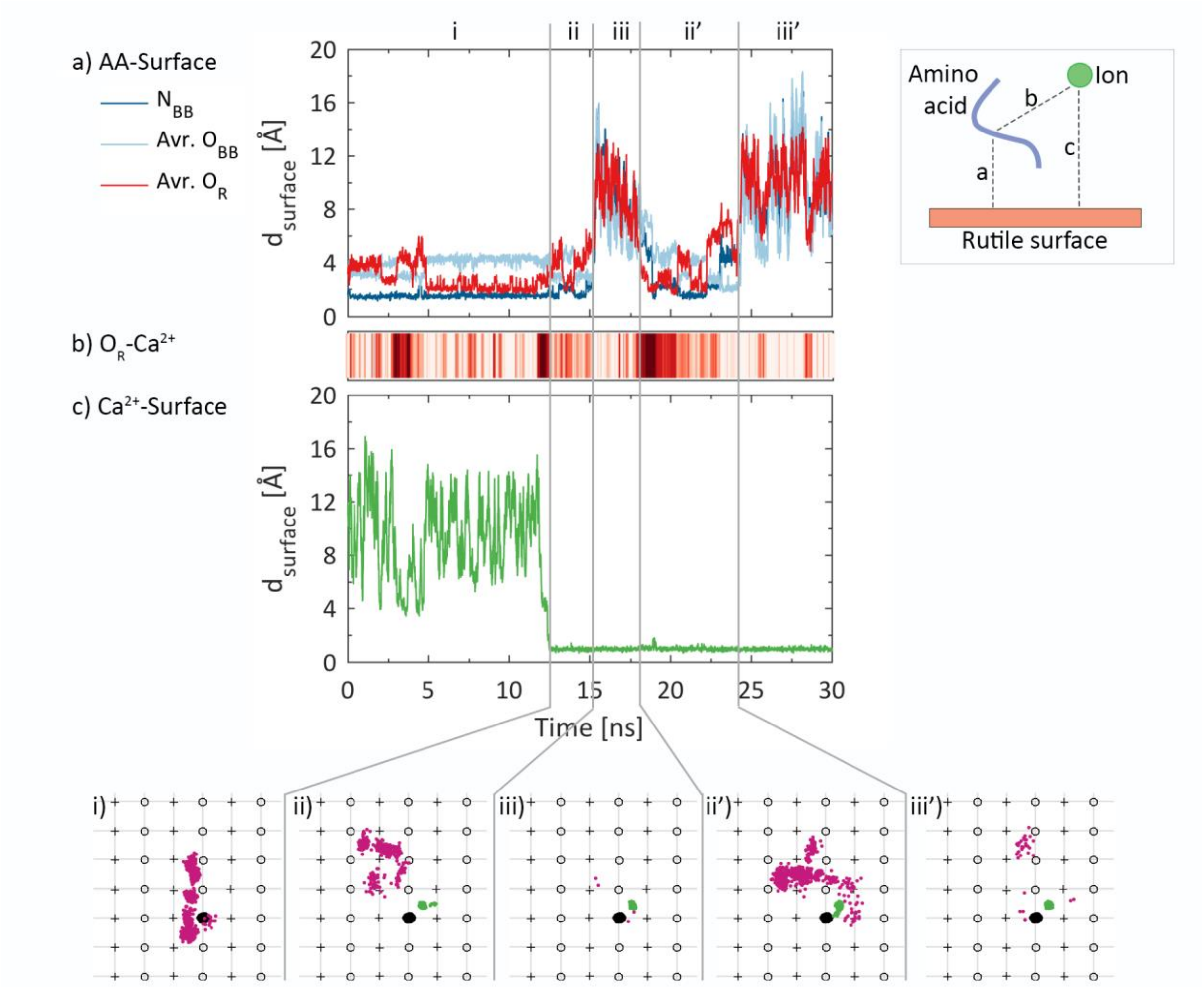

Figure 6.8 Distance of a) Asp from the surface, b) Asp atom from calcium (biased distance), darker color corresponds to a smaller value, and c) calcium from the surface. Different states are divided by grey lines. Top view distribution of Asp$_{COM}$ (pink) and calcium (green), in the xy-plane, when adsorbed on the surface in each state are also shown. The average in-plane position of the oxygen atoms of the bridging and terminal hydroxyl groups are shown via circle and plus signs, respectively. The negative charge point is shown via the filled black circle.

6.1.3 Role of the ion-amino acid distance in their adsorption on the surface

In previous sections, the ion-AA distance over the simulation time was shown as a color map in Figure 6.6 to Figure 6.7, but it was not discussed in detail. All adsorption events, for the three systems are summarized in Table 6.3. If one only considers the value of the biased distance (d in Table 6.2), it seems that adsorption events can take place even when the ion-AA distance is large (*e.g.*, Arg – Ca^{2+} and Arg – PO_4^{3-} systems). However, the amino acid has other groups than the one that the biased distance is defined to. For example, in the case of Arg – Ca^{2+}, the bias is defined between the ion and the carboxyl group of the backbone, but the ion can interact with the amine group and the side group, as well. Therefore, using atomistic trajectories, the distance of the ion from the amine, carboxyl and side groups were examined carefully, and the minimum value of these three values was compared to d. It was observed that d was indeed always the minimum ion-AA distance, except in one case for the Arg – PO_4^{3-} system, where the side group of Arg has a favorable electrostatic interaction with the ion. Therefore, it can be concluded that for Arg – PO_4^{3-} and Asp – Ca^{2+} systems, when one species is on the surface, the small ion-AA distance effectively leads to the adsorption of the other species. However, this is not the case in the Arg – Ca^{2+} system, where in the two adsorption events of Ca^{2+} and Arg at t 9.25 and 22.23 ns, d is not small. Compared to the other two systems, in the Arg – Ca^{2+} system, both species are positively charged and have an attractive electrostatic interaction with the surface, which is believed to be the reason why these species adsorb on the surface, even when the biased distance is relatively large.

Table 6.3 Summary of the adsorption and desorption events for the three systems.

Event	System	t $[ns]$	Bias distance		Minimum ion-AA distance	
			Which group	d [Å]	Which group	d_{min} [Å]
Ion adsorbs on the surface	Arg-Ca^{2+}	9.25	Carboxyl	6.87	-	-
	Arg-PO_4^{3-}	0.65	Amine	8.76	Side	4.88
	Arg-PO_4^{3-}	8.93	Amine	3.34	-	-
	Asp-Ca^{2+}	12.46	Side	2.41	-	-
AA adsorbs on the surface	Arg-Ca^{2+}	22.23	Carboxyl	5.01	-	-
	Arg-PO_4^{3-}	18.47	Amine	2.96	-	-
	Arg-PO_4^{3-}	29.19	Amine	5.37	-	-
	Asp-Ca^{2+}	18.62	Side	2.35	-	-

6.1.4 Conclusion

In this section, the adsorption behavior of calcium and phosphate, under a bias with the pre-adsorbed Arg or Asp, was studied. These two ions were chosen due to their stronger interaction with the backbone of Gly. However, it should be noted that the physiological concentration of these two ions is much less than those of sodium and chlorine meaning that although weaker in interaction, sodium and chlorine may associate with the amino acids for a larger amount of time. This suggests that the interaction of sodium and chlorine with the pre-adsorbed amino acids on the rutile surface is also interesting, especially sodium, which has also shown a favorable adsorption on the rutile surface, based on the findings in Chapter 4.

All systems were initially in state i, where the AA was on the surface and the ion was not. In all three systems, although there was no bias applied between the species (ion or AA) and the surface, at any given point, at least one of the species (the ion or the AA) was adsorbed on the surface and none of the three systems, during the simulation time of 30 ns, ever entered state iv, being both the ion and the AA solvated in water. This highlights that despite the hydrophilicity of the rutile surface, and the bias between the ion and the amino acid, ions and amino acids still compete with water and have a high affinity for the surface causing their attachment to the surface.

For the three systems studied in this section, it was observed that the adsorption site of calcium, with respect to OS, was different for Arg and Asp. In the Arg $- Ca^{2+}$ system, calcium adsorbed relatively far from OS while in the Asp $- Ca^{2+}$ system, it adsorbed close to OS. This shows that the pre-adsorbed Arg electrostatically engages with the negative charge point so that it is not available for interaction with calcium, anymore. Between Arg and Asp, adsorption of Arg is electrostatically more favorable on the surface since it has a positive side group compared to Asp with a negative side group. Therefore, in competition with Arg, calcium adsorbed relatively far from OS while this is not the case, when the competition is between calcium and Asp. Arg favors adsorption close to surface charge points; it was observed in this section that when Arg only adsorbs close to the ion (which is driven by the bias), but not OS, it desorbs immediately (Figure 6.6iii and Figure 6.7iii').

As it was shown in Chapter 4, adsorption of phosphate is favorable even in the vicinity of OS, despite the repulsive electrostatic forces. This was also observed in this section where phosphate adsorbed relatively close to OS. Compared to phosphate, the adsorption of calcium on the surface occurred very slowly. The reason behind this might be that calcium tries to find the most favorable adsorption site, as after adsorption, the bias is not able to desorb it anymore.

Investigation of the effect of ion-AA distance on the adsorption of species on the surface showed that in fact for the Arg – PO_4^{3-} and Asp – Ca^{2+} systems, the small ion-AA distance (either the biased distance or the distance of the ion with other groups of the AA) is driving the adsorption. However, in the Arg – Ca^{2+} system, the adsorption of both species on the surface was not accompanied by a small ion-AA distance. Since both these species have an opposite charge to the surface, their attractive electrostatic interactions with the surface are considered responsible.

6.2 Interaction of amino acids with pre-adsorbed calcium ions on a rutile surface

6.2.1 Approach

6.2.1.1 Simulation box

A rutile (110) surface with a dimension of 35.51×38.98 Å^2 and a thickness of ~75 Å was modelled. The simulation box, in the z direction consisted of the rutile slab, a water layer with a thickness of ~80 Å, and a vacuum gap with a thickness of ~115 Å. The bottom face of the rutile slab, which was in contact with the vacuum gap, was fully hydroxylated. The top face, with which water, ions and amino acids could interact, was partially hydroxylated. On this face, 18 of the bridging hydroxyl groups were deprotonated, creating a surface charge density of -0.104 $C \cdot m^{-2}$, which is close to the surface charge density of rutile under physiological conditions (2,3). The partial charge of the rutile species for the surface charge density of -0.104 $C \cdot m^{-2}$ is taken from Predota *et al.* (4) (Table 6.4). The deprotonated oxygens were uniformly distributed on the surface as shown in Figure 6.1b.

Table 6.4 Charge distribution of rutile variable-charge species for a surface charge density of -0.104 $C \cdot m^{-2}$ (4).

Atomic species	TS	OT	HT	OB	HB	OS
Partial charge [e]	2.146	-0.949	0.420	-0.976	0.444	-1.028

TS: Ti atoms bound to the hydroxyl groups.
OT and OB: Oxygen of terminal and bridging hydroxyl groups, respectively; HT and HB are their hydrogen atoms.
OS: De-protonated oxygen atoms of the hydroxyl groups.
See section 3.8.1.1 for explanation of atomic labels.

Electrostatic interactions, as well as the comparison of close and far scenarios in Chapter 4, favors the adsorption of the calcium ion close to the charge point on the surface. One calcium ion was put close to each charge point on the surface, first, at a distance of 2-3 Å far from the surface and a short molecular dynamics simulation was performed during which all the calcium ions adsorbed on the surface (as shown in Figure 6.9). The system was equilibrated for 1 ns during which one of the calcium ions changed its position on the surface (Figure 6.9). The addition of 18 calcium ions on the rutile surface, which has 18 deprotonated oxygens, adds a surface charge density of +0.208 $C \cdot m^{-2}$ to the -0.104 $C \cdot m^{-2}$ due to the deprotonated oxygens, and results in a net positive charge density of +0.104 $C \cdot m^{-2}$ on the surface.

The total charge of the simulation box was neutralized by adding chlorine ions. In order to avoid the adsorption of chlorine ions on the surface, or their association with the amino acid, in the z direction, the water layer was hypothetically divided to four regions at 12 Å, 35 Å and 70 Å distances from the surface (Figure 6.10). The amino acids were limited to a distance of 12 Å from the surface. Chlorine ions were restrained in the third region that has a thickness of 35 Å and is 35 Å far from the surface. Adsorption of chlorine ions on the rutile surface, or their association with the amino acid are both present in the experimental setting, however such events, here, would affect the free energy of adsorption of amino acids on the surface in ways which cannot be easily determined. This is the reason why it was decided to restrain the chlorine ions in the chlorine-rich layer.

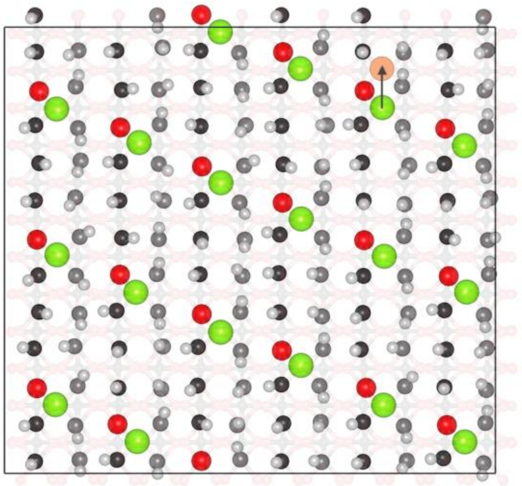

Figure 6.9 Top view of the surface with pre-adsorbed calcium ions. Terminal oxygens are shown in grey, bridging oxygens in black, hydrogen atoms in white, de-protonated oxygens, or surface charge points, in red and calcium ions in green. During the equilibration step, one of the calcium ions changed its position on the surface, as shown by the orange circle and the arrow.

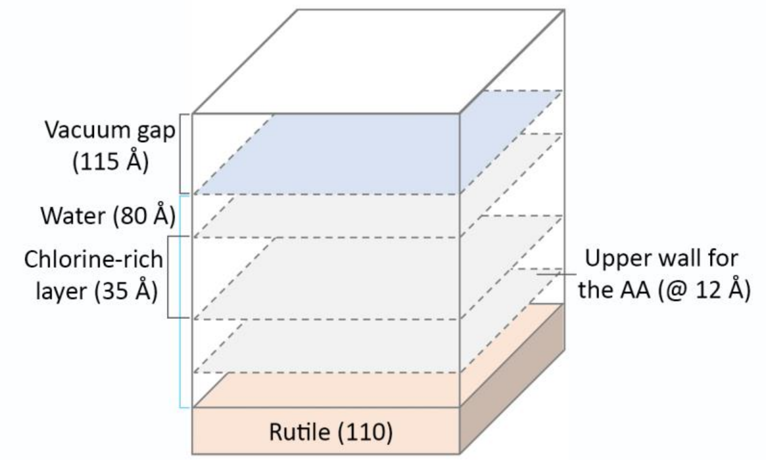

Figure 6.10 Schematic of the simulation box. In the z direction, the simulation box consisted of the rutile slab, water and the vacuum gap. The interaction of amino acids with the surface was restricted at a distance of 12 Å from the surface. To neutralize the simulation box, chlorine ions were distributed in a region of water with a thickness of 35 Å, at a distance of 35 Å from the surface.

6.2.1.2 Amino Acids

Out of the six amino acids studied in Chapter 5, one amino acid was chosen from each category of positively charged (Arg), negatively charged (Asp), non-polar (Leu) and polar (Ser). For those categories with more than one amino acid in Chapter 5, the larger amino acid was chosen as it is easier to differentiate the adsorption behavior of the backbone and the side group. Similar to Chapter 5, due to the general interest to the physiological pH, the protonation state of the amine, carboxyl and side groups of amino acids were chosen based on their dissociation constants in the pH of 7.4. Thus, the amine groups of the backbone were protonated while the carboxyl groups were deprotonated; the side group of Leu and Ser were intact while the side group of Arg was protonated and the side group of Asp was deprotonated.

6.2.1.3 Force field

The components in the simulation box are: rutile, amino acid, ions (calcium and chlorine) and water. Rutile, ions, water and their interactions with each other were defined the same as section 4.1.2. Amino acids and their interaction with rutile and water were defined the same as section 5.2.3. Ion-ion and ion-amino acid interactions were defined using the Lorentz-Berthelot mixing rules. All the parameters are previously defined and can be found in appendices B, C and D.

A cutoff distance of 12 Å was used to treat short-range van der Waals interactions. Long-range electrostatic interactions were treated using the Ewald summation with a maximum relative error of 10^{-6} (5). All simulations were performed at 37 °C using the Nosé-Hoover thermostat in the NVT ensemble. The Verlet leapfrog algorithm was used with a timestep of 0.7 fs.

6.2.1.4 Simulation details

Before performing well-tempered metadynamics simulations, all simulation boxes were equilibrated for 1 ns during which the C_α atom of the amino acids was restrained in a distance of 15 Å from the surface.

Similar to Chapter 5, the collective variable was the perpendicular distance of the center of mass of the amino acids from the surface (Figure 6.1d), which was defined as the average of positions of the oxygen atoms of the surface hydroxyl groups in the z direction. The collective variable was limited to an upper distance of 12 Å from the surface. Width, height and deposition frequency of Gaussians were 0.5 Å, 1 $kJ \cdot mol^{-1}$ and 2,000 timesteps (1.4 ps), respectively. A bias factor of 15 was used.

Since the surface is now uniform in terms of the distribution of hydroxyl groups, charge points and calcium ions (Figure 6.1 and Figure 6.9), the amino acids were not confined inside a cylinder around a charge point, anymore. All simulations were performed for 30 ns. During both equilibration and production runs all the calcium ions were un-restrained. As previously mentioned, the chlorine ions were kept restrained in the chlorine-rich layer. Only one titanium atom was kept restrained in the center of the rutile slab to avoid drifting.

6.2.2 Results and discussion

During the simulation time, the calcium ions were not restrained to remain in their position on the rutile surface, which was next to surface charge points (Figure 6.9). However, the interaction of the amino acids with the surface, and their occasional adsorption and desorption, and the presence of the counterions (chlorine ions) at a distance of 35 Å from the surface, did not cause any of the calcium ions to leave the surface. This can be due to the attractive electrostatic forces between calcium and surface charge points but also the affinity of calcium for the surface.

Before discussing the adsorption energetics and behaviors of amino acids, it is important to discuss the presence of pre-adsorbed calcium ions and chlorine counterions on the dynamics and the physical behavior of water, which controls the orientation and dynamics of an adsorbate interacting with an adsorbent.

6.2.2.1 (Un)physical behavior of water due to the relative position of ions in the system

Figure 6.11 shows the average density of water, calcium and chlorine in the direction normal to the surface, over the simulation time for the system containing Arg. Very similar trends were observed for the systems of Asp, Leu and Ser. As mentioned before, all the calcium ions stay adsorbed on the surface. This can also be seen in Figure 6.11, where the density distribution of calcium ions appears as a sharp peak close to the rutile surface. This figure also shows the position of restrained chlorine ions in the direction normal to the surface. Close to the rutile surface, high-density water layers, similar to those previously discussed in chapters 4 and 5, are detectable. The closest high-density water layer is at a distance of 2.46 Å from the surface, slightly further from the surface, due to the presence of calcium ions on the surface.

Compared to the density of bulk water (shown by the dashed line in this figure), the average density of water is higher than the liquid water in the distance between the surface and the chlorine rich layer, at approximately 35 Å from the surface. The average density of water in this region (neglecting the high-density water layers close to the rutile surface at d_z <12 Å), is 1.04 $\pm$ 0.015 $g \cdot cm^{-3}$, which is +4.3% higher than liquid water (0.9965 $g \cdot cm^{-3}$ (6)). The average density of water decreases in the chlorine-rich layer to 0.966 $\pm$ 0.03 $g \cdot cm^{-3}$, which is -3.0 % smaller than liquid water.

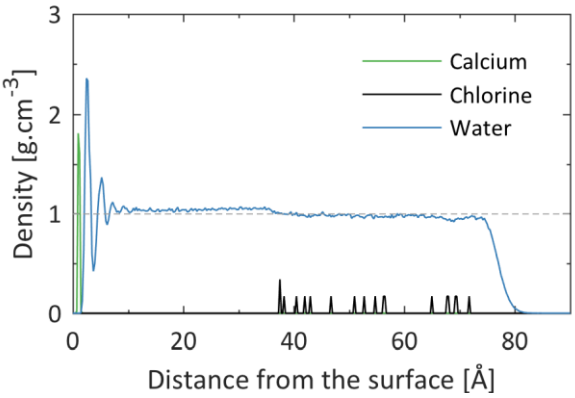

Figure 6.11 Average density of calcium, chlorine and water over the simulation time, for the system containing Arg. The dashed line shows the density of liquid water.

The higher density of water in the region between the surface and the chlorine-rich layer can be due to two reasons. The first one is the overall performance of the water model used, which is SPC/E throughout this thesis, in the presence of the rutile surface. In the original paper by Berendsen *et al.* (7) who proposed water SPC/E, the density of water using the SPC/E model was reported to be 0.998 $g \cdot cm^{-3}$, with a difference of -0.15% with the liquid water. However, the density of water interacting with the rutile surface, studied in different parts of this thesis, was observed to have a $\pm$1.5% difference with the value reported for the SPC/E water system.

The second reason, however, is driven by the relative position of the surface charge points, calcium and chlorine ions, in the direction normal to the surface, causing an electric field in the system. For one water molecule, one can define a vector $\vec{m} = \overrightarrow{OH_1} + \overrightarrow{OH_2}$. At any point in time, based on the orientation of the water molecule, $\vec{m}$ has an angle of α, β and γ with x, y and z axes, respectively. The mean cosine of these angles for all of the water molecules, over the simulation time is shown in Figure 6.12, which is for the system containing Arg, as other systems behaved very similarly. An average angle of 90° corresponds to water molecules forming all possible angles with the corresponding axis, meaning that there is no preferential orientation in water.

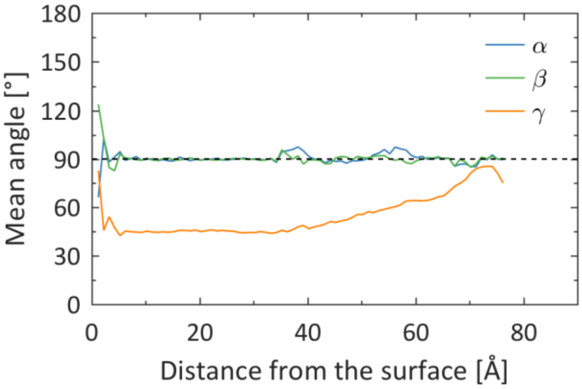

Figure 6.12 Orientation of water molecules, averaged over the simulation time, for the system containing Arg.

Very close to the rutile surface, the mean angle of water molecules with respect to x and y axes, deviates from 90° which is due to the presence of calcium ions. The mean angles α and β show a random distribution for water molecules over almost the whole thickness of the water layer on the surface. The distribution of water molecules is slightly perturbed in the chlorine-rich layer according to these two angles.

However, the mean angle, which water molecules form with the z axis, shows a directional orientation of water molecules caused by the electric field in the system. As it can be seen in Figure 6.12, up to the chlorine-rich layer, water molecules have a mean angle of 45° with the z axis. At distances larger than 35 Å from the surface, water starts to re-gain its random distribution, which only occurs at d~75Å. The mean angle of 45° reveals that water molecules have a preferential orientation in the simulation box with respect to the z axis. Atomic snapshots revealed that in the region between the surface and the chlorine-rich layer, water molecules are orientated with their oxygen atoms closer to the surface with the net positive charge, and their hydrogen atoms towards the chlorine-rich layer. The higher density of water in this region is therefore, caused by this preferential distribution of water, which itself is caused by the electric field due to the relative position of calcium and chlorine ions.

The electric field and its effect on the directional orientation of water affects the energetics, dynamics and orientation of amino acids when solvated in water, and during their adsorption on the surface, in a way that depends on the overall charge of the amino acid; therefore, the effect is the highest for Arg and Asp and the least for Leu. While this is problematic, chlorine atoms had to be kept restrained in the system as when free, they adsorbed on the surface due to attractive electrostatics with calcium ions. Keeping in mind that the system is now somehow unphysical due to the electric field and directional orientation of water molecules, adsorption of amino acids on the surface with pre-adsorbed calcium ions was studied further, mainly because this unphysical directional distribution of water was similar in all systems to the same extent. Nevertheless, the results provided in this section should be interpreted with care and with keeping in mind the excess electric field in the system.

6.2.2.2 Adsorption of amino acids on the surface

If the distance of the amino acids from the surface was not biased, given sufficient time, those with a favorable adsorption on the surface, would have reached the surface and adsorbed on it. Here, under the applied bias, the amino acids adsorbed and desorbed from the surface. Without the bias, such events will occur in a more extended time-scale, which depends on the energy barrier associated with the event. The distance of the side groups of amino acids, as well as their backbone atoms, from the rutile surface is shown in Figure 6.13. The effect of the relative position of calcium and chlorine ions in the system, on the orientation of the amino acids is clear in this figure; groups with a positive charge (*e.g.,* the amine group of the backbone) are closer to the chlorine-rich layer while negative groups (*e.g.,* the carboxyl group of the backbone) are closer to the rutile surface pre-adsorbed with calcium ions. Arg and Asp, one with a positive side group, and the other one with a negative side group, show a major preferential orientation over the simulation time (Figure 6.13a and b). The positive side group of Arg is mostly orientated towards the chlorine-rich layer and the adsorption of this amino acid is mainly via the backbone group – carboxyl group, in specific. However, for Asp, it is the negative side group which mainly interacts with the surface. Adsorption of Asp on the surface is occasionally accompanied by the carboxyl group in the backbone, in addition to the side group. Amino acids with un-charged side groups (Leu and Ser) seem to not be significantly affected by the electric field created by calcium and chlorine ions and the directional orientation of water, as their adsorption involves the backbone as well as the side group (Figure 6.13c and d). While the interaction of amino acids with the surface is driven by electrostatic forces, which is physical, their orientation due to the electric field in the system, and their dynamics affected by the directional orientation of water, is unphysical and results obtained here are different if the chlorine ions were allowed to move in the system and interact with the surface and the amino acids (the physical case).

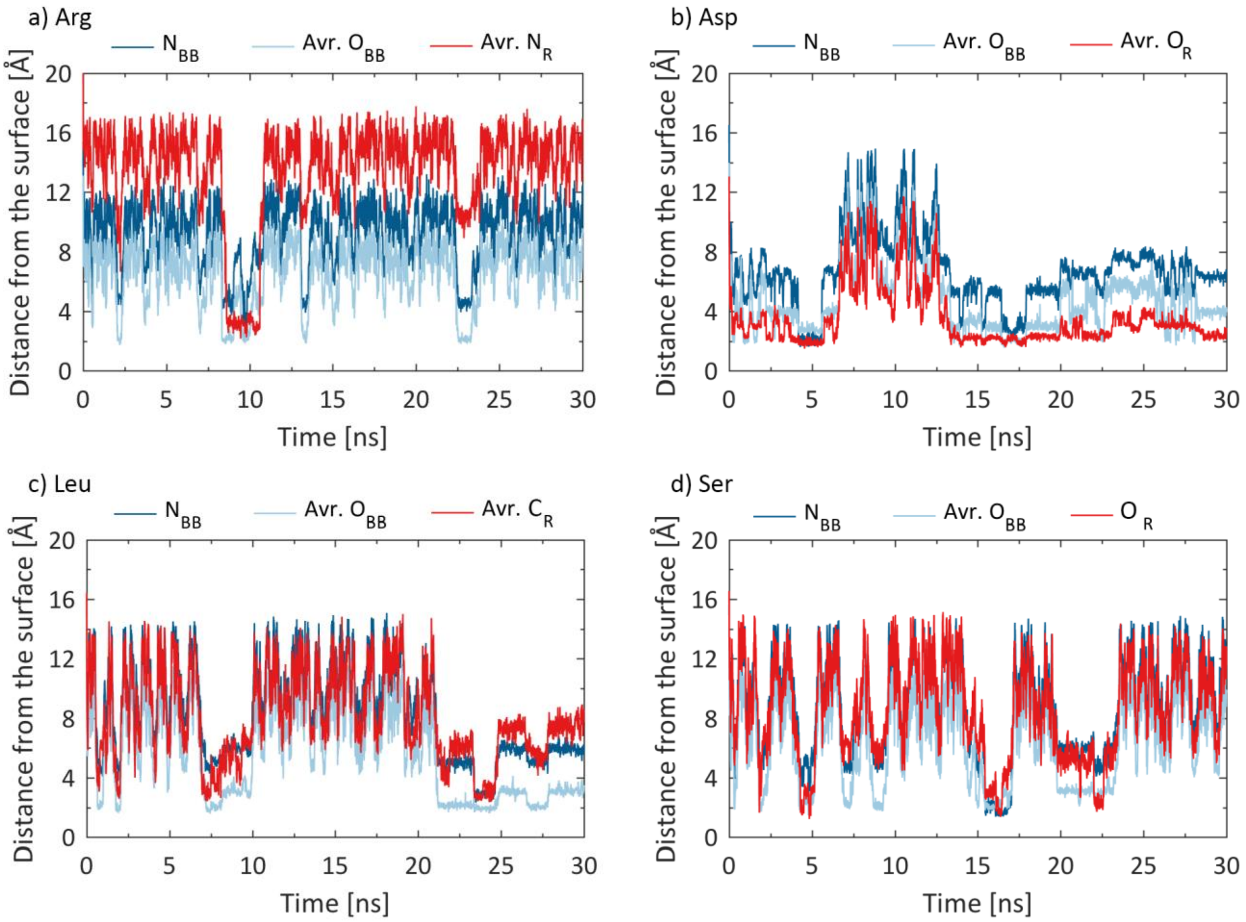

Figure 6.13 Distance of amino acid backbone and side groups atoms from the rutile surface. 'BB' stands for backbone while 'R' represents the side group.

Considering the adsorption energy as the energy difference between the adsorbed and solvated states, from Figure 6.14, it can be seen that the adsorption energy increases in the order of Arg, Ser, Leu, Asp. Compared to Chapter 5, where the same collective variable was used for amino acids, in this chapter, the relative position of ions in the system, which leads to the electric field and the preferential orientation of amino acids in water, causes the free energy profiles to possess distinguishable states based on the group which is driving the adsorption. Therefore, reweighting or projection of the results based on the adsorption group is not necessary here. In the following, the free energy of adsorption of amino acids will be separately discussed. Hereafter, a group is considered to be adsorbed on the surface if its distance from the surface is smaller than the distance of the closest water layer to the surface, which is at 2.46 Å (Figure 6.11).

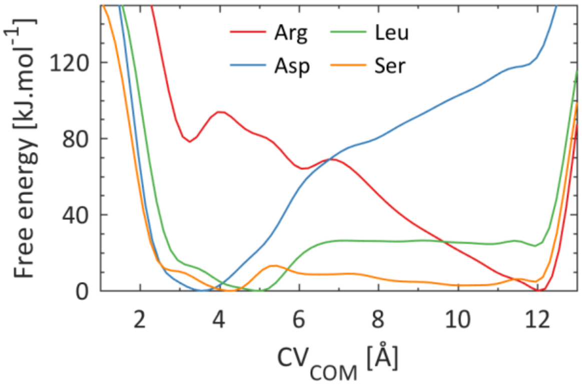

Figure 6.14 Free energy of adsorption of amino acids on the surface with pre-adsorbed calcium ions.

6.2.2.2.1 Arg

Arg, with the positive side group, is in a lower energy state in distances further from the surface (Figure 6.15a), which is due to the repulsive electrostatics between the amino acid and the rutile surface pre-adsorbed by calcium ions, but also the electric field in the system, which favours Arg to be further from the surface and closer to the chlorine-rich layer. In the solvated state, the preferential orientation of Arg between pre-adsorbed calcium and solvated chlorine ions can be seen in Figure 6.15(iv).

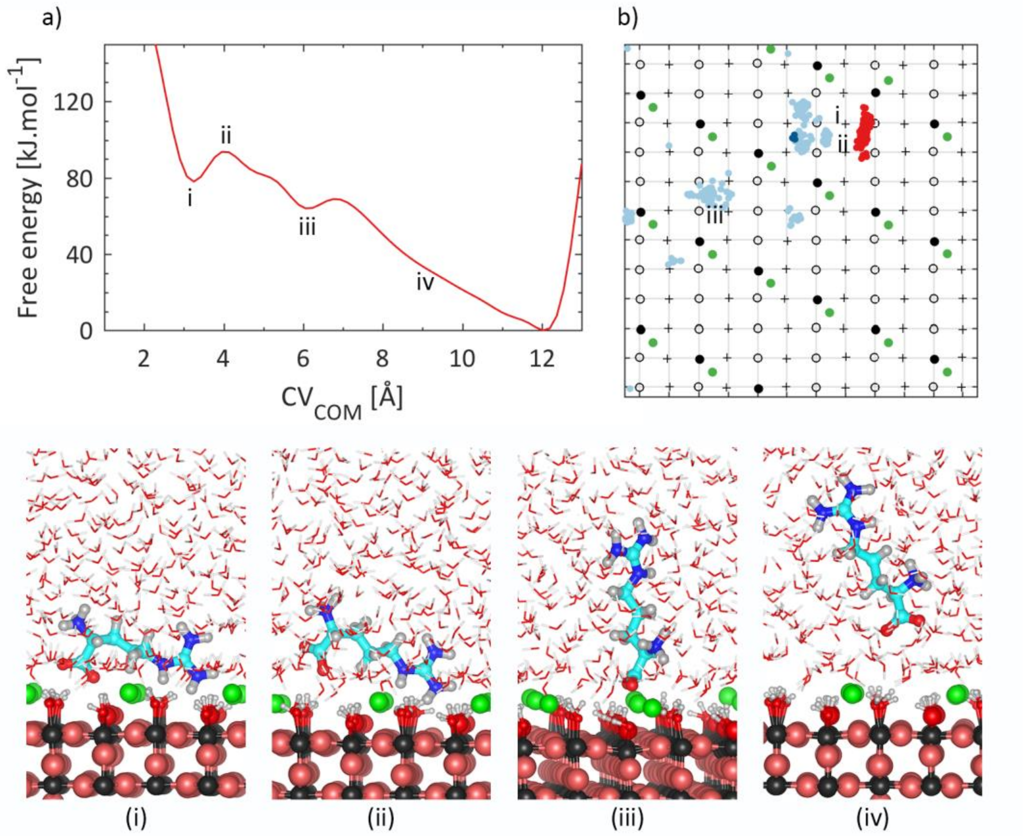

Figure 6.15 a) Free energy of adsorption of Arg on the rutile surface with pre-adsorbed calcium ions and b) in-plane distribution of amine group (dark blue), carboxyl group (light blue) and red (side group), when adsorbed on the surface (Terminal oxygens are shown via plus signs, bridging oxygens via circles, deprotonated oxygens via filled black circles, calcium via filled green circles). (i) to (iv) are the atomic snapshots of the system and are labeled in a and b (Ti: grey, O: red, C: turquoise, N: blue, H: white, Ca: green).

Close to the rutile surface, the free energy profile of Arg shows two local minima (Figure 6.15(i) and (iii)). The one with the smaller CV_{COM}, at point (i), corresponds to the adsorption of Arg on the surface involving both backbone and side groups. The second local minimum, at point (iii), corresponds to a single-contact point adsorption, which due to the presence of calcium ions, is driven by the backbone. The system is in a lower energy state at point (iii) compared to point (i), meaning that the local minimum at point (iii) is more favorable. This is due to the net positive charge of the surface which causes repulsive electrostatics with the side group of Arg and making the local minimum (i), less favorable than local minimum (iii). During desorption, Arg has to cross two energy barriers, once between points (i) and (iii) (at point (ii)), and once between points (iii) and (iv). While, as mentioned, local minimum (iii) is a more favorable energy state, the desorption barrier from point (i) to (iii) is larger than point (iii) to (iv). The fact that desorption is more difficult when the positive side group also participates in the adsorption (point (i)), despite repulsive electrostatics, may be explained by the adsorption conformation of the amino acid between the surface groups of rutile. As it can be seen in Figure 6.15b, Arg adsorption mainly occurs on the surface hydroxyl groups, and even when the adsorption is driven only by the backbone, Arg does not significantly engage with surface charge points or calcium ions. Therefore, the larger desorption barrier at point (i) is simply because there are two contact points with the surface which should be desorbed, while in point (iii) there is only one.

6.2.2.2.2 Asp

Asp, with the negative side group, shows a very favorable adsorption on the rutile surface (Figure 6.16a). The adsorption of Asp on the surface is most favorable when both carboxyl groups of the backbone and the side group are involved (Figure 6.16(ii)). The amine group being close to the surface, or one of the carboxyl groups being further from the surface, causes the adsorption to be less favorable (Figure 6.16(i) and (iii)). During the adsorption, Asp interacts very frequently with the surface charge points and calcium ions (Figure 6.16b).

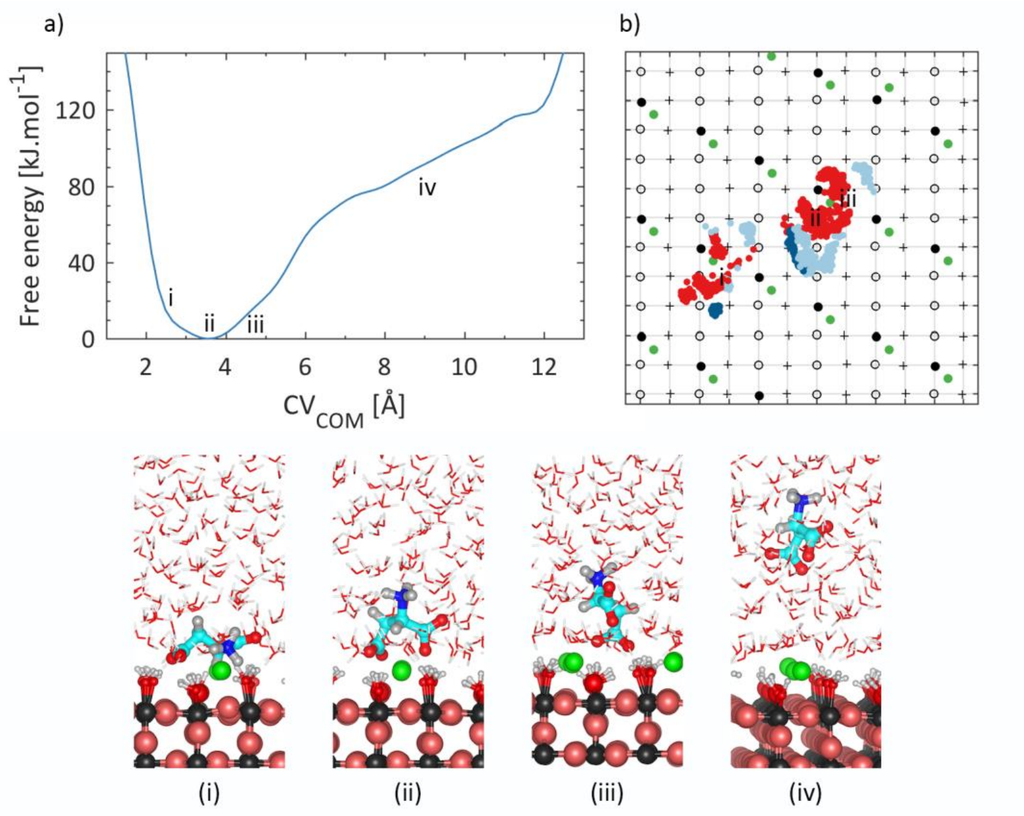

Figure 6.16 a) Free energy of adsorption of Asp on the rutile surface with pre-adsorbed calcium ions and b) in-plane distribution of amine group (dark blue), carboxyl group (light blue) and red (side group), when adsorbed on the surface. (i) to (iv) are the atomic snapshots of the system and are labeled in a and b.

6.2.2.2.3 Leu

The stable adsorption of Leu on the surface is via the carboxyl group (Figure 6.17a(ii)), during which, the amino acid occasionally interacts with the surface charge points and calcium ions (Figure 6.17b). The system has a less favorable energy state when the non-polar side group approaches the surface (Figure 6.17(i)).

Leu behaves the most similar, compared to other amino acids, to Chapter 5, where the surface had a single charge point with no pre-adsorbed species. In Chapter 5, the adsorption of Leu on the surface was driven by the amine group of the backbone due to the net negative charge of the surface, while here it is driven by the carboxyl group due to the net positive surface charge. The free energy of adsorption, which is the difference between the solvated and adsorbed states, for Leu in Chapter 5 was reported to be 30.92 $kJ \cdot mol^{-1}$. Here, the free energy of adsorption is 25.74 $kJ \cdot mol^{-1}$.

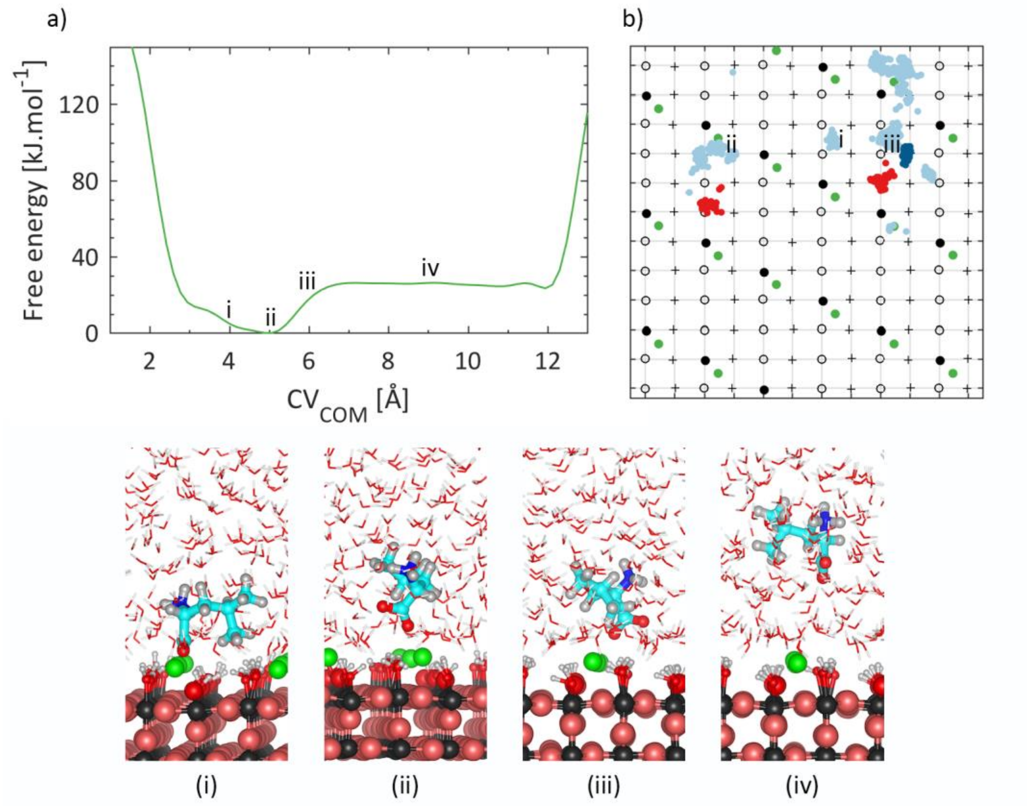

Figure 6.17 a) Free energy of adsorption of Leu on the rutile surface with pre-adsorbed calcium ions and b) in-plane distribution of amine group (dark blue), carboxyl group (light blue) and red (side group), when adsorbed on the surface. (i) to (iv) are the atomic snapshots of the system and are labeled in a and b.

Despite the directional orientation of water molecules in the system, and the relative position of ions, the behavior of Leu seems to have not been affected by these artefacts; this can be seen in Figure 6.13c, where Leu experiences adsorption via all its groups – the backbone as well as the side group. Therefore, the smaller adsorption energy on the surface with the large positive charge density (here), compared to the one on the surface with small negative charge density (Chapter 5), is due to the less favorable interaction of Leu with the surface with a higher charge.

6.2.2.2.4 Ser

Similar to Leu, Ser interacts with the surface via both its backbone and side groups (Figure 6.13d). Compared to Arg, Asp and Leu, with charged and non-polar side groups, Ser is in the relatively same energy state when solvated in water and when adsorbed on the surface (Figure 6.18a), which is due to its polar side group.

This is caused by the directional orientation of water which causes Ser, with a polar side group, to have a very favorable solvation in water.

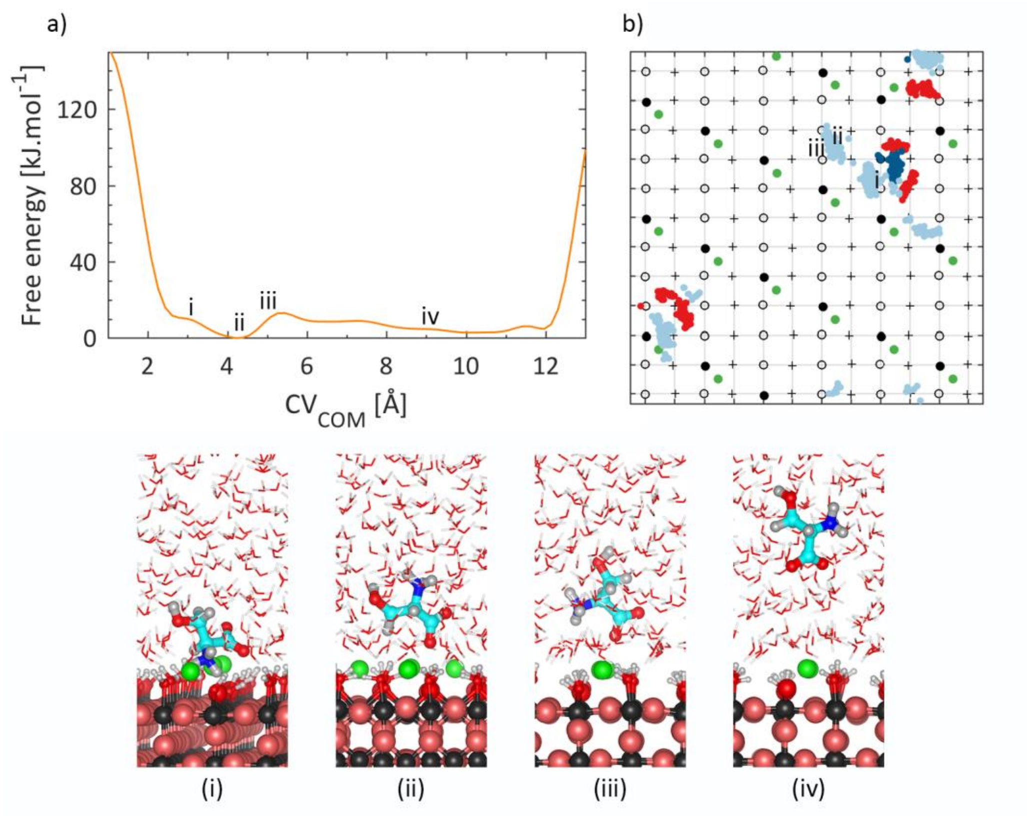

Figure 6.18 a) Free energy of adsorption of Ser on the rutile surface with pre-adsorbed calcium ions and b) in-plane distribution of amine group (dark blue), carboxyl group (light blue) and red (side group), when adsorbed on the surface. (i) to (iv) are the atomic snapshots of the system and are labeled in a and b.

6.2.3 Conclusion

The adsorption of amino acids on a rutile surface with a net positive charge, due to the presence of pre-adsorbed calcium ions on the surface, was studied in this section. Chlorine ions were added to neutralize the charge of the system. Since they were restrained in the chlorine-rich layer, at a distance of 35 Å from the surface, an electric field was present in the system which caused water molecules to acquire a directional distribution in the direction normal to the surface, which led to a higher density of water (+4.3%) in this region. The electric field, the directional distribution of water and its higher density are artefacts in the system which affect the orientation of amino acids in their solvated state, the manner they approach the surface (energetically), and their dynamics. Therefore, the results obtained in this section should be interpreted with care.

The directional distribution of water mainly affected amino acids with charged side groups (Arg and Asp) and polar side group (Ser). Arg with a positive charge was in a more favorable energy state when far from the positively charged surface, and solvated in water, while adsorption of Asp with the negative charge proved to be very favorable on the surface. The adsorption behavior of Leu on the surface proved to have not been significantly affected by the electric field and the directional distribution of water, due to its non-polar side group. Its adsorption energy decreased, compared to the findings of Chapter 5, due to the higher charge density of the surface. Behavior of Ser proved to have been also affected by the electric field and the directional distribution of water. Ser with the polar side group showed the smallest energy difference between its adsorbed and solvated states, among Arg, Asp and Leu.

Despite the artefacts in the systems studied in this section (the electric field which caused directional distribution of water and its higher density), results show that the adsorption of amino acids is controlled by the surface charge and electrostatic forces. A large surface charge density significantly favors the adsorption of amino acids with a counter charge to that of the surface, significantly disfavors the adsorption of those with the same charge to the surface, also disfavors adsorption of those with a non-polar side group.

In order to avoid the electric field in the simulation box, the chlorine ions should be free to move. Although they will interact with the amino acid and the surface, and the free energy obtained will not be uniquely for the adsorption of amino acids on a rutile surface with pre-adsorbed species, the modelled condition will be physical and results could be interpreted further.

6.3 Summary

Competitive adsorption of ions and amino acids on a rutile surface was studied in this chapter. In the simplistic setup of simulations, one of these species was pre-adsorbed on the surface, and the interaction of the other species with the surface and the pre-adsorbed species was studied. In the first section, the singly deprotonated surface was used, while in the second part, the surface had a charge density of -0.104 $C \cdot m^{-2}$ similar to physiological conditions.

Results of this chapter show that:

- Occupation of surface charge points with amino acids does not prevent ions to adsorb on the surface. In certain cases, where the interaction of the ion with the charge point is more favorable than that of the amino acid, the ion approaches the surface charge point.
- The surface charge strongly controls which species can adsorb on the surface. On the presence of a net positive charge on the surface, interaction of Asp, with an opposite charge to that of the surface was favorable on the surface, while for Arg, Leu and Ser, adsorption was weak or unfavorable.
- Interaction of amino acids with the rutile surface did not perturb the pre-adsorbed calcium ions on the surface.

These points suggest that the presence of the amino acids in the system do not strongly inhibit the interaction of other components in the system with the surface

In fact, a recent *in vitro* study on the hydroxyapatite deposition on a titanium surface shows that presence of bovine serum albumin (BSA) does not inhibit the deposition of hydroxyapatite for certain concentrations of BSA (8). Also, current protocols of SBF preparation for apatite formation do not contain any organic residue to mimic blood plasma in their organic content, but they usually contain a notable amount of tris (tris(hydroxymethyl)aminomethane – see Table A.2) as the buffering agent (9). While preliminary experimental studies showed that tris adsorbs on rutile, many *in vitro* studies report hydroxyapatite deposition on the surface. Therefore, it seems that the type of the organic content and its concentration controls whether there is an inhibition of the apatite deposition, and its extent, on a particular surface. However, it should be noted that here the focus is only on one face of the rutile crystal, namely the (110) surface.

This is in agreement with the findings of this chapter which suggest that a more realistic SBF solution is not simply a solution with any organic content, as amino acids neither prevented the adsorption of ions nor perturbed their adsorption on the surface.

References

1. Schmidt, J. A. *et al.* Plasma concentrations and intakes of amino acids in male meat-eaters, fish-eaters, vegetarians and vegans: A cross-sectional analysis in the EPIC-Oxford cohort. *Eur. J. Clin. Nutr.* **70,** 306 (2015).

2. Machesky, M. L. *et al.* Chapter 12 Ion adsorption into the hydrothermal regime. *Interface Sci. Technol.* **11,** 324–358 (2006).

3. Takahashi, K. & Fukuzaki, S. Cleanability of titanium and stainless steel particles in relation to surface charge aspects. *Biocontrol Sci.* **13,** 9–16 (2008).

4. Předota, M., Machesky, M. L., Wesolowski, D. J. & Cummings, P. T. Electric double layer at the rutile (110) surface. 4. Effect of temperature and ph on the adsorption and dynamics of ions. *J. Phys. Chem. C* **117,** 22852–22866 (2013).

5. Smith, W., Forester, T. R. & Todorov, I. T. The DL POLY classic user manual. (2012).

6. van der Spoel, D., van Maaren, P. J. & Berendsen, H. J. C. A systematic study of water models for molecular simulation: Derivation of water models optimized for use with a reaction field. *J. Chem. Phys.* **108,** 10220–10230 (1998).

7. Berendsen, H. J. C., Grigera, J. R. & Straatsma, T. P. The missing term in effective pair potentials. *J. Phys. Chem.* **91,** 6269–6271 (1987).

8. Zhao, W., Lemaître, J. & Bowen, P. A comparative study of simulated body fluids in the presence of proteins. *Acta Biomater.* **53,** 506–514 (2017).

9. ISO 23317 - Implants for surgery —*In vitro* evaluation for apatite-forming ability of implant materials. (2007).

Chapter 7 Preliminary work - Interaction of the TBP polypeptide with the rutile (110) surface

This chapter reports the preliminary study on the interaction of a hexapeptide, which is known to have a high affinity for several surfaces, e.g., silver, silicon and titanium, with the rutile (110) surface. The effect of the surface charge density, as well as the interacting side group, on the energetics of adsorption and desorption of the polypeptide from the rutile surface are reported and discussed. This chapter is meant as preliminary work as there is still a need to expand the simulation and sampling time of the studied systems to confirm the first findings and conclusions further.

7.1 Introduction

As opposed to chapters 5 and 6, where single amino acids and their interactions with the rutile surface were studied, in this chapter, the focus is on a polypeptide. Among all the possible abiotic or biotic organic molecules, the titanium-binding hexapeptide (TBP- Figure 7.1) was chosen. The interest in TBP, in this chapter, is two-fold.

The first reason resides in the name of this polypeptide. Experimental studies have shown that this hexapeptide has a high affinity for Ti, Au and Si but not Ag, Pt and Zn (1). In fact, in Chapter 5, the selection of amino acids was made based on the titanium-binding peptide (TBP), which has the following sequence: RKLPDA – Arg-Lys-Leu-Pro-Asp-Ala, but to consider amino acids with different side groups, the non-polar Pro was replaced by the polar Ser. In this chapter, however, the interaction of the TBP hexapeptide with the rutile (110) surface is investigated.

The second reason is that TBP contains four of the most accessible amino acids of human serum albumin (HSA) by the solvent. HSA is the most abundant protein in the human blood plasma (2). It accounts for 50-60% of the proteins in the human blood plasma (3), with a concentration of 40-50 g/l (4). One of the main functionalities of HSA is to transfer other components in the plasma, such as metallic cations, amino acids, drugs, etc., to their target organ (5–7). HSA is made of 585 amino acids and has a molecular weight of 66 kDa (6), which is around the average weight of proteins. HSA is a water-soluble protein (6), with 42% non-polar, 24% polar and 34% charged amino acids. The Swiss PDB viewer (8) was used to analyze HSA in order to find the most accessible amino acids of HSA by the solvent; *i.e.,* the amino acids which tend to be on the surface of HSA when solvated in water. The analysis was done for solvent accessibility of 15, 25 and 35%; the trend of accessible amino acids was similar for all these three values. Table 7.1 presents the percentage of amino acids with the highest accessibility for the solvent, using solvent accessibility of 25%. As it can be seen in this table, Lys, Asp, Pro and Ala are four of the HSA amino acids, which have high accessibility by the solvent, but also are present in the TBP hexapeptide. Based on these two reasons, the interaction of TBP with the rutile surface was studied in this chapter.

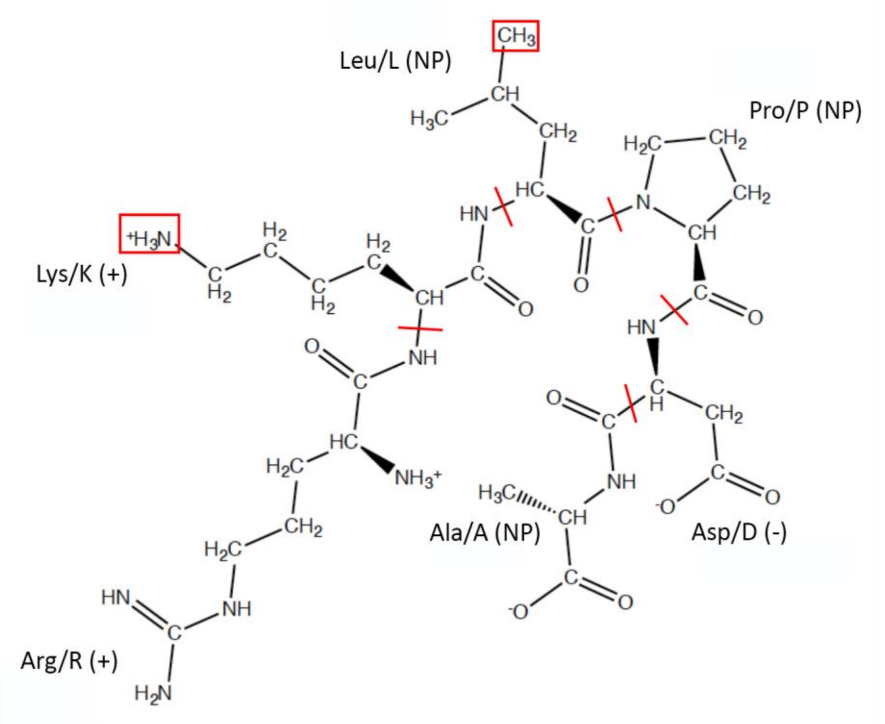

Figure 7.1 The TBP hexapeptide. The six amino acid of this residue are labelled with the charge or polarizability state of the side group (NP: non-polar), and are separated from each other by red lines. The functional groups of Leu and Lys, whose distances from the rutile surface are biased in this chapter, are shown by the red squares.

Table 7.1 The most accessible amino acids of HSA by solvent, for an accessibility of 25%.

Amino acid		Type of the side group of the AA	Accessible residue normalized by the number of that AA in HSA [%]
Glu	E	Charged (-)	72
Lys	K	Charged (+)	69
Asp	D	Charged (-)	58
Thr	T	Polar with OH	50
Asn	N	Polar with NH_2	47
Pro	P	Non-polar (aromatic)	45
Gln	Q	Polar with NH_2	45
Ala	A	Non-polar (linear)	30

Initially, Sano and Shiba (9) considered a motif of 12 amino acids, where the first six residues were the TBP sequence. Experimentally, they tested the relative binding of the motif to Ti, using a mutational analysis. This analysis consisted of exchanging each of the amino acids in the original motif with Ala. In specific, they observed that Ala mutations of Arg, Pro and Asp, in the TBP part of the motif, substantially affected the affinity of the motif for the Ti surface. The authors suggested several reasons why Arg, Pro and Asp are important in the binding of TBP, despite Pro and Asp being non-polar and negatively charged, but not Lys, with its positive side group.

At the neutral pH, the titanium oxide layer on the Ti surface has a net negative charge; therefore, the contribution of the positively charged Arg in the binding affinity of TBP seems reasonable and is believed to be via interaction with the surface deprotonated oxygen atoms. Although Pro is non-polar, it is a structure-determining amino acid in a residue. Pro was suggested to create a kink in TBP in a cis manner, causing Arg and Asp to be directed towards the surface. The affinity of Asp in TBP for the titanium oxide surface was attributed to its amphoteric nature and the presence of $Ti - OH_2^+$ groups on the surface (9). In conclusion, Sano and Shiba propose a model for the adsorption of TBP on the surface as Pro creating a king on the TBP chain, Arg interacting with the O^- groups on the surface, and Asp interacting with the $Ti - OH_2^+$ on the surface. The authors state that their model does not explain why Lys is not primarily involved in the adsorption of TBP, suggested by the mutation of Lys with Ala which did not change the affinity of TBP for the surface (9).

Mutation of Lys with Ala did not lead to a significant change in the affinity of the motif for Ti. Although both Lys and Arg are positively charged the subtle difference in their side group was believed to be responsible for their different contribution to the affinity of TBP. Also, Arg has a polar and a positively charged functional group in its side group while Lys has only one charged group. The extra polar functional group of Arg, compared to Lys, can participate in hydrogen bonding with the surface (10).

By comparing the adhesion of residues containing TBP on Si and Ti, Hayashi *et al.* (11) found that the adhesion force of TBP on Si is half of that on Ti. The reason for this observations was explained based on the surface groups of Si and Ti in neutral pH. The isoelectric point of Si and Ti is 2-3 and 5-6, respectively. Therefore, in the neutral pH, O^- and OH groups are present on the Si surface while O^-, OH and OH_2^+ groups are present on the titanium surface. The binding of Asp with the surface OH_2^+ on titanium was therefore accounted responsible for the two-times larger adhesion force of TBP to the Ti surface. Therefore, their work confirmed the proposed model and reasoning of Sano and Shiba and the contribution of Arg and Asp in the binding of TBP on titanium (9).

Here, two computational studies on the interaction of TBP with the titanium surface will be briefly discussed. In the first study, the interaction of TBP with an amorphous and amphoteric titanium oxide was studied (12). Similar to physiological conditions, a surface charge density of -0.123 $C \cdot m^{-2}$ was induced on the surface by introducing $TiOH^-$ and Ti_2OH^+ groups with a ratio of 16:5. Two adsorption conformation were reported for TBP on the amorphous titanium oxide surface. The first conformation was flat and worm-like and involved Arg, Lys and Asp; the second conformation was upright and involved Arg and Lys. The free energy of adsorption of TBP on the surface was calculated using metadynamics simulations and reported to be -38.59 $\pm$ 3.86 $kJ \cdot mol^{-1}$. However, Lys is present in both adsorption conformations reported by the computational study, which is contrary to the previously proposed model based on experimental findings (9).

The second study was conducted by Brandt and Lyubartsev (13), where the adsorption of TBP was studied on a rutile non-hydroxylated (100) surface. Unbiased molecular dynamics simulations were performed for 500 ns.

Almost over the entire simulation time, TBP was adsorbed on the surface, with a transition between two binding modes. The first binding mode was a worm-like and extended conformation in which the hexapeptide had more flexibility. The end-to-end (EED) distance of TBP in this conformation was ∼12 Å. This binding mode involved Arg, Lys and Asp and is similar to the first adsorption conformation observed on the amorphous titanium oxide surface (12). The second binding mode, with an EED of ∼16 Å, had a C-shaped conformation where Arg and Asp were involved in the adsorption, and this is, in fact, the adsorption conformation proposed before (9,10). The adsorption conformation, in this case, was locked on the surface and the mobility of TBP was very low. In both adsorption conformations, the adsorption was via the first water layer on the surface and not in direct contact with the rutile (100) surface. Biased simulations (adaptive well-tempered metadynamics) were performed and the free energy of adsorption of TBP on the surface was estimated to be -11.3±2.0 $kJ \cdot mol^{-1}$. As it can be seen, the adsorption energy is lower than what was estimated on the amorphous titanium oxide surface. The indirect adsorption mode of TBP to the non-hydroxylated (100) surface of rutile can be responsible, but also the zero charge on the surface.

The reported adsorption conformations and binding agents of TBP on titanium surfaces, from the literature, are summarized in Table 7.2. Interestingly, the C-shaped and worm-like conformations have been reported on different charge states of the surface (negative charge and neutral). The computational studies report the adsorption energy, but since the reported value has not been attributed to a certain conformation, the values in Table 7.2 are in parentheses.

Table 7.2 Summary of the observed and proposed adsorption conformations of TBP from literature.

Conformation	Surface	Surface charge state	Involved AAs in the adsorption	Ads. Energy $[kJ \cdot mol^{-1}]$	Reported/ Proposed by
C-shaped	Ti	Negative	Arg, Asp	-	(9,10)
	Non-hdrx. rutile (100)	Zero		(-11.3)	(13)
Upright	Amorphous titanium oxide	Negative	Arg, Lys	(-38.59)	(12)
Worm-like	Amorphous titanium oxide	Negative	Arg, Lys, Asp	(-38.59)	(12)
	Non-hdrx. rutile (100)	Zero		(-11.3)	(13)

As a follow-up to the previous work in the literature, in this chapter, the interaction of TBP with the rutile surface was conducted using well-tempered metadynamics. The previous work has studied the amorphous titanium oxide and the non-hydroxylated rutile (100) surface. Here, the rutile (110) surface, with two different surface charge densities, is studied. The two values of surface charge density are -0.012 and -0.104 $C \cdot m^{-2}$; the former is studied to be consistent with previous chapters in this thesis, and the latter is studied due to its relevance to the rutile surface charge density under physiological conditions. Results obtained are hoped to give insights to the effect of the crystallographic surface of rutile, and its charge density on the adsorption behavior of TBP on the surface. Simulations performed in this chapter are expected to add to the reported adsorption conformations or confirm some of them further, especially with respect to the controversial contribution of Lys in the adsorption behavior of TBP.

7.2 Approach

Well-tempered metadynamics simulations were performed to study the interaction of TBP with the rutile (110) surface. The simulation box consisted of the rutile slab, water layer, vacuum gap, with similar dimensions to previous chapters, and TBP. The same force field parameters as in previous chapters were used for rutile, water and their cross-term interactions. Force field parameters for TBP can be found in Appendix B. All cross-term interactions of TBP with rutile and water were defined using the Lorentz-Berthelot mixing rules.

Three sets of simulations were designed, which are summarized in Table 7.3. Hereafter, the systems will be referred to by two characteristics; the first one is the surface charge density, and the second one is the side group whose distance with the surface is biased. LSC and HSC in Table 7.3 stand for low and high surface charge density, respectively. Leu and Lys are the two side groups, whose distance from the surface was biased in this chapter. PP (polypeptide) is to draw attention to the fact that the side groups are part of TBP and not individual residues.

Table 7.3 Simulation details for the interaction of TBP with the rutile (110) surface.

System	σ [C·m^{-2}]	First CV	Second CV Distance of the chosen atom with the surface in the z-direction	
			Chosen Side group**	Chosen atom
LSC_Lys_PP*	-0.012	Gyration radius of TBP (R_g)	Lys	N_R
HSC_Lys_PP	-0.104		Lys	N_R
HSC_Leu_PP	-0.104		Leu	C_R

*<Surface charge density>_<the side group whose distance from the surface is biased>; LSC represents low surface charge density while HSC represents high surface charge density.

**These are marked with red squares in Figure 7.1.

Two of the simulations differ in the surface charge density: LSC_Lys_PP and HSC_Lys_PP. In the LSC_Lys_PP, there is only one negative charge point on the surface (Figure 7.2a) and as mentioned, LSC stands for the low surface charge density of -0.012 $C \cdot m^{-2}$. The partial charge of variable-charge of species of rutile can be found in Table D.2. In the other setting (HSC_Lys_PP - Figure 7.2b), there are 18 deprotonated oxygens on the surface leading to a high surface charge density of -0.104 $C \cdot m^{-2}$, similar to the rutile surface charge density under physiological conditions. The partial charges of the rutile species can be found in Table 6.4. On the HSC surface, the surface charge points were distributed uniformly on the surface in a manner that they are relatively far from each other. Comparison between the results of these two simulations will show the effect of the surface charge density on the adsorption energetics of the hexapeptide as a function of the distance of the same side group (here, Lys) from the surface.

Two collective variables were used. The first collective variable is the radius of gyration of the hexapeptide and the second collective variable is the distance of one of the side groups of TBP from the surface (Figure 7.2c). The first and second collective variables will be referred to as gyration and distance CVs, hereafter. While the distance CV will force the residue of interest to experience solvated and adsorbed states, the gyration CV will force TBP to fold in different conformations, and different adsorption conformations may be observed.

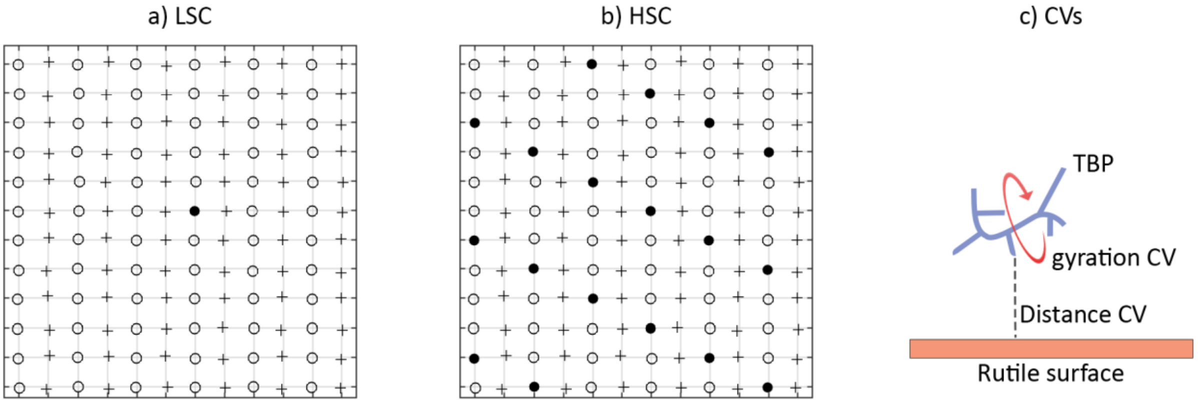

Figure 7.2 Distribution of surface charge points in a) low and b) high surface charge density. Terminal hydroxyl groups are shown via plus signs, bridging hydroxyls with circles and charge points with filled black circles. c) Schematic of the collective variables.

Root-mean-square deviation (RMSD) of a group of atoms at time t_1 with respect to a reference structure at time t_0 can be obtained by:

$$RMSD\ (t_0, t_1) = \sqrt{\frac{\sum_{i=1}^{n} m_i \| r_i(t_0) - r_i(t_1) \|^2}{\sum_{i=1}^{n} m_i}} \qquad \textit{Equation 7.1}$$

Where n is the number of atoms in the molecule, m_i is the mass of each atom and r_i is the coordinates of atoms. The radius of gyration can be a measure of the compactness of a group of atoms, and is the RMSD of the molecule, at time t, with respect to the position of the center of mass of the molecule (COM) at time t. It can be obtained by:

$$R_g(t) = \sqrt{\frac{\sum_{i=1}^{n} m_i \| r_i(t) - r_{COM}(t) \|^2}{\sum_{i=1}^{n} m_i}} \qquad \textit{Equation 7.2}$$

Where:

$$r_{COM}\ (t) = \frac{\sum_{i=1}^{n} m_i r_i(t)}{\sum_{i=1}^{n} m_i} \qquad \textit{Equation 7.3}$$

The mass of the body can be assumed to fit in the radius of gyration while the moment of inertia of the concentrated body in this radius and the actual unit is similar in both cases. To have an idea of the lower and upper extremes to be set for the gyration CV in well-tempered metadynamics simulations, TBP was solvated in a box of water with a size of 40×40×40 $Å^3$. Classical molecular dynamics were performed for 10 ns, once at 310 K and once at 900 K. The higher temperature simulation was performed to facilitate and accelerate the conformational changes of the polypeptide, which as it can be seen in Figure 7.3, was obtained, as the radius of gyration is in average smaller at the higher temperature. It is also interesting to highlight that the radius of gyration of TBP at 310 K, at t:8 - 9 ns is similar to the high-temperature simulation, meaning that the hexapeptide experiences different conformations and is not energetically trapped. Based on Figure 7.3, the gyration CV during the well-tempered metadynamics simulations was limited between 4.5 and 7.5 Å. Although the use of the radius of gyration as the collective variable is very common for polypeptides and proteins, this collective variable may need extended-time simulations since if the organic residue unfolds due to this CV, it may take a long time before it re-folds again.

HSC_Lys_PP and HSC_Leu_PP are similar in the surface charge density but the interaction of TBP with the surface is biased based on the distance of positively charged Lys in the former, and non-polar Leu in the latter, from the surface. One of the methyl groups of Leu was considered for the collective variable, as there are two such groups (Figure 7.1). These two amino acids were chosen since they are neighboring amino acids in TBP with different types of side groups in charge and polarizability (RKLPDA); R and K are both positively charged; L and P are both non-polar; D was not chosen due to its side group being negatively charged similar to the surface, hence A could not be chosen since it has only D as its neighboring amino acid. The distance CV (Figure 7.2c) was limited at a distance of 12 Å from the surface. In the xy-plane, the chosen atom for the distance CV (Table 7.3) was confined to move within a radius of 1.5 Å around the single charge point on the surface in LSC_Lys_PP system (Figure 7.2a), and the equivalent charge point in the other two surface, although there are several charge points on the surface in these cases (Figure 7.2b).

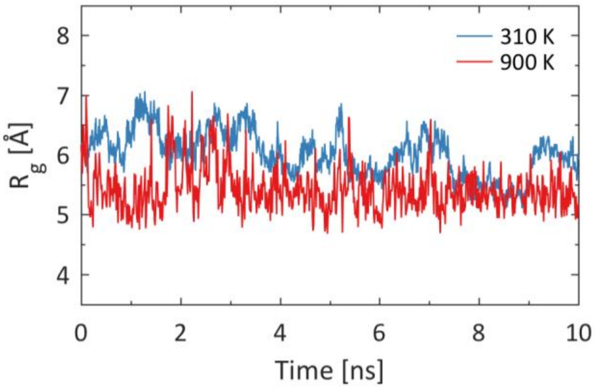

Figure 7.3 TBP radius of gyration when solvated in water.

TBP was initially at a distance of 10 Å from the surface. All systems were first equilibrated for 200 ps during which no bias was applied. Gaussian hills with an initial height of 1.0 $kJ \cdot mol^{-1}$, and a width of 0.5 Å and 1.0 Å for the distance CV and gyration CV, respectively, were deposited every 2,000 timesteps (1.4 ps) with a bias factor of 15. Simulations were performed for 30 ns.

7.3 Results and Discussion

In this section, first, adsorption conformations will be discussed for the three systems, and those residues which are involved in the adsorption will be highlighted. Then, the free energy profile of the adsorption of TBP based on the two previously defined collective variables will be presented.

7.3.1 Adsorption conformation

The distance of side groups of TBP from the surface is shown in Figure 7.4 for the three systems. For those with a single functional group (Lys and Ala), the distance of either the N or C of the functional group is considered while for those with two functional groups (Arg, Leu and Asp) the average distance between either N, C or O oxygens is plotted (Figure 7.1); for the aromatic Pro, the second C from the nitrogen atom is considered. Similar to previous chapters, the surface is defined based on the average position of the oxygen atoms of the hydroxyl groups over the simulation time. The side groups, which adsorb on the surface during the biased simulations, are:

- LSC_Lys_PP: Arg, (Lys), Asp, Ala
- HSC_Lys_PP: Arg, (Lys)
- HSC_Leu_PP: Arg and Lys, (Leu)

The amino acids which are in parentheses are the residue whose distance from the surface is biased via the distance CV.

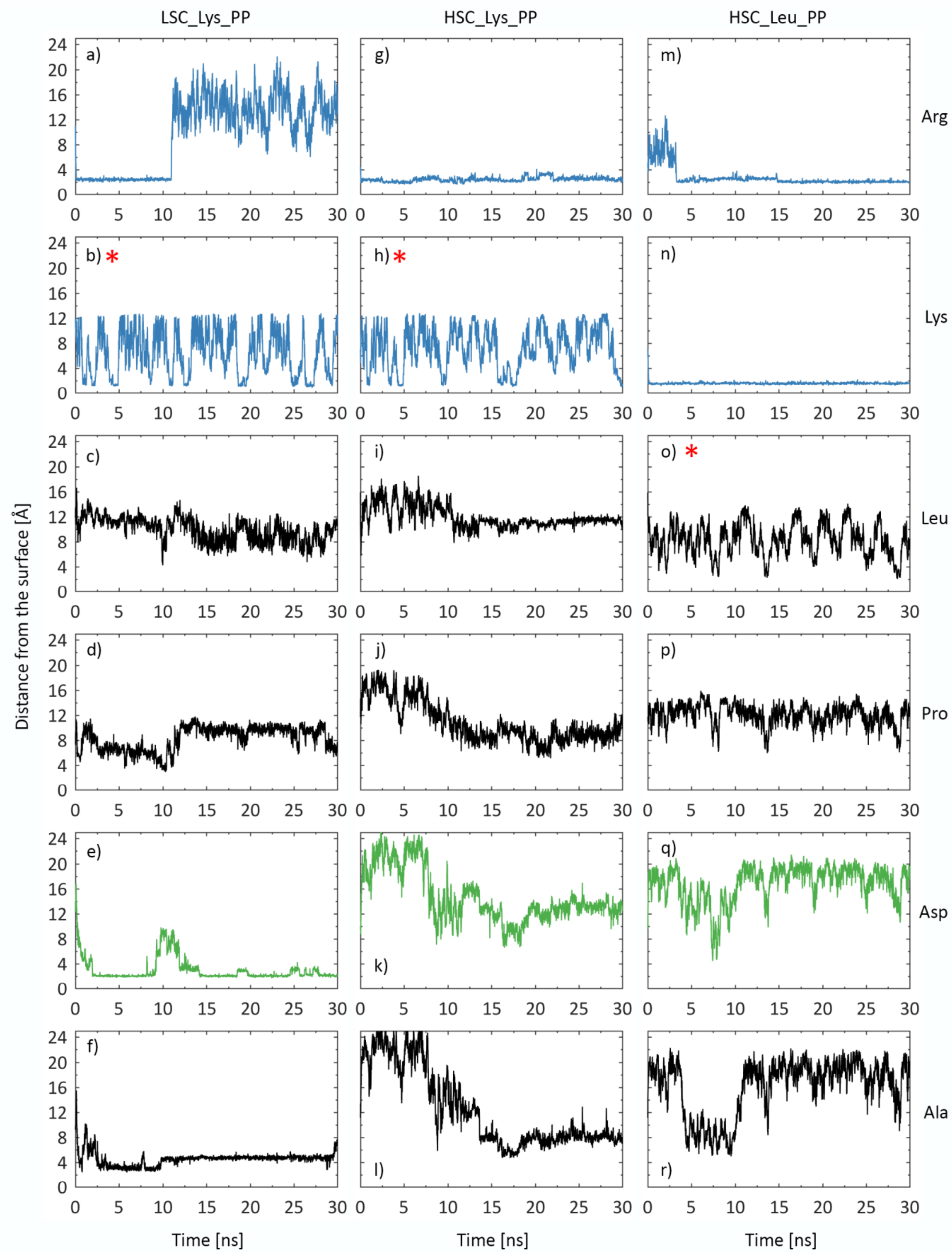

Figure 7.4 The distance of side groups of TBP from the surface. Each column corresponds to one of the systems: LSC_Lys_PP, HSC_Lys_PP and HSC_Leu_PP, respectively. Each row, as labelled on the right, corresponds to one of the amino acids, based on their order in TBP. The amino acids, whose distance from the surface is biased in each simulation, is shown by the red asterisk. Amino acids with a positively charged side group are plotted in blue, those with a negative side group are plotted in green; non-polar side groups are plotted in black.

In the LSC_Lys_PP system, TBP experiences adsorption due to the involvement of Arg, Asp and Lys residues. The distance of Lys from the surface is biased, and this residue is constantly adsorbed and desorbed on the surface, by the bias.

The attractive electrostatic interactions between the negatively charged surface of rutile and the positive Arg, causes this residue to participate in the adsorption conformation of TBP, not only in the LSC_Lys_PP system, but also the other two systems (Figure 7.4a, g, and m). Here, however, Arg desorbs from the surface after 10.93 ns (Figure 7.4a) which I believe is due to the applied bias on its neighboring residue, Lys. The stronger electrostatic interaction of Arg with the HSC surfaces, compared to the LSC surface here, does not allow the desorption of this residue from the surface (Figure 7.4g and m), especially in the HSC_Lys_PP system, despite the applied biased on Lys.

Comparison between the distance of Asp from the surface for different systems shows that on the LSC surface, where the charge is small, Asp can establish a favorable adsorption point on the surface, which lasts over the most part of the simulation time (Figure 7.4e). While on the surfaces with the higher negative charge (HSC), Asp stays relatively far from the surface and does not participate in the adsorption of the hexapeptide (Figure 7.4k and q). In the LSC_Lys_PP system, Ala also stays very close to the surface which is due to its relative position between Asp and the carboxyl end group of the TBP residue, both of which being bonded to the surface. In conclusion, in the LSC_Lys_PP system, the low surface charge density allows the interaction of negative (Asp) and non-polar (Ala) residues with the surface, as there is only one negative charge point on the surface.

For this system, TBP shows two adsorption conformations, once for t < 10.93 ns, which involves Arg, Asp and Ala, and one for t > 10.93 ns, which involves Asp and Ala. These two adsorption conformations can be seen in Figure 7.5. Interestingly in Figure 7.5a, the structure-making role of Pro can also be seen by keeping Arg and Asp, on the same side of the carbon chain (cis), as proposed by Sano and Shiba (9). As already explained, the desorption of Arg for t > 10.93 ns is believed to be due to the bias on the Lys residue, and therefore, the adsorption conformation of TBP for the LSC_Lys_PP system is Figure 7.5a, which correspond to either C-shaped or worm-like conformation (Table 7.2). In their study, Brandt and Lyubartsev (13) differentiated C-shaped and worm-like conformations based on the end-to-end distance of TBP. The end to end distance was defined as the distance between the alpha-carbon of Arg and Asp and had a value of $\sim$ 16 Å for the C-shaped conformation, and a value of 12 Å for the worm-like conformation. Therefore, the end-to-end distance of TBP for the conformation of Figure 7.5a was measured; this parameter had a value of 16.15 Å (and an average value of 15.31 for t < 10.93 ns), showing that the adsorption conformation of TBP in the LSC_Lys_PP system is the C-shaped conformation in Table 7.2, where Lys is not involved in the adsorption of TBP. Therefore, the C-shaped conformation occurred on the neutral (100) surface (13), but also LSC (110) surface, studied here.

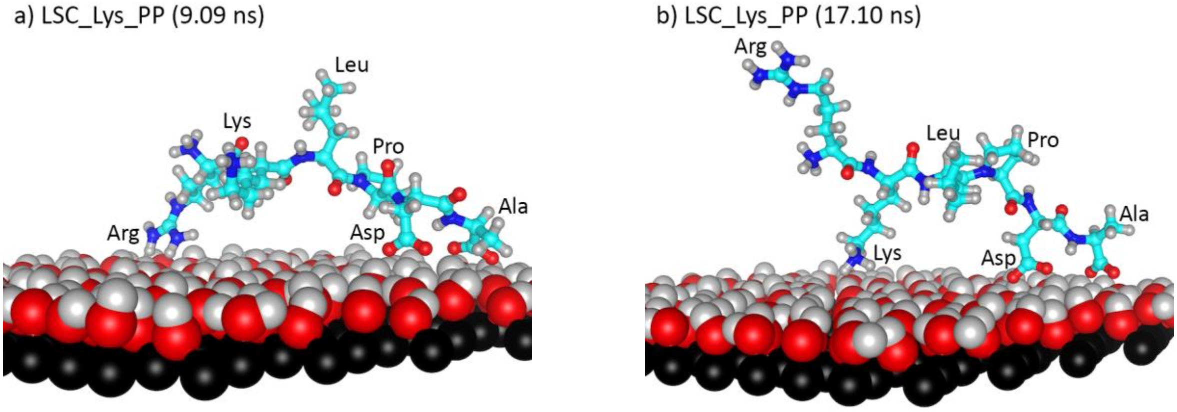

Figure 7.5 Adsorption conformations of TBP in the LSC_Lys_PP system for a) t < 10.93 ns and b) t > 10.93 ns. Only the Ti and hydroxyl groups of the rutile surface are shown. Water is not shown for the sake of clarity.

In both other systems (HSC_Lys_PP and HSC_Leu_PP), the high negative surface charge -0.104 $C \cdot m^{-2}$ (*cf.* -0.012 $C \cdot m^{-2}$ for the LSC_Lys_PP system) prevents Asp to approach and adsorb on the surface (Figure 7.4k and q). In the C-shaped and worm-like adsorption conformations of TBP reported in the literature, Asp participates in the adsorption (Table 7.2). The non-hydroxylated rutile (100) surface studied by Brandt *et al.* (13), does not have a charge. On the LSC surface also, the adsorption of Asp on the surface was observed.

In the other two work, one on Ti (9) and one on amorphous titanium oxide (12), the surface has a negative charge close to the physiological condition, similar to HSC surfaces here, but they do report the involvement of Asp in the adsorption. However, both these studies (9,12) have an amphoteric surface, where Asp can interact with the OH_2^+ and Ti_2OH^+ groups on the surface, contrary to the HSC surfaces which only have O^- and OH. This explains why the negatively charged simulated surface of rutile (110) here, did not attract Asp. The attractive electrostatic forces between the negative surface and positive side groups (Arg and Lys) are now stronger and both these amino acids contribute to the adsorption of TBP in HSC_Lys_PP and HSC_Leu_PP systems.

Two adsorption conformations can also be suggested for the HSC_Lys_PP system for t < 14 ns and t > 14 ns; as, Leu, Pro, Asp and Ala stay at the relatively same distance from the surface for t > 14 ns (in Figure 7.4). The adsorption conformation of TBP in the HSC_Lys_PP system for t < 14 ns indeed is similar to the adsorption conformation of TBP in the HSC_Leu_PP system, where over the simulation time, Arg and Lys govern the adsorption, but not the other residues (Figure 7.4m to r). So, here, the TBP conformation for the HSC_Lys_PP system is shown for t > 14 ns (Figure 7.6a), since for t < 14 ns it is similar to the HSC_Leu_PP system (Figure 7.6b).

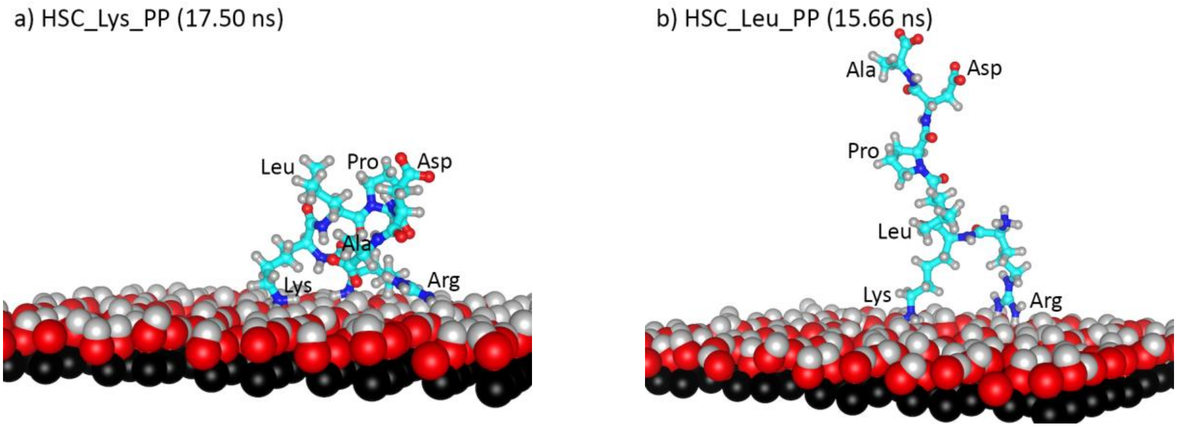
a) HSC_Lys_PP (17.50 ns)
b) HSC_Leu_PP (15.66 ns)

Figure 7.6 TBP adsorption conformation for a) t > 14 ns in the HSC_Lys_PP system, and b) HSC_Leu_PP system. For t < 14 ns, the adsorption conformation in the HSC_Lys_PP system is similar to (b). Only the Ti and hydroxyl groups of the rutile surface are shown.

The adsorption conformations in HSC_Lys_PP and HSC_Leu_PP systems can now be compared to those summarized in Table 7.2. For t < 14 ns in the HSC_Lys_PP system and for the entire range of simulation time in the HSC_Leu_PP system, Arg and Lys participate in the adsorption, which corresponds to the upright conformation observed by Schneider and Colombi Ciacchi (12). Their observation was also made on the negatively charge titanium oxide surface. Although the surface charge density in both cases are close, here this conformation was observed on the crystalline rutile surface while Schneider and Colombi Ciacchi (12) reported this conformation on the amorphous titanium oxide surface. Therefore, this conformation depends mostly on the surface charge density and not that crystallinity of the titanium oxide surface.

For t > 14 ns in the HSC_Lys_PP system, the adsorption conformation is very compact compared to those observed in LSC_Lys_PP and HSC_Leu_PP systems (Figure 7.5 and Figure 7.6b) and involves Arg and Lys. Hereafter, this conformation will be referred to as the compact conformation. The difference of this conformation with the upright conformation is, in fact, the involvement of the amine end and carboxyl end of TBP. As it can be seen in Figure 7.6a, for t > 14 ns, the amine end adsorbs on the surface. In addition, the carboxyl end approaches the Arg residue, which is adsorbed on the surface. These two end groups preserve their state until the end of the simulation time. The adsorption of the amine end on the surface and the coordination of the carboxyl end with Arg, in fact, stabilize the relative distance of other residues in TBP from the surface (Figure 7.4i to l) and causes an even more compact adsorption conformation of TBP on the surface compared to those previously reported. In the study by Schneider and Colombi Ciacchi (12), the end groups of TBP were capped by CH_3CO and $-NHCH_3$; therefore, such a conformation could not be present. However, this was not the case in the study by Brandt and Lyubartsev (13). Still, in their work, they did not report the compact adsorption in Figure 7.6a. Since they studied the neutral rutile (100) surface, while here the negatively charged rutile (110) surface is studied, this suggests that the more compact conformation is driven by the higher surface charge density.

The distribution of adsorbed species on the xy-plane for the three systems, as well as the biased residue, is shown in Figure 7.7. For the LSC_Lys_PP system, Asp adsorbs on the surface hydroxyl groups and relatively far from the surface charge point (Figure 7.7a). The adsorption of Asp on the surface is stable during the simulation time and the adsorption site does not change a lot. Arg adsorbs both close to the surface charge point and far from it. The adsorption close to the charge point shows that Arg has a tendency towards the surface charge point due to the attractive electrostatic forces. However, the bias applied between Lys and the charge point leads to continuous adsorption of Lys on the surface (Figure 7.4b), which is why Arg has to move further from the charge point, in its adsorbed conformations. On the HSC surface, several charge points are present. As it can be seen in Figure 7.7b, Arg interacts with the surface charge points. The upright adsorption conformation of TBP in the HSC_Leu_PP system is also resembled in Figure 7.7c, and both Arg and Lys interact with the charge points on the surface. Arg is much more mobile on the surface compared to Lys.

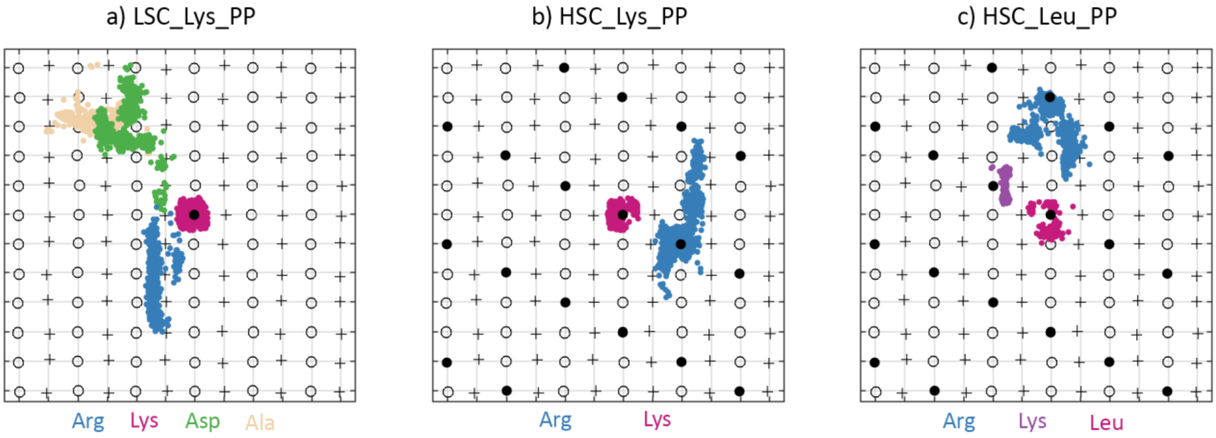

Figure 7.7 Distribution of adsorbed residue on the xy-plane for the three systems of a) LSC_Lys_PP, b) HSC_Lys_PP and c) HSC_Leu_PP. The terminal hydroxyl groups are shown via the plus signs, the bridging hydroxyl groups via circles, and surface charge points via black filled circles. The distance bias is always applied between the side chain and central charge point in (a), and the equivalent charge point in (b) and (c). Arg adsorption sites are in blue, Asp in green and Lys in purple and Ala in orange. The residue under the bias is shown in pink.

7.3.2 Free energy of adsorption

The free energy of systems under the applied bias on the R_g of TBP and the side group-surface distance for the three systems is shown in Figure 7.8. The width of the low free energy region along R_g is the narrowest for LSC_Lys_PP. This is because the adsorption conformations of TBP for $t < 10.93\ ns$ and $t > 10.93\ ns$ both correspond to a narrow range of R_g between 5.5 and 7 Å. Also, the worm-like conformation for $t < 10.93\ ns$ involves Arg and Asp. These amino acids are on two opposite ends of TBP (RKLPDA) and their adsorption on the surface, in the manner shown in Figure 7.5a and Figure 7.7a, limits the radius of gyration of the residue to be easily varied (Figure 7.8a). For $t > 10.93\ ns$, when Arg desorbs from the surface due to the applied bias on its neighboring residue (Lys), the polypeptide has unfolded and it is very difficult for it to acquire a more compact conformation (Figure 7.5b). This, however, may be resolved by extending the simulation time further.

For the HSC_Lys_PP system, the low free energy region is wider than the other two systems but also extends towards smaller values (Figure 7.8b). Between the two adsorption conformations observed for TBP in this system, the upright conformation for $t < 14\ ns$ leads to larger R_g values while the compact conformation in $t > 14\ ns$ leads to smaller R_g values.

The upright conformation in the HSC_Leu_PP system has an R_g similar to the LSC_Lys_PP system, but since adsorption is only driven by one end of TBP (RKLPDA), as opposed to both ends (RKLPDA), the radius of gyration extends more.

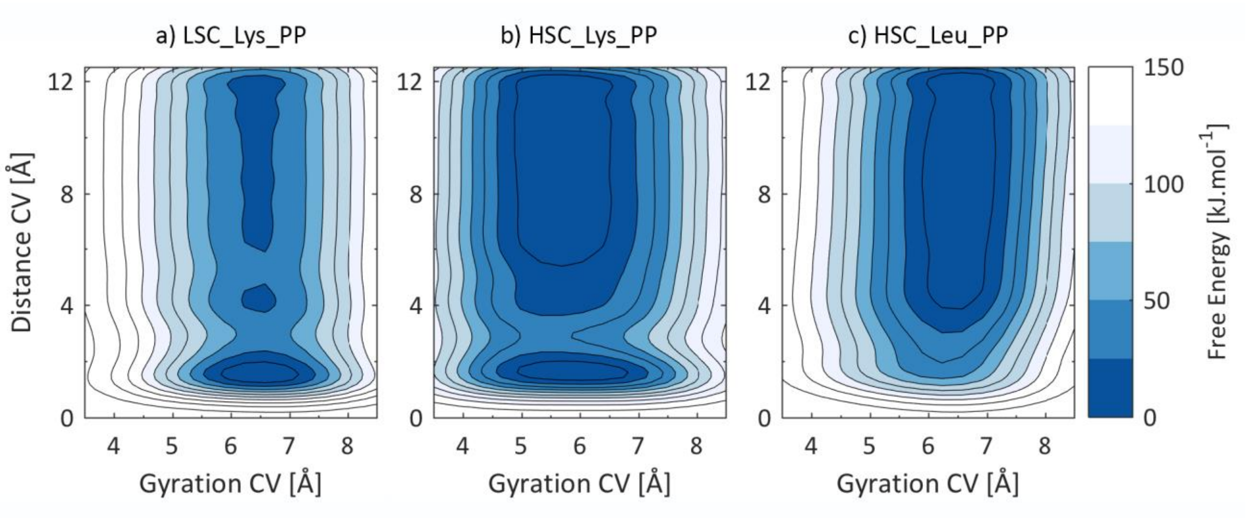

Figure 7.8 2D free energy profile as a function of the interacting side group of TBP with rutile and the radius of gyration of TBP for a) LSC_Lys_PP, b) HSC_Lys_PP and c) HSC_Leu_PP.

The projection of the free energy along the distance CV, over the entire range of R_g, is shown in Figure 7.9. Since the bias is only acting on one of the six residues of TBP, and it does not assure if all other residues are also adsorbed or desorbed, the adsorption energetics of TBP cannot be reported, and those in Figure 7.9, are for the side group of TBP which is under the bias. As expected, the adsorption of the non-polar Leu side group on the surface is not favorable.

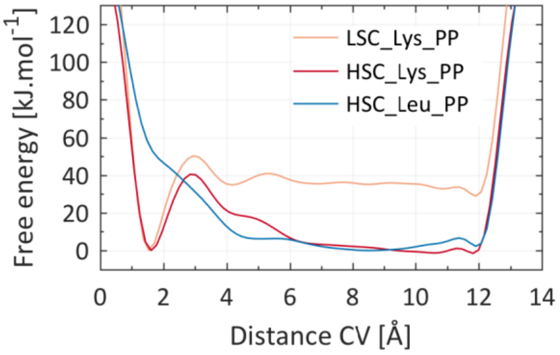

Figure 7.9 Free energy of interaction of TBP with rutile along the distance CV.

An interesting observation of this chapter is the energy difference between the solvated and adsorbed states of Lys in TBP for LSC_Lys_PP and HSC_Lys_PP systems. As it can be seen in Figure 7.9, on the surface with a lower charge density, the adsorption energy of Lys on the surface is -35.17 $kJ.mol^{-1}$, while on the surface with the higher charge density, the energy states for the solvated and adsorbed Lys are very similar, and the adsorption energy is -0.92 $kJ.mol^{-1}$. In the former, the C-shaped conformation was observed where Lys did not participate in the adsorption, and in the latter, the upright and compact conformations were observed, in both of which, Lys participated in the adsorption. Taking into account the higher surface charge density in the latter case, the reason for the behavior of adsorption energy for the LSC_Lys_PP and HSC_Lys_PP systems is not clear. The energy barrier to the desorption of Lys on the surface with the lower charge density (LSC) is 50.20 $kJ.mol^{-1}$ and larger than on the surface with the higher surface charge density (HSC), which is 41.91 $kJ.mol^{-1}$, or 16.5%. The adsorption conformations of TBP and the energetics of the systems are summarized in Table 7.4.

Table 7.4 TBP adsorption conformations observed in this work.

System	Ads. Conformation	Biased residue	Adsorption energy
LSC_Lys_PP	(t < 10.93 ns) C-shaped	Lys	-35.17
HSC_Lys_PP	(t < 14 ns) Upright (t > 14 ns) Compact	Lys	-0.92
HSC_Leu_PP	Upright	Leu	~60

7.4 Conclusion

This chapter investigates the interaction of the TBP hexapeptide with the rutile (110) surface. The effect of the surface charge density and the interacting side chain on the adsorption energetics of the hexapeptide on the surface were studied. Two collective variables were used which affected the conformation of TBP and adsorbed side chains on the surface.

The C-shaped conformation, where Asp participates in the adsorption of TBP, here, was only observed for the LSC system, where the negative charge on the surface is small. This conformation was not observed for HSC surfaces. Previously this conformation was reported on the titanium oxide surface based on experimental observation; in agreement with the suggestion of (9), the interaction of Asp with the titanium oxide surface should be due to the amphoteric characteristics of the surface, which is not present on the rutile surface studied here.

The compact conformation, in the HSC_Lys_PP system, occurs because the end groups of TBP (the amine and carboxyl) group also participate in the adsorption of the hexapeptide. These end groups are not present experimentally but were present in the previous work (13) on the neutral rutile (100) surface. The fact that this conformation was not reported in that study implies that it is driven either by the high surface charge density, or the (110) surface of rutile, or both. I believe that the former has the highest contribution.

The upright conformation was observed for both HSC surfaces; this conformation was previously reported for the amorphous titanium oxide surface (12). Therefore, the crystallinity of the surface is not driving this conformation, but rather the surface charge.

The overall remark of this chapter is that the adsorption conformations of TBP on titanium oxide surfaces depend most importantly on the surface charge density and not the crystallinity or crystallographic surface. Similar conformations were observed on rutile (110), rutile (100) and amorphous titanium oxide; but the surface charge density determined the adsorption conformation.

The obtained energy profile during the simulations only depends on the adsorption state of the biased residue (Lys or Leu), and not the other residues. Therefore, the adsorption energy of TBP cannot be reported. For the biased residues, while the adsorption of Lys on the surface is accompanied by an energy well for the system in the adsorbed state, the adsorption of non-polar Leu on the surface is very unfavorable.

Adsorption of Lys on surfaces with both lower and higher charge densities is accompanied by an energy minimum. However, the system is in a lower energy state, compared to when Lys is solvated in water, for the LSC_Lys_PP system. Unfortunately, this observation could not be explained and the reason why Lys does not participate in the C-shaped conformation was not understood.

Future work can study the adsorption conformation of TBP by biasing the Asp and Arg residues. To obtain the adsorption energy of TBP it is interesting to use two collective variables to bias the distance of two amino acids from the surface. For example, biasing Arg and Asp will result in the adsorption energy for the C-shaped conformation, while biasing Arg and Lys will give the adsorption energy of the upright conformation.

References

1. Sano, K.-I., Sasaki, H. & Shiba, K. Specificity and biomineralization activities of Ti-Binding Peptide-1 (TBP-1). *Langmuir* **21,** 3090–3095 (2005).

2. Tenzer, S. *et al.* Nanoparticle size is a critical physicochemical determinant of the human blood plasma corona: A comprehensive quantitative proteomic analysis. *ACS Nano* **5,** 7155–7167 (2011).

3. Marieb, E. N. & Hoehn, K. *Human anatomy & physiology: Pearson new international edition*. (Pearson Education Limited, 2013).

4. Dockal, M., Carter, D. C. & Rüker, F. The three recombinant domains of human serum albumin: Structural characterization and ligand binding properties. *J. Biol. Chem.* **274,** 29303–29310 (1999).

5. Sugio, S., Kashima, A., Mochizuki, S., Noda, M. & Kobayashi, K. Crystal structure of human serum albumin at 2.5 Å resolution. *Protein Eng. Des. Sel.* **12,** 439–446 (1999).

6. Baler, K. *et al.* Electrostatic Unfolding and interactions of albumin driven by pH changes: A molecular dynamics study. *J. Phys. Chem. B* **118,** 921–930 (2014).

7. He, X. M. & Carter, D. C. Atomic structure and chemistry of human serum albumin. *Nature* **358,** 209 (1992).

8. Guex Nicolas & Peitsch Manuel C. SWISS-MODEL and the Swiss-Pdb Viewer: An environment for comparative protein modeling. *ELECTROPHORESIS* **18,** 2714–2723 (1997).

9. Sano, K.-I. & Shiba, K. A hexapeptide motif that electrostatically binds to the surface of titanium. *J. Am. Chem. Soc.* **125,** 14234–14235 (2003).

10. Hayashi, T. *et al.* Critical amino acid residues for the specific binding of the Ti-recognizing recombinant ferritin with oxide surfaces of titanium and silicon. *Langmuir* **25,** 10901–10906 (2009).

11. Hayashi, T. *et al.* Mechanism underlying specificity of proteins targeting inorganic materials. *Nano Lett.* **6,** 515–519 (2006).

12. Schneider, J. & Colombi Ciacchi, L. Specific material recognition by small peptides mediated by the interfacial solvent structure. *J. Am. Chem. Soc.* **134,** 2407–2413 (2012).

13. Brandt, E. G. & Lyubartsev, A. P. Molecular dynamics simulations of adsorption of amino acid side chain analogues and a titanium binding peptide on the TiO_2 (100) Surface. *J. Phys. Chem. C* **119,** 18126–18139 (2015).

Chapter 8 Conclusion and perspective

The current thesis aims to provide essential information on the mechanism of apatite formation on the rutile surface. This task was undertaken in four steps:

- The current state of the art on the subject was extensively reviewed and further avenues to be investigated were highlighted.
- Interaction of different ionic species, either the most abundant ones or those considered important, with the surface was studied.
- Interaction of single amino acids with the surface was studied.
- The fate of pre-adsorbed species, as other species approach the surface, was studied.

In the following, first, the main findings of each step are presented in detail, and then, directions for future work are suggested.

8.1 Current stand of computational studies on the subject

The initial examination of the literature and studies on the interaction of ionic and organic species on rutile surfaces showed that while a few articles have reviewed and summarized the experimental studies on this subject, no attempt had been made for computational studies. In the course of this thesis, such studies were systematically studied and summarized in the form of a review article to highlight areas where future computational work will be beneficial. The review paper was framed in the main subject of the current thesis, meaning that the focus point was put on the interest in apatite formation and bio-relevant conditions to encourage more future studies on these areas.

Regarding studies on ionic species, it was found that only some of those, mainly the cations, which are present in physiological conditions, have been considered and studied so far. In addition, only classical molecular dynamics methods were used in these studies, and therefore, no statement on the energetics of the interactions could be made. Effectively, these two points were used as the rationale behind the question to be studied in chapter 4 of this thesis. Previous work on the interaction of ionic species with the rutile surface showed that the pH of the solution (which dictates the surface charge density), temperature and ionic valence affect the thermodynamics and kinetics of adsorption of ions on the surface. Electrostatic interactions proved to affect the adsorption of ions on the surface notably; higher charge density leading to stronger adsorption of oppositely charged ions on the surface. Furthermore, for ions with a higher valence, it was reported that the ions could not easily release their hydration shell. This caused smaller ions like magnesium or zinc to preserve their hydration shell in their adsorbed state, or in other words, adsorb in an outer-sphere mode.

Regarding studies on organic species, it was found again that not only the surface characteristics such as the crystal structure, charge density, surface defects and state of hydration but also the characteristics of the organic species, such as its structure and initial orientation with respect to the surface, control the organic-surface interactions. Organic species can adopt various orientations of their different functional groups towards the surface; such that those with a favorable interaction with the surface, approach the surface closer, while other groups with an unfavorable or less favorable interaction with the surface, stay further from the surface. The main findings of these studies can be summarized as the following:

- Adsorption behavior differs from one crystallographic surface to the other.
- Defective sites involve atomic species which are not fully coordinated and lack one or more interatomic bonds. Therefore, there exists excess energy in a defective site, which promotes adsorption of species on this site.
- Charged surfaces favor the adsorption of functional groups with the opposite charge. Although many studies were carried out on different surface charges and with different organic species, a general statement could not be made about which functional groups favor the adsorption more and which do not. Especially, in the cases where only the side group of amino acids were considered, no clear trend was observed based on the charge and polarizability state of the side group. Indeed, this was studied in chapter 5 of this thesis, where the reason behind this observation was explained.

For both ionic and organic species, water proved to play a vital role in mediating the interaction between solvated species as well as between these species and the surface. On a hydrophilic surface, the adsorbate has to displace water to reach the surface. The adsorbate itself may also have strong interactions with water, meaning that to adsorb on an adsorbent, it has to be partially dehydrated.

8.2 Ionic species interacting with rutile

In chapter 4, first, the distribution of ionic species in an SBF solution and under physiological condition was obtained using thermodynamic modelling. The force field parameters of carbonate, bicarbonate, phosphate and hydrogen phosphate were modified based on previously reported parameters to be able to model the interactions between these ions and rutile. Further comparison of the modified force field parameters with a recently proposed force field set for phosphate species (1) verified the performance of the force field for phosphate.

However, the water-hydrogen phosphate interactions were not properly captured by the modified force field in this work, mainly because no interaction was defined between the ion and hydrogen of water. Therefore, results obtained on hydrogen phosphate are not presented in this thesis but should be tested further and compared to the recent force field to examine their reliability.

Results with respect to other ions than hydrogen phosphate showed that all ionic species exist mainly in their free form, except carbonate and phosphate ions which favor their protonated form (bicarbonate and hydrogen phosphate, respectively). Based on these findings, the adsorption energetics of most of the free ionic species of SBF on the rutile surface were studied using well-tempered metadynamics simulations. Among the studied ions, adsorption of sodium, potassium, calcium, carbonate and phosphate proved to be favorable on the surface. Desorption of other ions (magnesium, chlorine, and bicarbonate) proved to be more frequent than their adsorption. Compared to the apatite formation model on an amorphous sodium titanate surface, the apatite formation on rutile seems to be driven by calcium and phosphate but also sodium, potassium and carbonate. If one takes into account the relative concentration of these species to each other, sodium seems to be very important. Although its affinity for the surface is not as much as calcium, it may govern the interactions more simply because it is more abundant in the solution.

Tests were performed on different adsorption sites of local charges of 0, -1 and -2 e. It was observed that electrostatic interactions between the ionic species and the local charge directly affect the energetics of the adsorption; the adsorption of cations becomes more favorable as the local charge becomes more negative.

Based on thermodynamic modelling and the interest in apatite formation, the adsorption of three ionic pairs on the rutile surface was studied. These pairs included $[NaCl]^0$, $[CaPO_4]^-$ and $[CaHCO_3]^+$. The energetics of the formation of these ions were calculated using WT-MTD and it was observed that among the three pairs, the formation of $[CaPO_4]^-$ is significantly more favorable than the other two.

In fact, the relatively small dissociation barrier of $[NaCl]^0$ and $[CaHCO_3]^+$ ionic pairs did not allow the study of the adsorption of these pairs on the rutile surface since these pairs dissociated well before sufficient data could be collected on their adsorption and desorption behavior. The adsorption of $[CaPO_4]^-$ proved to be favorable on the surface and without any notable energy barrier suggesting that it could be important in the apatite formation. The adsorption of a phosphate ion on a pre-adsorbed calcium ion on the surface was also investigated. This adsorption event proved to be very favorable, which is due to the affinity of the single calcium and phosphate ions for the surface, as well as the $[CaPO_4]^-$ pair which has a very favorable energy of formation.

Based on the free energy calculations, two mechanisms were proposed for the formation of hydroxyapatite, in a very simplistic manner. The first one involves the formation of the $[CaPO_4]^-$ pair in water, and then its adsorption on the surface. The second one suggests that first, calcium adsorbs on the surface, followed by the adsorption of phosphate. The free energy calculations show that the second mechanism is much more favorable, which is also the model proposed previously for apatite formation on an amorphous sodium titanate surface (2,3).

8.3 Amino acids interacting with rutile

Single amino acids were chosen as the organic species to interact with rutile in chapter 5. Single amino acids are present in human blood plasma in small quantities but their small size compared to other biomolecules makes it plausible for them to reach the surface of a biomaterial before other biomolecules. Six amino acids were chosen, covering charged, polar and non-polar side groups and their interaction with the rutile surface was studied via WT-MTD by using the distance of the center of mass of the amino acid from the surface as the collective variable, which is commonly used. However, this collective variable proved to be inefficient in differentiating adsorption conformations of the amino acids on the surface with respect to the side group and the backbone. Thus, a post-processing analysis, known as reweighting, was used where the free energy profile was projected to a two-dimensional collective-variable space. After projection, the energetics of different adsorption conformations of amino acids on the rutile surface were distinguishable and a clear statement could be made on the affinity of the amino acid for the surface. It was found that the backbone can always adsorb in the vicinity of a local charge of -1 e, mainly driven by attractive electrostatic interactions with the amine group. Polar and charged side groups were able to disrupt the structured water layer close to the rutile surface and adsorb directly on the surface whereas adsorption via non-polar side groups was not favorable.

Therefore, the use of two separate collective variables for interpreting adsorption conformations of single amino acids, achieved by the reweighting method, proved to be the key for explaining adsorption conformations based on the nature of the side group of the amino acids. In previous work (4), this was not possible because only the distance of center of mass of the amino acid was considered as the reaction coordinate, which is not able to distinguish adsorption via the backbone, the side group or both backbone and side group. Performing the calculations with the use of two collective variables acting on the backbone and the side group, in the original setting, would have been finer, but the post-processing on the data already obtained (having in mind that the wall time for a single amino acid is 40 days), proved to be much more efficient.

8.4 Competing adsorption: Who likes the surface more?

To understand how the adsorption of a species on the rutile surface can perturb the species already adsorbed a priori, in chapter 6 two cases were studied. In the first case, calcium and phosphate ions approached the rutile surface with pre-adsorbed Arg and Asp amino acids while in the second case, amino acids approached the rutile surface pre-adsorbed with several calcium ions.

For the first case, it was observed that in the competition between the ion and the amino acid for the local charge point on the surface, Arg with its positive side group and an electrostatically favorable interaction with the charge point, can prevent calcium approaching the charge point very closely; Asp, with its negative side group and repulsive electrostatic interaction with the local charge point, on the other hand, allowed calcium to adsorb very close to the charge point.

For the second case, it was observed that the simulation results are notably affected by the simulation setup, when the rutile surface has several pre-adsorbed calcium ions, and chlorine ions are added to the simulation box to neutralize the overall charge. The relative position of the calcium and chlorine ions with respect to each other and the surface caused water molecules to have a directional distribution in the direction normal to the surface, indicative of a spurious electrical field in the cell. The adsorption of four amino acids was studied on the rutile surface with pre-adsorbed calcium ions but the relative position of the ions in the system and the directional distribution of water affected the dynamics of the amino acids as well as their adsorption energetics on the surface. Generally, it seems that adsorption behavior, in this case, is still mainly driven by electrostatic forces. The adsorption of the non-polar Leu on the surface was the least affected by the artefacts in the system due to its non-polar side group, and it proved to be less favorable on the surface with a higher charge. More quantitative statements cannot be made due to the artefacts present in the system.

In general, findings of chapter 6 showed that amino acids neither inhibited nor perturbed the adsorption of ionic species on the surface. Considering that in-house studies have shown a clear inhibitory effect of the larger albumin protein for certain concentrations (5), the neutral effect of amino acids on the interaction of ions with the rutile surface, observed in chapter 6, may be due to the small size of amino acids compared to biomolecules and proteins.

8.5 Open questions and further directions

There are different levels of complexity to apatite formation and this work is a very simplified, yet necessary, step in understanding this phenomenon. Therefore, the complexity of the system under study could be increased in several ways.

8.5.1 The surface of the testing sample

The titanium oxide layer on the surface of a Ti-based material is a mixture of different amorphous and crystalline phases, such as rutile, anatase, sodium titanate and amorphous phases. Although in this thesis the focus was only on rutile, this phase may not be the most bioactive phase. The surface may also be different in terms of structure and the extent of crystallinity. In this thesis, the non-defective rutile (110) surface was studied, but clearly many other surfaces can be considered different in either or all of the following: crystallinity, polymorphism, crystallographic plane, level of defectiveness, surface charge.

8.5.2 Apatite formation mechanism – Nucleation and growth

In this thesis, interactions of only some of the ionic species which are present under physiological condition, either in their free form or an ionic pair, were studied. Although importance should be given to those species with a higher concentration, there are still some species whose interaction with the surface seem interesting (for example, sulphate), and which were not covered in this thesis, and could be studied.

The simulation setting in this thesis mainly considers single ions, which due to the small size of the simulation box, leads to a higher concentration of species compared to real systems. However, since multiple species are not present in the system, their further effects are also absent; for example, in an experimental setting, the double layer is present. It would be interesting to study the interactions of ions with the surface, also in the presence of the double layer and to understand how the interactions are affected, even though it will lead to a more concentrated setting compared to the experimental conditions.

Finally, importance should also be given to those species with a higher concentration. While in this thesis, mainly calcium and phosphate were chosen due to their contribution to apatite formation, sodium and chlorine should also be investigated, especially sodium which has an opposite charge to the charge of the titanium oxide surface, under physiological conditions. Even if species high in concentration show a lower affinity for the surface, overall, they may govern the interactions to a larger extent simply because they are more in number.

8.5.3 *In vivo* and *in vitro* conditions

Apatite forms both *in vivo*, despite the presence of many different components in blood plasma other than ionic species, and *in vitro*, despite the presence of a notable amount of tris (tris(hydroxymethyl)aminomethane) used as the buffering agent, which preliminary experimental studies show its adsorption on the (rutile) surface. Therefore, one can conclude that every component which is present in the system, can either promote or inhibit apatite formation to some extent. So, a false positive can be considered a system where the promoting factors outweigh the inhibiting ones, and a false negative is the other way around. Although very difficult, it would be beneficial if one can systematically identify the conditions which lead to a false positive from those which lead to a false negative. If these two types of parameters are identified and categorized, it will be a great help to unravel the mechanism of apatite formation.

In this study, several amino acids were considered which did not show a significant inhibiting factor. There remain many other organic molecules which can be studied, in specific polypeptides and proteins.

8.6 Outlook

The above points can be summarized as interaction of many different species, with many different phases and surfaces, and under many different conditions should be investigated, which seems a computational, but also experimental, challenge. Therefore, it is essential to devise questions in a systematic manner and with tackling each step, once at a time. In my personal point of view, the following can be beneficial to the understanding of apatite formation in future work.

Based on experimental observations, Posner's clusters ($Ca_9(PO_4)_6$) can aggregate and form clusters, nano-metric in size. The hydroxyapatite structure can be considered as ordered Posner's clusters, with the intercluster volume filled with water. Therefore, it seems very probable that hydroxyapatite may be initiated by the adsorption of Posner's clusters on the surface. The adsorption behavior of these clusters, and similar clusters but deficient of calcium, on the surface, can thus be studied.

Although as mentioned in section 8.5.1, many different structures may be present in the titanium oxide layer on the surface of Ti-based biomaterials, still, the interaction of at least some of the main ionic species (such as calcium, phosphate, sodium and chlorine), with sodium titanate should be studied, as experimental results suggest this surface to be more active, compared to other phases, for apatite formation. The difficulty of working with the amorphous sodium titanate surface is both experimental and computational. Experimentally, it is not straightforward to present the characteristics of this amorphous phase, since they are affected by many experimental settings, *e.g.,* the procedure of heat and alkali treatment. This makes it very challenging to study such a surface computationally, as, besides its amorphous structure and probably missing force field parameters to be developed, there is not only one unique structure to be tested, again facing the problem of having many different combinations. Nevertheless, starting with one specific stoichiometry of sodium, titanium and oxygen, one may computationally generate several amorphous structures, by heating and then rapidly cooling down the system. QM methods can then be used, although limited to a small length-scale, to obtain the interaction energy of the main ionic species with the generated (and limited) amorphous sodium titanate surface. The leverage of QM methods to other computational methods is that the collection of empirical force field parameters can be avoided. The QM study can be established on several crystallographic surfaces of rutile and anatase. Results then can be compared to understand whether the experimental statement on the higher apatite formation activity of the amorphous phase compared to anatase and rutile is valid.

Organic species, based on their functional group, associate with the ionic species to different extents. In this thesis, it was observed that single amino acids did not disturb the adsorption of ionic species on the surface. Although the small size of the simulation box leads to a higher concentration of species compared to physiological conditions, it is appealing to add multiple species to the box to be able to observe more events, given the limited time-scale of the computational methods. However, having multiple organic species in the same box will make the interpretation of the free energy profile challenging, since it would be very difficult to differentiate the contribution of each species on the free energy associated with an event. Consequently, instead of having multiple organic species, one can consider a larger organic species, which will have many more functional groups. The downside of working with larger organic species is the high computational cost, especially for molecular dynamics methods. Therefore, using larger scale atomistic simulation methods, such as coarse-grained can be a promising approach. After understanding the adsorption conformations and interactions of the organic residue with other components in the system, hybrid QM/MM methods can be used to gain insight to the details of the electronic structure of the interactions and the chemical bonds which form or break.

Last but not least, investigation of apatite growth mechanism could be carried out by using free energy barriers of events, obtained by free energy calculation such as the work in the present thesis, to kinetic Monte Carlo. This will reveal the dynamical evolution of the system in a more experimental-like setting, where different species can be present in the system. The parametrization of the rate constants including inter-species interactions could prove challenging.

References

1. Demichelis, R. *et al.* Simulation of calcium phosphate species in aqueous solution: Force field derivation. *J. Phys. Chem. B* **122,** 1471–1483 (2018).

2. Kim, H-M., Miyaji, F., Kokubo, T. & Nakamura, T. Preparation of bioactive Ti and its alloys via simple chemical surface treatment. *J. Biomed. Mater. Res.* **32,** 409–417 (1996).

3. Kokubo, T., Kim, H.-M. & Kawashita, M. Novel bioactive materials with different mechanical properties. *Focus Biomater. Sci. Asia* **24,** 2161–2175 (2003).

4. Palafox-Hernandez, J. P. *et al.* Comparative study of materials-binding peptide interactions with gold and silver surfaces and nanostructures: A thermodynamic basis for biological selectivity of inorganic materials. *Chem. Mater.* **26,** 4960–4969 (2014).

5. Zhao, W., Lemaître, J. & Bowen, P. A comparative study of simulated body fluids in the presence of proteins. *Acta Biomater.* **53,** 506–514 (2017).

Appendix A Supporting Information - Interaction of biologically relevant ions and organic molecules with titanium oxide (rutile) surfaces: A review on molecular dynamics studies

---

Supporting Information[2]
Colloids and Surfaces B: Biointerfaces 161 (2018) 563–577

Interaction of biologically relevant ions and organic molecules with titanium oxide (rutile) surfaces: A review on molecular dynamics studies

Azade YazdanYar[✦], *Ulrich Aschauer*[✦✦], *Paul Bowen*[✦]
[✦] Department of Materials Science and Engineering, École Polytechnique Fédérale de Lausanne (EPFL), Lausanne, Switzerland
[✦✦] Department of Chemistry and Biochemistry, University of Bern, Bern, Switzerland

---

List of Abbreviations

BMP2: Bone morphogenetic protein-2

DFT: Density functional theory

ECM: Extracellular matrix

EED: End-to-end distance

FN: Fibronectin

HSA: Human serum albumin

LF: Lactoferrin

MD: Molecular dynamics

---

[2] The permission for reusing the figures from the literature, in this appendix, is taken from the corresponding publishers. For any further use, the reader should refer to the corresponding publisher.

RAD: The Arg-Ala-Asp sequence

REST: Replica exchange solute tempering

RGD: The Arg-Gly-Asp sequence

SBF: Simulated body fluid

SCA: Side-chain analogues

SPC/E: Extended simple point charge

SSD: Surface separation distance

TIP3P: Three-site transferable intermolecular potential

TIP4P: Four-site transferable intermolecular potential

TBP: Titanium-binding peptide (RKLPDA: the Arg-Lys-Leu-Pro-Asp-Ala sequence)

THS: A triple helical segment

Table A.1 Amino acids.

Amino acids	One-letter abbreviation	Three-letter abbreviation	Representation
Alanine	A	Ala	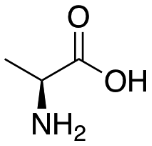
Arginine	R	Arg	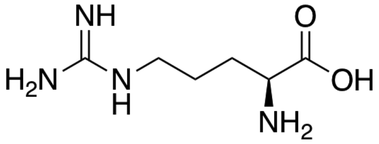
Asparagine	N	Asn	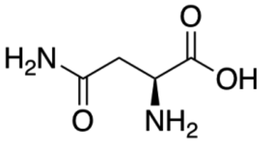
Aspartic acid	D	Asp	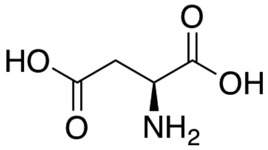
Cysteine	C	Cys	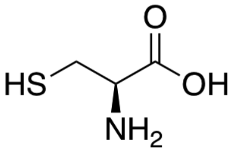
Glutamine	Q	Gln	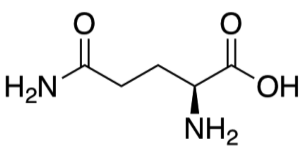
Glutamic acid	E	Glu	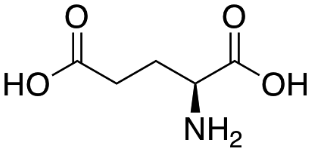

Glycine	G	Gly	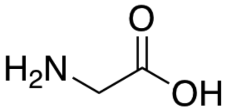
Histidine	H	His	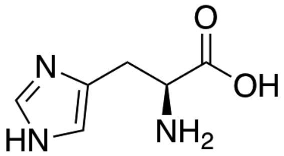
Isoleucine	I	Ile	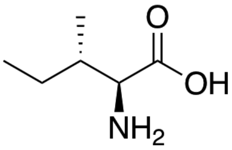
Leucine	L	Leu	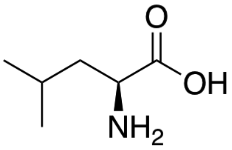
Lysine	K	Lys	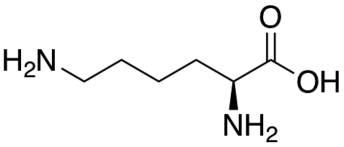
Methionine	M	Met	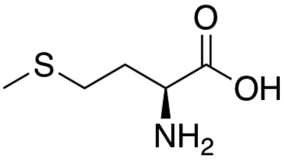
Phenylalanine	F	Phe	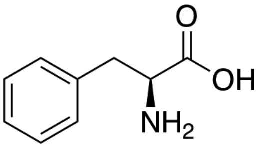
Proline	P	Pro	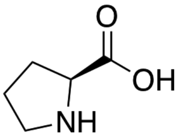
Serine	S	Ser	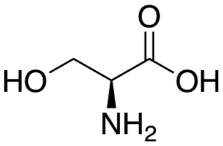
Threonine	T	Thr	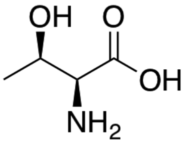

Tryptophan	W	Trp	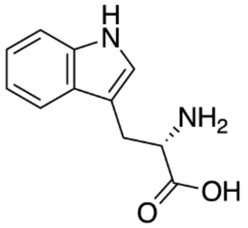
Tyrosine	Y	Tyr	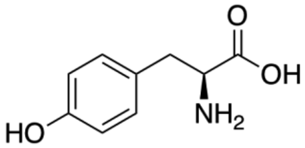
Valine	V	Val	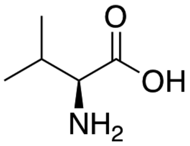

Table A.2 Chemical formula of most of the organic molecules mentioned in the review.

Name	Formula	Representation
Ace	$-C(=O)-CH_3$	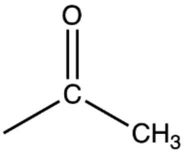
Adenine	$C_5H_5N_5$	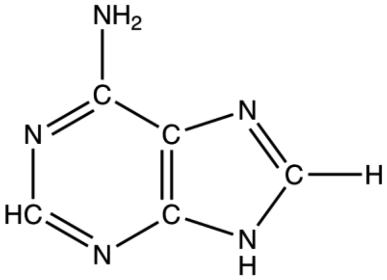
Ammonium cation	NH_4^+	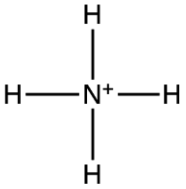
Benzene	C_6H_6	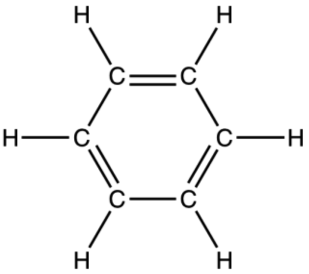

Cytosine	$C_4H_5N_3O$	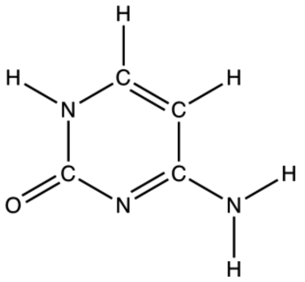
Formate anion or Methanoate anion	$CHOO^-$	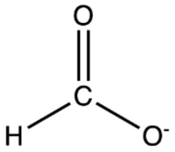
Glycolate anion	$C_2H_3O_3^-$	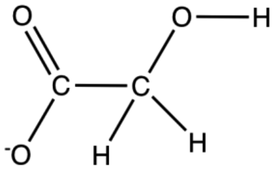
Guanidinium cation	CN_3H_5	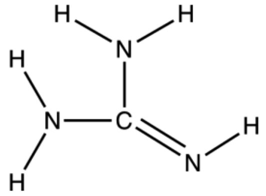
Guanine	$C_5H_5N_5O$	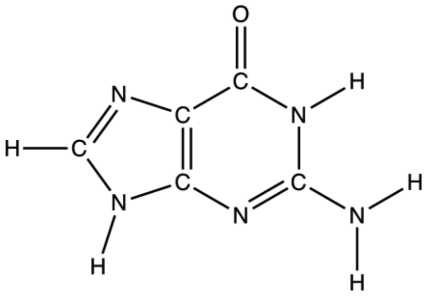
Methane	CH_4	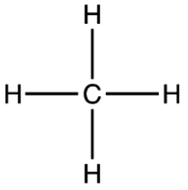
Methanol	CH_3OH	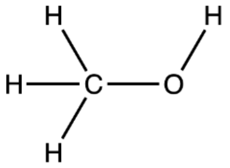
Nme	$C(=O)-NH-CH_3$	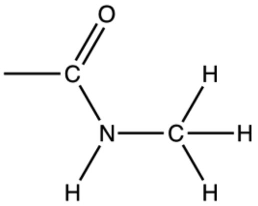

Thymine	$C_5H_6N_2O_2$	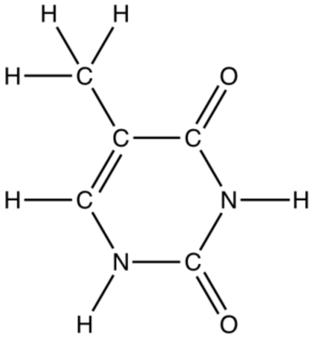
Tris or tris(hydroxymethyl-aminomethane)	$C_4H_{11}NO_3$	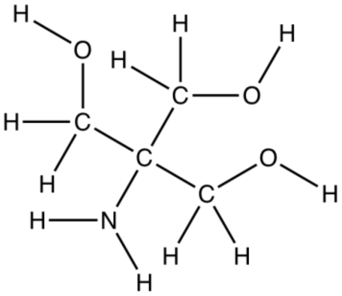

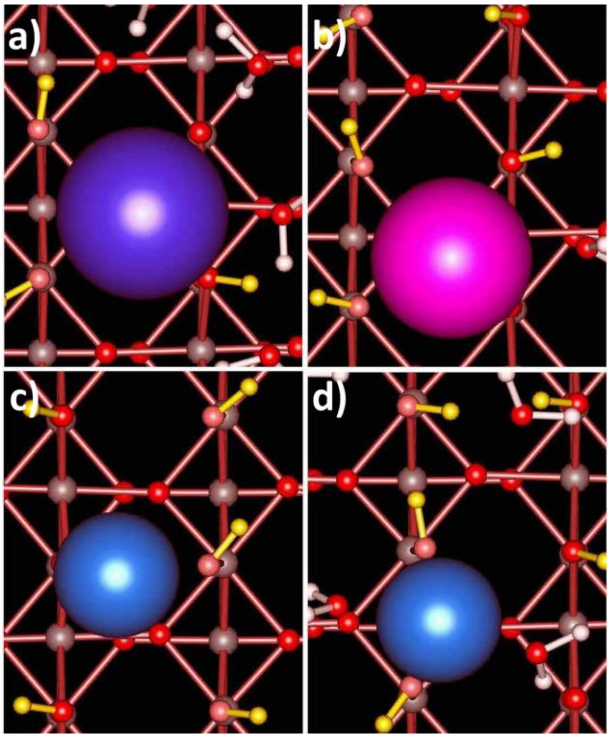

Figure A.1 Top view of the rutile (110) hydroxylated surface. Tetradentate adsorption sites for a) Rb^+ and b) Sr^{2+} and bidentate adsorption sites for Zn^{2+} between c) bridging and terminal oxygens and d) two terminal oxygens. The adsorbed ions are shown larger than other atoms for clarity. Only water molecules not farther than the adsorbed ions from the surface are shown. Color code: Ti: brown, O: red, H_H_2O: white, H (surface hydroxyls): yellow. Reprinted with permission from Předota, M. et al. 'Electric Double Layer at the Rutile (110) Surface. 2. Adsorption of Ions from Molecular Dynamics and X-Ray Experiments'. J. Phys. Chem. B 2004, 108 (32), 12061–12072. © 2004 American Chemical Society.

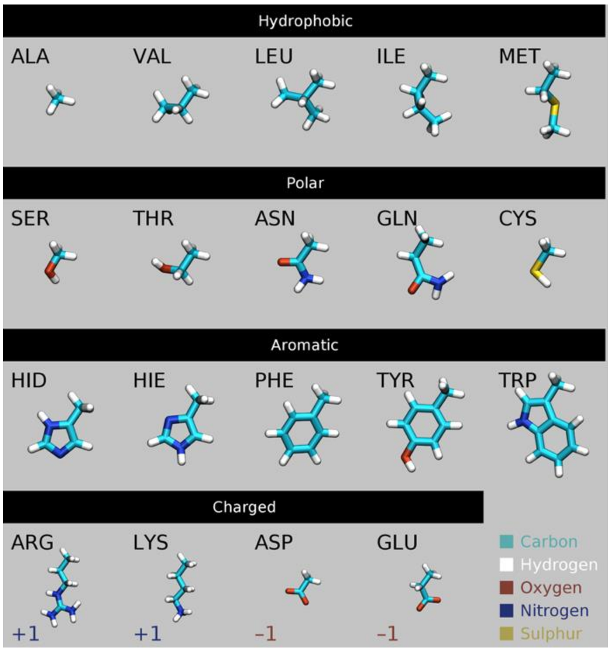

Figure A.2 Side-chain analogues (SCAs) of 18 (out of 20) naturally occurring amino acids, classified as i. hydrophobic without hydrogen bonding capability, ii. polar with hydrogen bonding capability, iii. aromatic (with ring structures) and iv. carrying net charge ±1. Reprinted with permission from Brandt, E. G.; Lyubartsev, A. P. 'Molecular Dynamics Simulations of Adsorption of Amino Acid Side Chain Analogues and a Titanium Binding Peptide on the TiO_2 (100) Surface'. J. Phys. Chem. C 2015, 119 (32), 18126–18139. © 2015 American Chemical Society.

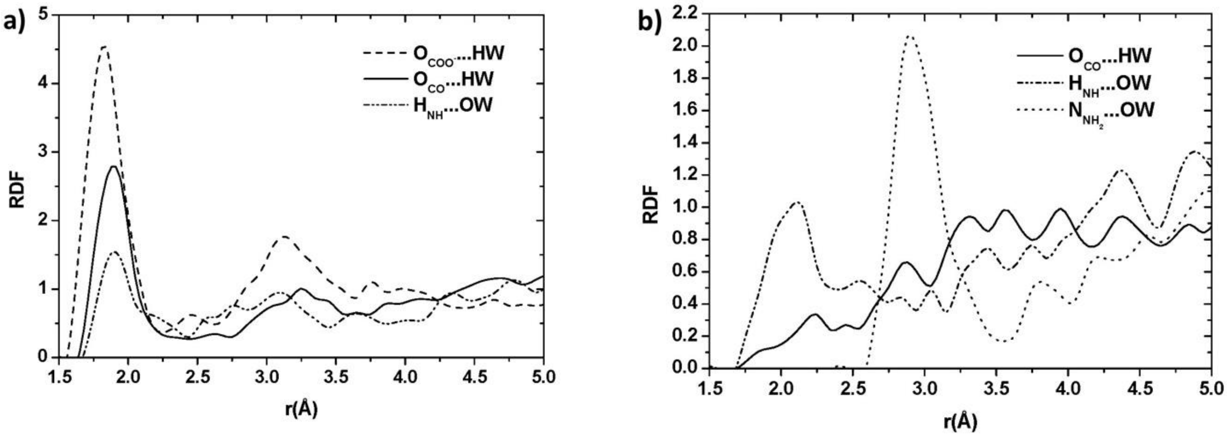

Figure A.3 Radial distribution function of different side groups (carboxyl: COO, carbonyl: CO, amide: NH and amine: NH_2) of a) Ala-Ace and b) Ala-Nme terminated molecules with water atoms (HW and OW are the hydrogen and the oxygen of water, respectively). Adapted with permission from Carravetta, V.; Monti, S. 'Peptide−TiO_2 Surface Interaction in Solution by Ab Initio and Molecular Dynamics Simulations'. J. Phys. Chem. B 2006, 110 (12), 6160–6169. © 2006 American Chemical Society.

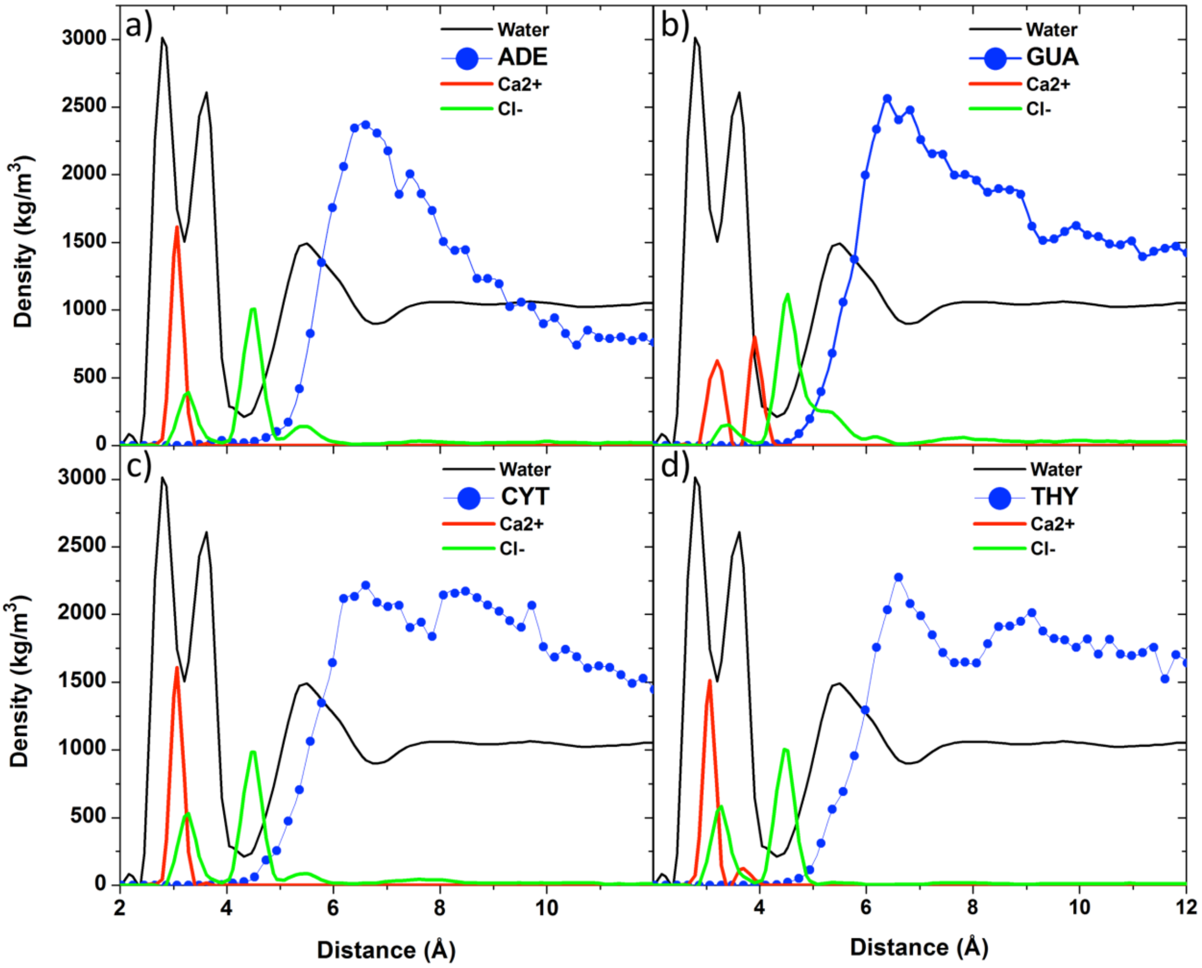

Figure A.4 Density as a function of the distance from the rutile (110) negatively charged (partially hydroxylated) surface for water, ions and center of mass of a) adenine, b) guanine, c) cytosine and d) thymine. Reprinted with permission from Monti, S.; Walsh, T. R. 'Molecular Dynamics Simulations of the Adsorption and Dynamical Behavior of Single DNA Components on TiO$_2$'. J. Phys. Chem. C 2011, 115 (49), 24238–24246. © 2011 American Chemical Society.

Appendix B Force field parameters of organic molecules

Generated by DL_FIELD v4.10

Units eV

B.1 Molecule Alanine

nummols 1

atoms 13

N3	14.0067	-0.3
HN	1.00797	0.33
HN	1.00797	0.33
HN	1.00797	0.33
C1	12.011	0.21
H3	1.00797	0.1
C3	12.011	-0.27
H1	1.00797	0.09
H1	1.00797	0.09
H1	1.00797	0.09
C6	12.011	0.34
OC3	15.9994	-0.67
OC3	15.9994	-0.67

bonds 48

harm	1	2	34.95	1.04
harm	1	3	34.95	1.04
harm	1	4	34.95	1.04
harm	1	5	17.35	1.48
harm	5	6	28.62	1.08
harm	5	11	17.35	1.522
harm	5	7	19.3	1.538
harm	7	8	27.93	1.111
harm	7	9	27.93	1.111
harm	7	10	27.93	1.111
harm	11	12	45.53	1.26
harm	11	13	45.53	1.26
-hrm	2	5	1.73	2.074
-hrm	3	5	1.73	2.074
-hrm	4	5	1.73	2.074
-hrm	5	8	1.95	2.179
-hrm	5	9	1.95	2.179
-hrm	5	10	1.95	2.179
-126	2	6	0.25799378	0.03801007
-126	2	11	36.7043797	0.6058414
-126	2	7	7.60823444	0.16549817
-126	3	6	0.25799378	0.03801007
-126	3	11	36.7043797	0.6058414
-126	3	7	7.60823444	0.16549817
-126	4	6	0.25799378	0.03801007
-126	4	11	36.7043797	0.6058414
-126	4	7	7.60823444	0.16549817
-126	1	12	26842.983	26.8214829
-126	1	13	26842.983	26.8214829
-126	6	12	1266.13096	3.33795633
-126	6	13	1266.13096	3.33795633
-126	7	12	7106.63105	6.52991473
-126	7	13	7106.63105	6.52991473
-126	1	8	2985.51212	5.88489088
-126	1	9	2985.51212	5.88489088
-126	1	10	2985.51212	5.88489088

-hrm	8	9	0.47	1.802
-hrm	8	10	0.47	1.802
-hrm	9	10	0.47	1.802
-hrm	5	12	4.34	2.388
-hrm	5	13	4.34	2.388
-hrm	12	13	6.07	2.225
-126	6	8	114.63251	0.67714846
-126	6	9	114.63251	0.67714846
-126	6	10	114.63251	0.67714846
-126	11	8	3048.83954	4.55325256
-126	11	9	3048.83954	4.55325256
-126	11	10	3048.83954	4.55325256

angles 21

harm	2	1	3	3.81594	109.5
harm	2	1	4	3.81594	109.5
harm	2	1	5	2.60178	109.5
harm	3	1	4	3.81594	109.5
harm	3	1	5	2.60178	109.5
harm	4	1	5	2.60178	109.5
harm	1	5	6	4.46639	107.5
harm	1	5	11	3.78993	110
harm	1	5	7	5.87135	110
harm	6	5	11	4.3363	109.5
harm	6	5	7	3.03541	111
harm	11	5	7	4.50975	108
harm	5	7	8	2.89925	110.1
harm	5	7	9	2.89925	110.1
harm	5	7	10	2.89925	110.1
harm	8	7	9	3.07877	108.4
harm	8	7	10	3.07877	108.4
harm	9	7	10	3.07877	108.4
harm	5	11	12	3.46904	118
harm	5	11	13	3.46904	118
harm	12	11	13	8.6726	124
harm	11	5	7	4.50975	108

dihedral 25

cos	2	1	5	6	0.00434	0	3	1	0
cos	2	1	5	11	0.00434	0	3	1	0
cos	2	1	5	7	0.00434	0	3	1	0
cos	3	1	5	6	0.00434	0	3	1	0
cos	3	1	5	11	0.00434	0	3	1	0
cos	3	1	5	7	0.00434	0	3	1	0
cos	4	1	5	6	0.00434	0	3	1	0
cos	4	1	5	11	0.00434	0	3	1	0
cos	4	1	5	7	0.00434	0	3	1	0
cos	1	5	11	12	0.13876	180	2	1	0
cos	1	5	11	13	0.13876	180	2	1	0
cos	6	5	11	12	0.00217	180	6	1	0
cos	6	5	11	13	0.00217	180	6	1	0
cos	7	5	11	12	0.00217	180	6	1	0
cos	7	5	11	13	0.00217	180	6	1	0
cos	1	5	7	8	0.00867	0	3	1	0
cos	1	5	7	9	0.00867	0	3	1	0
cos	1	5	7	10	0.00867	0	3	1	0
cos	6	5	7	8	0.00867	0	3	1	0
cos	6	5	7	9	0.00867	0	3	1	0
cos	6	5	7	10	0.00867	0	3	1	0
cos	11	5	7	8	0.00867	0	3	1	0
cos	11	5	7	9	0.00867	0	3	1	0
cos	11	5	7	10	0.00867	0	3	1	0
harm	11	5	12	13	8.3257	0	0	0	0

finish

B.2 Molecule Arginine

nummols 1

atoms 27

N3	14.0067	-0.3
C2	12.011	-0.18
N7	14.0067	-0.8

HN	1.00797	0.33	H1	1.00797	0.09	HN	1.00797	0.46
HN	1.00797	0.33	H1	1.00797	0.09	HN	1.00797	0.46
HN	1.00797	0.33	C2	12.011	0.2	N7	14.0067	-0.8
C1	12.011	0.21	H1	1.00797	0.09	HN	1.00797	0.46
H3	1.00797	0.1	H1	1.00797	0.09	HN	1.00797	0.46
C2	12.011	-0.18	N7	14.0067	-0.7	C6	12.011	0.34
H1	1.00797	0.09	HN	1.00797	0.44	OC3	15.9994	-0.67
H1	1.00797	0.09	C7	12.011	0.64	OC3	15.9994	-0.67

bonds 110

harm	1	2	34.95	1.04	-126	3	7	7.60823444	0.16549817
harm	1	3	34.95	1.04	-126	4	6	0.25799378	0.03801007
harm	1	4	34.95	1.04	-126	4	25	36.7043797	0.6058414
harm	1	5	17.35	1.48	-126	4	7	7.60823444	0.16549817
harm	5	6	28.62	1.08	-126	6	26	1266.13096	3.33795633
harm	5	25	17.35	1.522	-126	6	27	1266.13096	3.33795633
harm	5	7	19.3	1.538	-126	1	26	26842.983	26.8214829
harm	7	8	26.8	1.111	-126	1	27	26842.983	26.8214829
harm	7	9	26.8	1.111	-126	7	26	7106.63105	6.52991473
harm	7	10	19.3	1.53	-126	7	27	7106.63105	6.52991473
harm	10	11	26.8	1.111	-126	6	8	114.63251	0.67714846
harm	10	12	26.8	1.111	-126	6	9	114.63251	0.67714846
harm	10	13	19.3	1.53	-126	6	10	745.474586	1.33758701
harm	13	14	26.8	1.111	-126	1	8	2985.51212	5.88489088
harm	13	15	26.8	1.111	-126	1	9	2985.51212	5.88489088
harm	13	16	22.64	1.49	-126	1	10	14695.1935	10.5680401
harm	16	17	39.46	1	-126	25	8	3048.83954	4.55325256
harm	16	18	40.15	1.365	-126	25	9	3048.83954	4.55325256
harm	18	19	40.15	1.365	-126	25	10	13619.4782	7.74116942
harm	18	22	40.15	1.365	-126	5	11	745.474586	1.33758701
harm	19	20	39.46	1	-126	5	12	745.474586	1.33758701
harm	19	21	39.46	1	-126	5	13	3626.1007	2.40868452
harm	22	23	39.46	1	-126	8	11	114.63251	0.67714846
harm	22	24	39.46	1	-126	8	12	114.63251	0.67714846
harm	25	26	45.53	1.26	-126	8	13	745.474586	1.33758701
harm	25	27	45.53	1.26	-126	9	11	114.63251	0.67714846
-hrm	2	5	1.73	2.074	-126	9	12	114.63251	0.67714846
-hrm	3	5	1.73	2.074	-126	9	13	745.474586	1.33758701
-hrm	4	5	1.73	2.074	-126	7	14	745.474586	1.33758701
-hrm	5	8	1.95	2.179	-126	7	15	745.474586	1.33758701
-hrm	5	9	1.95	2.179	-126	7	16	14695.1935	10.5680401
-hrm	5	10	0.97	2.561	-126	11	14	114.63251	0.67714846
-hrm	8	9	0.47	1.802	-126	11	15	114.63251	0.67714846
-hrm	8	10	1.95	2.179	-126	11	16	2985.51212	5.88489088
-hrm	9	10	1.95	2.179	-126	12	14	114.63251	0.67714846
-hrm	7	11	1.95	2.179	-126	12	15	114.63251	0.67714846
-hrm	7	12	1.95	2.179	-126	12	16	2985.51212	5.88489088
-hrm	7	13	0.97	2.561	-126	10	17	7.60823444	0.16549817
-hrm	11	12	0.47	1.802	-126	10	18	17333.8813	9.85239745
-hrm	11	13	1.95	2.179	-126	14	17	0.25799378	0.03801007
-hrm	12	13	1.95	2.179	-126	14	18	3766.21355	5.6246061
-hrm	10	14	1.95	2.179	-126	15	17	0.25799378	0.03801007
-hrm	10	15	1.95	2.179	-126	15	18	3766.21355	5.6246061
-hrm	14	15	0.47	1.802	-126	13	19	14695.1935	10.5680401
-hrm	16	19	7.81	2.3642	-126	13	22	14695.1935	10.5680401
-hrm	16	22	7.81	2.3642	-126	17	19	26.6868228	0.66958093
-hrm	19	22	7.81	2.3642	-126	17	22	26.6868228	0.66958093

-hrm	5	26	4.34	2.388
-hrm	5	27	4.34	2.388
-hrm	26	27	6.07	2.225
-126	2	6	0.25799378	0.03801007
-126	2	25	36.7043797	0.6058414
-126	2	7	7.60823444	0.16549817
-126	3	6	0.25799378	0.03801007
-126	3	25	36.7043797	0.6058414
-126	16	20	26.6868228	0.66958093
-126	16	21	26.6868228	0.66958093
-126	22	20	26.6868228	0.66958093
-126	22	21	26.6868228	0.66958093
-126	16	23	26.6868228	0.66958093
-126	16	24	26.6868228	0.66958093
-126	19	23	26.6868228	0.66958093
-126	19	24	26.6868228	0.66958093

angles 45

harm	2	1	3	3.81594	109.5
harm	2	1	4	3.81594	109.5
harm	2	1	5	2.60178	109.5
harm	3	1	4	3.81594	109.5
harm	3	1	5	2.60178	109.5
harm	4	1	5	2.60178	109.5
harm	6	5	1	4.46639	107.5
harm	6	5	25	4.3363	109.5
harm	6	5	7	3.03541	111
harm	1	5	25	3.78993	110
harm	1	5	7	5.87135	110
harm	25	5	7	4.50975	108
harm	5	7	8	2.89925	110.1
harm	5	7	9	2.89925	110.1
harm	5	7	10	5.06046	113.5
harm	8	7	9	3.07877	109
harm	8	7	10	2.29824	110.1
harm	9	7	10	2.29824	110.1
harm	7	10	11	2.29824	110.1
harm	7	10	12	2.29824	110.1
harm	7	10	13	5.06046	113.6
harm	11	10	12	3.07877	109
harm	11	10	13	2.29824	110.1
harm	12	10	13	2.29824	110.1
harm	10	13	14	2.29824	110.1
harm	10	13	15	2.29824	110.1
harm	10	13	16	5.87135	107.5
harm	14	13	15	3.07877	109
harm	14	13	16	4.46639	107.5
harm	15	13	16	4.46639	107.5
harm	13	16	17	3.50373	120
harm	13	16	18	5.40303	120
harm	17	16	18	4.24957	120
harm	16	18	19	4.50975	120
harm	16	18	22	4.50975	120
harm	19	18	22	4.50975	120
harm	18	19	20	4.24957	120
harm	18	19	21	4.24957	120
harm	20	19	21	2.16815	120
harm	18	22	23	4.24957	120
harm	18	22	24	4.24957	120
harm	23	22	24	2.16815	120
harm	5	25	26	3.46904	118
harm	5	25	27	3.46904	118
harm	26	25	27	8.6726	124

dihedral 62

cos	2	1	5	6	0.00434	0	3	1	0
cos	2	1	5	25	0.00434	0	3	1	0
cos	2	1	5	7	0.00434	0	3	1	0
cos	3	1	5	6	0.00434	0	3	1	0
cos	3	1	5	25	0.00434	0	3	1	0
cos	3	1	5	7	0.00434	0	3	1	0
cos	4	1	5	6	0.00434	0	3	1	0
cos	4	1	5	25	0.00434	0	3	1	0
cos	4	1	5	7	0.00434	0	3	1	0
cos	6	5	25	26	0.00217	180	6	1	0
cos	6	5	25	27	0.00217	180	6	1	0
cos	1	5	25	26	0.13876	180	2	1	0
cos	1	5	25	27	0.13876	180	2	1	0
cos	7	5	25	26	0.00217	180	6	1	0
cos	7	5	25	27	0.00217	180	6	1	0
cos	6	5	7	8	0.00867	0	3	1	0
cos	6	5	7	9	0.00867	0	3	1	0
cos	6	5	7	10	0.00867	0	3	1	0
cos	1	5	7	8	0.00867	0	3	1	0
cos	1	5	7	9	0.00867	0	3	1	0

cos	1	5	7	10	0.00867	0	3	1	0
cos	25	5	7	8	0.00867	0	3	1	0
cos	25	5	7	9	0.00867	0	3	1	0
cos	25	5	7	10	0.00867	0	3	1	0
cos	5	7	10	11	0.00846	0	3	1	0
cos	5	7	10	12	0.00846	0	3	1	0
cos	5	7	10	13	0.00846	0	3	1	0
cos	8	7	10	11	0.00846	0	3	1	0
cos	8	7	10	12	0.00846	0	3	1	0
cos	8	7	10	13	0.00846	0	3	1	0
cos	9	7	10	11	0.00846	0	3	1	0
cos	9	7	10	12	0.00846	0	3	1	0
cos	9	7	10	13	0.00846	0	3	1	0
cos	7	10	13	14	0.00846	0	3	1	0
cos	7	10	13	15	0.00846	0	3	1	0
cos	7	10	13	16	0.00846	0	3	1	0
cos	11	10	13	14	0.00846	0	3	1	0
cos	11	10	13	15	0.00846	0	3	1	0
cos	11	10	13	16	0.00846	0	3	1	0
cos	12	10	13	14	0.00846	0	3	1	0
cos	12	10	13	15	0.00846	0	3	1	0
cos	12	10	13	16	0.00846	0	3	1	0
cos	10	13	16	17	0	180	6	1	0
cos	10	13	16	18	0	180	6	1	0
cos	14	13	16	17	0	180	6	1	0
cos	14	13	16	18	0	180	6	1	0
cos	15	13	16	17	0	180	6	1	0
cos	15	13	16	18	0	180	6	1	0
cos	13	16	18	19	0.09757	180	2	1	0
cos	13	16	18	22	0.09757	180	2	1	0
cos	17	16	18	19	0.09757	180	2	1	0
cos	17	16	18	22	0.09757	180	2	1	0
cos	16	18	19	20	0.09757	180	2	1	0
cos	16	18	19	21	0.09757	180	2	1	0
cos	22	18	19	20	0.09757	180	2	1	0
cos	22	18	19	21	0.09757	180	2	1	0
cos	16	18	22	23	0.09757	180	2	1	0
cos	16	18	22	24	0.09757	180	2	1	0
cos	19	18	22	23	0.09757	180	2	1	0
cos	19	18	22	24	0.09757	180	2	1	0
harm	18	16	22	19	3.46904	0	0	0	0
harm	25	5	26	27	8.3257	0	0	0	0

finish

B.3 Molecule Aspartic acid

nummols 1

atoms 15

N3	14.0067	-0.3	H3	1.00797	0.1	OC3	15.9994	-0.76
HN	1.00797	0.33	C2	12.011	-0.28	OC3	15.9994	-0.76
HN	1.00797	0.33	H1	1.00797	0.09	C6	12.011	0.34
HN	1.00797	0.33	H1	1.00797	0.09	OC3	15.9994	-0.67
C1	12.011	0.21	C6	12.011	0.62	OC3	15.9994	-0.67

bonds 58

harm	1	2	34.95	1.04
harm	1	3	34.95	1.04
harm	1	4	34.95	1.04
harm	1	5	17.35	1.48
harm	5	6	28.62	1.08
harm	5	13	17.35	1.522
harm	5	7	19.3	1.538
harm	7	8	26.8	1.111
harm	7	9	26.8	1.111
harm	7	10	17.35	1.522
harm	10	11	45.53	1.26
harm	10	12	45.53	1.26
harm	13	14	45.53	1.26
harm	13	15	45.53	1.26
-hrm	2	5	1.73	2.074
-hrm	3	5	1.73	2.074
-hrm	4	5	1.73	2.074
-hrm	5	8	1.95	2.179
-hrm	5	9	1.95	2.179
-hrm	8	9	0.47	1.802
-hrm	8	10	2.6	2.163
-hrm	9	10	2.6	2.163
-hrm	7	11	4.34	2.388
-hrm	7	12	4.34	2.388
-hrm	11	12	6.07	2.225
-hrm	5	14	4.34	2.388
-hrm	5	15	4.34	2.388
-hrm	14	15	6.07	2.225
-126	2	6	0.25799378	0.03801007
-126	2	13	36.7043797	0.6058414
-126	2	7	7.60823444	0.16549817
-126	3	6	0.25799378	0.03801007
-126	3	13	36.7043797	0.6058414
-126	3	7	7.60823444	0.16549817
-126	4	6	0.25799378	0.03801007
-126	4	13	36.7043797	0.6058414
-126	4	7	7.60823444	0.16549817
-126	6	14	1266.13096	3.33795633
-126	6	15	1266.13096	3.33795633
-126	1	14	26842.983	26.8214829
-126	1	15	26842.983	26.8214829
-126	7	14	7106.63105	6.52991473
-126	7	15	7106.63105	6.52991473
-126	6	8	114.63251	0.67714846
-126	6	9	114.63251	0.67714846
-126	6	10	3048.83954	4.55325256
-126	13	8	3048.83954	4.55325256
-126	13	9	3048.83954	4.55325256
-126	13	10	50332.517	24.5762122
-126	1	8	2985.51212	5.88489088
-126	1	9	2985.51212	5.88489088
-126	1	10	54095.3093	33.2196374

angles 24

harm	2	1	3	3.81594	109.5
harm	2	1	4	3.81594	109.5
harm	2	1	5	2.60178	109.5
harm	3	1	4	3.81594	109.5
harm	3	1	5	2.60178	109.5
harm	4	1	5	2.60178	109.5
harm	6	5	13	4.3363	109.5
harm	6	5	1	4.46639	107.5
harm	6	5	7	3.03541	111
harm	13	5	1	3.78993	110
harm	13	5	7	4.50975	108
harm	1	5	7	5.87135	110
harm	5	7	8	2.89925	110.1
harm	5	7	9	2.89925	110.1
harm	5	7	10	4.50975	108
harm	8	7	9	3.07877	109
harm	8	7	10	2.86196	109.5
harm	9	7	10	2.86196	109.5
harm	7	10	11	3.46904	118
harm	7	10	12	3.46904	118
harm	11	10	12	8.6726	124
harm	5	13	14	3.46904	118
harm	5	13	15	3.46904	118
harm	14	13	15	8.6726	124

dihedral 32

cos	2	1	5	6	0.00434	0	3	1	0
cos	2	1	5	13	0.00434	0	3	1	0
cos	2	1	5	7	0.00434	0	3	1	0
cos	3	1	5	6	0.00434	0	3	1	0
cos	3	1	5	13	0.00434	0	3	1	0
cos	3	1	5	7	0.00434	0	3	1	0
cos	4	1	5	6	0.00434	0	3	1	0
cos	4	1	5	13	0.00434	0	3	1	0
cos	4	1	5	7	0.00434	0	3	1	0
cos	6	5	13	14	0.00217	180	6	1	0
cos	6	5	13	15	0.00217	180	6	1	0
cos	1	5	13	14	0.13876	180	2	1	0
cos	1	5	13	15	0.13876	180	2	1	0
cos	7	5	13	14	0.00217	180	6	1	0

cos	7	5	13	15	0.00217	180	6	1	0
cos	6	5	7	8	0.00867	0	3	1	0
cos	6	5	7	9	0.00867	0	3	1	0
cos	6	5	7	10	0.00867	0	3	1	0
cos	13	5	7	8	0.00867	0	3	1	0
cos	13	5	7	9	0.00867	0	3	1	0
cos	13	5	7	10	0.00867	0	3	1	0
cos	1	5	7	8	0.00867	0	3	1	0
cos	1	5	7	9	0.00867	0	3	1	0
cos	1	5	7	10	0.00867	0	3	1	0
cos	5	7	10	11	0.00217	180	6	1	0
cos	5	7	10	12	0.00217	180	6	1	0
cos	8	7	10	11	0.00217	180	6	1	0
cos	8	7	10	12	0.00217	180	6	1	0
cos	9	7	10	11	0.00217	180	6	1	0
cos	9	7	10	12	0.00217	180	6	1	0
harm	10	7	12	11	8.3257	0	0	0	0
harm	13	5	14	15	8.3257	0	0	0	0

finish

B.4 Molecule Glycine

nummols 1

atoms 10

N3	14.0067	-0.3	C2	12.011	0.13	OC3	15.9994	-0.67
HN	1.00797	0.33	H3	1.00797	0.09	OC3	15.9994	-0.67
HN	1.00797	0.33	H3	1.00797	0.09			
HN	1.00797	0.33	C6	12.011	0.34			

bonds 30

harm	1	2	34.95	1.04	-126	2	6	0.25799378	0.03801007
harm	1	3	34.95	1.04	-126	2	7	0.25799378	0.03801007
harm	1	4	34.95	1.04	-126	2	8	36.7043797	0.6058414
harm	1	5	17.35	1.48	-126	3	6	0.25799378	0.03801007
harm	5	6	28.62	1.08	-126	3	7	0.25799378	0.03801007
harm	5	7	28.62	1.08	-126	3	8	36.7043797	0.6058414
harm	5	8	17.35	1.522	-126	4	6	0.25799378	0.03801007
harm	8	9	45.53	1.26	-126	4	7	0.25799378	0.03801007
harm	8	10	45.53	1.26	-126	4	8	36.7043797	0.6058414
-hrm	2	5	1.73	2.074	-126	6	9	1266.13096	3.33795633
-hrm	3	5	1.73	2.074	-126	6	10	1266.13096	3.33795633
-hrm	4	5	1.73	2.074	-126	1	9	26842.983	26.8214829
-hrm	5	9	4.34	2.388	-126	1	10	26842.983	26.8214829
-hrm	5	10	4.34	2.388	-126	7	9	1266.13096	3.33795633
-hrm	9	10	6.07	2.225	-126	7	10	1266.13096	3.33795633

angles 15

harm	2	1	3	3.81594	109.5	harm	6	5	8	4.3363	109.5
harm	2	1	4	3.81594	109.5	harm	1	5	7	4.46639	107.5
harm	2	1	5	2.60178	109.5	harm	1	5	8	3.78993	110
harm	3	1	4	3.81594	109.5	harm	7	5	8	4.3363	109.5
harm	3	1	5	2.60178	109.5	harm	5	8	9	3.46904	118
harm	4	1	5	2.60178	109.5	harm	5	8	10	3.46904	118

harm	6	5	1	4.46639	107.5
harm	6	5	7	3.12214	115
harm	9	8	10	8.6726	124

dihedral 16

cos	2	1	5	6	0.00434	0	3	1	0
cos	2	1	5	7	0.00434	0	3	1	0
cos	2	1	5	8	0.00434	0	3	1	0
cos	3	1	5	6	0.00434	0	3	1	0
cos	3	1	5	7	0.00434	0	3	1	0
cos	3	1	5	8	0.00434	0	3	1	0
cos	4	1	5	6	0.00434	0	3	1	0
cos	4	1	5	7	0.00434	0	3	1	0
cos	4	1	5	8	0.00434	0	3	1	0
cos	6	5	8	9	0.00217	180	6	1	0
cos	6	5	8	10	0.00217	180	6	1	0
cos	1	5	8	9	0.13876	180	2	1	0
cos	1	5	8	10	0.13876	180	2	1	0
cos	7	5	8	9	0.00217	180	6	1	0
cos	7	5	8	10	0.00217	180	6	1	0
harm	8	5	9	10	8.3257	0	0	0	0

finish

B.5 Molecule Leucine

nummols 1

atoms 22

N3	14.0067	-0.3
HN	1.00797	0.33
HN	1.00797	0.33
HN	1.00797	0.33
C1	12.011	0.21
H3	1.00797	0.1
C2	12.011	-0.18
H1	1.00797	0.09
H1	1.00797	0.09
C1	12.011	-0.09
H1	1.00797	0.09
C3	12.011	-0.27
H1	1.00797	0.09
H1	1.00797	0.09
H1	1.00797	0.09
C3	12.011	-0.27
H1	1.00797	0.09
H1	1.00797	0.09
H1	1.00797	0.09
C6	12.011	0.34
OC3	15.9994	-0.67
OC3	15.9994	-0.67

bonds 102

harm	1	2	34.95	1.04
harm	1	3	34.95	1.04
harm	1	4	34.95	1.04
harm	1	5	17.35	1.48
harm	5	6	28.62	1.08
harm	5	20	17.35	1.522
harm	5	7	19.3	1.538
harm	7	8	26.8	1.111
harm	7	9	26.8	1.111
harm	7	10	19.3	1.538
harm	10	12	19.3	1.538
harm	10	11	26.8	1.111
harm	10	16	19.3	1.538
harm	12	13	27.93	1.111
harm	12	14	27.93	1.111
-126	2	6	0.25799378	0.03801007
-126	2	20	36.7043797	0.6058414
-126	2	7	7.60823444	0.16549817
-126	3	6	0.25799378	0.03801007
-126	3	20	36.7043797	0.6058414
-126	3	7	7.60823444	0.16549817
-126	4	6	0.25799378	0.03801007
-126	4	20	36.7043797	0.6058414
-126	4	7	7.60823444	0.16549817
-126	1	21	26842.983	26.8214829
-126	1	22	26842.983	26.8214829
-126	6	21	1266.13096	3.33795633
-126	6	22	1266.13096	3.33795633
-126	7	21	7106.63105	6.52991473
-126	7	22	7106.63105	6.52991473

harm	12	15	27.93	1.111
harm	16	17	27.93	1.111
harm	16	18	27.93	1.111
harm	16	19	27.93	1.111
harm	20	21	45.53	1.26
harm	20	22	45.53	1.26
-hrm	2	5	1.73	2.074
-hrm	3	5	1.73	2.074
-hrm	4	5	1.73	2.074
-hrm	5	8	1.95	2.179
-hrm	5	9	1.95	2.179
-hrm	5	10	0.97	2.561
-hrm	8	9	0.47	1.802
-hrm	8	10	1.95	2.179
-hrm	9	10	1.95	2.179
-hrm	7	12	0.69	2.561
-hrm	7	11	1.95	2.179
-hrm	7	16	0.69	2.561
-hrm	12	11	1.95	2.179
-hrm	12	16	0.69	2.561
-hrm	11	16	1.95	2.179
-hrm	10	13	1.95	2.179
-hrm	10	14	1.95	2.179
-hrm	10	15	1.95	2.179
-hrm	13	14	0.47	1.802
-hrm	13	15	0.47	1.802
-hrm	14	15	0.47	1.802
-hrm	10	17	1.95	2.179
-hrm	10	18	1.95	2.179
-hrm	10	19	1.95	2.179
-hrm	17	18	0.47	1.802
-hrm	17	19	0.47	1.802
-hrm	18	19	0.47	1.802
-hrm	5	21	4.34	2.388
-hrm	5	22	4.34	2.388
-hrm	21	22	6.07	2.225

-126	1	8	2985.51212	5.88489088
-126	1	9	2985.51212	5.88489088
-126	1	10	14695.1935	10.5680401
-126	6	8	114.63251	0.67714846
-126	6	9	114.63251	0.67714846
-126	6	10	745.474586	1.33758701
-126	20	8	3048.83954	4.55325256
-126	20	9	3048.83954	4.55325256
-126	20	10	13619.4782	7.74116942
-126	5	12	3626.1007	2.40868452
-126	5	11	745.474586	1.33758701
-126	5	16	3626.1007	2.40868452
-126	8	12	745.474586	1.33758701
-126	8	11	114.63251	0.67714846
-126	8	16	745.474586	1.33758701
-126	9	12	745.474586	1.33758701
-126	9	11	114.63251	0.67714846
-126	9	16	745.474586	1.33758701
-126	7	13	745.474586	1.33758701
-126	7	14	745.474586	1.33758701
-126	7	15	745.474586	1.33758701
-126	11	13	114.63251	0.67714846
-126	11	14	114.63251	0.67714846
-126	11	15	114.63251	0.67714846
-126	16	13	745.474586	1.33758701
-126	16	14	745.474586	1.33758701
-126	16	15	745.474586	1.33758701
-126	7	17	745.474586	1.33758701
-126	7	18	745.474586	1.33758701
-126	7	19	745.474586	1.33758701
-126	12	17	745.474586	1.33758701
-126	12	18	745.474586	1.33758701
-126	12	19	745.474586	1.33758701
-126	11	17	114.63251	0.67714846
-126	11	18	114.63251	0.67714846
-126	11	19	114.63251	0.67714846

angles 39

harm	2	1	3	3.81594	109.5
harm	2	1	4	3.81594	109.5
harm	2	1	5	2.60178	109.5
harm	3	1	4	3.81594	109.5
harm	3	1	5	2.60178	109.5
harm	4	1	5	2.60178	109.5
harm	1	5	6	4.46639	107.5
harm	1	5	20	3.78993	110
harm	1	5	7	5.87135	110
harm	6	5	20	4.3363	109.5
harm	6	5	7	3.03541	111
harm	20	5	7	4.50975	108
harm	5	7	8	2.89925	110.1
harm	5	7	9	2.89925	110.1
harm	5	7	10	5.06046	113.5
harm	8	7	9	3.07877	109
harm	8	7	10	2.89925	110.1
harm	9	7	10	2.89925	110.1
harm	7	10	12	4.62683	114
harm	7	10	16	4.62683	114
harm	12	10	11	2.99205	110.1
harm	12	10	16	4.62683	114
harm	11	10	16	2.99205	110.1
harm	10	12	13	2.89925	110.1
harm	10	12	14	2.89925	110.1
harm	10	12	15	2.89925	110.1
harm	13	12	14	3.07877	108.4
harm	13	12	15	3.07877	108.4
harm	14	12	15	3.07877	108.4
harm	10	16	17	2.89925	110.1
harm	10	16	18	2.89925	110.1
harm	10	16	19	2.89925	110.1
harm	17	16	18	3.07877	108.4
harm	17	16	19	3.07877	108.4
harm	18	16	19	3.07877	108.4
harm	5	20	21	3.46904	118
harm	5	20	22	3.46904	118
harm	21	20	22	8.6726	124

```
  harm    7     10     11    2.99205   110.1

dihedral 52
    cos    2     1     5     6    0.00434    0     3     1     0
    cos    2     1     5    20    0.00434    0     3     1     0
    cos    2     1     5     7    0.00434    0     3     1     0
    cos    3     1     5     6    0.00434    0     3     1     0
    cos    3     1     5    20    0.00434    0     3     1     0
    cos    3     1     5     7    0.00434    0     3     1     0
    cos    4     1     5     6    0.00434    0     3     1     0
    cos    4     1     5    20    0.00434    0     3     1     0
    cos    4     1     5     7    0.00434    0     3     1     0
    cos    1     5    20    21    0.13876  180     2     1     0
    cos    1     5    20    22    0.13876  180     2     1     0
    cos    6     5    20    21    0.00217  180     6     1     0
    cos    6     5    20    22    0.00217  180     6     1     0
    cos    7     5    20    21    0.00217  180     6     1     0
    cos    7     5    20    22    0.00217  180     6     1     0
    cos    1     5     7     8    0.00867    0     3     1     0
    cos    1     5     7     9    0.00867    0     3     1     0
    cos    1     5     7    10    0.00867    0     3     1     0
    cos    6     5     7     8    0.00867    0     3     1     0
    cos    6     5     7     9    0.00867    0     3     1     0
    cos    6     5     7    10    0.00867    0     3     1     0
    cos   20     5     7     8    0.00867    0     3     1     0
    cos   20     5     7     9    0.00867    0     3     1     0
    cos   20     5     7    10    0.00867    0     3     1     0
    cos    5     7    10    12    0.00867    0     3     1     0
    cos    5     7    10    11    0.00867    0     3     1     0
    cos    5     7    10    16    0.00867    0     3     1     0
    cos    8     7    10    12    0.00867    0     3     1     0
    cos    8     7    10    11    0.00867    0     3     1     0
    cos    8     7    10    16    0.00867    0     3     1     0
    cos    9     7    10    12    0.00867    0     3     1     0
    cos    9     7    10    11    0.00867    0     3     1     0
    cos    9     7    10    16    0.00867    0     3     1     0
    cos    7    10    12    13    0.00867    0     3     1     0
    cos    7    10    12    14    0.00867    0     3     1     0
    cos    7    10    12    15    0.00867    0     3     1     0
    cos   11    10    12    13    0.00867    0     3     1     0
    cos   11    10    12    14    0.00867    0     3     1     0
    cos   11    10    12    15    0.00867    0     3     1     0
    cos   16    10    12    13    0.00867    0     3     1     0
    cos   16    10    12    14    0.00867    0     3     1     0
    cos   16    10    12    15    0.00867    0     3     1     0
    cos    7    10    16    17    0.00867    0     3     1     0
    cos    7    10    16    18    0.00867    0     3     1     0
    cos    7    10    16    19    0.00867    0     3     1     0
    cos   12    10    16    17    0.00867    0     3     1     0
    cos   12    10    16    18    0.00867    0     3     1     0
    cos   12    10    16    19    0.00867    0     3     1     0
    cos   11    10    16    17    0.00867    0     3     1     0
    cos   11    10    16    18    0.00867    0     3     1     0
    cos   11    10    16    19    0.00867    0     3     1     0
   harm   20     5    21    22    8.3257     0     0     0     0
finish
```

B.6 Molecule Lysine

nummols 1

atoms 25

N3	14.0067	-0.3
HN	1.00797	0.33
HN	1.00797	0.33
HN	1.00797	0.33
C1	12.011	0.21
H3	1.00797	0.1
C2	12.011	-0.18
H1	1.00797	0.09
H1	1.00797	0.09
C2	12.011	-0.18
H1	1.00797	0.09
H1	1.00797	0.09
C2	12.011	-0.18
H1	1.00797	0.09
H1	1.00797	0.09
C2	12.011	0.21
H1	1.00797	0.05
H1	1.00797	0.05
N3	14.0067	-0.3
HN	1.00797	0.33
HN	1.00797	0.33
HN	1.00797	0.33
C6	12.011	0.34
OC3	15.9994	-0.67
OC3	15.9994	-0.67

bonds 116

harm	1	2	34.95	1.04
harm	1	3	34.95	1.04
harm	1	4	34.95	1.04
harm	1	5	17.35	1.48
harm	5	6	28.62	1.08
harm	5	23	17.35	1.522
harm	5	7	19.3	1.538
harm	7	8	26.8	1.111
harm	7	9	26.8	1.111
harm	7	10	19.3	1.53
harm	10	11	26.8	1.111
harm	10	12	26.8	1.111
harm	10	13	19.3	1.53
harm	13	14	26.8	1.111
harm	13	15	26.8	1.111
harm	13	16	19.3	1.53
harm	16	17	26.8	1.111
harm	16	18	26.8	1.111
harm	16	19	17.35	1.48
harm	19	20	34.95	1.04
harm	19	21	34.95	1.04
harm	19	22	34.95	1.04
harm	23	24	45.53	1.26
harm	23	25	45.53	1.26
-hrm	2	5	1.73	2.074
-hrm	3	5	1.73	2.074
-hrm	4	5	1.73	2.074
-hrm	5	8	1.95	2.179
-hrm	5	9	1.95	2.179
-hrm	5	10	0.97	2.561
-hrm	8	9	0.47	1.802
-hrm	8	10	1.95	2.179
-hrm	9	10	1.95	2.179
-hrm	7	11	1.95	2.179
-hrm	7	12	1.95	2.179
-hrm	7	13	0.97	2.561
-hrm	11	12	0.47	1.802
-hrm	11	13	1.95	2.179
-hrm	12	13	1.95	2.179
-hrm	10	14	1.95	2.179
-hrm	10	15	1.95	2.179
-126	2	6	0.25799378	0.03801007
-126	2	23	36.7043797	0.6058414
-126	2	7	7.60823444	0.16549817
-126	3	6	0.25799378	0.03801007
-126	3	23	36.7043797	0.6058414
-126	3	7	7.60823444	0.16549817
-126	4	6	0.25799378	0.03801007
-126	4	23	36.7043797	0.6058414
-126	4	7	7.60823444	0.16549817
-126	6	24	1266.13096	3.33795633
-126	6	25	1266.13096	3.33795633
-126	1	24	26842.983	26.8214829
-126	1	25	26842.983	26.8214829
-126	7	24	7106.63105	6.52991473
-126	7	25	7106.63105	6.52991473
-126	6	8	114.63251	0.67714846
-126	6	9	114.63251	0.67714846
-126	6	10	745.474586	1.33758701
-126	1	8	2985.51212	5.88489088
-126	1	9	2985.51212	5.88489088
-126	1	10	14695.1935	10.5680401
-126	23	8	3048.83954	4.55325256
-126	23	9	3048.83954	4.55325256
-126	23	10	13619.4782	7.74116942
-126	5	11	745.474586	1.33758701
-126	5	12	745.474586	1.33758701
-126	5	13	3626.1007	2.40868452
-126	8	11	114.63251	0.67714846
-126	8	12	114.63251	0.67714846
-126	8	13	745.474586	1.33758701
-126	9	11	114.63251	0.67714846
-126	9	12	114.63251	0.67714846
-126	9	13	745.474586	1.33758701
-126	7	14	745.474586	1.33758701
-126	7	15	745.474586	1.33758701
-126	7	16	3626.1007	2.40868452
-126	11	14	114.63251	0.67714846
-126	11	15	114.63251	0.67714846
-126	11	16	745.474586	1.33758701
-126	12	14	114.63251	0.67714846
-126	12	15	114.63251	0.67714846

-hrm	10	16	0.97	2.561
-hrm	14	15	0.47	1.802
-hrm	14	16	1.95	2.179
-hrm	15	16	1.95	2.179
-hrm	13	17	1.95	2.179
-hrm	13	18	1.95	2.179
-hrm	17	18	0.47	1.802
-hrm	17	19	3.04	2.101
-hrm	18	19	3.04	2.101
-hrm	16	20	1.73	2.074
-hrm	16	21	1.73	2.074
-hrm	16	22	1.73	2.074
-hrm	5	24	4.34	2.388
-hrm	5	25	4.34	2.388
-hrm	24	25	6.07	2.225

-126	12	16	745.474586	1.33758701
-126	10	17	745.474586	1.33758701
-126	10	18	745.474586	1.33758701
-126	10	19	14695.1935	10.5680401
-126	14	17	114.63251	0.67714846
-126	14	18	114.63251	0.67714846
-126	14	19	2985.51212	5.88489088
-126	15	17	114.63251	0.67714846
-126	15	18	114.63251	0.67714846
-126	15	19	2985.51212	5.88489088
-126	13	20	7.60823444	0.16549817
-126	13	21	7.60823444	0.16549817
-126	13	22	7.60823444	0.16549817
-126	17	20	0.25799378	0.03801007
-126	17	21	0.25799378	0.03801007

angles 45

harm	2	1	3	3.81594	109.5
harm	2	1	4	3.81594	109.5
harm	2	1	5	2.60178	109.5
harm	3	1	4	3.81594	109.5
harm	3	1	5	2.60178	109.5
harm	4	1	5	2.60178	109.5
harm	6	5	1	4.46639	107.5
harm	6	5	23	4.3363	109.5
harm	6	5	7	3.03541	111
harm	1	5	23	3.78993	110
harm	1	5	7	5.87135	110
harm	23	5	7	4.50975	108
harm	5	7	8	2.89925	110.1
harm	5	7	9	2.89925	110.1
harm	5	7	10	5.06046	113.5
harm	8	7	9	3.07877	109
harm	8	7	10	2.29824	110.1
harm	9	7	10	2.29824	110.1
harm	7	10	11	2.29824	110.1
harm	7	10	12	2.29824	110.1
harm	7	10	13	5.06046	113.6
harm	11	10	12	3.07877	109
harm	11	10	13	2.29824	110.1
harm	12	10	13	2.29824	110.1
harm	10	13	14	2.29824	110.1
harm	10	13	15	2.29824	110.1
harm	10	13	16	5.06046	113.6
harm	14	13	15	3.07877	109
harm	14	13	16	2.29824	110.1
harm	15	13	16	2.29824	110.1
harm	13	16	17	2.29824	110.1
harm	13	16	18	2.29824	110.1
harm	13	16	19	5.87135	110
harm	17	16	18	3.07877	109
harm	17	16	19	3.90267	107.5
harm	18	16	19	3.90267	107.5
harm	16	19	20	2.60178	109.5
harm	16	19	21	2.60178	109.5
harm	16	19	22	2.60178	109.5
harm	20	19	21	3.81594	109.5
harm	20	19	22	3.81594	109.5
harm	21	19	22	3.81594	109.5
harm	5	23	24	3.46904	118
harm	5	23	25	3.46904	118
harm	24	23	25	8.6726	124

dihedral 61

cos	2	1	5	6	0.00434	0	3	1	0
cos	2	1	5	23	0.00434	0	3	1	0
cos	2	1	5	7	0.00434	0	3	1	0
cos	3	1	5	6	0.00434	0	3	1	0
cos	3	1	5	23	0.00434	0	3	1	0
cos	3	1	5	7	0.00434	0	3	1	0
cos	4	1	5	6	0.00434	0	3	1	0
cos	4	1	5	23	0.00434	0	3	1	0
cos	4	1	5	7	0.00434	0	3	1	0
cos	6	5	23	24	0.00217	180	6	1	0
cos	6	5	23	25	0.00217	180	6	1	0
cos	1	5	23	24	0.13876	180	2	1	0
cos	1	5	23	25	0.13876	180	2	1	0
cos	7	5	23	24	0.00217	180	6	1	0

cos	7	5	23	25	0.00217	180	6	1	0
cos	6	5	7	8	0.00867	0	3	1	0
cos	6	5	7	9	0.00867	0	3	1	0
cos	6	5	7	10	0.00867	0	3	1	0
cos	1	5	7	8	0.00867	0	3	1	0
cos	1	5	7	9	0.00867	0	3	1	0
cos	1	5	7	10	0.00867	0	3	1	0
cos	23	5	7	8	0.00867	0	3	1	0
cos	23	5	7	9	0.00867	0	3	1	0
cos	23	5	7	10	0.00867	0	3	1	0
cos	5	7	10	11	0.00846	0	3	1	0
cos	5	7	10	12	0.00846	0	3	1	0
cos	5	7	10	13	0.00846	0	3	1	0
cos	8	7	10	11	0.00846	0	3	1	0
cos	8	7	10	12	0.00846	0	3	1	0
cos	8	7	10	13	0.00846	0	3	1	0
cos	9	7	10	11	0.00846	0	3	1	0
cos	9	7	10	12	0.00846	0	3	1	0
cos	9	7	10	13	0.00846	0	3	1	0
cos	7	10	13	14	0.00846	0	3	1	0
cos	7	10	13	15	0.00846	0	3	1	0
cos	7	10	13	16	0.0065	0	1	1	0
cos	11	10	13	14	0.00846	0	3	1	0
cos	11	10	13	15	0.00846	0	3	1	0
cos	11	10	13	16	0.00846	0	3	1	0
cos	12	10	13	14	0.00846	0	3	1	0
cos	12	10	13	15	0.00846	0	3	1	0
cos	12	10	13	16	0.00846	0	3	1	0
cos	10	13	16	17	0.00846	0	3	1	0
cos	10	13	16	18	0.00846	0	3	1	0
cos	10	13	16	19	0.00846	0	3	1	0
cos	14	13	16	17	0.00846	0	3	1	0
cos	14	13	16	18	0.00846	0	3	1	0
cos	14	13	16	19	0.00846	0	3	1	0
cos	15	13	16	17	0.00846	0	3	1	0
cos	15	13	16	18	0.00846	0	3	1	0
cos	15	13	16	19	0.00846	0	3	1	0
cos	13	16	19	20	0.00434	0	3	1	0
cos	13	16	19	21	0.00434	0	3	1	0
cos	13	16	19	22	0.00434	0	3	1	0
cos	17	16	19	20	0.00434	0	3	1	0
cos	17	16	19	21	0.00434	0	3	1	0
cos	17	16	19	22	0.00434	0	3	1	0
cos	18	16	19	20	0.00434	0	3	1	0
cos	18	16	19	21	0.00434	0	3	1	0
cos	18	16	19	22	0.00434	0	3	1	0
harm	23	5	24	25	8.3257	0	0	0	0

finish

B.7 Molecule Serine

nummols 1

atoms 14

N3	14.0067	-0.3	H3	1.00797	0.1	HO	1.00797	0.43
HN	1.00797	0.33	C2	12.011	0.05	C6	12.011	0.34

HN	1.00797	0.33
HN	1.00797	0.33
C1	12.011	0.21
H1	1.00797	0.09
H1	1.00797	0.09
OH	15.9994	-0.66
OC3	15.9994	-0.67
OC3	15.9994	-0.67

bonds 49

harm	1	2	34.95	1.04
harm	1	3	34.95	1.04
harm	1	4	34.95	1.04
harm	1	5	17.35	1.48
harm	5	6	28.62	1.08
harm	5	12	17.35	1.522
harm	5	7	19.3	1.538
harm	7	8	26.8	1.111
harm	7	9	26.8	1.111
harm	7	10	37.12	1.42
harm	10	11	47.27	0.96
harm	12	13	45.53	1.26
harm	12	14	45.53	1.26
-hrm	2	5	1.73	2.074
-hrm	3	5	1.73	2.074
-hrm	4	5	1.73	2.074
-hrm	5	8	1.95	2.179
-hrm	5	9	1.95	2.179
-hrm	8	9	0.47	1.802
-hrm	5	13	4.34	2.388
-hrm	5	14	4.34	2.388
-hrm	13	14	6.07	2.225
-126	2	6	0.25799378	0.03801007
-126	2	12	36.7043797	0.6058414
-126	2	7	7.60823444	0.16549817
-126	3	6	0.25799378	0.03801007
-126	3	12	36.7043797	0.6058414
-126	3	7	7.60823444	0.16549817
-126	4	6	0.25799378	0.03801007
-126	4	12	36.7043797	0.6058414
-126	4	7	7.60823444	0.16549817
-126	6	13	1266.13096	3.33795633
-126	6	14	1266.13096	3.33795633
-126	1	13	26842.983	26.8214829
-126	1	14	26842.983	26.8214829
-126	7	13	7106.63105	6.52991473
-126	7	14	7106.63105	6.52991473
-126	6	8	114.63251	0.67714846
-126	6	9	114.63251	0.67714846
-126	6	10	1894.45908	4.35253843
-126	1	8	2985.51212	5.88489088
-126	1	9	2985.51212	5.88489088
-126	1	10	38493.8905	34.2083948
-126	12	8	3048.83954	4.55325256
-126	12	9	3048.83954	4.55325256
-126	12	10	37095.9994	25.8404332
-126	5	11	7.60823444	0.16549817
-126	8	11	0.25799378	0.03801007
-126	9	11	0.25799378	0.03801007
-126	3	6	0.25799378	0.03801007

angles 22

harm	2	1	3	3.81594	109.5
harm	2	1	4	3.81594	109.5
harm	2	1	5	2.60178	109.5
harm	3	1	4	3.81594	109.5
harm	3	1	5	2.60178	109.5
harm	4	1	5	2.60178	109.5
harm	6	5	1	4.46639	107.5
harm	6	5	12	4.3363	109.5
harm	6	5	7	3.03541	111
harm	1	5	12	3.78993	110
harm	1	5	7	5.87135	110
harm	12	5	7	4.50975	108
harm	5	7	8	2.89925	110.1
harm	5	7	9	2.89925	110.1
harm	5	7	10	6.56516	110.1
harm	8	7	9	3.07877	109
harm	8	7	10	3.98072	108.89
harm	9	7	10	3.98072	108.89
harm	7	10	11	4.98674	106
harm	5	12	13	3.46904	118
harm	5	12	14	3.46904	118
harm	13	12	14	8.6726	124

dihedral 30

cos	2	1	5	6	0.00434	0	3	1	0
cos	2	1	5	12	0.00434	0	3	1	0
cos	2	1	5	7	0.00434	0	3	1	0
cos	3	1	5	6	0.00434	0	3	1	0
cos	3	1	5	12	0.00434	0	3	1	0
cos	3	1	5	7	0.00434	0	3	1	0
cos	4	1	5	6	0.00434	0	3	1	0
cos	4	1	5	12	0.00434	0	3	1	0
cos	4	1	5	7	0.00434	0	3	1	0

cos	6	5	12	13	0.00217	180	6	1	0
cos	6	5	12	14	0.00217	180	6	1	0
cos	1	5	12	13	0.13876	180	2	1	0
cos	1	5	12	14	0.13876	180	2	1	0
cos	7	5	12	13	0.00217	180	6	1	0
cos	7	5	12	14	0.00217	180	6	1	0
cos	6	5	7	8	0.00867	0	3	1	0
cos	6	5	7	9	0.00867	0	3	1	0
cos	6	5	7	10	0.00867	0	3	1	0
cos	1	5	7	8	0.00867	0	3	1	0
cos	1	5	7	9	0.00867	0	3	1	0
cos	1	5	7	10	0.00867	0	3	1	0
cos	12	5	7	8	0.00867	0	3	1	0
cos	12	5	7	9	0.00867	0	3	1	0
cos	12	5	7	10	0.00867	0	3	1	0
cos	5	7	10	11	0.05637	0	1	1	0
cos	5	7	10	11	0.01301	0	2	0	0
cos	5	7	10	11	0.01821	0	3	0	0
cos	8	7	10	11	0.00607	0	3	1	0
cos	9	7	10	11	0.00607	0	3	1	0
harm	12	5	13	14	8.3257	0	0	0	0

finish

B.8 Lennard-Jones parameters for amino acids studied

Lennard-Jones potential parameters ($U(r) = 4\epsilon\,[(\frac{\sigma}{r})^{12} - (\frac{\sigma}{r})^{6}]$)

i-j	ϵ [eV]	σ [Å]	Amino acid
N3	0.0087	3.2963	All
HN	0.002	0.4	
C1	0.0009	4.0536	
H3	0.001	2.352	
H1	0.001	2.352	
C6	0.003	3.5636	
OC3	0.0052	3.0291	
C3	0.0035	3.6705	Ala, Leu
C2	0.0024	3.8754	Arg, Asp, Leu, Lys, Ser
N7	0.0087	3.2963	Arg
C7	0.0048	3.5636	Arg
OH	0.0066	3.1538	Ser
HO	0.002	0.4	Ser

B.9 Molecule TBP – RKLPDA

nummols 1

atoms 104

N3	14.0067	-0.67051
HN	1.00797	0.47351
HN	1.00797	0.47351
HN	1.00797	0.47351
C1	12.011	0.0939
HP	1.00797	0.025
C1	12.011	0.02917
HC	1.00797	0.02873
HC	1.00797	0.02873
HC	1.00797	0.01021
C1	12.011	-0.04784
HC	1.00797	0.07072
HC	1.00797	0.07072
C1	12.011	-0.06997
HP	1.00797	0.11952
HP	1.00797	0.11952
N3	14.0067	-0.25036
HN	1.00797	0.29456
C1	12.011	-0.00335
HC	1.00797	0.01935
HC	1.00797	0.01935
C1	12.011	0.01306
HC	1.00797	0.01957
HC	1.00797	0.01957
C1	12.011	-0.01191
H1	1.00797	0.04395
H1	1.00797	0.04395

C1	12.011	-0.01621
HC	1.00797	0.00204
HC	1.00797	0.00204
C1	12.011	0.17657
H1	1.00797	0.04848
H1	1.00797	0.04848
N2	14.0067	-0.45057
HN	1.00797	0.33847
CA	12.011	0.56136
N2	14.0067	-0.70647
HN	1.00797	0.40593
HN	1.00797	0.40593
N2	14.0067	-0.70647
HN	1.00797	0.40593
HN	1.00797	0.40593
C	12.011	0.77028
O	15.9994	-0.64723
N1	14.0067	-0.43588
HN	1.00797	0.2513
C1	12.011	-0.03877
H1	1.00797	0.12948
C1	12.011	-0.10827
HC	1.00797	0.04521
HC	1.00797	0.04521
C1	12.011	0.03334
HC	1.00797	0.01021
HN	1.00797	0.29456
HN	1.00797	0.29456
C	12.011	0.72513
O	15.9994	-0.56316
N1	14.0067	-0.35515
HN	1.00797	0.26242
C1	12.011	-0.1015
H1	1.00797	0.13695
C1	12.011	-0.1444
HC	1.00797	0.05253
HC	1.00797	0.05253
C1	12.011	0.19198
HC	1.00797	0.00082
C1	12.011	-0.12304
HC	1.00797	0.02238
HC	1.00797	0.02238
HC	1.00797	0.02238
C1	12.011	-0.12304
HC	1.00797	0.02238
HC	1.00797	0.02238
HC	1.00797	0.02238
C	12.011	0.57347
O	15.9994	-0.55785
N1	14.0067	-0.08812
C1	12.011	-0.03458
H1	1.00797	0.05998
C	12.011	0.33372
O	15.9994	-0.43456
N1	14.0067	-0.5582
HN	1.00797	0.31968
C1	12.011	0.00722
H1	1.00797	0.08238
C1	12.011	-0.04756
HC	1.00797	-0.01484
HC	1.00797	-0.01484
C	12.011	0.74517
OC	15.9994	-0.73038
OC	15.9994	-0.73038
C	12.011	0.4432
O	15.9994	-0.50145
N1	14.0067	-0.6222
HN	1.00797	0.35978
C1	12.011	-0.0541
H1	1.00797	0.12328
C1	12.011	-0.18572
HC	1.00797	0.06965
HC	1.00797	0.06965
HC	1.00797	0.06965
C	12.011	0.66401
OC	15.9994	-0.74701
OC	15.9994	-0.74701

bonds 104

harm	1	2	37.64	1.01
harm	1	3	37.64	1.01
harm	1	4	37.64	1.01
harm	1	5	31.83	1.471
harm	5	6	29.49	1.09
harm	5	25	27.49	1.522
harm	5	7	26.89	1.526
harm	7	8	29.49	1.09
harm	7	9	29.49	1.09
harm	7	10	26.89	1.526
harm	10	11	29.49	1.09
harm	10	12	29.49	1.09
harm	10	13	26.89	1.526
harm	13	14	29.49	1.09
harm	13	15	29.49	1.09
harm	13	16	29.23	1.463
harm	16	17	37.64	1.01
harm	16	18	41.72	1.34
harm	18	19	41.72	1.34
harm	18	22	41.72	1.34
harm	19	20	37.64	1.01
harm	19	21	37.64	1.01
harm	22	23	37.64	1.01
harm	22	24	37.64	1.01
harm	25	26	49.43	1.229
harm	27	28	37.64	1.01
harm	27	29	29.23	1.449
harm	29	30	29.49	1.09
harm	29	47	27.49	1.522
harm	53	55	29.49	1.09
harm	53	56	26.89	1.526
harm	56	58	26.89	1.526
harm	56	57	29.49	1.09
harm	56	62	26.89	1.526
harm	58	59	29.49	1.09
harm	58	60	29.49	1.09
harm	58	61	29.49	1.09
harm	62	63	29.49	1.09
harm	62	64	29.49	1.09
harm	62	65	29.49	1.09
harm	66	67	49.43	1.229
harm	68	77	29.23	1.449
harm	68	69	29.23	1.449
harm	69	70	29.49	1.09
harm	69	80	27.49	1.522
harm	69	71	26.89	1.526
harm	71	72	29.49	1.09
harm	71	73	29.49	1.09
harm	71	74	26.89	1.526
harm	74	77	26.89	1.526
harm	74	75	29.49	1.09
harm	74	76	29.49	1.09
harm	77	78	29.49	1.09
harm	77	79	29.49	1.09
harm	80	81	49.43	1.229
harm	82	83	37.64	1.01
harm	82	84	29.23	1.449
harm	84	85	29.49	1.09

harm	29	31	26.89	1.526
harm	31	32	29.49	1.09
harm	31	33	29.49	1.09
harm	31	34	26.89	1.526
harm	34	35	29.49	1.09
harm	34	36	29.49	1.09
harm	34	37	26.89	1.526
harm	37	38	29.49	1.09
harm	37	39	29.49	1.09
harm	37	40	26.89	1.526
harm	40	41	29.49	1.09
harm	40	42	29.49	1.09
harm	40	43	31.83	1.471
harm	43	44	37.64	1.01
harm	43	45	37.64	1.01
harm	43	46	37.64	1.01
harm	47	48	49.43	1.229
harm	49	50	37.64	1.01
harm	49	51	29.23	1.449
harm	51	52	29.49	1.09
harm	51	66	27.49	1.522
harm	51	53	26.89	1.526
harm	53	54	29.49	1.09
harm	84	92	27.49	1.522
harm	84	86	26.89	1.526
harm	86	87	29.49	1.09
harm	86	88	29.49	1.09
harm	86	89	27.49	1.522
harm	89	90	56.89	1.25
harm	89	91	56.89	1.25
harm	92	93	49.43	1.229
harm	94	95	37.64	1.01
harm	94	96	29.23	1.449
harm	96	97	29.49	1.09
harm	96	102	27.49	1.522
harm	96	98	26.89	1.526
harm	98	99	29.49	1.09
harm	98	100	29.49	1.09
harm	98	101	29.49	1.09
harm	102	103	56.89	1.25
harm	102	104	56.89	1.25
harm	25	27	42.5	1.335
harm	47	49	42.5	1.335
harm	66	68	42.5	1.335
harm	80	82	42.5	1.335
harm	92	94	42.5	1.335

angles 192

harm	2	1	3	3.03541	109.5
harm	2	1	4	3.03541	109.5
harm	2	1	5	4.3363	109.5
harm	3	1	4	3.03541	109.5
harm	3	1	5	4.3363	109.5
harm	4	1	5	4.3363	109.5
harm	6	5	1	4.3363	109.5
harm	6	5	25	4.3363	109.5
harm	6	5	7	4.3363	109.5
harm	1	5	25	6.93808	111.2
harm	1	5	7	6.93808	111.2
harm	25	5	7	5.46374	111.1
harm	5	7	8	4.3363	109.5
harm	5	7	9	4.3363	109.5
harm	5	7	10	3.46904	109.5
harm	8	7	9	3.03541	109.5
harm	8	7	10	4.3363	109.5
harm	9	7	10	4.3363	109.5
harm	7	10	11	4.3363	109.5
harm	7	10	12	4.3363	109.5
harm	7	10	13	3.46904	109.5
harm	11	10	12	3.03541	109.5
harm	11	10	13	4.3363	109.5
harm	12	10	13	4.3363	109.5
harm	10	13	14	4.3363	109.5
harm	10	13	15	4.3363	109.5
harm	10	13	16	6.93808	111.2
harm	14	13	15	3.03541	109.5
harm	14	13	16	4.3363	109.5
harm	15	13	16	4.3363	109.5
harm	13	16	17	4.3363	118.4
harm	53	56	62	3.46904	109.5
harm	58	56	57	4.3363	109.5
harm	58	56	62	3.46904	109.5
harm	57	56	62	4.3363	109.5
harm	56	58	59	4.3363	109.5
harm	56	58	60	4.3363	109.5
harm	56	58	61	4.3363	109.5
harm	59	58	60	3.03541	109.5
harm	59	58	61	3.03541	109.5
harm	60	58	61	3.03541	109.5
harm	56	62	63	4.3363	109.5
harm	56	62	64	4.3363	109.5
harm	56	62	65	4.3363	109.5
harm	63	62	64	3.03541	109.5
harm	63	62	65	3.03541	109.5
harm	64	62	65	3.03541	109.5
harm	51	66	67	6.93808	120.4
harm	77	68	69	4.3363	118
harm	68	69	70	4.3363	109.5
harm	68	69	80	5.46374	110.1
harm	68	69	71	6.93808	109.7
harm	70	69	80	4.3363	109.5
harm	70	69	71	4.3363	109.5
harm	80	69	71	5.46374	111.1
harm	69	71	72	4.3363	109.5
harm	69	71	73	4.3363	109.5
harm	69	71	74	3.46904	109.5
harm	72	71	73	3.03541	109.5
harm	72	71	74	4.3363	109.5
harm	73	71	74	4.3363	109.5
harm	71	74	77	3.46904	109.5

harm	13	16	18	4.3363	123.2
harm	17	16	18	4.3363	120
harm	16	18	19	6.07082	120
harm	16	18	22	6.07082	120
harm	19	18	22	6.07082	120
harm	18	19	20	4.3363	120
harm	18	19	21	4.3363	120
harm	20	19	21	3.03541	120
harm	18	22	23	4.3363	120
harm	18	22	24	4.3363	120
harm	23	22	24	3.03541	120
harm	5	25	26	6.93808	120.4
harm	28	27	29	4.3363	118.04
harm	30	29	27	4.3363	109.5
harm	30	29	47	4.3363	109.5
harm	30	29	31	4.3363	109.5
harm	27	29	47	5.46374	110.1
harm	27	29	31	6.93808	109.7
harm	47	29	31	5.46374	111.1
harm	29	31	32	4.3363	109.5
harm	29	31	33	4.3363	109.5
harm	29	31	34	3.46904	109.5
harm	32	31	33	3.03541	109.5
harm	32	31	34	4.3363	109.5
harm	33	31	34	4.3363	109.5
harm	31	34	35	4.3363	109.5
harm	31	34	36	4.3363	109.5
harm	31	34	37	3.46904	109.5
harm	35	34	36	3.03541	109.5
harm	35	34	37	4.3363	109.5
harm	36	34	37	4.3363	109.5
harm	34	37	38	4.3363	109.5
harm	34	37	39	4.3363	109.5
harm	34	37	40	3.46904	109.5
harm	38	37	39	3.03541	109.5
harm	38	37	40	4.3363	109.5
harm	39	37	40	4.3363	109.5
harm	37	40	41	4.3363	109.5
harm	37	40	42	4.3363	109.5
harm	37	40	43	6.93808	111.2
harm	41	40	42	3.03541	109.5
harm	41	40	43	4.3363	109.5
harm	42	40	43	4.3363	109.5
harm	40	43	44	4.3363	109.5
harm	40	43	45	4.3363	109.5
harm	40	43	46	4.3363	109.5
harm	44	43	45	3.03541	109.5
harm	44	43	46	3.03541	109.5
harm	45	43	46	3.03541	109.5
harm	29	47	48	6.93808	120.4
harm	50	49	51	4.3363	118.04
harm	49	51	52	4.3363	109.5
harm	49	51	66	5.46374	110.1
harm	49	51	53	6.93808	109.7
harm	52	51	66	4.3363	109.5
harm	52	51	53	4.3363	109.5
harm	66	51	53	5.46374	111.1
harm	51	53	54	4.3363	109.5
harm	51	53	55	4.3363	109.5
harm	71	74	75	4.3363	109.5
harm	71	74	76	4.3363	109.5
harm	77	74	75	4.3363	109.5
harm	77	74	76	4.3363	109.5
harm	75	74	76	3.03541	109.5
harm	68	77	74	6.93808	109.7
harm	68	77	78	4.3363	109.5
harm	68	77	79	4.3363	109.5
harm	74	77	78	4.3363	109.5
harm	74	77	79	4.3363	109.5
harm	78	77	79	3.03541	109.5
harm	69	80	81	6.93808	120.4
harm	83	82	84	4.3363	118.04
harm	85	84	92	4.3363	109.5
harm	85	84	82	4.3363	109.5
harm	85	84	86	4.3363	109.5
harm	92	84	82	5.46374	110.1
harm	92	84	86	5.46374	111.1
harm	82	84	86	6.93808	109.7
harm	84	86	87	4.3363	109.5
harm	84	86	88	4.3363	109.5
harm	84	86	89	5.46374	111.1
harm	87	86	88	3.03541	109.5
harm	87	86	89	4.3363	109.5
harm	88	86	89	4.3363	109.5
harm	86	89	90	6.07082	117
harm	86	89	91	6.07082	117
harm	90	89	91	6.93808	126
harm	84	92	93	6.93808	120.4
harm	95	94	96	4.3363	118.04
harm	94	96	97	4.3363	109.5
harm	94	96	102	5.46374	110.1
harm	94	96	98	6.93808	109.7
harm	97	96	102	4.3363	109.5
harm	97	96	98	4.3363	109.5
harm	102	96	98	5.46374	111.1
harm	96	98	99	4.3363	109.5
harm	96	98	100	4.3363	109.5
harm	96	98	101	4.3363	109.5
harm	99	98	100	3.03541	109.5
harm	99	98	101	3.03541	109.5
harm	100	98	101	3.03541	109.5
harm	96	102	103	6.07082	117
harm	96	102	104	6.07082	117
harm	103	102	104	6.93808	126
harm	5	25	27	6.07082	116.6
harm	26	25	27	6.93808	122.9
harm	28	27	25	4.3363	120
harm	29	27	25	4.3363	121.9
harm	29	47	49	6.07082	116.6
harm	48	47	49	6.93808	122.9
harm	50	49	47	4.3363	120
harm	51	49	47	4.3363	121.9
harm	51	66	68	6.07082	116.6
harm	67	66	68	6.93808	122.9
harm	77	68	66	4.3363	121.9
harm	69	68	66	4.3363	121.9
harm	69	80	82	6.07082	116.6
harm	81	80	82	6.93808	122.9

harm	51	53	56	3.46904	109.5	harm	83	82	80	4.3363	120
harm	54	53	55	3.03541	109.5	harm	84	82	80	4.3363	121.9
harm	54	53	56	4.3363	109.5	harm	84	92	94	6.07082	116.6
harm	55	53	56	4.3363	109.5	harm	93	92	94	6.93808	122.9
harm	53	56	58	3.46904	109.5	harm	95	94	92	4.3363	120
harm	53	56	57	4.3363	109.5	harm	96	94	92	4.3363	121.9

dihedral 365

cos	2	1	5	6	0.00675	0	3	0.83333	0.5
cos	2	1	5	25	0.00675	0	3	0.83333	0.5
cos	2	1	5	7	0.00675	0	3	0.83333	0.5
cos	3	1	5	6	0.00675	0	3	0.83333	0.5
cos	3	1	5	25	0.00675	0	3	0.83333	0.5
cos	3	1	5	7	0.00675	0	3	0.83333	0.5
cos	4	1	5	6	0.00675	0	3	0.83333	0.5
cos	4	1	5	25	0.00675	0	3	0.83333	0.5
cos	4	1	5	7	0.00675	0	3	0.83333	0.5
cos	6	5	25	26	0	0	2	0.83333	0.5
cos	1	5	25	26	0	0	2	0.83333	0.5
cos	7	5	25	26	0	0	2	0.83333	0.5
cos	6	5	7	8	0.00675	0	3	0.83333	0.5
cos	6	5	7	9	0.00675	0	3	0.83333	0.5
cos	6	5	7	10	0.00675	0	3	0.83333	0.5
cos	1	5	7	8	0.00675	0	3	0.83333	0.5
cos	1	5	7	9	0.00675	0	3	0.83333	0.5
cos	1	5	7	10	0.00675	0	3	0.83333	0.5
cos	25	5	7	8	0.00675	0	3	0.83333	0.5
cos	25	5	7	9	0.00675	0	3	0.83333	0.5
cos	25	5	7	10	0.00675	0	3	0.83333	0.5
cos	5	7	10	11	0.00694	0	3	0.83333	0.5
cos	5	7	10	12	0.00694	0	3	0.83333	0.5
cos	5	7	10	13	0.00781	0	3	0.83333	0.5
cos	5	7	10	13	0.01084	180	2	0	0
cos	5	7	10	13	0.00867	180	1	0	0
cos	8	7	10	11	0.0065	0	3	0.83333	0.5
cos	8	7	10	12	0.0065	0	3	0.83333	0.5
cos	8	7	10	13	0.00694	0	3	0.83333	0.5
cos	9	7	10	11	0.0065	0	3	0.83333	0.5
cos	9	7	10	12	0.0065	0	3	0.83333	0.5
cos	9	7	10	13	0.00694	0	3	0.83333	0.5
cos	7	10	13	14	0.00675	0	3	0.83333	0.5
cos	7	10	13	15	0.00675	0	3	0.83333	0.5
cos	7	10	13	16	0.00675	0	3	0.83333	0.5
cos	11	10	13	14	0.00675	0	3	0.83333	0.5
cos	11	10	13	15	0.00675	0	3	0.83333	0.5
cos	11	10	13	16	0.00675	0	3	0.83333	0.5
cos	12	10	13	14	0.00675	0	3	0.83333	0.5
cos	12	10	13	15	0.00675	0	3	0.83333	0.5
cos	12	10	13	16	0.00675	0	3	0.83333	0.5
cos	10	13	16	17	0	0	3	0.83333	0.5
cos	10	13	16	18	0	0	3	0.83333	0.5
cos	14	13	16	17	0	0	3	0.83333	0.5
cos	14	13	16	18	0	0	3	0.83333	0.5
cos	15	13	16	17	0	0	3	0.83333	0.5
cos	15	13	16	18	0	0	3	0.83333	0.5
cos	13	16	18	19	0.10407	180	2	0.83333	0.5
cos	13	16	18	22	0.10407	180	2	0.83333	0.5

cos	17	16	18	19	0.10407	180	2	0.83333	0.5
cos	17	16	18	22	0.10407	180	2	0.83333	0.5
cos	16	18	19	20	0.10407	180	2	0.83333	0.5
cos	16	18	19	21	0.10407	180	2	0.83333	0.5
cos	22	18	19	20	0.10407	180	2	0.83333	0.5
cos	22	18	19	21	0.10407	180	2	0.83333	0.5
cos	16	18	22	23	0.10407	180	2	0.83333	0.5
cos	16	18	22	24	0.10407	180	2	0.83333	0.5
cos	19	18	22	23	0.10407	180	2	0.83333	0.5
cos	19	18	22	24	0.10407	180	2	0.83333	0.5
cos	28	27	29	30	0	0	2	0.83333	0.5
cos	28	27	29	47	0	0	2	0.83333	0.5
cos	28	27	29	31	0	0	2	0.83333	0.5
cos	30	29	47	48	0.03469	0	1	0.83333	0.5
cos	30	29	47	48	0.00347	180	3	0	0
cos	27	29	47	48	0	0	2	0.83333	0.5
cos	31	29	47	48	0	0	2	0.83333	0.5
cos	30	29	31	32	0.00675	0	3	0.83333	0.5
cos	30	29	31	33	0.00675	0	3	0.83333	0.5
cos	30	29	31	34	0.00675	0	3	0.83333	0.5
cos	27	29	31	32	0.00675	0	3	0.83333	0.5
cos	27	29	31	33	0.00675	0	3	0.83333	0.5
cos	27	29	31	34	0.00675	0	3	0.83333	0.5
cos	47	29	31	32	0.00675	0	3	0.83333	0.5
cos	47	29	31	33	0.00675	0	3	0.83333	0.5
cos	47	29	31	34	0.00675	0	3	0.83333	0.5
cos	29	31	34	35	0.00694	0	3	0.83333	0.5
cos	29	31	34	36	0.00694	0	3	0.83333	0.5
cos	29	31	34	37	0.00781	0	3	0.83333	0.5
cos	29	31	34	37	0.01084	180	2	0	0
cos	29	31	34	37	0.00867	180	1	0	0
cos	32	31	34	35	0.0065	0	3	0.83333	0.5
cos	32	31	34	36	0.0065	0	3	0.83333	0.5
cos	32	31	34	37	0.00694	0	3	0.83333	0.5
cos	33	31	34	35	0.0065	0	3	0.83333	0.5
cos	33	31	34	36	0.0065	0	3	0.83333	0.5
cos	33	31	34	37	0.00694	0	3	0.83333	0.5
cos	31	34	37	38	0.00694	0	3	0.83333	0.5
cos	31	34	37	39	0.00694	0	3	0.83333	0.5
cos	31	34	37	40	0.00781	0	3	0.83333	0.5
cos	31	34	37	40	0.01084	180	2	0	0
cos	31	34	37	40	0.00867	180	1	0	0
cos	35	34	37	38	0.0065	0	3	0.83333	0.5
cos	35	34	37	39	0.0065	0	3	0.83333	0.5
cos	35	34	37	40	0.00694	0	3	0.83333	0.5
cos	36	34	37	38	0.0065	0	3	0.83333	0.5
cos	36	34	37	39	0.0065	0	3	0.83333	0.5
cos	36	34	37	40	0.00694	0	3	0.83333	0.5
cos	34	37	40	41	0.00675	0	3	0.83333	0.5
cos	34	37	40	42	0.00675	0	3	0.83333	0.5
cos	34	37	40	43	0.00675	0	3	0.83333	0.5
cos	38	37	40	41	0.00675	0	3	0.83333	0.5
cos	38	37	40	42	0.00675	0	3	0.83333	0.5
cos	38	37	40	43	0.00675	0	3	0.83333	0.5
cos	39	37	40	41	0.00675	0	3	0.83333	0.5
cos	39	37	40	42	0.00675	0	3	0.83333	0.5
cos	39	37	40	43	0.00675	0	3	0.83333	0.5
cos	37	40	43	44	0.00675	0	3	0.83333	0.5
cos	37	40	43	45	0.00675	0	3	0.83333	0.5

cos	37	40	43	46	0.00675	0	3	0.83333	0.5
cos	41	40	43	44	0.00675	0	3	0.83333	0.5
cos	41	40	43	45	0.00675	0	3	0.83333	0.5
cos	41	40	43	46	0.00675	0	3	0.83333	0.5
cos	42	40	43	44	0.00675	0	3	0.83333	0.5
cos	42	40	43	45	0.00675	0	3	0.83333	0.5
cos	42	40	43	46	0.00675	0	3	0.83333	0.5
cos	50	49	51	52	0	0	2	0.83333	0.5
cos	50	49	51	66	0	0	2	0.83333	0.5
cos	50	49	51	53	0	0	2	0.83333	0.5
cos	49	51	66	67	0	0	2	0.83333	0.5
cos	52	51	66	67	0.03469	0	1	0.83333	0.5
cos	52	51	66	67	0.00347	180	3	0	0
cos	53	51	66	67	0	0	2	0.83333	0.5
cos	49	51	53	54	0.00675	0	3	0.83333	0.5
cos	49	51	53	55	0.00675	0	3	0.83333	0.5
cos	49	51	53	56	0.00675	0	3	0.83333	0.5
cos	52	51	53	54	0.00675	0	3	0.83333	0.5
cos	52	51	53	55	0.00675	0	3	0.83333	0.5
cos	52	51	53	56	0.00675	0	3	0.83333	0.5
cos	66	51	53	54	0.00675	0	3	0.83333	0.5
cos	66	51	53	55	0.00675	0	3	0.83333	0.5
cos	66	51	53	56	0.00675	0	3	0.83333	0.5
cos	51	53	56	58	0.00781	0	3	0.83333	0.5
cos	51	53	56	58	0.01084	180	2	0	0
cos	51	53	56	58	0.00867	180	1	0	0
cos	51	53	56	57	0.00694	0	3	0.83333	0.5
cos	51	53	56	62	0.00781	0	3	0.83333	0.5
cos	51	53	56	62	0.01084	180	2	0	0
cos	51	53	56	62	0.00867	180	1	0	0
cos	54	53	56	58	0.00694	0	3	0.83333	0.5
cos	54	53	56	57	0.0065	0	3	0.83333	0.5
cos	54	53	56	62	0.00694	0	3	0.83333	0.5
cos	55	53	56	58	0.00694	0	3	0.83333	0.5
cos	55	53	56	57	0.0065	0	3	0.83333	0.5
cos	55	53	56	62	0.00694	0	3	0.83333	0.5
cos	53	56	58	59	0.00694	0	3	0.83333	0.5
cos	53	56	58	60	0.00694	0	3	0.83333	0.5
cos	53	56	58	61	0.00694	0	3	0.83333	0.5
cos	57	56	58	59	0.0065	0	3	0.83333	0.5
cos	57	56	58	60	0.0065	0	3	0.83333	0.5
cos	57	56	58	61	0.0065	0	3	0.83333	0.5
cos	62	56	58	59	0.00694	0	3	0.83333	0.5
cos	62	56	58	60	0.00694	0	3	0.83333	0.5
cos	62	56	58	61	0.00694	0	3	0.83333	0.5
cos	53	56	62	63	0.00694	0	3	0.83333	0.5
cos	53	56	62	64	0.00694	0	3	0.83333	0.5
cos	53	56	62	65	0.00694	0	3	0.83333	0.5
cos	58	56	62	63	0.00694	0	3	0.83333	0.5
cos	58	56	62	64	0.00694	0	3	0.83333	0.5
cos	58	56	62	65	0.00694	0	3	0.83333	0.5
cos	57	56	62	63	0.0065	0	3	0.83333	0.5
cos	57	56	62	64	0.0065	0	3	0.83333	0.5
cos	57	56	62	65	0.0065	0	3	0.83333	0.5
cos	69	68	77	74	0	0	2	0	0
cos	69	68	77	78	0	0	2	0.83333	0.5
cos	69	68	77	79	0	0	2	0.83333	0.5
cos	77	68	69	70	0	0	2	0.83333	0.5
cos	77	68	69	80	0	0	2	0.83333	0.5

cos	77	68	69	71	0	0	2	0	0
cos	68	69	80	81	0	0	2	0.83333	0.5
cos	70	69	80	81	0.03469	0	1	0.83333	0.5
cos	70	69	80	81	0.00347	180	3	0	0
cos	71	69	80	81	0	0	2	0.83333	0.5
cos	68	69	71	72	0.00675	0	3	0.83333	0.5
cos	68	69	71	73	0.00675	0	3	0.83333	0.5
cos	68	69	71	74	0.00675	0	3	0	0
cos	70	69	71	72	0.00675	0	3	0.83333	0.5
cos	70	69	71	73	0.00675	0	3	0.83333	0.5
cos	70	69	71	74	0.00675	0	3	0.83333	0.5
cos	80	69	71	72	0.00675	0	3	0.83333	0.5
cos	80	69	71	73	0.00675	0	3	0.83333	0.5
cos	80	69	71	74	0.00675	0	3	0.83333	0.5
cos	69	71	74	77	0.00781	0	3	0	0
cos	69	71	74	77	0.01084	180	2	0	0
cos	69	71	74	77	0.00867	180	1	0	0
cos	69	71	74	75	0.00694	0	3	0.83333	0.5
cos	69	71	74	76	0.00694	0	3	0.83333	0.5
cos	72	71	74	77	0.00694	0	3	0.83333	0.5
cos	72	71	74	75	0.0065	0	3	0.83333	0.5
cos	72	71	74	76	0.0065	0	3	0.83333	0.5
cos	73	71	74	77	0.00694	0	3	0.83333	0.5
cos	73	71	74	75	0.0065	0	3	0.83333	0.5
cos	73	71	74	76	0.0065	0	3	0.83333	0.5
cos	71	74	77	68	0.00675	0	3	0	0
cos	71	74	77	78	0.00675	0	3	0.83333	0.5
cos	71	74	77	79	0.00675	0	3	0.83333	0.5
cos	75	74	77	68	0.00675	0	3	0.83333	0.5
cos	75	74	77	78	0.00675	0	3	0.83333	0.5
cos	75	74	77	79	0.00675	0	3	0.83333	0.5
cos	76	74	77	68	0.00675	0	3	0.83333	0.5
cos	76	74	77	78	0.00675	0	3	0.83333	0.5
cos	76	74	77	79	0.00675	0	3	0.83333	0.5
cos	83	82	84	85	0	0	2	0.83333	0.5
cos	83	82	84	92	0	0	2	0.83333	0.5
cos	83	82	84	86	0	0	2	0.83333	0.5
cos	85	84	92	93	0.03469	0	1	0.83333	0.5
cos	85	84	92	93	0.00347	180	3	0	0
cos	82	84	92	93	0	0	2	0.83333	0.5
cos	86	84	92	93	0	0	2	0.83333	0.5
cos	85	84	86	87	0.00675	0	3	0.83333	0.5
cos	85	84	86	88	0.00675	0	3	0.83333	0.5
cos	85	84	86	89	0.00675	0	3	0.83333	0.5
cos	92	84	86	87	0.00675	0	3	0.83333	0.5
cos	92	84	86	88	0.00675	0	3	0.83333	0.5
cos	92	84	86	89	0.00675	0	3	0.83333	0.5
cos	82	84	86	87	0.00675	0	3	0.83333	0.5
cos	82	84	86	88	0.00675	0	3	0.83333	0.5
cos	82	84	86	89	0.00675	0	3	0.83333	0.5
cos	84	86	89	90	0	0	2	0.83333	0.5
cos	84	86	89	91	0	0	2	0.83333	0.5
cos	87	86	89	90	0	0	2	0.83333	0.5
cos	87	86	89	91	0	0	2	0.83333	0.5
cos	88	86	89	90	0	0	2	0.83333	0.5
cos	88	86	89	91	0	0	2	0.83333	0.5
cos	95	94	96	97	0	0	2	0.83333	0.5
cos	95	94	96	102	0	0	2	0.83333	0.5
cos	95	94	96	98	0	0	2	0.83333	0.5

cos	94	96	102	103	0	0	2	0.83333	0.5
cos	94	96	102	104	0	0	2	0.83333	0.5
cos	97	96	102	103	0	0	2	0.83333	0.5
cos	97	96	102	104	0	0	2	0.83333	0.5
cos	98	96	102	103	0	0	2	0.83333	0.5
cos	98	96	102	104	0	0	2	0.83333	0.5
cos	94	96	98	99	0.00675	0	3	0.83333	0.5
cos	94	96	98	100	0.00675	0	3	0.83333	0.5
cos	94	96	98	101	0.00675	0	3	0.83333	0.5
cos	97	96	98	99	0.00675	0	3	0.83333	0.5
cos	97	96	98	100	0.00675	0	3	0.83333	0.5
cos	97	96	98	101	0.00675	0	3	0.83333	0.5
cos	102	96	98	99	0.00675	0	3	0.83333	0.5
cos	102	96	98	100	0.00675	0	3	0.83333	0.5
cos	102	96	98	101	0.00675	0	3	0.83333	0.5
cos	25	27	29	30	0	0	2	0.83333	0.5
cos	25	27	29	47	0.0098	0	3	0.83333	0.5
cos	25	27	29	47	0.01496	180	2	0	0
cos	25	27	29	47	0.04405	0	1	0	0
cos	25	27	29	31	0	1	4	0.83333	0.5
cos	25	27	29	31	0.00984	180	3	0	0
cos	25	27	29	31	0.03832	180	2	0	0
cos	25	27	29	31	0.01534	180	1	0	0
cos	27	25	5	6	0	0	2	0.83333	0.5
cos	27	25	5	1	0	0	2	0.83333	0.5
cos	27	25	5	7	0	0	4	0.83333	0.5
cos	27	25	5	7	0.00243	0	3	0	0
cos	27	25	5	7	0.00285	180	2	0	0
cos	27	25	5	7	0.03375	180	1	0	0
cos	5	25	27	28	0.10841	180	2	0.83333	0.5
cos	5	25	27	29	0.10841	180	2	0.83333	0.5
cos	26	25	27	28	0.10841	180	2	0.83333	0.5
cos	26	25	27	28	0.08673	0	1	0	0
cos	26	25	27	29	0.10841	180	2	0.83333	0.5
cos	47	49	51	52	0	0	2	0.83333	0.5
cos	47	49	51	66	0.0098	0	3	0.83333	0.5
cos	47	49	51	66	0.01496	180	2	0	0
cos	47	49	51	66	0.04405	0	1	0	0
cos	47	49	51	53	0	1	4	0.83333	0.5
cos	47	49	51	53	0.00984	180	3	0	0
cos	47	49	51	53	0.03832	180	2	0	0
cos	47	49	51	53	0.01534	180	1	0	0
cos	49	47	29	30	0	0	2	0.83333	0.5
cos	49	47	29	27	0.02001	180	3	0.83333	0.5
cos	49	47	29	27	0.06304	180	2	0	0
cos	49	47	29	27	0.02966	180	1	0	0
cos	49	47	29	31	0	0	4	0.83333	0.5
cos	49	47	29	31	0.00243	0	3	0	0
cos	49	47	29	31	0.00285	180	2	0	0
cos	49	47	29	31	0.03375	180	1	0	0
cos	29	47	49	50	0.10841	180	2	0.83333	0.5
cos	29	47	49	51	0.10841	180	2	0.83333	0.5
cos	48	47	49	50	0.10841	180	2	0.83333	0.5
cos	48	47	49	50	0.08673	0	1	0	0
cos	48	47	49	51	0.10841	180	2	0.83333	0.5
cos	66	68	77	74	0	1	4	0.83333	0.5
cos	66	68	77	74	0.00984	180	3	0	0
cos	66	68	77	74	0.03832	180	2	0	0
cos	66	68	77	74	0.01534	180	1	0	0

cos	66	68	77	78	0	0	2	0.83333	0.5
cos	66	68	77	79	0	0	2	0.83333	0.5
cos	66	68	69	70	0	0	2	0.83333	0.5
cos	66	68	69	80	0.0098	0	3	0.83333	0.5
cos	66	68	69	80	0.01496	180	2	0	0
cos	66	68	69	80	0.04405	0	1	0	0
cos	66	68	69	71	0	1	4	0.83333	0.5
cos	66	68	69	71	0.00984	180	3	0	0
cos	66	68	69	71	0.03832	180	2	0	0
cos	66	68	69	71	0.01534	180	1	0	0
cos	68	66	51	49	0.02001	180	3	0.83333	0.5
cos	68	66	51	49	0.06304	180	2	0	0
cos	68	66	51	49	0.02966	180	1	0	0
cos	68	66	51	52	0	0	2	0.83333	0.5
cos	68	66	51	53	0	0	4	0.83333	0.5
cos	68	66	51	53	0.00243	0	3	0	0
cos	68	66	51	53	0.00285	180	2	0	0
cos	68	66	51	53	0.03375	180	1	0	0
cos	51	66	68	77	0.10841	180	2	0.83333	0.5
cos	51	66	68	69	0.10841	180	2	0.83333	0.5
cos	67	66	68	77	0.10841	180	2	0.83333	0.5
cos	67	66	68	69	0.10841	180	2	0.83333	0.5
cos	80	82	84	85	0	0	2	0.83333	0.5
cos	80	82	84	92	0.0098	0	3	0.83333	0.5
cos	80	82	84	92	0.01496	180	2	0	0
cos	80	82	84	92	0.04405	0	1	0	0
cos	80	82	84	86	0	1	4	0.83333	0.5
cos	80	82	84	86	0.00984	180	3	0	0
cos	80	82	84	86	0.03832	180	2	0	0
cos	80	82	84	86	0.01534	180	1	0	0
cos	82	80	69	68	0.02001	180	3	0.83333	0.5
cos	82	80	69	68	0.06304	180	2	0	0
cos	82	80	69	68	0.02966	180	1	0	0
cos	82	80	69	70	0	0	2	0.83333	0.5
cos	82	80	69	71	0	0	4	0.83333	0.5
cos	82	80	69	71	0.00243	0	3	0	0
cos	82	80	69	71	0.00285	180	2	0	0
cos	82	80	69	71	0.03375	180	1	0	0
cos	69	80	82	83	0.10841	180	2	0.83333	0.5
cos	69	80	82	84	0.10841	180	2	0.83333	0.5
cos	81	80	82	83	0.10841	180	2	0.83333	0.5
cos	81	80	82	83	0.08673	0	1	0	0
cos	81	80	82	84	0.10841	180	2	0.83333	0.5
cos	92	94	96	97	0	0	2	0.83333	0.5
cos	92	94	96	102	0.0098	0	3	0.83333	0.5
cos	92	94	96	102	0.01496	180	2	0	0
cos	92	94	96	102	0.04405	0	1	0	0
cos	92	94	96	98	0	1	4	0.83333	0.5
cos	92	94	96	98	0.00984	180	3	0	0
cos	92	94	96	98	0.03832	180	2	0	0
cos	92	94	96	98	0.01534	180	1	0	0
cos	94	92	84	85	0	0	2	0.83333	0.5
cos	94	92	84	82	0.02001	180	3	0.83333	0.5
cos	94	92	84	82	0.06304	180	2	0	0
cos	94	92	84	82	0.02966	180	1	0	0
cos	94	92	84	86	0	0	4	0.83333	0.5
cos	94	92	84	86	0.00243	0	3	0	0
cos	94	92	84	86	0.00285	180	2	0	0
cos	94	92	84	86	0.03375	180	1	0	0

```
cos    84    92    94    95    0.10841   180   2   0.83333   0.5
cos    84    92    94    96    0.10841   180   2   0.83333   0.5
cos    93    92    94    95    0.10841   180   2   0.83333   0.5
cos    93    92    94    95    0.08673    0    1      0       0
cos    93    92    94    96    0.10841   180   2   0.83333   0.5
cos    16    19    18    22    0.45531   180   2      0       0
cos    13    18    16    17    0.04336   180   2      0       0
cos    18    20    19    21    0.04336   180   2      0       0
cos    18    23    22    24    0.04336   180   2      0       0
cos    86    90    89    91    0.45531   180   2      0       0
cos    96   104   102   103    0.45531   180   2      0       0
cos     5    27    25    26    0.45531   180   2      0       0
cos    25    29    27    28    0.0477    180   2      0       0
cos    29    49    47    48    0.45531   180   2      0       0
cos    47    51    49    50    0.0477    180   2      0       0
cos    51    68    66    67    0.45531   180   2      0       0
cos    66    77    68    69    0.04336   180   2      0       0
cos    69    82    80    81    0.45531   180   2      0       0
cos    80    84    82    83    0.0477    180   2      0       0
cos    84    94    92    93    0.45531   180   2      0       0
cos    92    96    94    95    0.0477    180   2      0       0

finish
```

B.10 Lennard-Jones parameters for TBP

Lennard-Jones potential parameters ($U(r) = 4\epsilon\ [(\frac{\sigma}{r})^{12} - (\frac{\sigma}{r})^{6}]$)

i-j	ϵ [eV]	σ [Å]
N3	0.0074	3.25
HN	0.0007	1.0691
C1	0.0047	3.3997
HP	0.0007	1.96
HC	0.0007	2.6495
H1	0.0007	2.4714
N2	0.0074	3.25
CA	0.0037	3.3997
C	0.0037	3.3997
O	0.0091	2.9599
N1	0.0074	3.25
OC	0.0091	2.9599

Appendix C Supporting Information - A well-tempered metadynamics study on the interactions of simulated body fluid ions with the rutile (110) surface

---

Supporting Information

A well-tempered metadynamics study on the interactions of simulated body fluid ions with the rutile (110) surface

Azade YazdanYar✦*, Ulrich Aschauer*✦✦*, Paul Bowen*✦
✦ Department of Materials Science and Engineering, École Polytechnique Fédérale de Lausanne (EPFL), Lausanne, Switzerland
✦✦ Department of Chemistry and Biochemistry, University of Bern, Bern, Switzerland

---

C.1 Ionic concentration and complexes in human blood plasma and SBFs

SBFs are solutions with an ionic concentration similar to human blood plasma (Table C.1).

Table C.1 Ionic composition [mM] of human blood plasma (HBP) and Kokubo SBF (K-SBF](1).

	Na^+	K^+	Mg^{2+}	Ca^{2+}	Cl^-	HCO_3^-	HPO_4^{2-}	SO_4^{2-}
HBP	142.00	5.00	1.50	2.50	103.0	27.00	1.00	0.50
K-SBF	142.00	5.00	1.50	2.50	148.80	4.2	1.00	0.50

The distribution of ionic species and complexes was obtained using the thermodynamic model previously developed by Vereecke *et al.* (2). Details of this model can be found elsewhere (3). This model was used for the physiological condition (T = 37 ℃ and pH of 7.4) and the ionic concentration of K-SBF. The distribution of ionic complexes, in percentage, is presented in Table C.2.

Table C.2 Distribution of ionic complexes of K-SBF under physiological condition [%].

Na^+	
Na^+	99.722078
$[NaHPO_4]^-$	0.145729
$[NaCl]^0$	0.130402
$[NaCO_3]^-$	0.001783
$[NaOH]^0$	0.000008
$[NaSO_4]^-$	0.000000

K^+	
K^+	97.445092
$[KCl]^0$	2.442244
$[KHPO_4]^-$	0.112660
$[KOH]^0$	0.000004
$[KSO_4]^-$	0.000000

Mg^{2+}	
Mg^{2+}	92.919406
$[MgHPO_4]^0$	3.262030
$[MgCl]^+$	2.750375
$[MgHCO_3]^+$	1.001085
$[MgPO_4]^-$	0.040865
$[Mg(OH)]^+$	0.002638
$[MgCO_3]^0$	0.023232
$[MgH_2PO_4]^+$	0.000369
$[MgSO_4]^0$	0.000000
$[Mg_4(OH)_4]^{4+}$	0.000000

Ca^{2+}	
Ca^{2+}	96.332774
$[CaHPO_4]^0$	2.253840
$[CaHCO_3]+$	1.010254
$[CaH_2PO_4]^+$	0.304068
$[CaPO_4]^-$	0.060810
$[CaCO_3]^0$	0.038153
$[Ca(OH)]^+$	0.000101
$[Ca(OH)_2]^0$	0.000000
$[CaSO_4]^0$	0.000000

HCO_3^-	
$[HCO_3]^-$	81.981344
$[H_2CO_3]^0$	16.882468
$[CaHCO_3]^+$	0.601342
$[MgHCO_3]^+$	0.357530
$[CO_3]^{2-}$	0.086025
$[NaCO_3]^-$	0.060283
$[CaCO_3]^0$	0.022710
$[MgCO_3]^0$	0.008297

HPO_4^{2-}	
$[HPO_4]^{2-}$	37.966205
$[H_2PO_4]^-$	29.265540
$[NaHPO_4]^-$	20.693562
$[CaHPO_4]^0$	5.634599
$[MgHPO_4]^0$	4.893046
$[CaH_2PO_4]^+$	0.760170
$[KHPO_4]^-$	0.563298
$[CaPO_4]^-$	0.152025
$[MgPO_4]^-$	0.061297
$[(H_2PO_4)_2]^{2-}$	0.008598
$[PO_4]^{3-}$	0.000644
$[MgH_2PO_4]^+$	0.000553
$[H_3PO_4]^0$	0.000462

SO_4^{2-}	
$[SO_4]^{2-}$	100.000000
$[HSO_4]^-$	0.000000
$[H_2SO_4]^0$	0.000000
$[NaSO_4]^-$	0.000000
$[CaSO_4]^0$	0.000000
$[MgSO_4]^0$	0.000000
$[KSO_4]^-$	0.000000

Cl^-	
Cl^-	99.765767
$[NaCl]^0$	0.124442
$[KCl]^0$	0.082065
$[MgCl]^+$	0.027726
$[HCl]^0$	0.000000

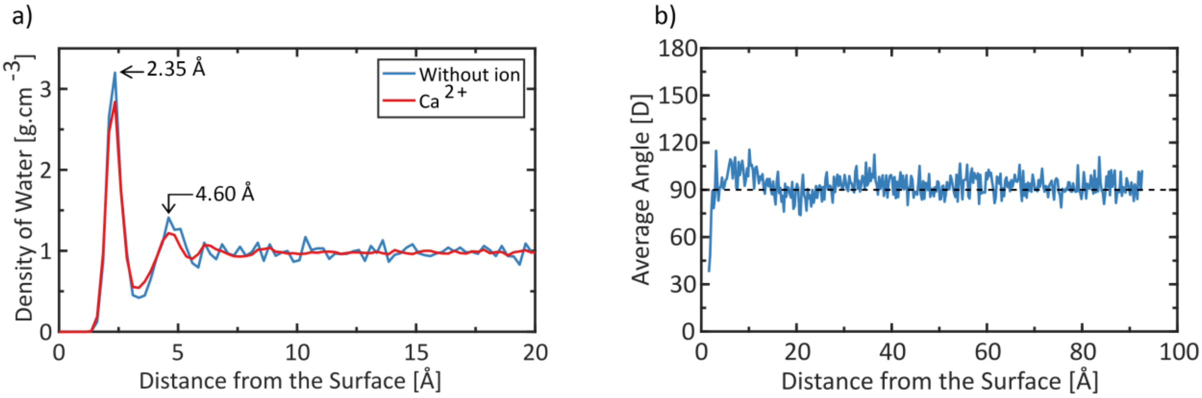

Figure C.1 a) Water density in the z-direction without any ion and with a Ca^{2+} ion; due to the low concentration of ions in the systems, this plot is similar for all the systems and it is only shown for the one which contains the Ca^{2+} ion. b) The average orientation (and consequently dipole) of water molecules in a system without any ion.

C.2 Force field set

The interactions between Ti and ions are considered to be purely electrostatic in Predota *et al.* (4). Interactions between O_{rutile} and ions are considered exactly like interactions between O_{water} and ions, which can be obtained by applying the mixing rules to the Lennard-Jones parameters. While the force field parameters for the cations and chlorine were available, we used the procedure described in the next section to obtain the parameters for CO_3^{2-}, PO_4^{3-}, and HCO_3^-. The parameters used for describing intra- and inter-molecular interactions in this work are presented in Table C.3.

Table C.3 List of all species, their charges and force field parameters.

Component	Species		Charge [e]	ϵ [eV]	σ [Å]
Rutile	Ti		+2.196	0.038419968	1.799239593
	TS (Ti bonded to either of surface hydroxyl groups)		+2.1529	0.038419968	1.799239593
	O		-1.098	0.005933267	2.922416267
	OS (De-protonated O on the surface: charge point)		-1.0174	0.005933267	2.922416267
	Terminal Hydroxyl	OT	-0.9388	0.005933267	2.922416267
		HT	+0.4312	-	-
	Bridging Hydroxyl	OB	-0.9624	0.005933267	2.922416267
		HB	+0.4548	-	-
Ions	K^+		+1	0.004336	3.332
	Na^+		+1	0.004336	2.583
	Ca^{2+}		+2	0.004336	2.895
	Mg^{2+}		+2	0.0379436	1.398
	Cl^-		-1	0.004336	4.401
	CO_3^{2-}	C1	+1.135	3.51E-14	13.7077
		O1	-1.045	2.53E-5	4.4899
	HCO_3^-	C2	+0.926858	3.51E-14	13.7077
		O2	-0.825861	2.53E-5	4.4899
		O3(H)*	-0.601173	2.53E-5	4.4899
		H1	+0.326037	1.07E-8	4.9138
	PO_4^{3-}	P1	+1.180	-	-
		O4	-1.045	2.53E-5	4.49
Water	OW		-0.8476	0.00674	3.166

	HW	+0.4238	-	-

Morse potential parameters ($U(r) = E_0\,[\{1-\exp(-k(r-r_0))\}^2 - 1]$)			
i-j	E_0 [eV]	r_0 [Å]	k [Å^{-2}]
OB-HB OT-HT	5.4245906	0.95	2.2682
C1-O1	4.7100	1.34	3.800
C2-O2	4.7100	1.30	3.800
C2-O3(H)	4.7100	1.50	3.800
O2-H1	7.0525	0.985	4.00
P1-O4	3.47	1.58	2.03

Harmonic potential parameters ($U(r) = \frac{k}{2}(r-r_0)^2$)			
i-j	k [eV Å^{-2}]	r_0 [Å]	
OB-HB	34.70	0.9940	
OT-HT	34.70	0.9830	

Intramolecular Coulombic interaction (%) ($U(r) = \frac{1}{4\pi\epsilon}\frac{q_i q_j}{r_{ij}}$)	
i-j	[%]
OB-HB OT-HT	0
C1-O1 C2-O2 C2-O3(H) O3(H)-H1 P1-O4	100

Three-body potential ($U(\theta) = \frac{k}{2}(\theta-\theta_0)^2$)			
i-j (central atom)-k	k [eV rad^{-2}]	θ_0 [°]	
O1-C1-O1	8.69000	120.00	
O2-C2-O2	12.66	132.60	
O2-C2-O3(H)	8.17	113.90	
C2-O3(H)-H1	4.52	105.82	
O4-P1-O4	1.322626	109.39	

Four-body potential ($U(\varphi) = \frac{k}{2}(\varphi-\varphi_0)^2$)			
i-j-k-l	k [eV rad^{-2}]	φ_0 [°]	
O1-C1-O1-O1 O3(H)-C2-O2-O2 H1-O3(H)-C2-O2	1.60	180.00	

Buckingham potential parameters ($U(r) = A\exp\left(\frac{-r}{\rho}\right) - \frac{C}{r^6}$)			
i-j	A [eV]	ρ [Å]	C [eV Å^6]
Ti-Ti TS-TS Ti-TS	31120.1336	0.1540	5.2500
Ti-O Ti-OS TS-O TS-OS	16957.4923	0.1940	12.5900
Ti-OB	13680.5410	0.2030	12.5900

TS-OB			
Ti-OT TS-OT	13680.5410	0.1940	12.5900
O-O O-OS O-OT O-OB OS-OS OS-OT OS-OB OT-OT OT-OB OB-OB	11782.7328	0.2340	30.2199
Ti-OW TS-OW	1239.9106	0.2650	6.418

Lennard-Jones potential parameters ($U(r) = 4\epsilon\ [(\frac{\sigma}{r})^{12} - (\frac{\sigma}{r})^{6}]$)		
i-j	ϵ [eV]	σ [Å]
K-O_{any}**	0.005405982	3.249
Na- O_{any}	0.005405982	2.8745
Ca- O_{any}	0.005383493	3.0305
Mg- O_{any}	0.015991869	2.282
Cl- O_{any}	0.005405982	3.7835
C1- O_{any}	1.54E-08	8.43685
O1- O_{any}	0.000412943	3.82795
C2- O_{any}	1.54E-08	8.43685
O2- O_{any}	0.000412943	3.82795
H1- O_{any}	8.49E-06	4.0399
O4- O_{any}	0.000412943	3.828
O_{any}-O_{any}	0.00674	3.166

*O(H) represents the protonated oxygen in bicarbonate.

**O_{any} can be O, OS, OT, OB or OW.

C.3 Force fields for polyatomic ions

The same procedures were used for carbonate and phosphate ions:

- The initial parameters for the carbonate ion and the phosphate ion were taken from de Leeuw *et al.* (5) and de Leeuw (6), respectively.
- The oxygen atom in these two references is described with a core-shell model. In order to be able to use a larger timestep, we changed the core-shell model to core-only model. In other words, we considered the charge of the oxygen atom to be the sum of the charge of the core and shell.
- DFT calculations (see below for details) were performed to obtain the structural parameters of the anion (the averaged bond length, angles and dihedrals are shown in Table C.4). Afterwards, we ran MD simulations on a box of vacuum containing several anions and compared their structural properties with the DFT results. The parameters for the bonded interactions were then slightly modified so the structural properties were in a better agreement with DFT results.
- We fitted the two-body non-bonded interactions in the Buckingham form to the Lennard-Jones form. This will enable us to obtain the cross-term interactions using the mixing rules.

Table C.4 Average of structural parameters obtained via DFT. O(H) is the protonated oxygen.

Ion	Bond length [Å]	Angle [°]	Dihedral [°]
CO_3^{2-}	C-O: 1.29	O-C-O: 120.00	O-C-O-O: 0.00
HCO_3^{-}	C-O: 1.25 C-O(H): 1.47 O-H: 0.98	O-C-O: 132.69 O-C-O(H): 113.66 C-O(H)-H: 100.83	O-C-O-O: 0.04 O-C-O-H: 0.06
PO_4^{3-}	P-O: 1.56	O-P-O: 109.39	-

To obtain the force field parameters for bicarbonate, the following steps were performed:

- One hydrogen atom was added to the carbonate anion. The bonded and non-bonded interactions of an OH group were extracted from de Leeuw *et al.* (5) (which is similar to those of de Leeuw (6)).
- The partial charges of the bicarbonate ion were taken from Demichelis *et al.* (7).
- DFT calculations (see below for details) were performed to obtain the structural parameters of the bicarbonate anion (the bond lengths and the angles). Afterwards, we ran MD simulations on a box of vacuum containing several bicarbonate anions and compared their structural properties with the DFT results. The parameters for the bonded interactions were then slightly modified so the structural properties are in a better agreement with DFT results.
- The Lennard-Jones parameters for C and O atoms of the bicarbonate ion were defined similarly to those of the carbonate ion.
- The non-bonded Buckingham potential parameter for the $O-H$ group taken from de Leeuw *et al.* (5) was used to obtain the Lennard-Jones parameter for the H atom.

It is important to note that the carbonate ion has a planar molecular structure (8) which was also confirmed for the bicarbonate ion in our DFT calculations. The bonded parameters in the force field of this ion were set in a way which retained this structural property.

The DFT calculations, needed to determine structural parameters of the polyatomic anions, were carried out using the Quantum ESPRESSO package (9). We used the Perdew-Burke-Ernzerhof (10) gradient-corrected exchange-correlation functional and ultra-soft pseudopotentials (11) with P(3s, 3p), C(2s, 2p), O(2s, 2p) and H(1s) valence electrons. Wave functions were expanded in planewaves up to a kinetic energy cutoff of 40 Ry together with a cutoff of 320 Ry for the augmented density. Reciprocal space was sampled at the gamma point only. The polyatomic anions were placed in a 20×20×20 $Å^3$ cell and the total charge adjusted to the charge of the anion. Structures were then relaxed until forces converged to 0.01 $eV/Å$. We computed Bader pseudo charges by decomposition of the pseudo charge density (12).

The solvation enthalpy of ions in water was calculated to confirm our re-parameterization for the polyatomic anions, as well as the performance of the force field for the monoatomic anions. For this purpose, similar to Dang *et al.* (13) the enthalpy of a box of water was compared to the enthalpy of a box of water containing an ion. Results are presented in Table C.5.

Table C.5 Solvation enthalpy of ions in water.

Ion	Solvation Enthalpy [kJ·mol^{-1}]	Ion	Solvation Enthalpy [kJ·mol^{-1}]
K^+	-264.00[a] -356[c], -330[e]	Cl^-	-326.4[a] -364[b], -335[b] -365[e], -266.94[g]
Na^+	-355.20[a] -468.6[b], -439.3[b] -447.7[c], -415[e], -406.68[g]	CO_3^{2-}	-1252.8[a] -1395[e], -1390[f]
Ca^{2+}	-1509.12[a] -1600[e], -1532[f]	HCO_3^{-}	-325.536[a] -380[e]
Mg^{2+}	-1936.32[a] -1945[e], -1876[f]	PO_4^{3-}	-2370.9[a] -2636.7[d], -2875[e]

[a]This work, [b]Dang *et al.* (13), [c]Dang (14), [d]Demichelis *et al.* (15), [e]Marcus (16), [f]Raiteri *et al.* (17), [g]Zhu *et al.* (18)

MD simulations on a box of water containing the anions were carried out to assure the stability and performance of the modified force field parameters. Figure C.2 to Figure C.4 show the radial distribution function of different atoms of polyatomic anions with water which we obtained using our modified force field parameters. We also present those previously reported by other groups obtained by either *ab initio* or MD studies, extracted from the original paper by WebPlotDigitizer v4.0 (19).

The overall coordination number for different ions and the first minimum of the RDF can be seen in Table C.6 and are acceptable compared to the values found in the literature.

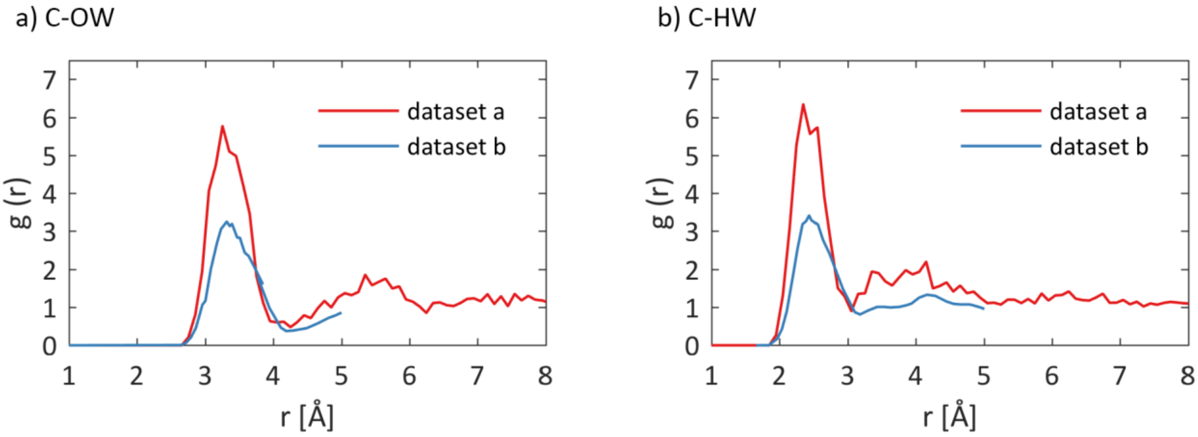

Figure C.2 Radial distribution function between carbonate and water, a) C-OW and b) C-HW. Dataset a is this work and dataset b is Zeebe (20).

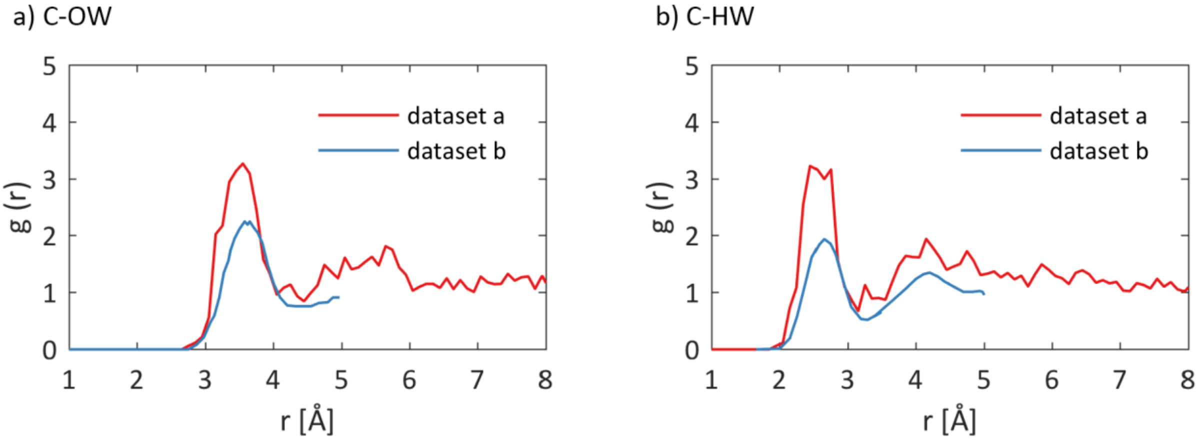

Figure C.3 Radial distribution function between bicarbonate and water, a) C-OW and b) C-HW. Dataset a is this work and dataset b is Zeebe (20).

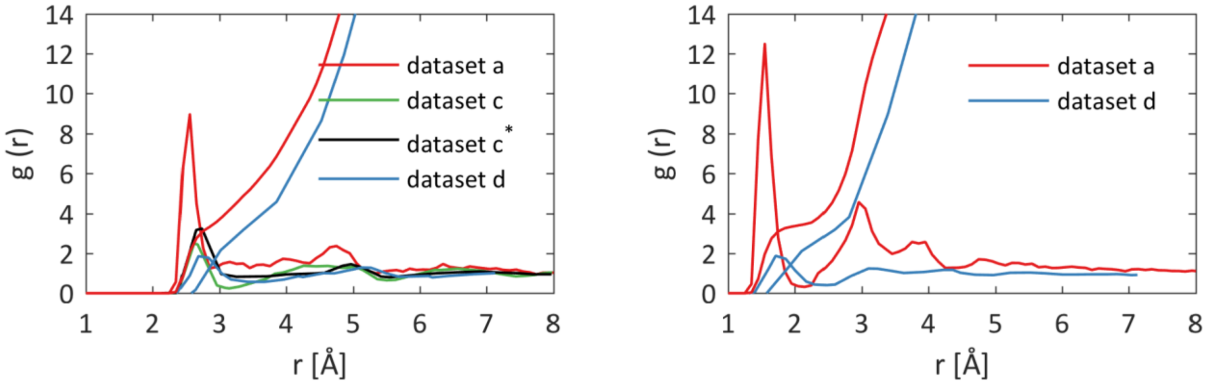

a) O-OW

b) O-HW

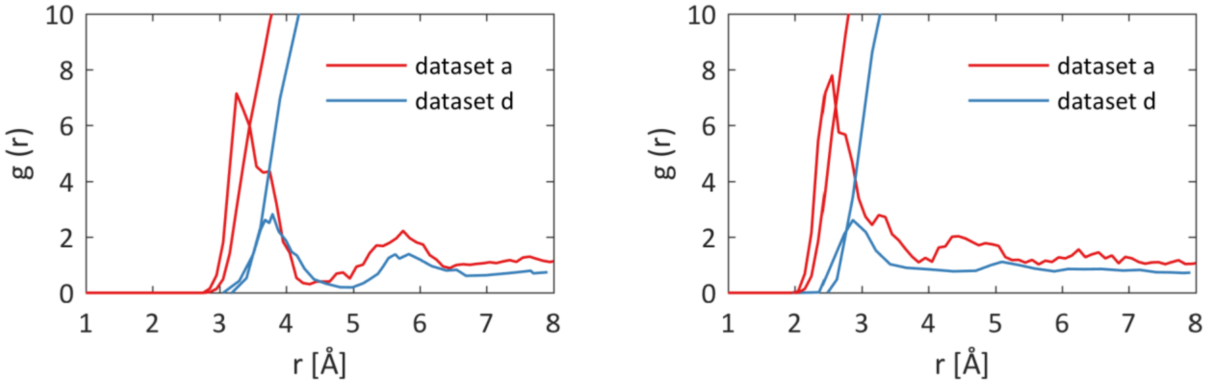

c) P-OW

d) P-HW

Figure C.4 Radial distribution function between phosphate and water, a) O-OW, b) O-HW, c) P-OW and d) P-HW. Dataset a is this work, datasets c and c are from Demichelis et al. (15); dataset c is obtained from ab initio calculations while dataset c* is from force field simulations. Dataset d is taken from Pribil et al. (21).*

Table C.6 The coordination number of ions and the position of the first minimum of the RDF with the oxygen of water at 298 K.

Ion	Coordination number	$r_{\text{first minimum}}$ [Å]	Ion	Coordination number	$r_{\text{first minimum}}$ [Å]
K^+	6.4$^{\text{this work}}$ 5.0^a 5.3^a 7.2^b	3.45	Cl^-	6.7$^{\text{this work}}$ 6.48^a 7.4^b	3.95
Na^+	5.1$^{\text{this work}}$ 4.75^a 5.6^a 5.9^b	3.05	CO_3^{2-}	10.9$^{\text{this work}}$ 12.1^c 8.7^e 9.1^f	4.15
Ca^{2+}	6.6$^{\text{this work}}$ 6.1^a 7.2^c 7.5^d 7-8.1^d	2.85	HCO_3^-	6.9$^{\text{this work}}$ 6.9^e	4.05
Mg^{2+}	5.9$^{\text{this work}}$ 6.0^{a,c,d}	2.35	PO_4^{3-}	11.5$^{\text{this work}}$	4.25

[a]David *et al.* (22), [b]Lee *et al.* (23), [c]Raiteri *et al.* (17), [d]Larentzos *et al.* (24), [e]Leung *et al.* (25), [f]Kameda *et al.* (26)

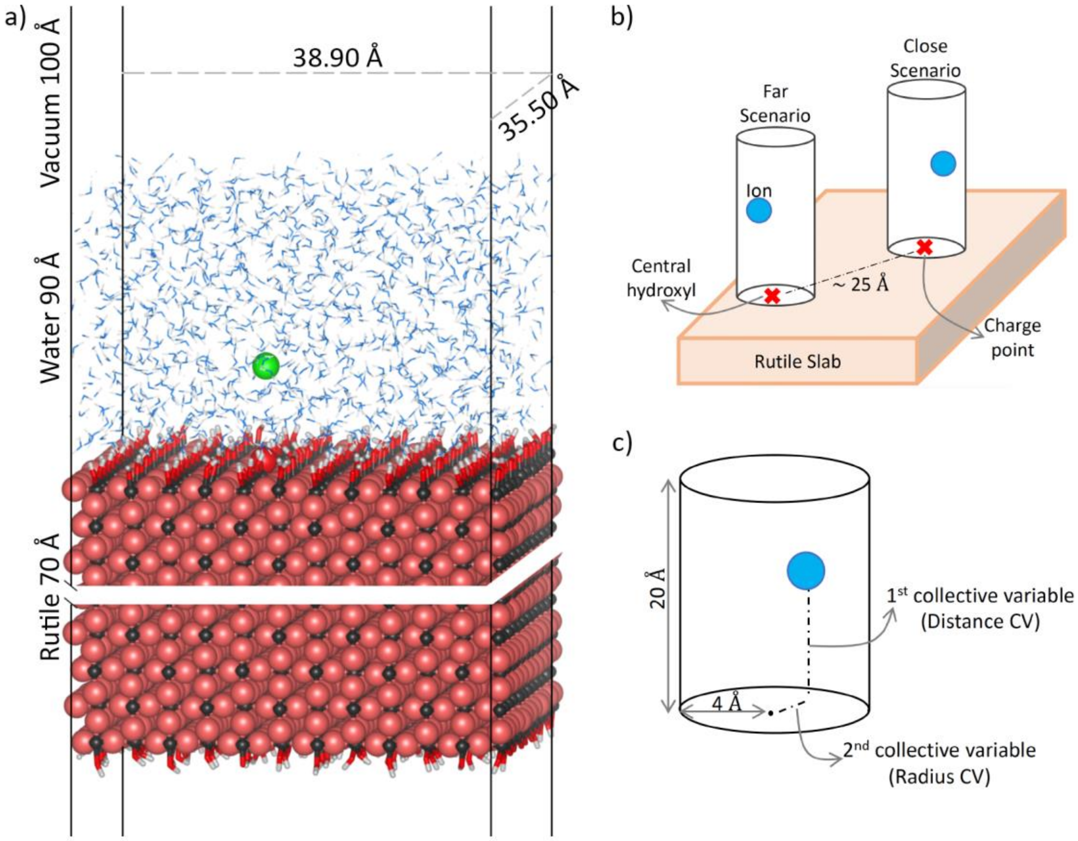

Figure C.5 a) Schematic of the simulation box. Ti: grey, bulk rutile O: bright red, surface rutile O: red, water O: blue, H: white, ion: green. The de-protonated oxygen on the surface is shown slightly larger. Water molecules and surface hydroxyl groups are shown in the ball-and-stick model for the sake of clarity. Vesta (27) was used for visualization. b) schematic of the close and far scenarios and c) distance and radius collective variables.

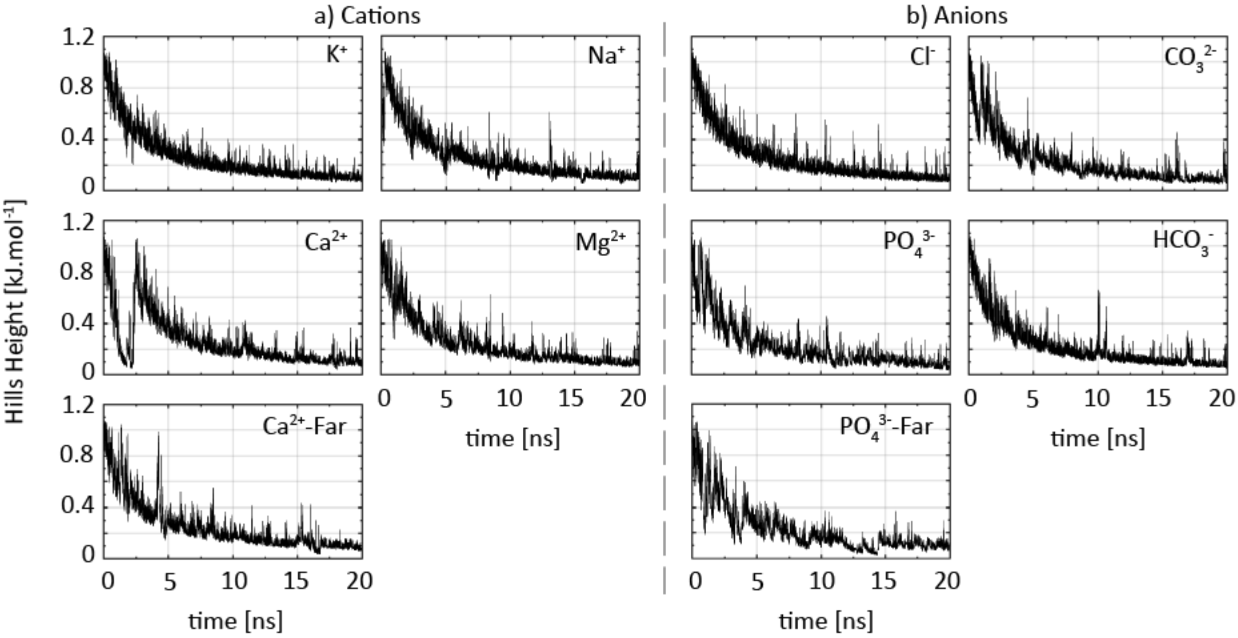

Figure C.6 Hills height over the simulation time.

C.4 Collective variables

In Figure C.7, we present distance CV and radius CV, as well as the coordination number with respect to water molecules, for different ions. The coordination number as a function of time was calculated using PLUMED which requires a cutoff distance up to which the coordination number will be calculated. The coordination number of the ion can be obtained via the integration of the radial distribution function of the water and the ion, up to its first minimum (18,28). Therefore, first, we plotted the RDF between the ion and the oxygen of water at 310 K, based on which we determined the cutoff radius used in PLUMED.

It is interesting to mention that neither of the walls applied to the distance CV and radius CV cause the ions to stay close to the wall. As it can be seen in Figure C.7, the ions are immediately sent back to intermediate CV values. By comparing Figure 4.1 and Figure C.7, we conclude that regions with a smaller free energy close to the walls, either in the direction of distance CV or radius CV, are physically in a lower energy state and this is not an artifact due to the walls.

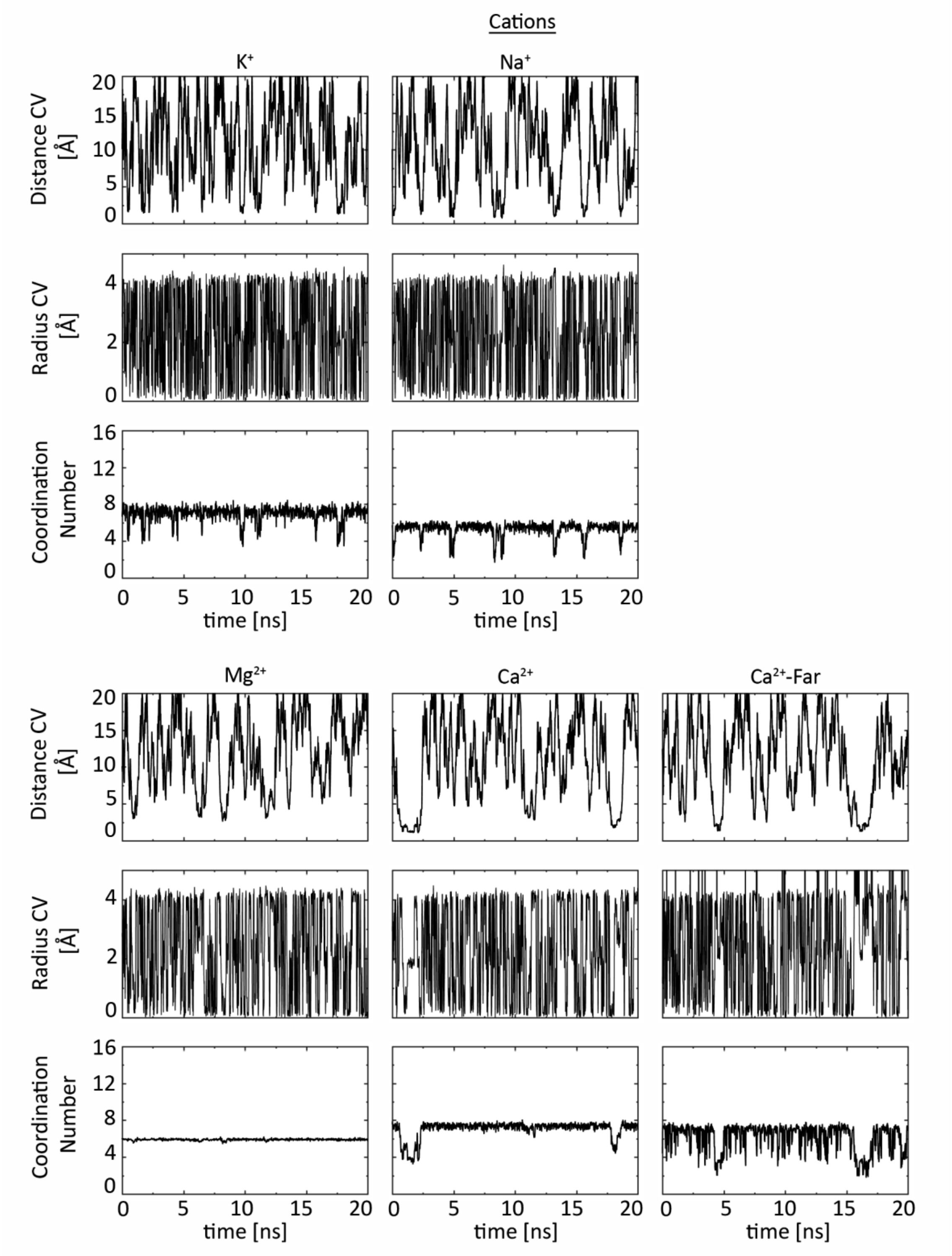
Cations
K⁺
Na⁺
Mg²⁺
Ca²⁺
Ca²⁺-Far
Distance CV [Å]
Radius CV [Å]
Coordination Number
time [ns]
0
5
10
15
20
0
2
4
0
4
8
12
16

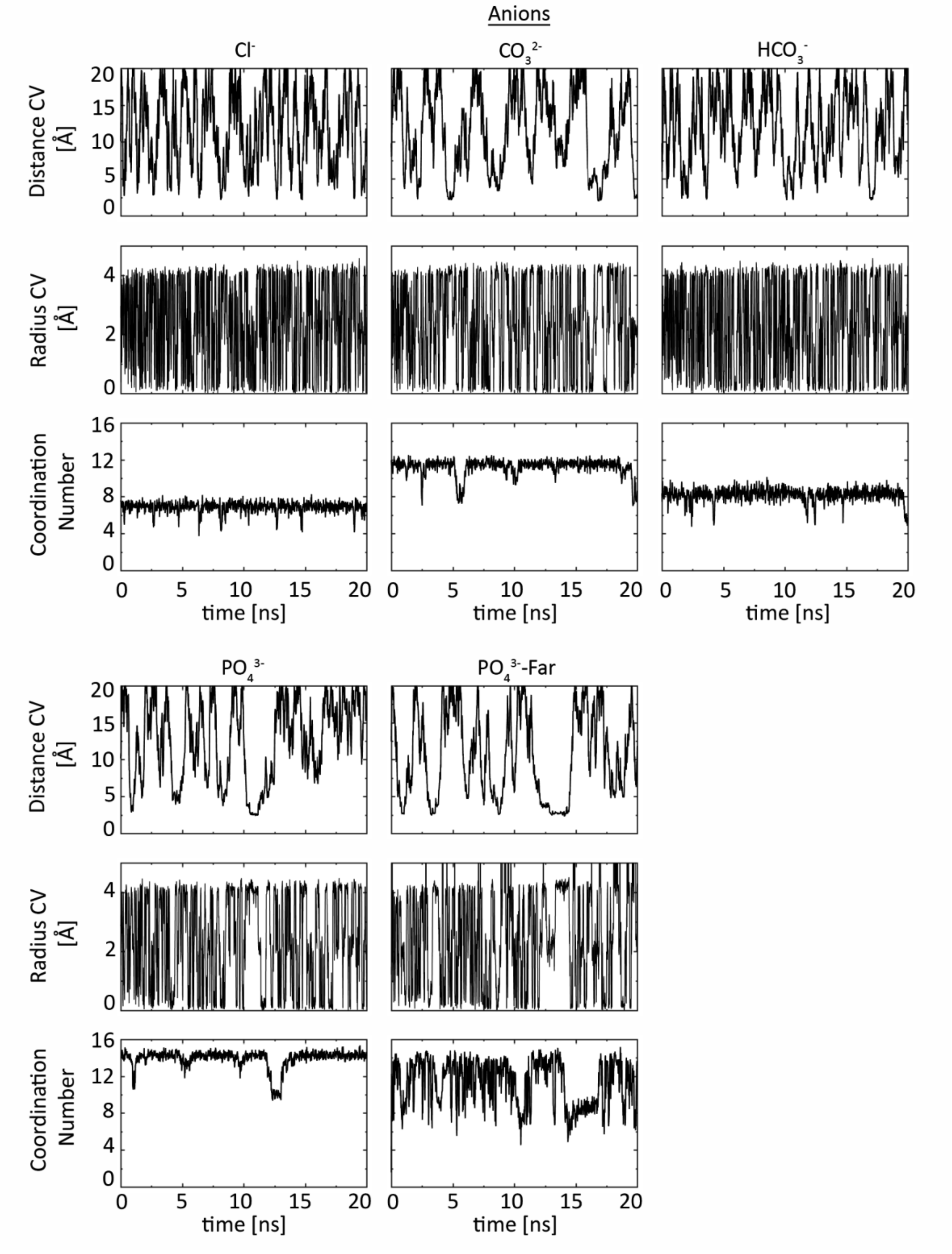

Figure C.7 Variation of the collective variables (Red: distance CV and Blue: radius CV), as well as Black: coordination number, over the simulation time for cations and anions.

References

1. Kokubo, T., Kim, H.-M. & Kawashita, M. Novel bioactive materials with different mechanical properties. *Focus Biomater. Sci. Asia* **24,** 2161–2175 (2003).

2. Vereecke, G. & Lemaître, J. Calculation of the solubility diagrams in the system $Ca(OH)_2$-H_3PO_4-KOH-HNO_3-CO_2-H_2O. *J. Cryst. Growth* **104,** 820–832 (1990).

3. Zhao, W., Lemaître, J. & Bowen, P. A comparative study of simulated body fluids in the presence of proteins. *Acta Biomater.* **53,** 506–514 (2017).

4. Předota, M. *et al.* Electric double layer at the rutile (110) surface. 1. Structure of surfaces and interfacial water from molecular dynamics by use of *ab initio* potentials. *J. Phys. Chem. B* **108,** 12049–12060 (2004).

5. de Leeuw, N. H., Bowe, J. R. & Rabone, J. A. L. A computational investigation of stoichiometric and calcium-deficient oxy- and hydroxy-apatites. *Faraday Discuss.* **134,** 195–214 (2007).

6. de Leeuw, N. H. A computer modelling study of the uptake and segregation of fluoride ions at the hydrated hydroxyapatite (0001) surface: introducing a $Ca_{10}(PO_4)_6(OH)_2$ potential model. *Phys. Chem. Chem. Phys.* **6,** 1860–1866 (2004).

7. Demichelis, R., Raiteri, P., Gale, J. D., Quigley, D. & Gebauer, D. Stable prenucleation mineral clusters are liquid-like ionic polymers. *Nat. Commun.* **2,** 590 (2011).

8. Patrito, E. M. & Olivera, P. P. Adsorption of carbonate species on silver. I. Nature of the surface bond. *Electrochim Acta* **44,** 1237–1245 (1998).

9. Giannozzi, P. *et al.* QUANTUM ESPRESSO: A modular and open-source software project for quantum simulations of materials. *J. Phys. Condens. Matter* **21,** 395502 (2009).

10. Perdew, J. P., Burke, K. & Ernzerhof, M. Generalized gradient approximation made simple. *Phys. Rev. Lett.* **77,** 3865–3868 (1996).

11. Vanderbilt, D. Soft self-consistent pseudopotentials in a generalized eigenvalue formalism. *Phys. Rev. B* **41,** 7892–7895 (1990).

12. Tang, W., Sanville, E., & Henkelman, G. A grid-based Bader analysis algorithm without lattice bias. *J. Phys. Condens. Matter* **21,** 084204 (2009).

13. Dang, L. X., Rice, J. E., Caldwell, J. & Kollman, P. A. Ion solvation in polarizable water: Molecular dynamics simulations. *J. Am. Chem. Soc.* **113,** 2481–2486 (1991).

14. Dang, L. X. Mechanism and thermodynamics of ion selectivity in aqueous solutions of 18-crown-6 ether: A molecular dynamics study. *J. Am. Chem. Soc.* **117,** 6954–6960 (1995).

15. Demichelis, R. *et al.* Simulation of calcium phosphate species in aqueous solution: force field derivation. *J. Phys. Chem. B* **122,** 1471–1483 (2018).

16. Marcus, Y. A simple empirical model describing the thermodynamics of hydration of ions of widely varying charges, sizes, and shapes. *Biophys. Chem.* **51,** 111–127 (1994).

17. Raiteri, P., Demichelis, R. & Gale, J. D. Thermodynamically consistent force field for molecular dynamics simulations of alkaline-earth carbonates and their aqueous speciation. *J. Phys. Chem. C* **119,** 24447–24458 (2015).

18. Zhu, S. & Robinson, G. W. Molecular-dynamics computer simulation of an aqueous NaCl solution: Structure. *J. Chem. Phys.* **97,** 4336–4348 (1992).

19. Rohatgi, A. WebPlotDigitizer. v4.0. (2017).

20. Zeebe, R. E. On the molecular diffusion coefficients of dissolved CO_2,HCO_3^-, and CO_3^{2-} and their dependence on isotopic mass. *Geochim. Cosmochim. Acta* **75,** 2483–2498 (2011).

21. Pribil Andreas B., Hofer Thomas S., Randolf Bernhard R. & Rode Bernd M. Structure and dynamics of phosphate ion in aqueous solution: An *ab initio* QMCF MD study. *J. Comput. Chem.* **29,** 2330–2334 (2008).

22. David, F., Vokhmin, V. & Ionova, G. Water characteristics depend on the ionic environment. Thermodynamics and modelisation of the aquo ions. *J. Mol. Liq.* **90,** 45–62 (2001).

23. Lee, S. H. & Rasaiah, J. C. Molecular dynamics simulation of ion mobility. 2. Alkali metal and halide ions using the SPC/E model for water at 25 °C. *J. Phys. Chem.* **100,** 1420–1425 (1996).

24. Larentzos, J. P. & Criscenti, L. J. A Molecular dynamics study of alkaline earth metal−chloride complexation in aqueous solution. *J. Phys. Chem. B* **112,** 14243–14250 (2008).

25. Leung, K., Nielsen, I. M. B. & Kurtz, I. *Ab Initio* molecular dynamics study of carbon dioxide and bicarbonate hydration and the nucleophilic attack of hydroxide on CO_2. *J. Phys. Chem. B* **111,** 4453–4459 (2007).

26. Kameda, Y., Sasaki, M., Hino, S., Amo, Y. & Usuki, T. Neutron diffraction study on the hydration structure of carbonate ion by means of 12C/13C isotopic substitution method. *Phys. B Condens. Matter* **385–386,** 279–281 (2006).

27. Momma, K. & Izumi, F. VESTA: A three-dimensional visualization system for electronic and structural analysis. (2014).

28. Impey, R. W., Madden, P. A. & McDonald, I. R. Hydration and mobility of ions in solution. *J. Phys. Chem.* **87,** 5071–5083 (1983).

Appendix D Supporting Information - Adsorption Free Energy of Single Amino Acids at the Rutile (110)/Water Interface Studied by Well-tempered Metadynamics

---

Supporting Information
Journal of Physical Chemistry C 122 (2018) 11355-11363

Adsorption Free Energy of Single Amino Acids at the Rutile (110)/Water Interface Studied by Well-tempered Metadynamics

Azade YazdanYar[✦], *Ulrich Aschauer*[✦✦], *Paul Bowen*[✦]
[✦] Department of Materials Science and Engineering, École Polytechnique Fédérale de Lausanne (EPFL), Lausanne 1015, Switzerland
[✦✦] Department of Chemistry and Biochemistry, University of Bern, Bern 3012, Switzerland

---

D.1 Top view of the rutile surface

Figure D.1 shows the top view of the surface and the position of the deprotonated hydroxyl group on the surface. Since periodic boundary conditions are applied in all three directions, we could have deprotonated any of the bridging hydroxyl groups as long as we restraint the in-plane movement of the amino acid around the charge point, as shown by the circle in Figure D.1. For more details on the hydroxylated rutile (110) surface, please refer to Predota *et al.* (1) or YazdanYar *et al.* (2).

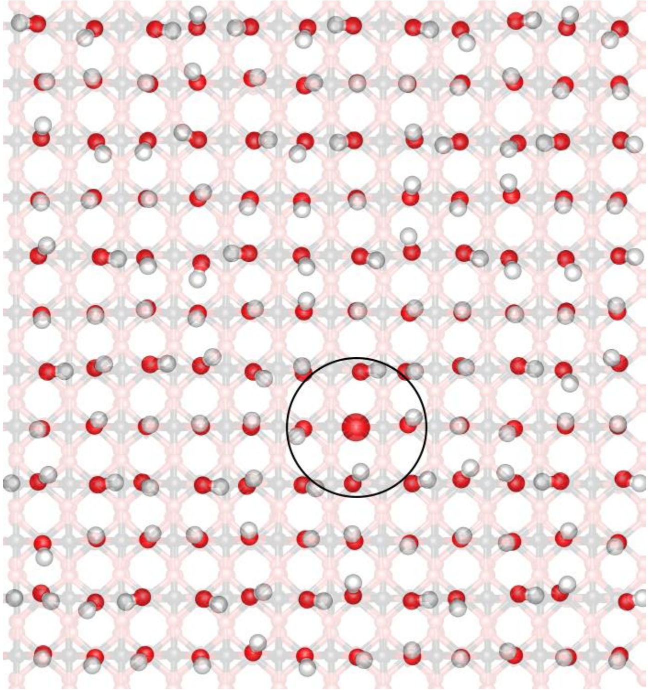

Figure D.1 Top view of the rutile surface. For the sake of clarity, bulk atoms are shown transparent (Ti: grey, O of rutile: orange, O of the hydroxyl groups: red and H of the hydroxyl groups: white). The deprotonated oxygen is shown slightly larger than protonated hydroxyls. The area around the charge point, to which the amino acids are restrained, is shown by the circle.

D.2 Partial charge of atomic species in the surface charge density of -0.011 C·m^{-2}

We used a solid slab of rutile (110) with similar dimensions to Predota *et al.* (1,3); as they mention in table 2 of Predota *et al.* (3), there are 144 bridging and 144 terminal hydroxyls in total on the two surfaces of the slab.

In their calculations, they use the surface area of both faces of the solid slab to obtain the surface charge density. They mention that: 'deprotonation of 36 bridging hydrogens results in a surface charge density of -0.208 $C \cdot m^{-2}$:

$$\sigma = \frac{Charge}{Area} \Longrightarrow Area = \frac{Charge}{\sigma}$$

$$Charge = \frac{-36}{6.24 * 10^{18}} = -5.769 * 10^{-18}\ [C]$$

$$Area = \frac{-5.769 * 10^{-18}}{-0.208} \Rightarrow Area = 2.77 * 10^{-17}\ m^2 = 2.77 * 10^3\ [\text{Å}^2]$$

which is the sum of the surface area of both faces of the slab.

In our calculations, however, we consider only the surface area of one of the faces for calculating the surface charge density since the thickness of the slab and the vacuum gap are chosen in a way which prevent the interaction of the bottom and upper faces of the slab. In this manner, deprotonating one bridging hydroxyl leads to a surface charge density of -0.011 $C \cdot m^{-2}$.

$$\sigma = \frac{(-1/(6.24 * 10^{18}))}{35 * 38 * 10^{-20}} = -0.011 C \cdot m^{-2}$$

In table 3 of Predota *et al.* (3), the partial charges of atomic species of rutile in different surface charge densities are summarized; we present this table here with the difference that we double the surface charge density due to different manner with which we define the surface area for this parameter (Table D.1). Detailed analysis of this table revealed that the change in charge of atomic species with respect to the charge density is linear (Figure D.2). We obtained the linear equation for each species (partial charge $= a *$ charge density $+ b$) and calculated the values at the surface charge density of -0.011 $C \cdot m^{-2}$. The final partial charges, which we used in our simulations for the surface charge density of -0.011 $C \cdot m^{-2}$, are presented in Table D.2.

Table D.1 The partial charge [e] of atomic species of rutile in different surface charge densities. The values are adapted from Predota et al. (3).

Atomic species	details	σ[C·m^{-2}]			
		-0.832	-0.416	-0.208	0.208
TS	Ti atom bound to hydroxyl groups	2.112	2.134	2.146	2.167
OT	Terminal hydroxyl groups	-0.984	-0.960	-0.949	-0.928
HT		0.385	0.409	0.420	0.440
OB	Bridging hydroxyl groups	-1.009	-0.985	-0.976	-0.953
HB		0.410	0.434	0.444	0.465
OS	Deprotonated oxygen in a bridging hydroxyl group	-1.063	-1.039	-1.028	-

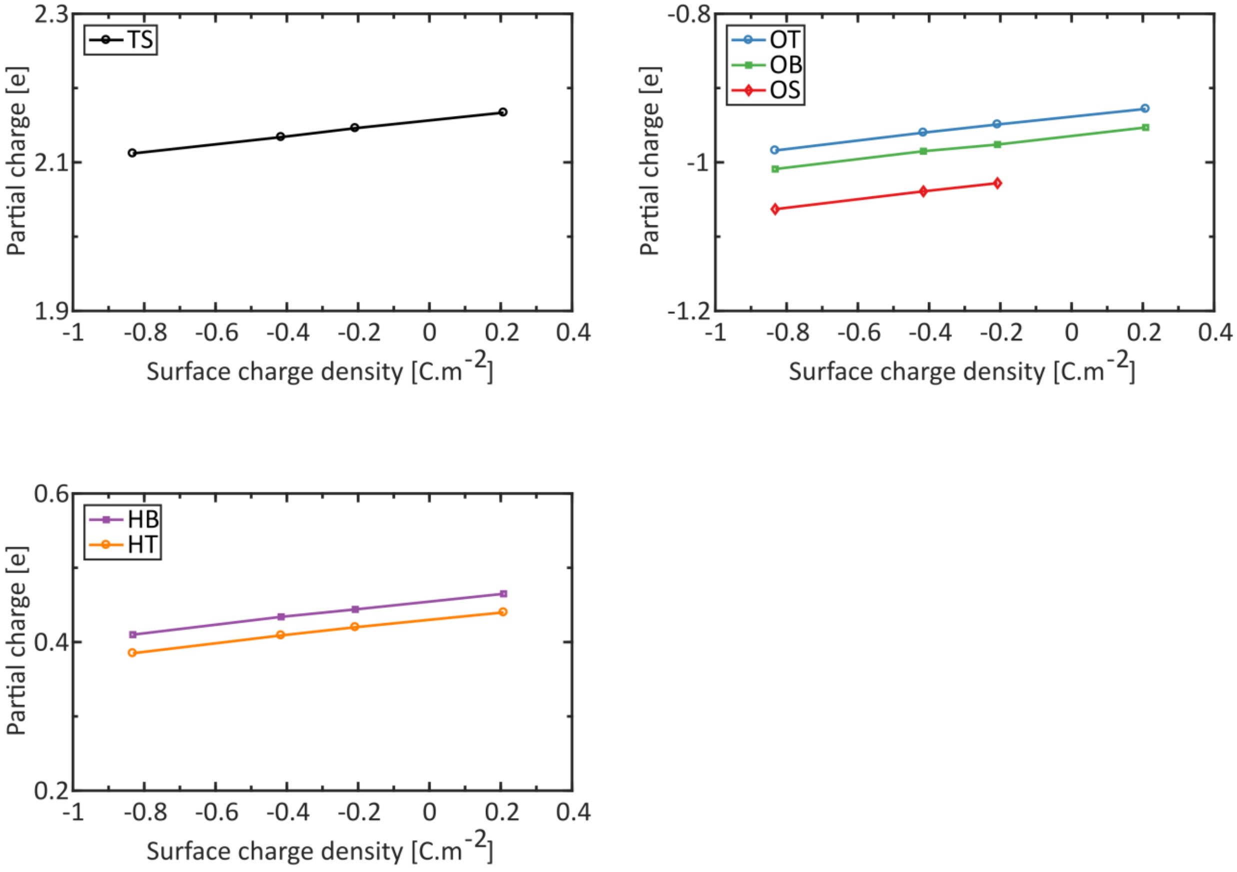

Figure D.2 Variation of partial charge of the atomic species of rutile as a function of the surface charge density.

Table D.2 Partial charge [e] of atomic species of rutile in a surface charge density of -0.011 C·m^{-2}.

Atomic species	TS	OT	HT	OB	HB	OS
Partial charge [e]	2.1529	-0.9388	0.4312	-0.9624	0.4548	-1.0174

D.3 Fitting Lennard-Jones to Buckingham to obtain LJ parameters of rutile

To be able to obtain the parameters needed for describing the interactions between rutile and the organic molecules via the Lorentz-Berthelot mixing rules, we fitted the Lennard-Jones form to the available Buckingham parameters presented by Predota *et al.* (1). The parameters for the Lennard-Jones force field are presented in Table D.3. We also present those previously reported by Kang *et al.* (4). As it can be seen, parameters obtained by us are not very different than those of Kang *et al.* The lattice constants and density were measured after running molecular dynamics simulation using the fitted parameters. Results were compared with the experimental values and those obtained by molecular dynamics simulation using the force field parameters presented by Predota *et al.* (1) (

Table D.4).

Table D.3 LJ parameters for the atomic species of rutile.

Atomic species	This work		Kang *et al.* (4)	
	ϵ [eV]	σ [Å]	ϵ [eV]	σ [Å]
Ti TS	0.0384	1.799	0.0264	1.9565
O	0.0059	2.922	0.0061	2.9273
OT OB OS	0.0059	2.922	0.0067	3.1656

Table D.4 Comparison of experimental values with results obtained from simulation using the parameters presented by Predota et al. and parameters obtained by fitting Lennard-Jones form to the Buckingham form.

	Experimental	Using force field parameters of Predota *et al.* (1)	Using the parameters obtained by fitting
a (=b) [Å]	4.59	4.49	4.47
c [Å]	2.96	3.01	3.01
ρ [g·cm^{-3}]	4.24	4.37	4.41

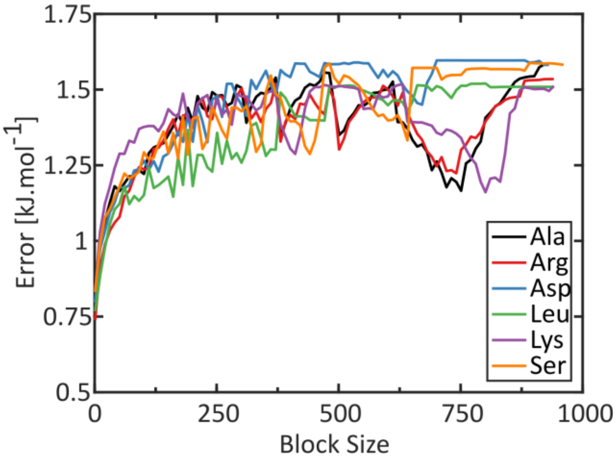

Figure D.3 The error associated with the calculations as a function of the block size in the block analysis (before reweighting).

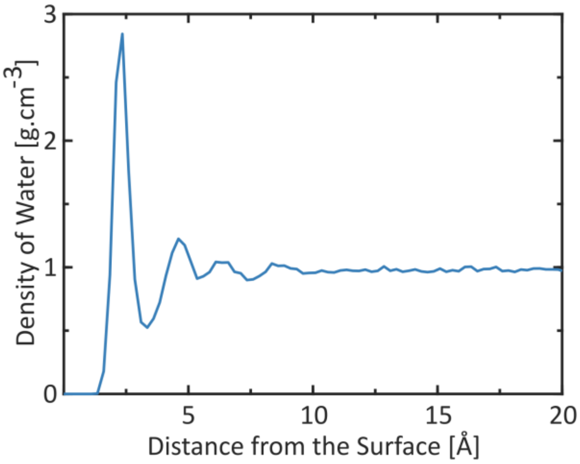

Figure D.4 Density of water in the normal direction of the rutile (110) surface. This plot is for the system containing Ala, but the plot is similar for all other amino acids that are not shown.

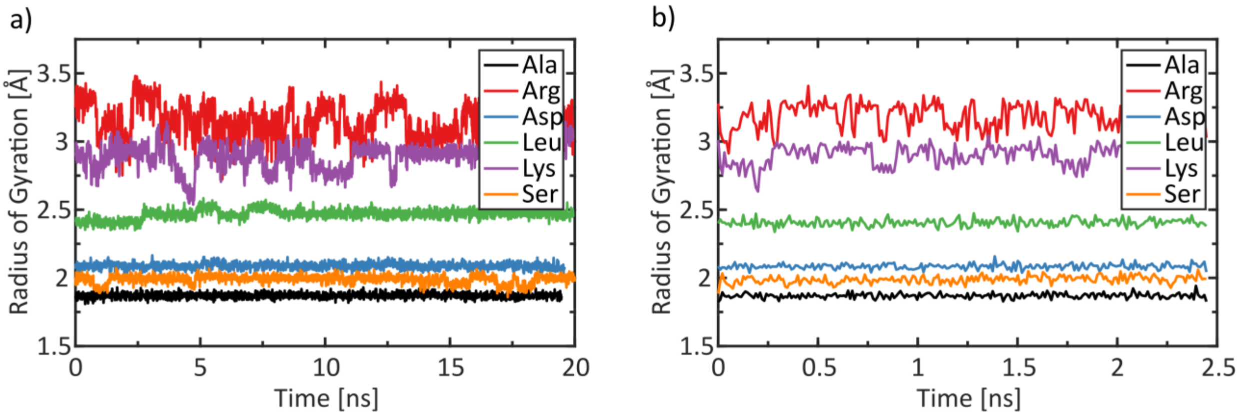

Figure D.5 Radius of gyration of different amino acids solvated in water a) and b) without the inorganic surface. The Rg is similar in both systems for all amino acids.

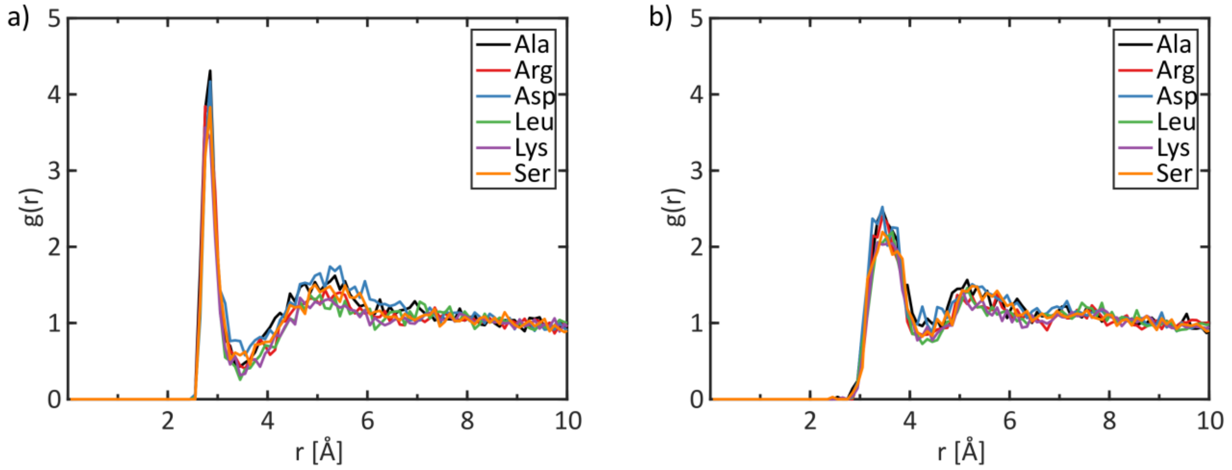

Figure D.6 Radial distribution function of the a) amine group and b) carboxyl group with oxygen of water (OW).

References

1. Předota, M. *et al.* Electric double layer at the rutile (110) surface. 1. Structure of surfaces and interfacial water from molecular dynamics by use of *ab initio* potentials. *J. Phys. Chem. B* **108,** 12049–12060 (2004).

2. YazdanYar, A., Aschauer, U. & Bowen, P. Interaction of biologically relevant ions and organic molecules with titanium oxide (rutile) surfaces: A review on molecular dynamics studies. *Colloids Surf. B Biointerfaces* **161,** 563–577 (2018).

3. Předota, M., Machesky, M. L., Wesolowski, D. J. & Cummings, P. T. Electric double layer at the rutile (110) surface. 4. Effect of temperature and pH on the adsorption and dynamics of ions. *J. Phys. Chem. C* **117,** 22852–22866 (2013).

4. Kang, Y., Li, X., Tu, Y., Wang, Q. & Ågren, H. On the mechanism of protein adsorption onto hydroxylated and nonhydroxylated TiO_2 surfaces. *J. Phys. Chem. C* **114,** 14496–14502 (2010).

Curriculum Vitae

AZADE YAZDANYAR

May 21st, 1989
Iranian
Azade.yazdanyar@gmail.com

EDUCATION

- **Ph.D.** in Material Science, École polytechnique fédérale de Lausanne (EPFL), Lausanne, Switzerland 2014-2018
    - Atomistic simulation of bio-relevant ionic and organic species interacting with rutile – Towards the understanding of apatite formation
    - Supervised by Prof. P. Bowen and Prof. U. Aschauer
- **M.Sc.** of Material Science and Engineering (Design and Selection), Sharif University of Technology (SUT), Tehran, Iran 2011-2013
    - Study of melting and rapid solidification of TiAl alloy and formation of its diffusion bonded structure using molecular dynamics simulation
    - Supervised by Prof. H. Aashuri and Prof. A. Simchi
- **B.Sc.** of Material Science and Engineering, Sharif University of Technology (SUT), Tehran, Iran 2007-2011
    - A study on NiO-YSZ suspension stability for SOFC's anode fabrication
    - Supervised by Prof. A. Simchi

PROFESSIONAL EXPERIENCE

- **Doctoral assistant** – Laboratory of Powder Technology, EPFL, Lausanne, Switzerland 2014-2018
    - Force field development and modification for inorganic and ionic materials
    - *In silico* study of solid-solution interfaces in semi *in vitro* conditions
    - In-depth study of the adsorption behaviour of ionic and organic residues on inorganic surfaces
- **IT administrator** – Laboratory of Powder Technology, EPFL, Lausanne, Switzerland 2017-2018
    - Coordination of IT tasks for the laboratory – solving user-end problems, setting up systems for new personnel, adding new workstations on the school domain
- **Teaching assistant** of "Ceramics and Colloids" – Laboratory of Powder Technology, EPFL, Lausanne, Switzerland 2014-2017
    - Supervision of B.Sc. students during the practical course – four semesters

SUPERVISED STUDENT PROJECTS

- Interaction of Simulated Body Fluid (SBF) ions with the titanium dioxide surface: Classical molecular dynamics, Amarnath Jayaprakash 2016
- Atomistic simulations of the interaction of titanium dioxide surface with SBF ions – MD, Manon Chastaing
- Adsorption of amino acids on a rutile powder in an ionic solution, Delphin Pantaloni 2017
- Measurement of adsorption isotherm of amino acids on the rutile powder using different methods, Mohammadreza Rostami 2018
- Amino acids adsorption on a rutile powder and the effect of Tris buffer on the adsorption, Léa Buswell

SKILLS

- Expertise in computational methods:
  - ✦ Metadynamics
  - ✦ Molecular Dynamics
  - ✦ Density Functional Theory, Finite Element Method and Phase Field Modelling
- Expertise using established simulation codes:
  - ✦ Dlpoly
  - ✦ Plumed
  - ✦ Lammps
  - ✦ Amber
- Programming expertise with:
  - ✦ Matlab, R and Mathematica / Bash, Python and Pascal

PUBLICATIONS

- A. YazdanYar, U. Aschauer, P. Bowen, 'Adsorption free energy of single amino acids at the rutile (110)/water interface studied by well-tempered metadynamics', Journal of Physical Chemistry C, 122 (2018) 11355-11363.
- A. YazdanYar, U. Aschauer, P. Bowen, 'Interaction of biologically relevant ions and organic molecules with titanium oxide (rutile) surfaces: A review on molecular dynamics studies', Colloids and Surfaces B: Biointerfaces, 161 (2018) 563-577.
- M. Mirzaei, A. Simchi, M.A. Faghihi-Sani, A. YazdanYar, 'Electrophoretic deposition and sintering of a nanostructured manganese–cobalt spinel coating for solid oxide fuel cell interconnects', Ceramics International, 42 (2016) 6648-6656.

TALK

- Invited speaker to "Plumed – User Meeting". Interaction of Simulated Body Fluid (SBF) ions with a rutile surface: Linking bioactivity and free energy calculations – May 25th 2017, Trieste, Italy.

SCIENTIFIC MEETINGS

- LTP Extramuros, A Powder Technology Workshop – 29 years of Badly Behaved Powders…or not?, 11-13 October, Rigi Kaltbad, Lucerne, Switzerland 2017
- EUROMAT, 18-22 September, Thessaloniki, Greece
- PLUMED meeting, 25-27 May, Scuola Internazionale di Studi Avanzati (SISSA), Trieste, Italy

- Free Energy Calculation and Molecular Kinetics Workshop, 13-15 September, King's College London, London, United Kingdom 2016
- Nucleation: past and future challenges for experiment, theory and simulation, 5-6 September, Chicheley Hall, United Kingdom
- CCMX Summer school, Multiscale modelling of materials, 29-31 August, EPFL, Lausanne, Switzerland
- Biointerfaces, 23-25 August, University of Zurich, Zurich, Switzerland
- SAOG, 22 January, University of Fribourg, Fribourg, Switzerland

- CCP5 Annual Meeting, 7-9 September, Lancaster University, Lancaster, United Kingdom 2015
- LTP Extramuros, 14-16 August, Villars, Switzerland
- Summer school, Crystal shape engineering, 6-10 July, ETH Zurich, Zurich, Switzerland

- DL_Software Workshop, 8-10 December, Hartree Center, Daresbury Laboratory, Cheshire, United Kingdom 2014
- CCMX Summer School, Atomistic Scale Modelling of Materials, 1-3 September, EPFL, Lausanne, Switzerland

LANGUAGES

- English: Fluent (C1)
- French: Intermediate (B1-B2)
- Farsi: Native

INTERESTS

Reading, Ice creams, Trees, Zumba, Dancing, Music, Knitting, Sewing – in no specific order